Experimental study of swimming flagellated bacteria and their collective behaviour in concentrated suspensions

Martin Li

A thesis submitted in the fulfilment of the requirements
for the degree of Doctor of Philosophy
to the University of Edinburgh

2010

Abstract

This thesis investigates bacterial motility from the mechanism permitting individual self-propulsion to the complex collective flocking motility in *Escherichia coli* and *Bacillus subtilis* cells. Understanding bacterial swimming has intrigued scientists for decades and recently there has been a growing interest in collective swimming behaviour. The first part of this thesis reviews the characteristics of *E. coli* and *B. subtilis* cells subsequently describing the governing physics and constraints of self-propulsion in the low Reynolds regime. The second part of this thesis presents three self-contained experimental sections, examining individual swimming in non-conventional body shaped cells and subsequently focusing on concentrated bacterial swimming in normal cells.

We first investigated motility in mutant spherical *E. coli* cells KJB24 motivated by simulations, which often model bacteria as self-propelled spheres. Somewhat unexpectedly these spherical cells do not exhibit runs and tumbles but diffuse slower than expected. As an introduction to working with microbiology and to familiarise with microbiology techniques we investigated why these spherical cells do not swim. Secondly we investigated how cellular motility varies as a function of body length by inhibiting cell division in wild-type *E. coli* with cephalexin; which remained motile despite body elongation. Fluorescent flagella visualization provided evidence of multiple bundle formations along the lateral walls as a mechanism to sustain motility. The average swimming velocity, body and flagella rotation rates, the number of flagella and number of flagella bundles were extracted experimentally as a function of length. The extracted experimental parameters for normal sized cells were consistent with Purcell's model. We explored simple adaptations and scaling of this model to describe motility for filamentous cells, which agrees with experimental values.

The main focus is on collective behaviour of *B. subtilis* by examining the onset from individual swimming to collective motility using time-lapse microscopy. Results demonstrated a smooth transition where cells self-organize into domains expanding rapidly by recruiting cells. We present advancements in *B. subtilis* fluorescent flagella staining which revealed unexpected multiple flagella bundle arrangements during runs, contradictory to general conjectures. Novel visualisation of flagella filaments during reversal events is presented in both *E. coli* and *B. subtilis* cells, providing experimental evidence for complex flagella 'flipping'. Cellular reversal is hypothesized as a mechanism for quorum polarity facilitating collective swimming. We present novel flagella imaging in the setting of collective behaviour showing evidence to support quorum polarity. Subsequently we extracted the run length distributions of cells as a function of concentration, yielding a decreasing trend with increasing concentration. Using particle tracking we quantitatively extracted the mean squared displacement of swimming cells versus passive tracers at different concentrations during collective swimming, these novel results are discussed in respect to recent simulations. These presented experiments provide new insights into collective behaviour improving current understanding of this phenomenon.

Declaration

This thesis has been composed by myself and has not been submitted for any other degree or professional qualification. The work within was executed by me, unless otherwise stated.

Martin Li

April 2010

Acknowledgements

This unforgettable experience would not have been the same without all the outstanding people I have met and whom have supported me on numerous fronts during my PhD. Firstly and foremost I would like to thank my supervisor Jochen Arlt for providing me the opportunity to carryout this research. His support, encouragement and his ability to find time for discussions is deeply appreciated. Without Jochen's passion, vision and commitment to the subject, this research would not have seen the light of day. Jochen has supported me during some of the most challenging times of my life, especially at the beginning of my PhD programme which I am truly grateful for and indebted to.

I thank Wilson Poon and Alexander Morozov for fruitful conversations and their expertises which have challenged me to search for scientific truth. I am also gratefully to Laurence Wilson for insightful conversations regarding optical tweezers and microscopy techniques. I am indebted to Angela Dawson for her expertise in biology, and the countless times she provided me with excellent advice and guidance. I sincerely thank Nhan Pham for his support and his knowledge regarding microfluidics and preparing my samples for AFM. I also thank Nhan for reading my thesis and I will always cherish the entertaining conversations regarding Formula One, and all the laughs we had.

Thank you to Caroline Miles, Jana Schwarz-Linek and Angela Dawson for their company during long hours in the lab, I will always cherish the interesting conversations and laughs, which made some of the mundane aspects of laboratory work more enjoyable. To my offices colleagues Greg, Paul, Tom and Andrew for their support, and epic lunch time conversations and great nights out. Thank you to my family for their moral support and their encouragement. Finally a special thanks to Wendy for all her support and understanding, her simple touch gave me the strength to face the challenges of the day ahead.

To everyone: Thank you.

Contents

Chapter 1 : Introduction

1.1 Why study bacterial motility

Bacteria are one of the most elementary forms of life which appeared on Earth billions of years ago. Although bacteria are millions of years older than mankind, we are still closely related in terms of storing genetic information and carrying out life essential processes. Thus, a number of early solutions to life's problems founded by bacteria have been passed down to us [1]. Bacteria are ubiquitous in nature, where bacteria can thrive naturally on most surfaces, aqueous environments, and in the soil. Bacteria are one of the major contributors of the biomass on Earth and approximately 40 % of bacterial species are motile [2]. Over 25 years ago Henrichsen examined hundreds of bacterial strains and identified six different categories of bacterial motility [3]; swimming, swarming, twitching, sliding, spreading and darting [4]. The advantages of motility enables microorganisms to translocate, actively searching for nutrients, favourable growth conditions and the ability to colonize and infect hosts. Bacterial motility is one of the fundamental means of spreading of infectious diseases, such as cholera (*Vibrio cholerae*), MRSA (Methicillin Resistant *Staphylococcus aureus*), and tuberculosis (*Mycobacterium tuberculosis)* which pose serious health problems. Spreading of highly contagious microorganisms can lead to global and economical impacts such as pandemics. Understanding how bacteria thrive and spread has intrigued scientists for decades whereas the transport and dynamical properties of interacting self-propelled particles (bacteria) have generated much scientific interest as of late [5 - 7]. The main motivation for engaging in biophysical research is to apply physics methodologies to the challenges and complexities of biological problems regarding cellular motility and collective swimming of cells. These include various fields within physics ranging from fluid dynamics, mechanics, and statistical physics; which can provide fruitful insights into the mechanism of collective swimming behaviour.

The bacteria of interest are non-pathogenic *Escherichia coli* (*E. coli)* and *Bacillus subtilis* (*B. subtilis)* cells, which swim via rotation of semi-flexible protein whips [1, 5, 8]. Due to the microscopic length scales, the governing physics is vastly different from our own intuition on these length scales. These cells experience large viscous drag forces where inertia plays an insignificant role; first described by Purcell [9], whom described what it would be like to live on a microscopic level. Bacteria have evolved to overcome these physical constraints and as a result it has given rise to a broad and challenging field of study. Various aspects of microbiology have generated scientific interest ranging from motility, chemotaxis (chemical sensory mechanism), genetics, reproduction and pathogenicity, where there is still much to learn [1].

Often physicists are drawn into the field of microbiology because biological systems are nontrivial and present a broad range of challenges in understanding various types of bacteria motility. Moreover simulations are often used to describe the hydrodynamics of swimming bacteria nears interfaces and neighbouring cells. These simulations approximate swimming cells as spherical bodies for simplicity [6, 10, 11]. This was the motivation for the search of a motile spherical strain of *E. coli*. We investigated *E. coli* since it is the world's most understood microorganism and various mutants are available from the Keio collection [12]. Under certain growth conditions wild-type *E. coli* cells can be extremely motile. The discovery of a spherical shaped motile strain of *E. coli* (easy to maintain and characterize) permits experimental verification of predictions from hydrodynamic models and simulations. Often in nature when *E. coli* cells are stressed, they form into filaments triggered by an SOS response [13], where there is scientific interest in understanding the cellular structure, motility and chemotaxis in filamentous cells. This thesis explores the mechanism which sustains motility in filamentous cells and how this differs from normal *E. coli* cells; extracting essential swimming parameters as a function of cell length.

Finally we investigate how large numbers of interacting cells 10^9 cells/ml exhibits spatial-temporal patterns, cooperative swimming and self-organization [5, 6, 14 - 16]. Collective swimming (multiple interacting cells swimming coherently) is under intensive study, where this behaviour is believed to be governed by the complex interplay between buoyancy, hydrodynamic interactions, oxygen consumption and mixing [5, 6]. Groups of interacting cells exhibit diverse swimming strategies and hydrodynamic interactions between neighbouring cells and the localized environment; generating a broad and complex spectrum of phenomena. The mechanism which facilitates the transitions between individual swimming to cooperative swimming is not well understood, nor is the mechanism which sustains this phenomenon. It is generally accepted that cells generate localized hydrodynamic fluid flow-fields which manifest into collective swimming; where the combination of hydrodynamic interactions and cell collisions are believed to be the origin of collective behaviour [17 - 19]. Large-scale collaborative swimming of cells exhibit significant enhanced diffusion of passive particles [5, 6, 10]; this swimming phenomenon is linked to active transport of oxygen, nutrients, and waste produces. Although the precise reasons for this observed behaviour in large groups of cells is still unclear; however it has been associated with ideas of evolution, multicellularity and statistical mechanics [5, 6]. This thesis investigates the mechanism which facilitates and sustains collective swimming among densely populated bacterial suspensions. Not only are these biological systems scientifically interesting, but are relevant in terms of nanotechnology and biomedical/industrial applications.

Bibliography and References

[1] H. C. Berg, *E. coli in Motion,* Biological and Medical Physical Series, Spring Verlag, (2003).

[2] M. T. Madigan and J. M. Martinko, *Brock Biology of microorganisms.* Prentice Hall, Eleventh Edition, (2006).

[3] J. Henrichsen, *Bacterial surface translocation: a survey and a classification*. Bacteriol. Rev, **36**:478–503, (1972).

[4] R. M. Harshey, *BACTERIAL MOTILITY ON A SURFACE: Many Ways to a Common Goal.* Annu. Rev. Microbiol, **57**:249–73, (2003).

[5] C. A. Solari, J. O. Kessler, and R. E. Goldstein, *Motility, mixing and multicellularity*. Genet programme evolvable mach, **8**:11-129, (2007).
[6] L. H. Cisneros, R. Cortez, C. Dombrowski, R. E. Goldstein and J. O. Kessler, *Fluid dynamics of self-propelled microorganisms from individuals to concentrated population.* Exp. Fluids, **43**:737-754, (2007).
[7] M. B. Short, C. Solari, S. Ganguly, T. R. Powers, J. O. Kessler, and R. E. Goldstein, *Flow driven by flagella of multicellular organisms enhance long-range molecular transport*. Proc.Natl.Acad.Sci, **103**:8315-8319, (2006).
[8] H. C. Berg, *The rotary motor of bacterial flagella,* Annu.Rev.Biochem, **72:**19-54, (2003).
[9] E. M. Purcell, *Life at low Reynolds number.* American Journal of Physics, **45**:3-11, (1977).
[10] E. Lauga, W. R. Diluzio, G. M. Whitesides and H. A. Stone, *Swimming in circles: Motion of bacteria near solid boundaries.* Biophysical Journals, **90**:400-412, (2006).
[11] T. Ishikawa, G. Sekiya, Y. Imai, and T. Yamaguchi, *Hydrodynamic interactions between two swimming bacteria.* Biophysical Journal, **93**:2217-2225, (2007).
[12] T. Baba *et al*, *Construction of Escherichia coli K-12 in-frame, single-gene knockout mutants: the Keio collection. Mol. Syst. Biol.* **2**:16738554, (2006).
[13] R D'Ari and O Huisman, *Novel mechanism of cell division inhibition associated with the SOS response in Escherichia coli.* J. Bacteriol, **156**:243-250, (1983).
[14] X. L. Wu and A. Libchaber, *Particle Diffusion in a Quasi-Two-Dimensional Bacterial Bath.* Phys. Rev. Lett, **84**:3017-3020, (2000).
[15] J. Toner, Y. Tu, *Long-range order in a two-dimensional dynamical XY model: how birds fly together.* Phys. Rev. Lett, **75**:1326-4329, (1995).
[16] T. Vicsek *et al 'Novel type of Phase transition in a System of Self-Driven Particles'* Phys. Rev. Lett, **75**:1226-1229, (1995).
[17] A. Sokolov, I. S. Aranson, J. O. Kessler and R. E. Goldstein, *Large-scale collective behaviour of swimming micro organisms at high concentrations.* Traffic and Granular, Flow '07, Springer Berlin Heidelberg, (2009).
[18] A. Sokolov, I. S. Aranson, J. O. Kessler and R. E. Goldstein, *Concentration Dependence of the collective dynamics of swimming bacteria.* Phys. Rev. Lett, **98**:158102, (2007).
[19] A. Sokolov, R. E Goldstein, F. I. Feldchtein, and I. S. Aranson, *Enhanced mixing and spatial instability in the concentrated bacterial suspensions*. Phys. Rev. Lett, **80**:031903, (2009).

Chapter 2 : Flagellated bacteria

2.1 Introduction to Microbiology

The research presented in this thesis was conducted with two species of motile bacteria *Escherichia coli* and *Bacillus subtilis;* which over decades of research have been well characterized and studied [1, 2]. *Escherichia coli (E. coli)* and *Bacillus subtilis (B. subtilis)* are unicellular microorganisms and are one of the simplistic forms of a living entity. Understanding bacterial gene regulation, DNA replication and life sustaining processes are anything but simplistic, presenting a broad range of challenges. A brief introduction to historical overview of microbiology is presented. We review the general characteristics of both bacterial species; regarding growth, bacterial category, morphology, habitat, and motility. Finally we discuss the mechanism of cellular motility and chemical signalling which enables cells to sample the environment, and swim towards attractants or away from chemical repellents.

The field of microbiology was formed shortly after the advent of the single lens optical microscope in 1687 by Antonie van Leeuwenhoek [3]. Leeuwenhoek is considered as the father of microbiology and the first microbiologist. Leeuwenhoek examined droplets of rain water underneath a microscope and noted that it contained miniature creatures which he called '*animalcules*'. In actual fact, Leeuwenhoek was the first to observe and analyze swimming bacteria [4, 5]. He noted that these animalcules are able to swim, although he was unable to observe the apparatus/mechanism for cellular motility; we now know that some bacteria synthesize external organelles i.e. flagella/cilia in order to swim. At the time Leeuwenhoek speculated these creatures retained little '*paws*' which they used to swim. The advent of optical microscopy permitted investigations of bacterial morphology where bacteria display a diverse range of shapes; such as coccus, vibrio, spirochete and bacillus ranging from 0.5 µm – 500 µm in size [6].

The first static images of bacteria flagella were imaged by Christian Ehrenberg in *Chromatium okenii* cells [7]. Advancements in dark-field microscopy carried out by Karl Reichert permitted visualization of flagella bundles in swimming cells; however individual flagella filaments were not resolvable at the time [8]. Subsequently, Theodor Engelmann demonstrated that bacteria do not swim randomly, but respond to chemical stimuli in the surrounding environment. Engelmann demonstrated that *B. subtilis,* an aerobic bacterium concentrates around regions of oxygen production in algae [9 - 11]. These experiments provided the foundations for understanding chemotaxis, discussed later.

At the time it was commonly believed that flagella generate thrust by periodic undulations, idealized by propagating waves travelling along the filament similar to spermatozoa cells. In the 1950's Taylor [12] provided a mathematical explanation of the thrust generated by travelling waves in the low Reynolds number regime. From this, he proposed that bacteria such as *E. coli* are motile due to flagella rotation rather than flagella undulations, see references [12,13] for details. Rotation of flagella filaments as a mechanism of propulsion requires a reversible motor. In 1974 Silverman and Simon proved the existence of a reversible molecular motor at the base of each flagella filament in *E. coli* cells [14]. The experiment utilized *E. coli* mutants tethered to the surface of a glass slide, cells rotated in both directions providing empirical evidence for a reversible motor. In 1976 Purcell published an influential paper '*Life at low Reynolds number*' on the efficiency of bacterial swimming via the rotation of flagella filaments. Purcell estimated the efficiency of cellular swimming via modelling a simplified rotating helix as a bundle, to be ~ 1 %, he also demonstrated that rotation of any asymmetrical filament will generate thrust in a viscous environment [15], (discussed in *Chapter 3*).

At the same time Macnab *et al* developed a working model to study the dynamical behaviour of rotating left-handed helices; they examined the bundling process of several filaments with a physical model [16, 17]. The model provided an invaluable insight into the mechanism leading to bundling of several flagella filaments without

jamming. In 1982 Hotani demonstrated that hydrodynamic stress/load is sufficient to induce transitions between stable polymorphic conformations in flagella filaments with varying pitch lengths [18]. Recently polymorphic transitions have been investigated via fluorescent labelling techniques permitting visualization of flagella filaments with rapid video acquisition rates [19 - 21]. Thus technological advancements have provided an important insight into the mechanism of cellular reorientation and motility, see references [22, 23].

2.2 Bacterial categories

E. coli and *B. subtilis* cells are subcategorized into two general types of bacteria; species are either Gram positive or Gram negative [6]. The difference in classification type originates from a cell surface staining procedure known as the *Gram stain.* Gram staining was invented by Hans Christian Gram in 1882 to differentiate bacterial strains based upon a chemical reaction of the cell wall structure [24, 25]. The fundamental difference between Gram positive and Gram negative bacteria is the lack of the outer membrane (lipopolysaccharide layer) in Gram positive cells; which offers a barrier against chemical attacks. Thus Gram negative species are often more resistant to antibiotics, detergents and dyes; whereas Gram positive species are more sensitive and susceptible to chemical attacks. The typical cell structures of Gram positive and Gram negative cells are depicted in *Figure.2.1*, further details are in references [6, 24, 25].

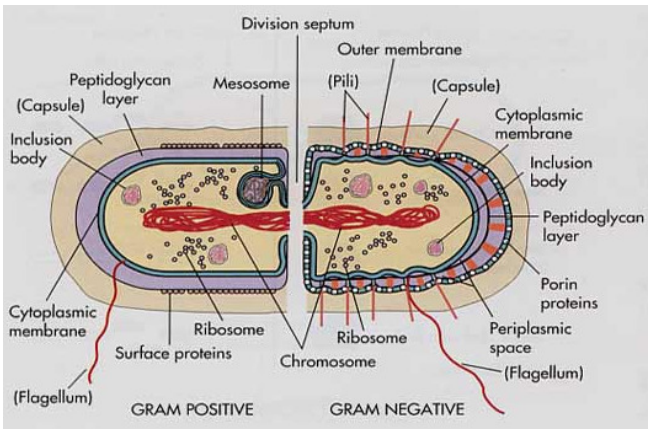

Figure.2.1: Schematic diagram of the cellular structure of Gram positive and Gram negative bacterium. Images sourced from [26] where additional details can be found.

E. coli cells are therefore more resistant against most chemical repellents and poisons compared to *B. subtilis* cells which lack the outer membrane [6]. *Figure.2.2* shows scanning electron micrographs of both *E. coli* (Gram negative) and *B. subtilis* (Gram positive) cells, depicting the differences in the cellular surface respectively.

(a)

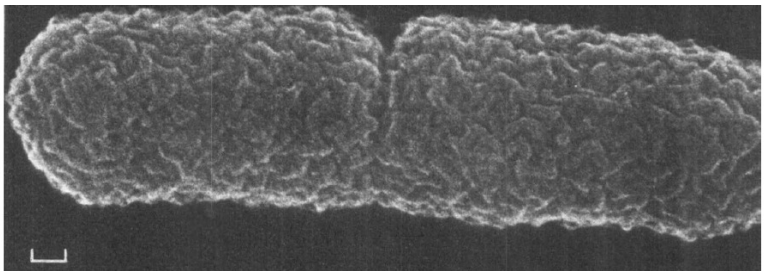

(b)

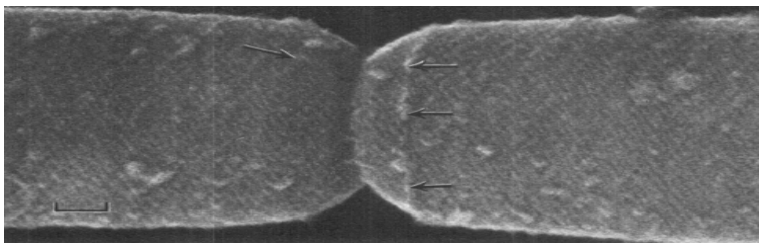

Figure.2.2: (a) Scanning electron micrograph of Gram negative Escherichia coli highlighting the textured cell surface due to the additions lipopolysaccharide layer. (b) A similar micrograph of Gram positive Bacillus subtilis which lacks the outer cell membrane, thus the surface is non-textured. The arrows indicate the formation of the septum ring. Both scale bar represents 100 nm Iimages sourced from [27] with permission from the Society for General Microbiology.

Common to both Gram positive (*B. subtilis)* and Gram negative (*E. coli*) bacteria is the cell wall. The cell wall consists of several layers of peptidoglycan (murein) [6], which are cross-linked to form a robust and thick layer [28]. The cell wall (peptioglycan layer) provides the cell structural rigidity, strength and cellular morphology [24, 25]. Typically Gram positive bacteria such as *B. subtilis* has a thicker peptidoglycan layer ~ 150 Å [28]; which render the Gram positive cells mechanically more robust and suited to life in exposed environments, typical of many other Gram positive bacteria [6]. Gram negative bacteria such as *E. coli* has a thinner peptiodoglycan layer ~ 95 Å [29], rendering cells prone to cell wall rupture and lysis (cell death from leaking of cytoplasm) [6]. Underneath the cell wall is the inner membrane common to both Gram positive and Gram negative bacterium. The primary function of the inner membrane is to regulate the transport of nucleic acids, proteins and solutes; and behaves like a permeability barrier essential for life sustaining processes. The cell structure/morphology of *E. coli* and *B. subtilis* is reviewed in the following subsection.

2.3 Cellular growth rates

All bacterial species regardless of cellular category (Gram positive/negative) grow and multiply by *binary fission,* a process of asexual reproduction in which a single mother cell divides into two approximately equal length daughter cells [24, 25]. Each daughter cell is genetically identical [6]. *Figure.2.3* is a schematic diagram illustrating how bacteria divide by binary fission into two independent daughter cells. The time it takes for one mother cell to divide into two daughter cells is known as the generation time g (also known as doubling time), which is strongly dependant on the growth conditions [6]. Typically *E. coli* and *B. subtilis* cells under optimal growth conditions have a generation time of 20 - 30 minutes[1] when incubated in a

[1] The generation time was quantitatively measured by the author of this thesis, shown in subsequent Chapters, *Figure.4.5* and *Figure.6.5*.

batch culture[2] [6, 22]. The progressive doubling of the cells results in a continually increasing population referred to as exponential growth [6, 24, 25]. Thus mother cell divides into two independent daughter cells; these two daughter cells subsequently divide into four daughter cells and so forth.

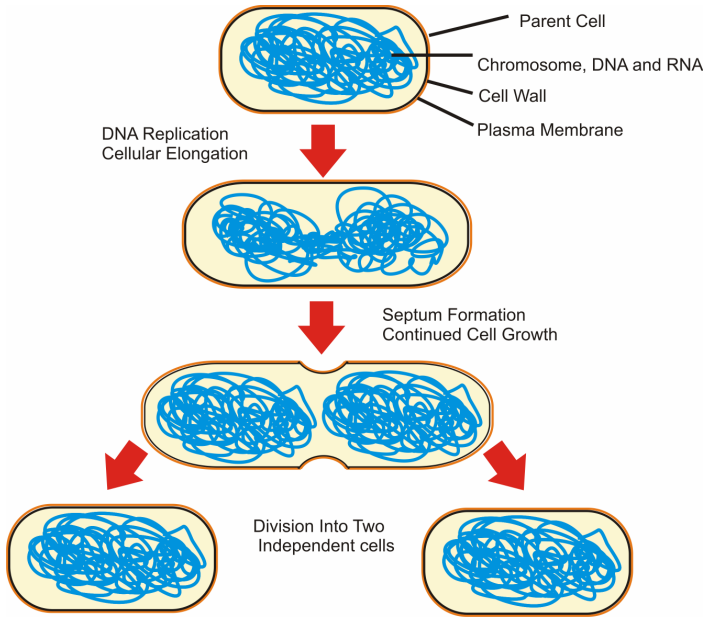

Figure.2.3: A schematic diagram of the binary fission process of a rod-shaped bacterium, illustrates a cell growing until it is approximately twice the size prior to cell division. The DNA material is duplicated into each daughter cell. Cell division occurs in the order of 10's of minutes dependant on growth phase and incubation conditions.

E. coli and *B. subtilis* cells exhibit analogous growth cycles, with four very distinctive growth phases in batch cultures [6, 24, 25], which is dependant on the growth conditions illustrated in, *Figure.2.4*. These growth regimes are called lag phase, exponential phase, stationary phase and death phase. Cells in the exponential phase are the most active in terms of DNA replication; therefore the growth rate is faster in this regime. Newly inoculated bacterial cultures do not initiate cell growth immediately, but only multiply after a delayed period known as the lag phase. This

[2] Batch culture is defined as: a bacterial culture incubated in a fixed volume of nutrients under specific growth conditions, such as a fixed temperature.

occurs because of the culture requires time to adapt to the growing medium; this generally lasts for ~ 20 minutes to several hours depending on the organism and growth conditions [6]. Cells subsequently enter the exponential phase of growth; where cells continually grow and divide, and the cell population rapidly increases. Cells in the exponential phase are most active in terms of motility and genetic DNA replication. Exponential growth can be sustained for several hours (5 – 7 hours) [6]; however exponential growth is unsustainable indefinitely in batch culture. Increasing accumulation of secreted waste products and limited nutrient supply inhibits cellular growth, thus the growth rate decreases and the cell population enters the stationary phase. The stationary phase is defined as, zero net increase or decrease in cell numbers, i.e. a sustained population. Despite no net growth, the majority of the cells still function and adapt to the environment. The stationary phase is followed by the death phase; whereby organisms in the population begin to perish. Death occurs either because the organisms undergo starvation or by intolerable accumulation of secreted waste products in the living environment rendering it toxic. The number of cells in the death phase decays exponentially, but at a significantly slower rate than the exponential phase [6].

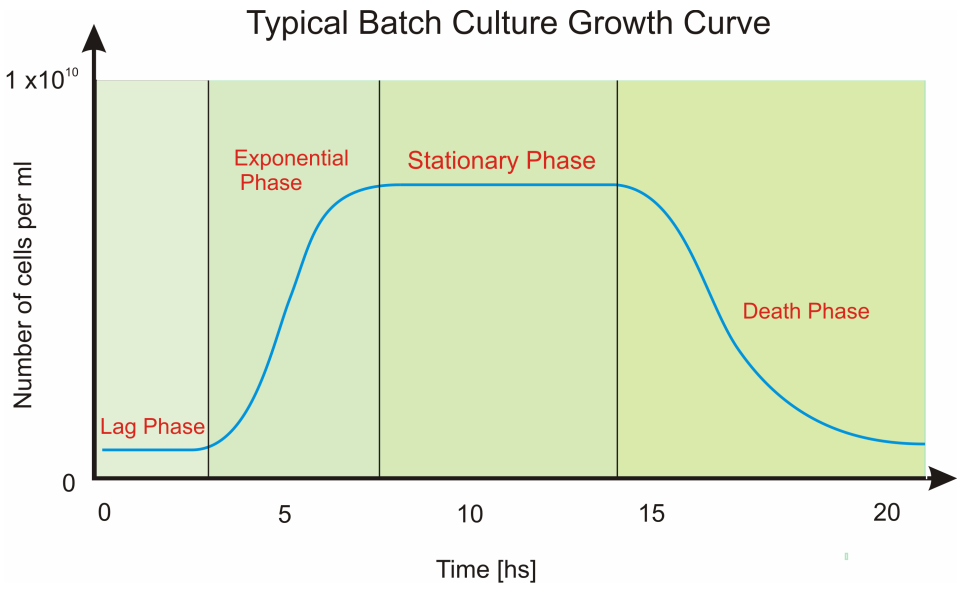

Figure.2.4: A schematic representation of bacterial growth in a nutrient liquid batch culture; indicating the distinct growth phases and the number of cells as a function of incubation time.

2.4 Overview of *Escherichia coli* and *Bacillus subtilis*

E. coli is predominately found in the human gut and digestive track. In microbiology *E. coli* is regarded as the ideal microorganism for laboratory studies and it is regarded by many as the workhorse microorganism. Despite *E. coli* being one of the simplest forms of life, it has demonstrated remarkable sophistication in terms of genetics, the regulatory sensory system, cellular functionality and motility [22, 23]. Thus *E. coli* has become the world's most understood and researched microorganism. *E. coli* cells are extremely robust and resourceful in adverse environments [6]; moreover *E. coli* is also experimentally easy to manage and maintain.

This project exclusively uses an attenuated laboratory strain of *E. coli* (i.e. a less virulent strain of *E. coli*), the K12 strains (Keio collection) [30]. These strains are non-pathogenic to humans and suitable for laboratory work; although some *E. coli* strains are pathogenic causing severe infections and food poisoning [22]. The first published detailed images of *E. coli* cells was presented in 1965 by Adler; who studied chemotactic motility of individual cells [31]. The physiology and morphology of *E. coli* cells have been well characterized [22, 23, 30, 32]; *Figure.2.5* depicts a typical *E. coli* cell. These cells are self-contained capsules, comprising of multilayered structures each with a defined purpose which encapsulates the cytoplasm [6, 22]. The cytoplasm is regarded as a quasi-homogenous ensemble of DNA, RNA, proteins and lipids [22], essentially the internal fluid of a cell. The rigid structure of the cell is provided by the combination of an inner membrane, a cell wall, and the outer cell membrane; further details of cellular structure are in references [6, 33]. The total thickness of the external layers[3] in *E. coli* cells is ~ 0.03 µm [6, 22]. *Figure.2.5* highlights the physiology of a single *E. coli* cell depicting external appendages/organelles such as pili, fimbriae and flagella [22].

[3]External layers is in reference to the inner membrane, cell wall and outer membrane.

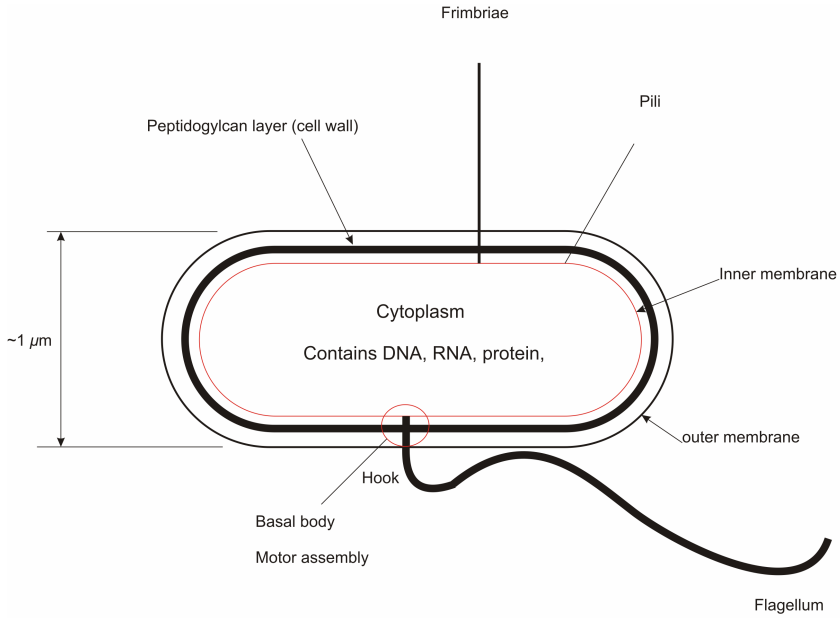

Figure.2.5: A schematic diagram depicting the typical cellular structure of E. coli cells.

E. coli are rod shaped ~ 2 µm in length end to end and ~1 µm in diameter with hemispherical end caps often described as an prolate spheroid. *E. coli* are Gram negative bacteria and is a facultative aerobe, i.e. cells can survive with or without the presence of oxygen [6, 24, 25]. These cells are peritrichously flagellated (randomly distributed over the cell body), where flagella filaments are randomly distributed over the outer cell membrane [6, 34]. Each flagella filament is attached to a reversible motor at its base by a flexible universal joint, known as the hook. Individual *E. coli* cells have approximately 4 - 6 flagellum, each flagellum is 10 – 15 µm in length and approximately 25 nm in diameter [6, 22, 23]. *Figure.2.6* illustrates the external morphology of a fluorescently labelled *E. coli* cell. Fluorescently labelling of cells highlights several flagella filaments asymmetrically distributed over the cell body. Moreover, it depicts the general length and shape (normal left-handed helix) of de-energized flagella filaments.

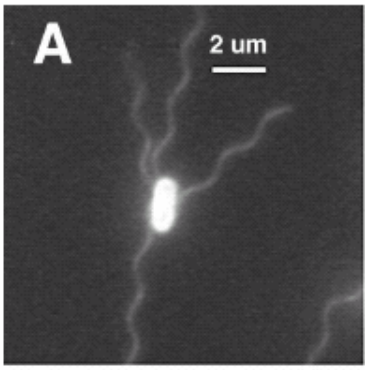

Figure.2.6: Highlights a fluorescently labelled de-energized cells E. coli cell tethered to a glass coverslip. The cell has several flagella filaments distributed asymmetrically, demonstrating normal left-handed flagella conformation. Image sourced from [19], reproduced with permission from the American Society of Microbiology.

Flagella synthesis, polymorphic transitions and thrust generation is discussed in the following subsection; but first let's introduce the second bacteria species used in this project *Bacillus subtilis.* *B. subtilis* is a Gram positive, non-pathogenic, motile bacterium [36, 37]. *B. subtilis* cells are often regarded as the Gram positive equivalent to *E. coli* cells in terms of physiology and the characteristic swimming behaviour [6, 37, 38]. *B. subtilis* is found naturally in soil and in decomposing vegetation, thus *B. subtilis* is an obligate aerobe and requires the presence of an oxygenated environment for optimal cellular respiration [6]. *B. subtilis* has an inherently strong chemotactic response to oxygen [39, 40, 41], unlike *E. coli* which is a facultative aerobe which can live without oxygen. *B. subtilis* cells are naturally exposed to the elements where they live a life of penury; and they are subjected to frequent fluctuations in osmotic conditions due to drying and wetting of the soil [42]. Thus these cells are mechanically robust, and survive by regulating the internal turgor pressure. Moreover cells have evolved to cope with varying temperature, pH and nutrient concentration. Thus naturally *B. subtilis* cells are extremely robust even more so than *E. coli* cells.

B. subtilis cells are ~ 4 µm in length and ~ 1 µm in diameter, depending on growth conditions, such as nutrient concentration, temperature, pH and oxygen concentration [43]. Analogous to *E. coli*, *B. subtilis* are peritrichously flagellated [6]. Flagella filaments are distributed randomly over the cell membrane, although the number of flagella varies considerably [44], typically *B. subtilis* retains ~ 14 flagella filaments. The flagella filaments in *B .subtilis* cells are assumed to be analogous to *E. coli* cells in terms of shape, length and flexibility. The physiology and morphology of two dividing *B. subtilis* cells is depicted in an electron micrograph, *Figure.2.7.* Numerous flagella filaments emerge randomly from the cell membrane with varying length. The large variations in flagella lengths due to suspected shearing during sample preparation [43].

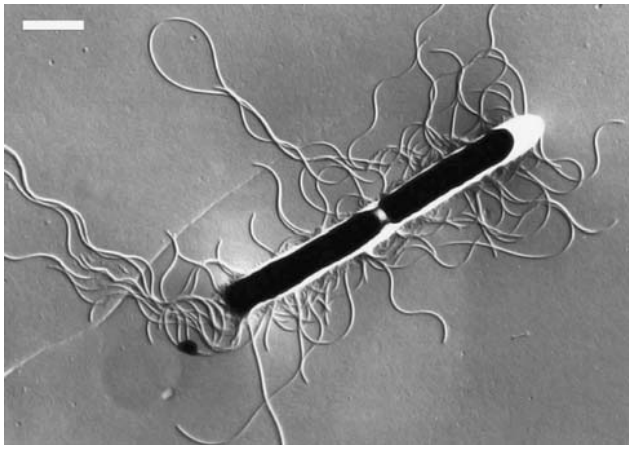

Figure.2.7: Electron micrograph of two Bacillus subtilis cells prior to cell division. Micrograph highlights numerous filaments protruding from the cell membrane. It depicts the typical physiology of the cells, ~ 4 µm in length and ~ 0.8 µm in diameter. Scale bar is 1 µm, image is sourced from references [43], reproduced with permission from Springer.

Further details of physiology, morphology, habitat and genetics for both bacterial species can be found in references [6, 22 - 25, 37, 38, 44].

2.5 Flagella motor assembly and bacterial locomotion

The understanding of bacterial motility has been investigated over several decades [16, 23]. Self-propelled bacteria swim by converting a carbon source such as (ATP) adenosine triphosphate into kinetic energy. *E. coli* and *B. subtilis* achieve motility by synthesising flagella filaments, to generate thrust by the co-rotation of flagella. Recently there has been much scientific interest in understanding bacterial chemotaxis and motility [19 - 21, and 23]. Berg *et al* demonstrated the remarkable reversible behaviour of the rotary motor assembly which propels cells forwards. Although there are still many unanswered questions regarding torque generation and abrupt motor switching [45]; fully understanding how the motor functions is still a mystery and there is still much to learn. The following sections address the motor assembly, the hook, flagella synthesis, and overview of the genetics required to construct such remarkable machinery on nanometer length scales.

In *E. coli* and *B. subtilis* cells, every individual flagellum is powered by a reversible motor anchored in the inner cell membrane [23, 46, 45]. Flagella filaments are passive and are only driven by the motor embedded in the cell membrane, unlike the algae such as chlamydomonas where the motor is located inside the flagellum [47]. The flagella motor assembly in *E. coli* and *B. subtilis* consists of the three pivotal components, the flagella filament, the hook and the basal body. The most inner part of the assembly, the flagellum motor consists of a basal body. The basal body is located underneath the cell surface and consists of a rod, a series of rings located in the inner membrane, peptidoglycan layer and in the outer membrane [22]. The rod connects the hook and the terminal rotor, passing through several protein rings these rings act as bearings insuring smooth rotation of the rod [22, 23, 48].

There are two main components of the motor assembly (basal body), the stator and the rotor depicted in *Figure.2.8*. The stator is secured to the peptidoglycan layer and remains stationary, the rotor is the component which rotates and generates

torque. The flagella motor is assembled in the inner membrane where 26 subunits of an integral membrane protein FliF assemble to form the MS ring [22, 23]. The FliG protein subsequently forms underneath the MS ring and the proteins FliM and FliN form the base of the rotor known as the C-ring. The C-ring is comprised of a switch governing the direction of the motor rotation [22, 23]. The Fli proteins act as a relay switch alternating motor rotation direction due to intracellular signals such as the phosphorylation of CheY-P discussed later. MotA and MotB are then assembled to form the stator, which are both integral membrane proteins. These two proteins are located in the inner membrane; however MotB protein is also anchored in the ridged peptidoglycan layer which restrains the stator proteins from rotating. The rod is formed in the centre of the motor assembly (basal body), extending through the peptidoglycan layer and outer membrane (lipopolysccharide layer, but not present in *B. subtilis* cells) via a set of rings connecting to the hook assembly [49]. The P-ring and L-rings refers to the anchoring locations of the rings i.e. the peptiodglycan and lipopolysccharide layers respectively acting like bearing for the rod; and are not associated with torque generation [22, 23]. The rod essentially is a drive shaft translating torque generated by the motor to hook and flagellum filament (propeller). Torque is generated by electrostatic interactions between the cytoplasmic domains of the MotA and the C-terminal domain of FliG acting over very short distances in the order of several angstroms, for further details see references [23, 48, 49, 50].

The external hook assembly is a highly curved and extremely flexible cylindrical structure permitting larger angular deflections of the flagellum, assisting in the flagella bundling process [17, 18, 23]. The hook links the motor to the flagellum (propeller) and it is often described as a flexible universal joint. The hook is 55 nm in length and is constructed from 120 copies of the protein FlgE [51], where the length of the hook is regulated by FliK [52]. The Young's modulus of the hook is in the order of 10^5 – 10^6 N/m^2 and the shear modulus is typically 10^7 N/m^2 [53] demonstrating the remarkable flexibility of the hook essential for flagella bundling. The hook is two orders of magnitude more flexible than the flagella filament (10^{10} – 10^{11} N/m^2), thus this enable the flagella filaments to bundle without jamming.

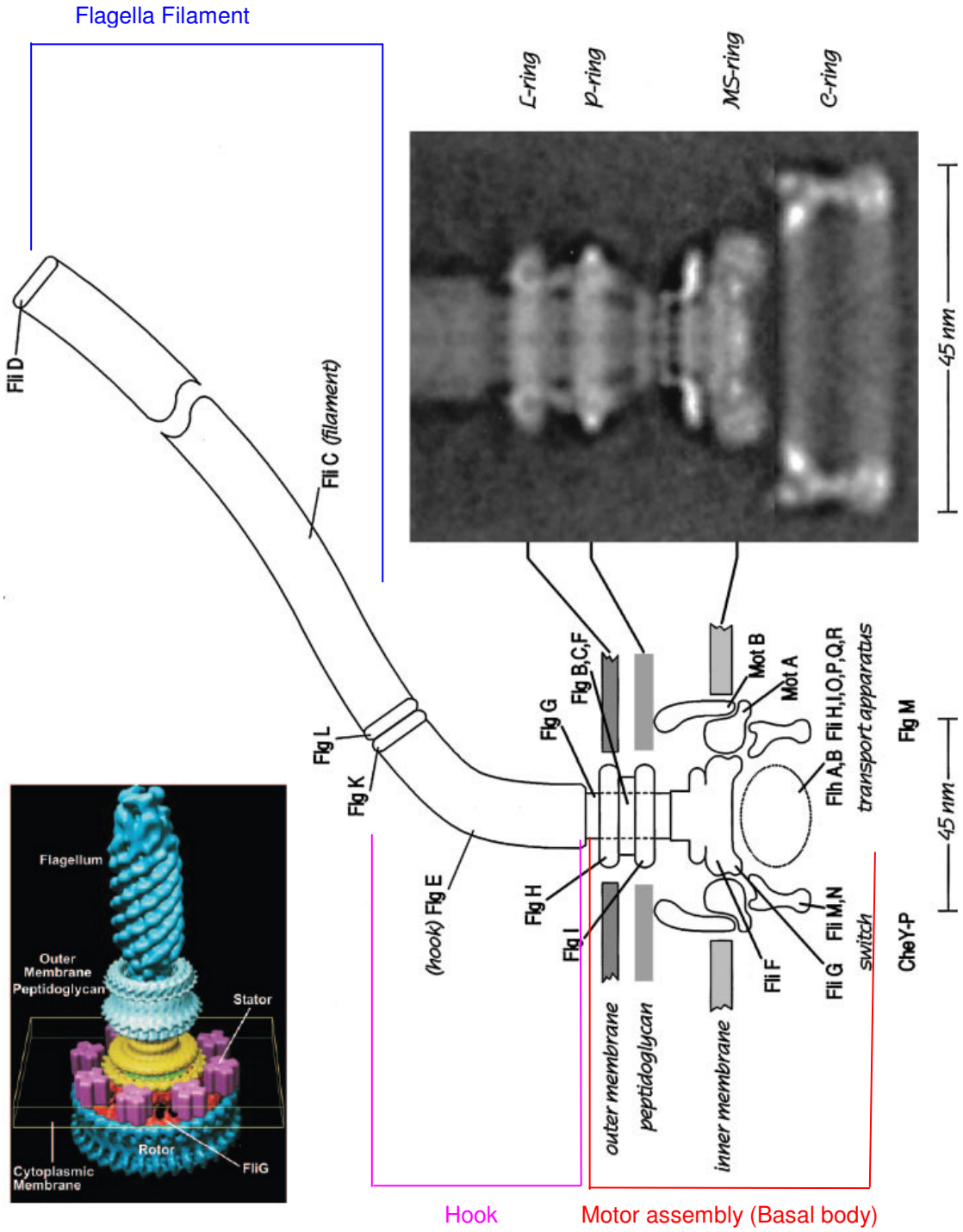

Figure.2.8: A schematic diagram of the flagella motor assembly, inset is a rotational average superposition observed via an electron microscope. The general structure of the motor assembly consists of the C-ring, MS-ring, P-ring, L-ring, hook, and the flagella filament. Lower inset is a model of the basal body (without the hook), sourced from [72], courtesy of David DeRosier . Further details on the structure and genetics can be found in reference [22, 23]. Iimage sourced from [23] posted with permission from the Annual Review of Biochemistry, Volume 72 © 2003 by Annual Review.

Flagella filaments are essentially semi-rigid protein whips, containing multiple copies of a single protein, flagellin FliC [17, 22, 23]. A single flagellum can have as many as 20,000 subunits of flagellin dependant on length [16, 17, 23]; where there is no apparent biological length control mechanism, thus resulting in a diverse range of flagella filament lengths. Longer filaments are more fragile, therefore flagella truncation occurs more readily in longer filaments[5] [22]; however truncated filaments can be re-synthesized [6, 22, 23]. Each flagellum is hollow, this allows for transport of subunits from the inside of the flagellum. During flagella synthesis new protein subunits are transported up thought the hollow core ~ 30 Å in diameter [17, 23], and bind to the end of the flagellum. Thus flagella are synthesized from the distal end and not at the proximal end. Flagella filaments are believed to compose of at least 11 protofilaments which switch between left and right handedness during tumble events for more details see reference [17, 23, 54].

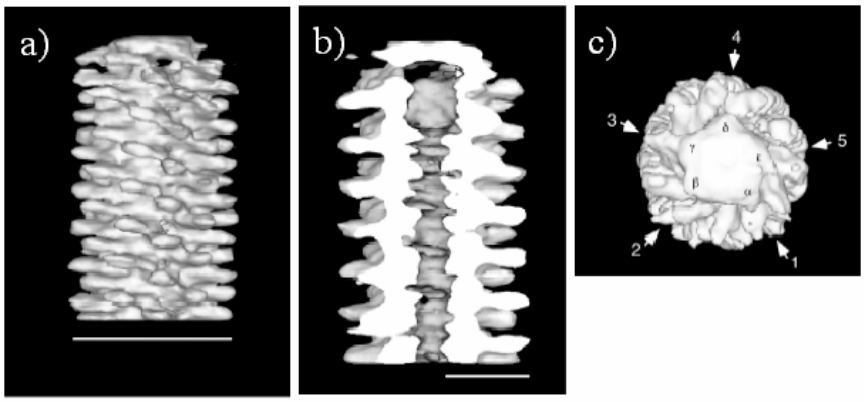

Figure.2.9: A three dimensional reconstruction of the distal end of flagellum and cap assembly. (a) Lateral view of the flagella filament depicting a regular helical formation of FliC subunits. Scale bar is 230 Å (b) Lateral cross section of a flagellum depicting the cavity in which the subunits are transported. Note the cavity widens at the tip believed to allow new subunits to manoeuvre into place. Scale bar is 115 Å (c) A plan view of the distal end depicting the cap and its distinctive pentagon shape highlighted by the arrows. The Greek letters refer to the orientation of the pentagon. Image sourced from [54], reproduced with permission from the American Association for Advancement of Science, where the details of the flagella synthesis are explained.

[5] Flagella truncation often occurs naturally by hydrodynamic shearing and by rough cell handling [19].

The end of the flagellum is the capped with the protein FliD. The purpose of the cap is primarily to prevent the flagellin subunits from diffusing out of the end of flagellum; essentially anchoring flagella subunits. Moreover, it is an annular pentameric (fivefold) structure *Figure.2.9 (c),* which retains a plane top surface, and semi-flexible '*leg*' like domains [17, 54]. These legs accommodate and determine the location of the new flagellin subunits; the cap rotates as the FliC subunits are arranged in a spiral-like staircase, similar to a crude helix [54]. The flagella filaments are normally a left-handed helix when viewed from behind [19, 22, 23], however it can alter its shape since it is semi-flexible. Flagella undergo bi-stable polymorphic transitions, typically in tumble events discussed later. There are several stable flagella pitch conformations, both left and right handed demonstrated by Hotani [18]. Recent developments of fluorescent flagella labelling and high speed imaging, suggests more complex polymorphic transitions and stable configurations are possible, generating significant scientific interest. These studies provide insight into the tumbling processes and the role of polymorphic transitions in cellular motility. Further details on polymorphic transitions can be found in references [18, 19, 22, 55].

Flagella motors are powered by proton motive forces caused by the flow of hydrogen ions through the cytoplasmic membrane due to a concentration gradient [56]. The transfer of protons ratchets the MotA protein along the FliG protein, subsequently driving the rotor and rotating the flagellum [23, 46]. Approximately 1000 protons are required for a single rotation of the flagellum [56]; which can rotate up to speeds of 200 - 1000 rpm [22, 23], and exerts viscous drag forces (in the order of a few pN) on the fluid generating forward motion [23]. *E. coli* and *B. subtilis* are peritrichously flagellated and invoke locomotion via the co-rotation (i.e. the flagella motors rotating synchronously in the counter clockwise direction) of multiple flagella filaments in the bundle [46, 17]. As several left-handed flagella filaments rotate in the same counter clockwise direction, hydrodynamic attraction between adjacent filaments results in the formation of a cohesively rotating bundle; resulting in forward propulsion, *Figure.2.10.*

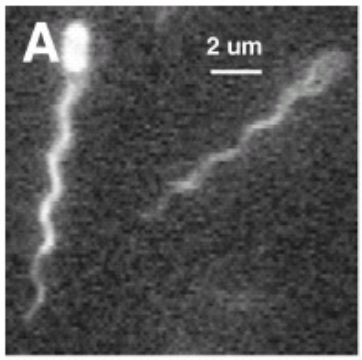

Figure.2.10: Fluorescently labelled swimming E. coli illustrating the formation of the propulsive flagella bundle by the co-rotation of flagella filaments. The flagella bundle consists of approximately six filaments which rotate at ~ 100 Hz, the force generated by the bundle is translated along the body axis generating swimming speed up to 40 μms $^{-1}$. Imaged sourced from [19], reproduced with permission from the American Society of Microbiology.

The co-rotation of multiple flagella filaments often leads to the formation of a single helical propulsive coil referred to as a bundle; the rotation of the helical shaped bundle is sufficient to generate propulsion [17, 23]. There are numerous studies on the formation of flagella bundles [16, 46, 57 - 62], and it is regarded purely as a hydrodynamic process between flagella filaments [17, 64, 61]. The thrust produced by the bundle (discussed in *Chapter 3*) is transmitted along the main axis of the cell body as the bundle is fixed at one polar end, *Figure.2.10*. This maximizes swimming efficiently and minimizes viscous drag. The formation of bundles occurs at one pole of the cell, in the opposing direction of net motion which acts like a rudder, helping to direct the cell, and cell propulsion is along the central axis of the cell's orientation. The flagella bundle can form at either end of the cell, the swimming efficiency and velocity is intrinsically indistinguishable between bundles formed at either end [63]. When all the normal left-handed flagella helical filaments rotate counter-clockwise (**CCW**) they form a flagella bundle; this drives the cell in a forward direction with typical velocities ranging between 20 - 40 μms^{-1}. **CCW** rotation generates relatively straight line swimming trajectories and is recognized as a '*run*', which typically last for ~ 1.0 s. Conversely when one or more flagella abruptly switches from **CCW** to clockwise rotation (**CW**) the flagella bundle disperses, thus the swimming immediately stops and the cell body re-orientates [19, 22]. This chaotic process re-

orientates the cell body and varies the swimming trajectory whilst the cell's swimming velocity remains small; this is known as a '*tumble*' which lasting ~ 0.1 s [19, 22]. The initiation of tumble events, at least one or more flagella motor changes its rotational direction from **CCW** to **CW**, such that a single filament detaches itself from the bundle [19], ultimately terminating forward motion and chaotically re-orientating the cell, [19] *(See Movie: HCB1-Run&Tumble.avi).* The change in motor's rotational direction from **CCW** to **CW** induces hydrodynamic stress and load on the flagellum, thus polymorphic transition occurs [21, 31, 51]. Polymorphic transitions changes the shape of the flagellum (i.e. the pitch length), resulting in chaotic re-orientation often triggered by environmental changes. There are several stable conformations depicted in, *Figure.2.11*; during a tumble a flagellum changes from normal to semi-coiled then to curly 1 and back to normal. Recent advances in real-time flagella imaging has permitted in depth studies regarding polymorphic transitions, further details see references [19, 55].

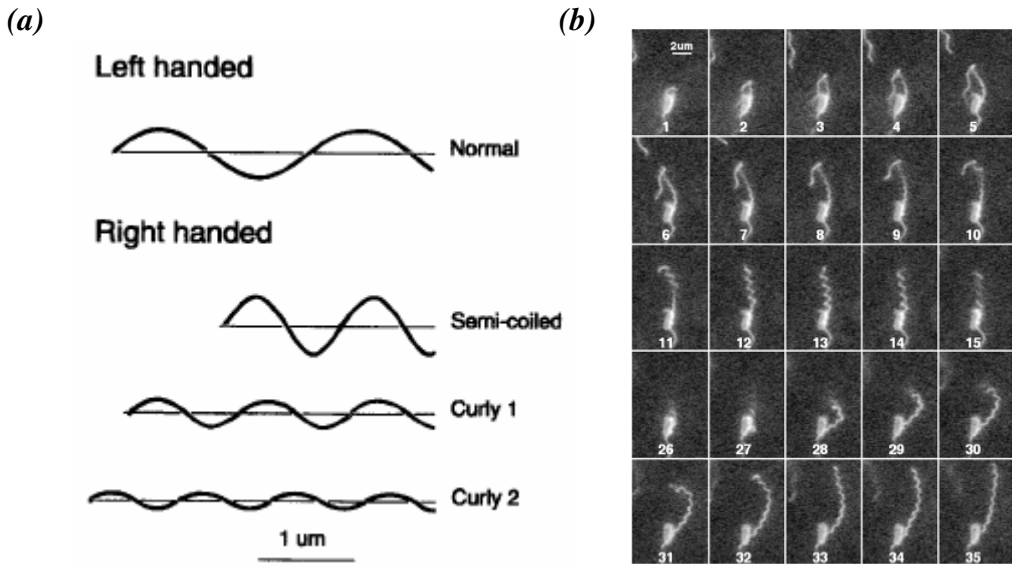

Figure.2.11: (a) Depicts the four identified stable polymorphic transitions observed in E. coli cells. (b) Demonstrates polymorphic transition in fluorescently labelled E. coli cells depicting the various stable conformations. Frames 1 – 8 is a normal filament, subsequently in frames 10 - 14 depicts a curly 2 to a semicoiled conformation and 27 – 35 from semicoiled to curly 1; image sourced from [19] reproduced with permission from the American Society of Microbiology.

Figure.2.12 illustrates a simplified representation of the two distinct modes of swimming for flagellated bacteria such as *E. coli* and *B. subtilis*. The run mode generates forward thrust by the bundling of flagella filaments which is interrupted by brief periods of cell reorientation, via tumbling. Cells migrate large distances by deploying the run and tumble swimming modes.

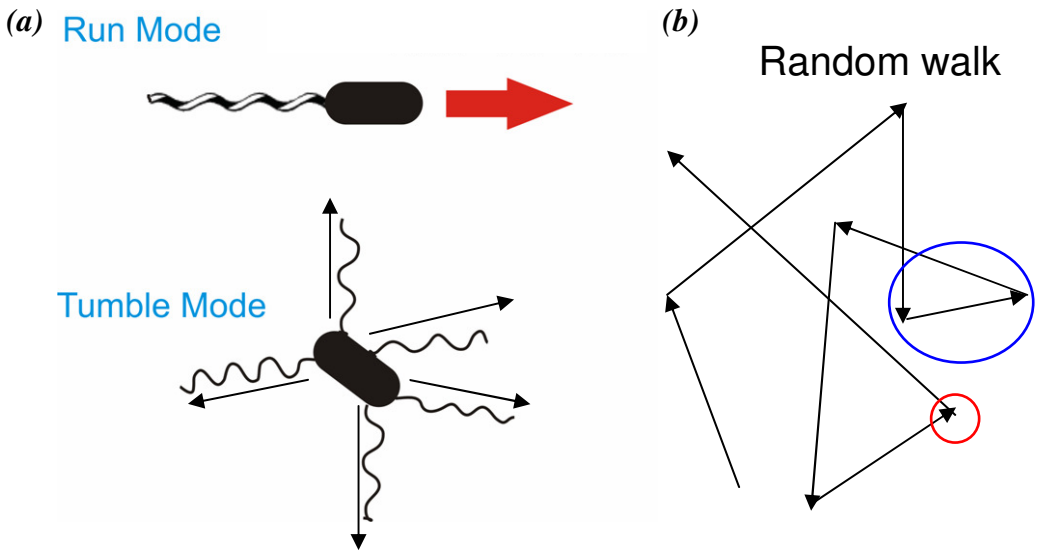

Figure.2.12: (a) Depicts a simplified representation of the run and tumble swimming mode; bundling of flagella at one polar end propels cells forward during a run. Tumbling interrupts the runs where a single flagellum motor switches rotation direction chaotically re-orientating where the thrust force is exerted in an incoherent direction. (b) The combination for runs and tumbles results in a random walk, blue circle is a run and red circle is a tumble.

Generally *E. coli* and *B. subtilis* cells are in either two states; the run state or the tumble state *Figure.2.12*. In the absence of a chemical gradients and stimuli, the reorientations of the cells trajectories are random and the switching between **CW** and **CCW** of motor rotation occurs stochastically with a well established distribution [23, 63], hence swimming bacteria perform a '*random walk'* [19, 23, 58]. However, cells respond to chemical stimuli in the surrounding environment using chemical receptors located at the poles in the cell membrane. Receptors measure the levels of attractants and repellent molecules and through a sampling process bacteria can respond to gradient changes; and cells are able to bias their swimming towards attractive chemical gradients and away from harmful substances. This sampling process is referred to as chemotaxis.

2.6 Bacterial chemotaxis

There have been extensive studies of chemotaxis in *E. coli* and *B. subtilis* cells investigating the intracellular systems for receptor signalling and signalling transduction. It is believed that *B. subtilis* cells perform a similar method of chemical sensing to that of *E. coli* cells; although *B. subtilis* is strongly influenced by the presence of oxygen [40, 43, 64]. Motile *E. coli* and *B. subtilis* cells actively seek out environments which are deemed to be more beneficial via detecting extracellular chemical signals. Detection of chemical signals is performed by chemoreceptors located at the poles of the cell, and beneath the cellular membrane. These chemoreceptors are known as methylaccepting chemotaxis proteins MCP's (there are 5 MCP proteins) present in both *E. coli* and *B. subtilis* cells [65]. Activation of these proteins mediates a phosphorylation and dephosphorylation cascade which switches rotational direction of the motor, i.e. **CCW** to **CW** and vice versa to vary the swimming mode from run to tumble. MCPs continuously sample and monitor chemical compounds in the surrounding vicinity, typically every 1 - 3 s. In response cells vary their swimming mode, to benefit the cell's living conditions [6, 22, 31]. In the presences of chemical gradients such as attractants, the frequencies of tumbles events are reduced and the average runs lengths of cells are extended in the direction towards the attractant. This bias enables cells to swim towards chemical attractants and away from repellents. For further reviews see [66 - 71].

2.7 Conclusion

This chapter has introduced and discussed the general characteristics such as habitat, growth, morphology, motility and chemical signalling in the microorganisms of interest, *E. coli* and *B. subtilis*. Both bacteria species (*E. coli* and *B. subtilis*) are rod shaped ~ 1 µm in diameter, where *E. coli* is ~ 2 µm in length, and *B. subtilis* is ~ 4 µm in length. Similarly both grow and divide by binary fission with analogous

growth curves, which are strongly influenced by growth conditions. *E. coli* is naturally found in the human gut and is a Gram negative bacterium; whereas *B. subtilis* natural habitat is in the soil and it is Gram positive. Gram positive cells lack the outer membrane, thus prone to chemical attacks. Both bacteria are peritrichously flagellated, and swim via the rotation of multiple flagella filaments; cells either run or tumble which executes a random walk. As demonstrated the motor assembly is a remarkable feature in biology, evolution and engineering where there is still much to learn. *E. coli* and *B. subtilis* cells are remarkably sophisticated where the precise bundling process, polymorphic changes and cell to cell interactions are not fully understood leaving room for exciting research regarding bacterial motility.

Bibliography and References

[1] F. C. Neidhardt, R. I. Curtiss, J. L. Ingraham, *et al*, *Escherichia coli and Salmonella: cellular and Molecular Biology.* ASM Press, Washington, DC, (1996).

[2] F. Kunst *et al*, *The complete genome sequence of the Gram-positive bacterium Bacillus subtilis.* Nature, **390**: 249-256, (1997).

[3] C. Dobell, *Antony van Leeuwenhoek and His "Little Animals"*. John Bale, Sons & Danielsson, London 1932. Reprinted by Dover, New York, (1960).

[4] B. J. Ford, *The Leeuwenhoek Legacy.* Biopress, Bristol and Farrand Press, London, (1991).

[5] B. J. Ford, *Single Lens: The Story of the Simple Microscope.* Harper & Row, New York, (1985).

[6] M. T. Madigan and J. M. Martinko, *Brock Biology of microorganisms.* Prentice Hall, Eleventh Edition, (2006).

[7] C. G. Ehrengerg, *Die Infusionsthierchen als Vollkommene Oraganismen.* Leopold Voss, Leipzig, Germany, (1838).

[8] K. Reichert, *Uber die Sichtbarmachung der Geisseln und die Geisselbewegung der Bakterien.* Zentralbl. Bakteriol. Parasitenk. Infektionskr. Abt. 1 Orig, **51**:14-94, (1909).

[9] T. W. Engelmann, *Neue methode zur Untersuchung der Sauerstoffausscheidung pflanzlicher und thierischer Organismen.* Pflugers Arch. Gesamte Physiol. Menschen Thiere, **25**:285-292, (1881a).

[10] T. W. Engelmann, *Zur Biologie der Schizomyceten.* Pflugers Arch. Gesamte Physiol. Menschen Thiere, **26**:537-545, (1881b).

[11] T. W. Engelmann, *Bacterium photometricum.* Pflugers Arch. Gesamte Physiol. Menschen Thiere, **30**:95-124, (1883).

[12] G. I. Taylor, *The action of waving cylindrical tails in propelling microscopic organisms.* Proc R Soc London A, **211**:225-239, (1952).
[13] G. K. Batchelor, *The Scientific Papers of Sir Geoffrey Ingram Taylor. Volume IV, Mechanics of Fluids: Miscellaneous Papers*. Cambridge University Press, Cambridge, (1971).
[14] M. Silverman and M. Simon, *Flagellar rotation and the mechanism of bacterial motility*. *Nature* **249**:73-74, (1974).
[15] E. M. Purcell, *Life at low Reynolds number.* American Journal of Physics, **45**:3-11, (1977).
[16] R. M. Macnab, *Bacterial flagella rotating in bundles: a study in helical geometry.* Proc.*Natl.Acad.Sci* **74**:221-25, (1977).
[17] R. M. Macnab, *How bacteria assemble flagella.* Annu.rev.microbiol, **57**:77-100, (2003).
[18] H. Hotani, *Micro-video study of moving bacterial flagellar filaments. III. Cyclic transformation induced by mechanical force*. J. Mol. Biol. **156**:791-806, (1982).
[19] L. Turner, W. S. Ryu and H. C. Berg, *Real-time imaging of fluorescent flagellar filaments. J. Bacteriol, **182**:2793-2801, (2000).*
[20] N. C. Darnton and H. C. Berg, *Force-Extension Measurements on Bacterial Flagella: Triggering Polymorphic Transformations.* Biophysical Journal, **92**:2230–2236, (2007).
[21] N. C. Darnton, L. Turner, S. Rojevsky, and H. C. Berg, *On Torque and Tumbling in Swimming Escherichia coli,* Journal of Bacteriology, **189**:1756–1764, (2007).
[22] H. C. Berg, *E. coli in Motion,* Biological and Medical Physical Series, Spring Verlag, (2003).
[23] H. C. Berg, *The rotary motor of bacterial flagella,* Annu.Rev.Biochem, **72:**19-54, (2003).
[24] M. Wheelis, *Principles of Modern Microbiology.* Jones & Bartlett, (2007).
[25] G. J. Tortora, B. R. Funke, and C. L. Case, *Microbiology: An Introduction.* Benjamin Cummings; 7th Edition, (2000).
[26] www.micro.digitalproteus.com
[27] K. Amako, and A. Umeda, *Bacterial Surfaces as Revealed by the High Resolution Scanning Electron Microscpe.* Journal of General Microbiology, **98**: 297-299, (1977).
[28] W. Vollmer and J. V. Höltje, *The Architecture of the Murein (Peptidoglycan) in Gram-Negative Bacteria: Vertical Scaffold or Horizontal Layer(s).* Journal of Bacteriology, **186**:5978-5987, (2004).
[29] M. E. Bayer, *Areas of Adhesion between Wall and Membrane of Escherichia coli,* Journal of General Microbiology, **53**:395-404, (1968).
[30] T. Baba *et al, Construction of the Escherichia coli K-12 in-frame, single-gene knockout mutants: The Keio collection,* Molecular systems biology, **2**:E1–E11, (2006).
[31] J. Adler, *Chemotaxis in Escherichia coli*, Quant.Bio, **30:**289-292, (1965).
[32] J. B. Armstrong, J. Adler, and M. M. Dahl, *Nonchemotactic Mutants of Escherichia coli.* J.Bacteriology, **93**:390-398, (1967).

[33] S. M. Finegold and W. J. Martin, *Diagnostic Microbiology*. Mosby Co, ISt. Louis, 6th ed, (1982).
[34] R. N Doetsch and R. D Sjoblad, *Flagella structure and function in eubacteria.* Ann. Rev.Microbiol, **34**:69-108, (1980).
[35] D. C Ihde, and D. Armstrong, *Clinical spectrum of infection due to Bacillus species.* Amer.J.Med. **55**:839-845, (1973).
[36] A. L Sonenshein, J. A. Hoch, and R. Losick, *Bacillus subtilis and its closest relatives. From genes to cells.* America Society for Microbiology, Washington DC, (2002).
[37] P. Grauman, *Bacillus: cellular and molecular biology*. Caister Academic Press, (2007).
[38] K. Kobayashi *et al,* Essential *Bacillus subtilis* genes, Proc.Natl.Acad.Sci. **100**:4678-83, (2003).
[39] M. M. Nakano, *Essential Role of Flavohemoglobin in Long-Term Anaerobic Survival of Bacillus subtilis.* J.Bacteriol, **188**:6415-6418, (2006).
[40] T. Hoffmann, B. Troup, A. Szabo, C. Hunggerer, and D. Jahn, *Anaerobic life of Bacillus subtilis: cloning of the genes encoding the respiratory nitrate reductase system.* FEMS.Microbiol.Lett, **131**:219-225, (1995).
[41] A. Czirók, I. Jánosi, and J. O Kessler, *Bioconvective dynamics: Dependence on organism behaviour.* The Journal of Experimental Biology, **203**:3345–3354, (2000).
[42] J. Boch, B. Kempf, R. Schimd, and E. Bremer, *Synthesis of the Osmoprotectant Glycine Betaine in Bacillus subtilis: Characterization of the gbsAB Genes.* Journals of Bacteriology, **17**:5121–5129, (1996).
[43] L. H. Cisneros, R. Cortez, C. Dombrowski, R. E. Goldstein and J. O. Kessler, *Fluid dynamics of self-propelled microorganisms from individuals to concentrated population.* Exp. Fluids **43**:737-754, (2007).
[44] C. A Solari, J. O. Kessler, and R. E. Goldstein, *Motility, mixing and multicellularity*. Genet Programme Evolvable Mach, **8**:11-129, (2007).
[45] W. S. Ryu, R. M. Berry, and H. C Berg, *Torque-generating units of flagellar motor of Escherichia coli have a high duty ratio.* Nature, **403**:444-447, (2000).
[46] H. C. Berg and R. A. Anderson, *Bacteria swim by rotating their flagellar filaments*. Nature, **245**:380-382, (1973).
[47] E. H Harris, *Chlamydomonas as a model organism.* Annual Review of Plant Physiology and Plant Molecular Biology, **52**:363-406, (2001).
[48] S. Khan, M. Dapice. and T. Reese, *Effects of mot gene expression on the structure of the flagellar motor.* J. Mol. Biol. **202**:575-584, (1988).
[49] H. Suzuki, K. Yonekura, and K. Namba, *Structure of the rotor of the bacterial flagellar motor revealed by electron cryomicroscopy and single-particle image analysis*. J. Mol. Biol, **337**:105–113, (2004).
[50] J. Zhou, S. A. Lloyd, and D. F. Blair, *Electrostatic interactions between rotor and stator in the bacterial flagellar motor.* Proc.Natl.Acad.Sci. **95**:6436-6441, (1998).
[51] F. A. Samatey et al, *Structure of the bacterial flagellar hook and implication for the molecular universal joint mechanism.* Nature, **431**:1062-1068, (2004).

[52] S. Satoshi et al, *FliK regulates flagellar hook length as an internal ruler*, Molecular Microbiology, **64**:1404-1415, (2007).
[53] T. C. Flynn and J. Ma, *Theoretical analysis of Twist/bend ratio and mechanical moduli of bacterial flagella hook and filament.* Biophysical journal, **86**: 3204-3210, (2004).
[54] K. Yonekura et al, *Bacterial Flagellar Cap as the Rotary Promoter of Flagellin Self-Assembly*, Science, **290**: 2148-2152, (2000).
[55] R. Macnab. and M. K. Ornston, *Normal-to-curly flagella transitions and their role in bacterial tumbling. Stabilization of an alternative quaternary structure by mechanical force.* J.Mol.Biol, **112**:1-30, (1977).
[56] M. D.Manson, P. Tedesco, H. C. Berg, F. M. Harold and C. van der Drift, *A protonmotive force drives bacterial flagella,* Proc.Natl.Acad.Sci, **74**:3060-3064, (1977).
[57] Y. Magariyama, S. Sugiyama, and S. Kudo*, Bacterial swimming speed and rotation rate of bundle flagella.* FEMS Microbiology.Letters, **199**:125-129, (2001).
[58] H. C. Berg, *Random Walks in Biology*, Princeton Paperbacks (Princeton University Press, Princeton, New Jersey, (1993).
[59] M. Kim and T. R. Powers, *Hydrodynamic interactions between rotating helices.* Physical Review E, **69**:061910, (2004).
[60] H. Flores, E. Lobaton, S. Méndez-Diez, S. Tlupova, and R. Cortez, *A study of bacterial flagellar bundling*, Bulletin of Mathematical Biology **67**:137-168, (2005).
[61] M. Kim, J.C. Bire, Annearie J. V. Parys, K. Breuer and T. R. Powers, *A Macroscopic scale model of bacterial flagella bundling*. Proc.Natl.Acad.Sci. **100**:15481-15485, (2003).
[62] T. R. Powers, *Role of body rotation in bacterial flagellar bundling*. Physical Review E, **65**:0409031-040903-4, (2002).
[63] H. C. Berg and L. Turner, *Cells of Escherichia coli swim either end* forward. Proc.Natl.Acad.Sci, **92**:477- 479, (1995).
[64] M. M. Nakano, *Essential Role of Flavohemoglobin in Long-Term Anaerobic Survival of Bacillus subtilis*. J. Bacteriol, **188**:6415-6418, (2006).
[65] D. O. Nettleton and G. W. Ordal, *Functional Homology of Chemotactic Methylesterases from Bacillus subtilis and Escherichia coli.* J. Bacteriol, **171**:120-123, (1989).
[66] J. Liu and J. S. Parkinson, *Role of CheW protein in coupling membrane receptors to the intracellular signalling system of bacterial chemotaxis.* Proc.Natl.Acad.Sci, **86**:8703-8707, (1989).
[67] J. S Parkinson, *Bacterial Chemotaxis: a New Player in Response Regulator Dephosphorylation.* Journal of Bacteriology, **185**:1492-1494, (2003).
[68] J. S. Parkinson, P. Ames and C. A. Studdert, *Collaborative signaling by bacterial chemoreceptors.* Curr. Opin. Microbiol. **8**:116–121, (2005).
[69] M. B. Elowitz *et al*, *Protein mobility in the cytoplasm of Escherichia coli.* J. Bacteriol, **181**:197–203, (1999).

[70] R. Jasuja, J. Keyoung, G. P. Reid, D. R. Trentham, and S. Khan, *Chemotactic responses of Escherichia coli to small jumps of photoreleased L-aspartate*. Biophys. J, **76**:1706–1719, (1999).

[71] J. E. Segall, M. D. Manson, and H. C. Berg, *Signal processing times in bacterial chemotaxis*. Nature, **296**:855–857, (1982).

[72] J. Xing, F. Bai, R. Berry, and G. Oster, *Torque-speed relationship of the bacterial flagellar motor.* Proc.Natl.Acad.Sci, **103**: 1260-1265, (2006).

Chapter 3 : Bacterial motility

3.1 Flagella locomotion at low Reynolds number

This chapter introduces the boundary conditions which govern bacterial locomotion at low Reynolds number. We consider the low Reynolds regime for the remainder of this chapter unless stated otherwise. It discusses what it might be like to live and to swim at low Reynolds number, eloquently described by Purcell in 1977, '*Life at low Reynolds number'* [1, 2]. In this regime our physical intuitions of swimming fails, since the governing physics at high Reynolds number is somewhat different. This chapter primarily discusses how swimming is achieved by rotating flagella filaments; introducing the Reynolds number and its interpretation [3, 4]. Subsequently, it discusses the Péclet number [5, 6] and the underlining physics principles and concepts of the *Scallop Theorem* [1], which only permits certain swimming modes. It introduces the propulsion matrix [1, 7, 8] derived from an idealized flagella bundle (left-hand helix). Subsequently this chapter discusses the resistive force theory (RFT) [9] and the ideas of thrust based drag [2], and how this theory is able to describe thrust generation in flagellated microorganisms such as *E. coli* and *B. subtilis.* Typically, flagellated bacteria are modelled as spheroids with a single rotating helix as a flagella bundle. These models are often used to analyze thrust, torque, and motility [8, 10].

3.1.1 Self propulsion

Microorganisms use locomotion as one method to seek improvements to their living environment [1, 2] through chemotaxis [11]. To do so, a microorganism must achieve a swimming velocity faster than the rate of molecular diffusion [1, 2]. If this is not achieved the microorganism does not change its environment [1]. Thus to

actively search for greener pastures a microorganism must swim faster than the rate of molecular diffusion [2]. The advantage of self motility enables microorganisms to actively search for nutrients, significantly more beneficial than being static. Moreover, this permits motile microorganisms to find suitable environments for cell reproduction and the capability to infect hosts [12]. Bacteria such as *E. coli* and *B. subtilis* propel themselves by converting internal chemical energy (ATP) into mechanical motion [13]. There are several method of bacterial motility such as swimming, swarming, gliding and twitching [14, 15], although we focus on swimming in this study. Microorganisms often achieve locomotion via cyclic motion of external appendages such as cilia and flagella [16]; for example chlamydomonas which performs as breast stroke like motion [17]. A successful technique of thrust generation is to periodically deform external appendages in a time-reversed independent manner, breaking time-reversal symmetry [1, 4, 18]. *E. coli* and *B. subtilis* cells deploy flagella filaments described in *Chapter 2*, *Figure.2.10.* This propulsive helical bundle exerts localized forces on the surrounding viscous fluid in order to generate thrust, *pushing/screwing* the cell through the medium [1].

A fundamental equation in fluid mechanics is the Navier-Stokes equations [3], these equations are essential for understanding bacteria locomotion and fluid systems alike. The Navier-Stokes equation fundamentally describes the motion of a fluid, by applying Newton's second law to fluid motion. This equation is used to determine the rate of change in acceleration of a fluid, which is proportional to the gradient of pressure. Solving the equation provides the fluid flow rate (at a given point in space and time), often known as the velocity field or flow field [19]. The flow field can provide an insight into many fluid phenomena such as, ocean currents, turbulence, and in aircraft design. In term of swimming bacteria the Navier-Stokes equations and flow fields are often used to examine collective swimming (cell-to-cell hydrodynamic interactions) *Chapter 6* and cells swimming near surfaces, typical of hydrodynamic models and simulations [20]. The general form of the Navier-Stokes equation for a unit volume of the fluid is defined as [3, 19]:

$$\rho\left(\frac{\partial \vec{V}}{\partial t} + \vec{V}\cdot\nabla\vec{V}\right) = -\nabla p + \nabla\cdot \mathrm{T} + \vec{F} \qquad \text{Eqn.3.1}$$

Where ρ is the fluid density and $\vec{V}$ is the fluid flow velocity, p is the pressure, T the stress tensor and $\vec{F}$ represents other external forces (per unit volume) exerted onto the given volume. The left-hand-side of Eqn.3.1 are the forces acting on the fluid; the first term in brackets represents the unsteady accelerations which are time-dependant and the second term represents the convective acceleration. The convective acceleration is fundamentally a measure of the change in velocity at a given position, as a fluid accelerates [3], such as forcing fluid through a nozzel. This equation is usually used with the continuity equation, stating the conservation of mass which is always conserved.

$$\frac{\partial \vec{V}}{\partial t} + \vec{V}\cdot(\rho\vec{V}) = 0 \qquad \text{Eqn.3.2}$$

Considering an incompressible[1] Newtonian fluid and constant viscosity η the Navier-Stokes equation and the continuity equation is defined as:

$$\rho\left(\frac{\partial \vec{V}}{\partial t} + \vec{V}\cdot\nabla\vec{V}\right) = -\nabla p + \eta\nabla^2\vec{V} + \vec{F} \qquad \text{Eqn.3.3}$$

$$\nabla\cdot\vec{V} = 0$$

The left hand side in the brackets represents the acceleration of the fluid. The stress tensor on the right hand side $\nabla\cdot T$ is now replaced by $\eta\nabla^2\vec{V}$ representing the local viscosity. More details on the derivation of the Navier-Stokes equation are in references [3, 19, 21]. This equation holds for the high Reynolds number regime.

[1] In our case we consider an incompressible fluid exclusively throughout this project.

For a bacterium on a micron length scale this equation is modified, discussed later in the chapter.

3.1.2 The Reynolds Number

The Reynolds number (R_e) is a dimensionless quantity which can be regarded simply as the ratio of inertial and viscous forces [1, 4, 5, 20] which is defined as:

$$\frac{f_{inertial}}{f_{viscous}} = \frac{\rho \vec{V}^2 L^2}{\eta \vec{V} L} = \frac{\rho \vec{V} L}{\eta} \equiv R_e \qquad \text{Enq.3.4}$$

Where; V and L are the typical flow velocity and length scales of the system. The Reynolds number is interpreted as the ratio of forces acting on the body. Viscous stress exerted on a body is given by ~ $\eta \vec{V} / L$ and therefore the viscous force acting on the body is simply given by $f_{viscous} \sim \eta \vec{V} L$. Inertial stress is given by the Bernoulli-like dynamic pressure, which is approximated as $\sim \rho \vec{V}^2$, subsequently we derive the inertial force by multiplying by L^2 [4]. Therefore the inertial force is defined by $f_{inertial} \sim \rho \vec{V}^2 L^2$ where Reynolds number is the ratio of inertial and viscous forces acting on the body. At low Reynolds number regime, viscous forces dominate in the fluid, thus fluid flow fields are derived primarily from viscous forces [1, 4]. The Navier-Stokes equation Eqn.3.3 can be nondimensionalized by implementing the following arguments:

$$\vec{V} \to \frac{\vec{V}}{V} \qquad t \to t\left(\frac{V}{L}\right) \qquad X \to \frac{X}{L}$$

Where; V and L are the typical flow velocity and length scales of the system. From equation Eqn.3.3 the Reynolds number is in a dimensionless form which is equal to:

$$\mathrm{Re}\left(\frac{\partial \vec{V}}{\partial t} + \vec{V}\cdot\nabla\vec{V}\right) = -\nabla p' + \nabla^2\vec{V} + f' \qquad \text{Eqn.3.5}$$

Where $p' = p(L/\eta V)$ and $f' = f\left(\rho L^2/\eta V\right)$. One can imagine swimming at low Reynolds number is analogous to swimming in syrup [1], where movements in the fluid are over-dampened. Therefore, in this regime momentum plays an insignificant role, and viscous drag/stress dominates. One can assume there is no drift or momentum transfer in this regime, therefore for a bacterium as soon as propulsion stops so does forward displacements [2, 4].

Here we asked, what is the typical value of the R_e for micron size organisms such as *E .coli* and *B. subtilis*? The properties of water are approximately: $\rho \approx 10^{3}$ kg/m^3 and $\eta \approx 10^{-3}$ Pa.s; the average swimming velocity of bacterium is $\vec{V}$ ~ 20 - 30 μms^{-1} and the typical length scale of a microorganism is L ~ 1 - 10 μm. Therefore, R_e for a bacterium in water is typically $R_e \sim 10^{-5}$ - 10^{-4} [1, 2, 4, 5, 8]. For swimming bacteria the viscous drag governs the locomotion and the Navier-Stokes equation Eqn.3.3 can be simplified, permitting us to neglect all the inertial terms [1]. Thus Eqn.3.6 is defined as the simplified Stokes equation [3, 4, 6, 22].

$$-\nabla\rho + \eta\nabla^2\vec{V} + F = 0 \qquad \text{Eqn.3.6}$$

Note Eqn.3.6 is for an incompressible fluid is independent of time and is a linear equation [1, 4]. This equation gives rise to the propulsion matrix discussed later in this chapter [7, 8]. Other interpretations of the Reynolds number can be found in reference [4].

3.1.3 The Péclet Number

The Péclet number is a convenient method of observing the ratio of bacterial length scales in terms of transport either by diffusion or advection [5, 6, 20]. The Péclet number (P_e) is a dimensionless quantity defined by the ratio of the diffusion time and advection time, $P_e = T_D/T_v$ [5, 6]. The advection time is defined as $T_v \sim L/V$ and diffusion time is given by $T_D \sim L^2/D$ which can be interpreted as the time required for a particle with a diffusion coefficient D to move a distance L; therefore the Péclet number is simplified to:

$$P_e \sim \frac{VL}{D}, \qquad \text{Eqn.3.7}$$

where V is the characteristic velocity and L is the characteristic length. Thus the Péclet number governs the regime in which transport of molecules are either dominated by Brownian motion i.e. diffusion or by advection such as mixing [5, 6]. If the Péclet number yields a value $P_e > 1$, this indicates that molecules are mainly transported by advection; whereas $P_e < 1$ indicates a regime in which particles are transported by diffusion. What is the typical Péclet number for oxygen molecules[2], a life essential molecule especially for *B. subtilis* cells? The typical diffusivity of oxygen molecules is in the order of $D \sim 10^{-5}$ cm^2s^{-1} [1, 5, 6] and using the typical length parameters of swimming bacteria, $\vec{V} \sim 10^{-3}$ cms^{-1} and $L \sim 10^{-3}$ cm. The Péclet Number is in the order of $P_e \sim 10^{-1}$ - 10^{-2} indicating that life essential molecule and solutes are transported by the process of diffusion, and advection plays an insignificant role [5, 6]. However this raises questions in regards to cell motility, why do cells swim if diffusion alone is capable for transporting life sustaining molecules? To render cellular motility an effective method of cell survival, cellular

[2] Or other small solutes such as nutrients.

translocation has to out run diffusion [1, 2] in order to experience a change in environment (i.e. swimming up chemical gradients to search for regions of higher nutrient concentration); such that $Pe > 1$, thus the system becomes advective. The characteristic length L in which cells have to swim to beat diffusion is given by [2, 4, 29]:

$$L \geq \frac{D}{V} \qquad \text{Eqn.3.8}$$

The average swimming velocity of *E. coli* or *B. subtilis* cells range between 20 – 30 μms^{-1}, where diffusion of small molecules $D \sim 10^{-5}$ cm^2s^{-1}, then equation Eqn.3.8 yields a minimal run distance of $L \sim 30$ μm in order to do better than diffusion. A typical run length of a bacterium observed in nature is in the same order of magnitude [2], demonstrating that cells swim at a velocity which beats molecular diffusion, enabling cells to actively search for improved living environments via chemotaxis [1, 2, 11].

3.2 Time-reversal symmetry and the *Scallop Theorem*

The living environment for low Reynolds number swimmers is somewhat different to our own intuition. The low Reynolds regime, $R_e \sim 10^{-5}$ - 10^{-4} implies that inertial forces play an insignificant role, where the mechanical movement is dampened by viscous forces. This was illustrated by Berg who considered how far an *E. coli* cell would coast if it was to stop swimming. The solution yielded a typical coasting distance of 0.04 Å, less than a diameter of a hydrogen atom, which occurs in a time of 0.3 μs [1, 23]. Therefore, how does this boundary condition influence the swimming mechanism and behaviour of bacteria in viscous liquids? As a consequence of the Stokes equation Eqn.3.6, on small length scales, reciprocal

motion[3] is an ineffective method of swimming at low Reynolds number; even when strokes are performed at different speeds [1, 4]. Purcell introduced the idea of reciprocal motion of a swimmer which led to the renowned *scallop theorem* [1]. He introduced the ideas of swimming at low Reynolds number by asking the fundamental question: *what is the simplest form of motion of a microorganism which can generate net motion at low Reynolds number?* The answer he concluded was that a swimming organism can swim by cyclic motions which deform its body or external appendages; these appendages could be cilia, flagella or even complete body deflections. However the motion of deformation must be time-independent and non-reciprocal[4] [1, 4, 7].

One of the simplest forms of a swimmer is a scallop which has a single hinge and therefore one degree of freedom, *Figure.3.1*. In nature (at high Reynolds number) a scallop generates thrust by opening and closing the hinge at different velocities. Opening the shell slowly and by rapidly closing it propels the scallop forward. At high Reynolds number the rate which the motion is executed determines the amount of thrust force generated, due to inertia and momentum transfer. In the low Reynolds regime the inertia terms are irrelevant, Eqn.3.6. Purcell demonstrated that this type of reciprocal motion at low Reynolds number fails to generate net motion. This regime is dominated by viscous drag and is time-independent; the scallop has one degree of freedom, therefore bound to reciprocal motion [1, 7]. This means that the motion of the scallop repeats itself, i.e. moving in cyclic sequence; therefore the scallop in this regime oscillates about a mean position and does not generate net propulsion. This is demonstrated in *Figure.3.1*, from the initial position 1 as the scallop goes to position 2 by closing its shell; this generates thrust and moves towards the left. Since the scallop has one degree of freedom, it can only open its shell as its next sequence, i.e. moving back to position 1. Thus by opening the shell,

[3] Motion that is cyclic which is identical in time-reversal.

[4] Whether the motion is performed fast or slowly or forward and backwards in time.

the scallop moves back towards the right to the original starting position 1, and zero net displacement is achieved.

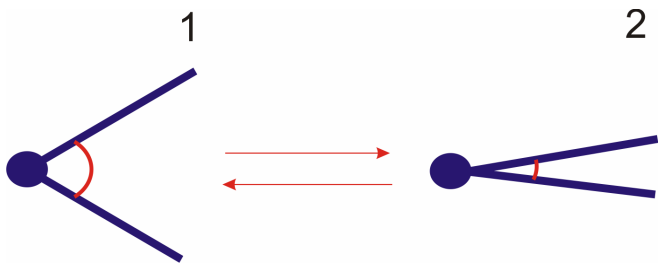

Figure.3.1: Schematic of a scallop hinge which opens and closes depicted by positions one and position two. At low Reynolds number, moving from position one to position two generates thrust towards the left direction. Since there is one degree of freedom the scallop has to go from position two back to position one moving the scallop toward the right. Thus this motion generates zero net displacement, since the viscous forces are identical when moving from position one to position two. Thus reciprocal and time reversible motion fails at low Reynolds regime.

Purcell argued that: *if the sequence of body deformations is in a time periodic way or is identical when viewed after a time-reversal transformation, then the swimmer cannot generate net displacement*. He clearly demonstrated that time is irrelevant, whether the deformation is fast or slow, or even when the motion is backwards or forwards in time, reciprocal motion at low Reynolds regime does not generate net motion [1]. Thus the general rule for a low Reynolds number swimmer states: *No time-reversible sequence of body deformation can swim.*

To elude the scallop theorem, Purcell introduced a theoretical microorganism with a secondary hinge, which breaks reciprocal motion[5] and time-reversal symmetry allowing locomotion, known as the Purcell swimmer[6] [1, 4]. Permitting an extra degree of freedom, the motion of the swimmer is no longer reciprocal. Purcell

[5] Reciprocal motion: the motion of a swimmer is called reciprocal if the sequence of shape which the swimmer assumes is invariant under time-reversal [4].
[6] Also known as Purcell three linked swimmer.

imagined a swimmer with three arms which are linked together by two hinges[7], *Figure.3.2 (a)* via translating each arm of the swimmer independently through angles θ_1 and θ_2 in a sequence going from 1 - 4. This in turn leads to the original starting position, implying the sequence is periodic. In this case, the theoretical three linked swimmer is able to break time-reversal symmetry, thus resulting in net motion. Recent studies have shown micro-scale artificial replicas of Purcell swimmer demonstrating locomotion at low Reynolds number [1, 6], *Figure.3.2 (c).* Plotting the phase-space diagram, *Figure.3.2 (b)* [1] of the angles θ_1 and θ_2 between the two *legs* and the *body* element, one finds that the theoretical swimmer follows an enclosed loop, sequence 1 - 4.

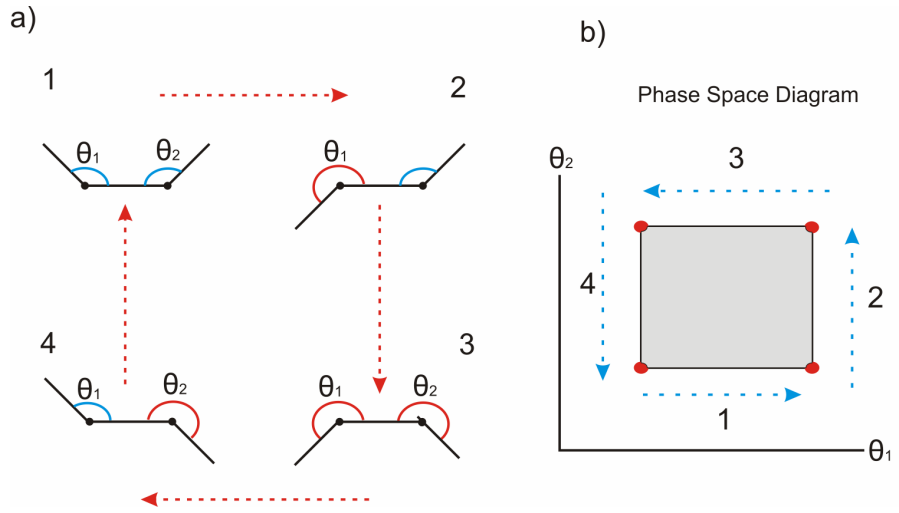

Figure.3.2: (a) A schematic representation of a Purcell's three link swimmer, this system can swim at low Reynolds number because it goes through a sequence of different positions and returns to the initial starting position in a periodic fashion, breaking time reversibility and reciprocal motion. (b) The phase space diagram of the change in angle of each arm of the three link swimmer, which results in an enclosed loop breaking time reversed symmetry; the direction of the swimmer is not obvious [1].

Purcell demonstrated that this theoretical three linked swimmer is able to swim at low Reynolds number. In nature there are many microorganisms which swim using a variety of methods to avoid reciprocal motion, but still remain periodic [12, 14, 15].

[7] No such organism has been observed in nature, however artificial micron scale models have demonstrated Purcell's swimmer to swim at low Reynolds number [6].

The most relevant is the rotation of flagella in *E. coli* and *B. subtilis* cells. The early work by Berg *et al* demonstrated *E. coli* swims by the rotation of a helical bundle [2, 24, 25], *Chapter 2*. A rotating helix in the low Reynolds regime breaks reciprocal symmetry due to the rotating shape of the helix[8] [1, 2, 26] thus leading to net propulsion. Moreover, it is fascinating to examine how a rotating helix is able to generate sufficient thrust to propel itself and a cell body [24 - 26]. Subsequently by analysing how the rotation of a rigid helix is able to generate propulsion by applying viscous drag forces on the surrounding fluid due to its helical shape. Moreover we discuss the relationship between force, torque, translation — and rotational velocity, and examines resistive force theory [9, 22, 28], a mathematical description of thrust generation from a rotating helix and other rotating propellers.

To summarize, in the low Reynolds number regime, the inertia terms in the Navier-Stokes equation Eqn.3.3 are neglected since inertia on these length scales has an insignificant role, thus movement is dampened by viscous drag forces. The Stokes equation is linear and independent of time, and net displacement is achieved only by non-reciprocal motion which breaks time-reversal symmetry, demonstrated by the underlining principles postulated from the scallop theorem.

3.3 The Propulsion matrix

Figure.2.10 illustrated a fluorescently labelled *E. coli* cell performing a run, where a helical bundle is formed at the rear of the cell [2, 24 - 26]. The co-rotation of flagella generates thrust which translates along the cell body and in the direction of cell orientation. To model the non-trivial process of swimming *E. coli*, the bundle can be approximated as a single effective helical propeller [1, 8]. This is similar to modelling monotrichous bacteria such as *Pseudomonas aeruginosa* which only has a single flagellum [29]. However with significant simplifications of the bundling

[8] Similar to propagating waves translating along the helix as it rotates periodically, analogous to a corkscrew.

process, there still remain theoretical challenges due to time-independent boundary conditions [8, 16]. Purcell introduced and generalized the thrust produced by a single propeller, formulating the propulsion matrix in the limits of low Reynolds regime which is governed by the Stokes flow.

Purcell considers swimming bacteria such as *E. coli* as a simple passive spheroid bodies propelled by a flagella bundle, where the flagella bundle is approximated as a single rotating helix [1,4]. This is a very simplistic interpretation of understanding thrust generation, where a number of assumptions in this model are made. For example this model does not consider hydrodynamic dynamic interactions between the cell body and the rotating flagella bundle, and it assumes that swimming bacteria are force and torque free. Despite these simplifying alterations, the problem of modelling swimming cells remain theoretically challenging because of time-dependant boundary conditions. Purcell considered a swimming bacterium as being force free and torque free if the cell is swimming at constant velocity v, which implies the forces and torques directly cancel except external forces [1, 7, 8]. Purcell examined two essential parameters of the flagellum bundle, (i.e. two degrees of freedom of a rotating helix), firstly the translation velocity v and secondly the angular velocity ω. In this simplified model, the flagella motor generates a torque N_{Mot} which acts on the propeller (i.e. rotating the rotating helix) subsequently generating a thrust force, $F_{thrust.}$ This thrust force; F_{thrust} essentially pushes against the localized fluid which propels the cell in the forward direction. The generated thrust force F_{thrust} and torque N_{Mot} are linearly related to the helix's angular velocity ω and translational velocity v due to Stokes equation, Eqn.3.6 [1, 7, 8]. Thus the equations for the thrust force of the flagellum and the exerted flagella motor torque are defined as:

$$F_{thrust} = Av - B\omega \qquad \text{Eqn.3.9}$$

$$N_{Mot} = Cv + D\omega \qquad \text{Eqn.3.10}$$

Where A, B, C and D are constant and are proportional to the fluid viscosity η and these only depend on the shape and size of the propeller [1, 7, 8]. These equations are often written in a 2 × 2 matrix form known as the propulsion matrix (resistance matrix):

$$P = \begin{bmatrix} A & -B \\ C & D \end{bmatrix}$$

The full derivation of the propulsion matrix can be found in reference [7], where a theoretical proof is given for the matrix elements, A, B, C, and D, and demonstrates that the matrix elements $C = -B$. Thus, the force and torque equations are simplified and summarized in equations Eqn.3.11 and Eqn.3.12, which are linearly related to the propeller's angular velocity ω and translation velocity v (relative to the background fluid) [8]. Where A, B and D are the drag coefficients of the filament which can be derived from resistive force theory [4, 7, 8].

$$F_{thrust} = Av - B\omega \qquad \text{Eqn.3.11}$$

$$N_{Mot} = -Bv + D\omega \qquad \text{Eqn.3.12}$$

The model for a typical swimming bacterium is illustrated in, *Figure.3.3* demonstrating a free body diagram of the forces acting on the swimming bacterium. The sign of ω and N_{Mot} obey the right-hand rule for a left-hand helix, typical of flagella bundles [8]. The free body diagram is only concerned with the total thrust force and total torque of the filament, i.e. the magnitude and respective direction. Both equations Eqn.3.11 and Eqn.3.12 are linear and therefore the propulsion matrix is reads:

$$P = \begin{bmatrix} A & -B \\ -B & D \end{bmatrix} \qquad \text{Eqn.3.13}$$

The underlining physical principles in this simple model of a swimming bacterium imply that: *in a force free and viscous environment such as low Reynolds number; a translating helical shaped propeller under the influence of an external force must rotate. Vice versa, when an external torque is applied to a helical propeller, the propeller translates with a thrust force* [1]. The propulsion matrix described by Purcell is applicable to any shape propeller as long as it is asymmetric. In this case we apply the propulsion matrix to a rigid helical coil with well defined physical parameters.

To complete this simple model, the cell body is considered independently of the helix, as a prolate spheroid which does not generate thrust [4, 8, 10]. The force acting on the cell body consists of two components, firstly the thrust generated by the flagella bundle F_{thrust} and secondly the viscous drag force of the cell body acting in opposing direction, $-F_{drag}$. In this model we make the assumption that the thrust force and the drag force directly balance each other; thus the model is considered force free [1, 8]. Similarly the torque generated by the flagella motor, N_{Mot} directly balances out with rotational viscous drag force of the cell body as it rotates in the opposing direction, $-N_{drag}$ *Figure.3.3*. Using these two fundamental assumptions based on the viscous drag of the cell body, the following equations are derived to equate the total forces acting on the cell body only:

$$-F_{drag} = A_0 v \qquad \text{Eqn.3.14}$$

$$-N_{drag} = D_0 \Omega \qquad \text{Eqn.3.15}$$

Where v and Ω are the linear and angular velocities respectively, and A_0 and D_0 are the drag coefficients defined as $A_0 = 4\pi\eta b/\left(\ln(\frac{2b}{a}) - \frac{1}{2}\right)$ and $D_0 = 16\pi a^2 b/3$ for a prolate spheroid in fluid bulk [8, 3]. The viscous drag force $-F_{drag}$ and torque $-N_{drag}$ act in the opposing direction to the flagella thrust force, F_{thrust} and torque N_{Mot}, which directly cancels each other hence a torque and force free system,

Figure.3.3. a is the semi-minor-axis and b semi-major-axis depicted in *Figure.3.3.* Substituting Eqn.3.14 into Eqn.3.11 and similarly Eqn.3.15 into Eqn.3.12, one obtains the following expressions:

$$(A + A_0)v = B\omega \qquad \text{Eqn.3.16}$$

$$D_0\Omega = -Bv + D\omega \qquad \text{Eqn.3.17}$$

The above expressions are used to model swimming bacterium, and current research aims to provide accurate empirical data to fit the parameters in order to improve mathematical models of swimming cells [8, 10].

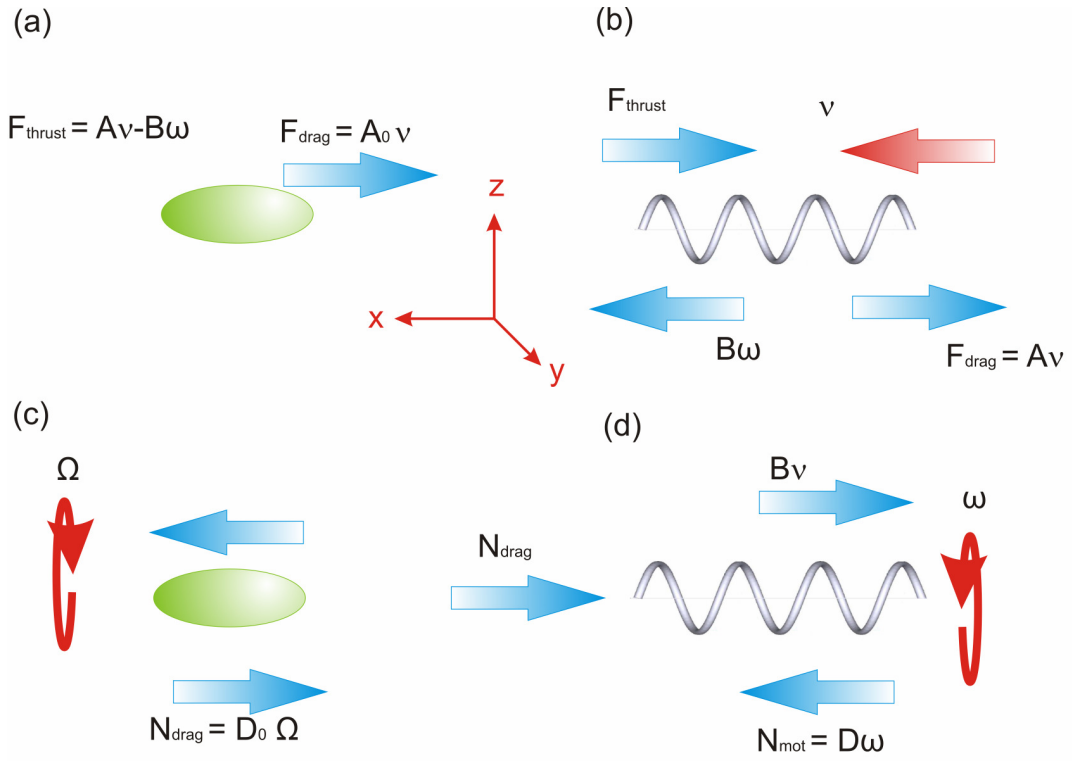

Figure.3.3: A free body diagram modelling a swimming bacterium depicting the thrust and torque forces. The total thrust and torque forces directly balances each out for a swimming bacterium, thus a force and torque free system. The arrows indicate the magnitude and direction of forces, where left is the positive x direction. F_{drag} *is the viscous drag force of the cell body and* N_{drag} *is the viscous drag of the cell body as it rotates, Adaptation of [30].*

In this model the thrust generated by the rotation of flagella, results in a thrust force being exerted on the cell body F_{thrust} and the body moves at a velocity v in the positive x direction. This thrust force is opposed by viscous drag forces of the cell body $A_0 v$, acting in the opposing direction i.e. $-F_{drag}$. (b) Rotation of the helix exerts a force pushing on the fluid in the negative x direction, leading to an equal and opposite pair reaction force with a magnitude $B\omega$ on itself, where it is opposed by the reaction force F_{thrust} from the cell body and its drag force $-F_{drag} = Av$. (c) The production of torque by the flagella motors N_{Mot} acting on the cell body is directly balanced by the viscous drag of rotating the cell body, $-N_{drag}$. (d) The helix rotates at a faster rate than the cell body to produce an identical torque N_{Mot} acting in the opposing direction which is used to translates the helix [2, 8, 10]. Therefore, the torque on the flagellum is equal to $Bv + D\omega$ which balances the cell body rotation rate $-N_{drag}$ hence equation Eqn.3.17.

In summery, *Figure.3.3* demonstrates a simple model for a flagellated swimming bacterium at constant velocity which is assumed to be force and torque free [8, 10]. This basic model of a single swimming bacterium implies that the magnitude of the thrust force generated by the flagellum $F_{thrust} = Av - B\omega$ is equal to the linear viscous drag of the cell body $-F_{drag} = A_0 v$, thus Eqn.3.16. Secondly the total torque generated by the helix (flagella motor) directly balances the rotational drag of the cell body, thus Eqn.3.17. The above describes a basic model used to illustrate swimming cells and is generally used to describe thrust generation and motility in *E. coli* and *B. subtilis* in a low Reynolds regime [8, 20].

3.4 Resistive force theory — Physics of drag-based thrust

This subsection introduces and explains the underlining physics of an idealized rotating helix enabling thrust generation, eluding the perils of the scallop theorem. Microorganisms exploit viscous drag as a mechanism to generate thrust [1, 4]. The Gray-Hancock theory of flagella propulsion was first introduced in 1955 and is now known as *resistive force theory* (RFT) [8, 9, 30]. This theory studies the motion of a single flagellum modelled as a wave travelling through a viscous fluid generating net propulsion [9, 31]. Moreover, it can be applied to a rotating helix, by considering a left-handed helix with a well defined length L, pitch length λ, helical radius R, and pitch angle of the helix relative to the swimming axis θ depicted in, *Figure.3.4*.

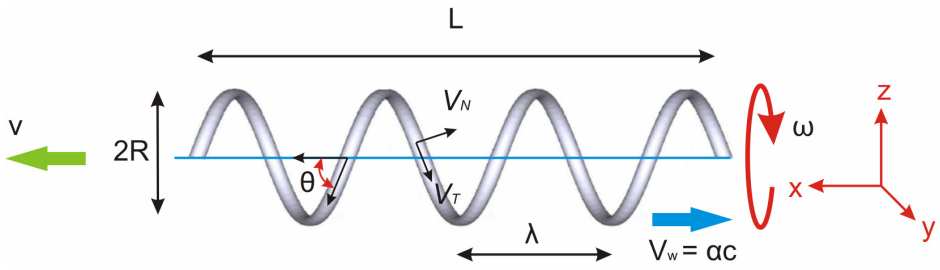

Figure.3.4: A schematic showing the parameterization of the filament used to derive the force thrust of a typical helix. The net velocity of each segment is a combination of the forward translational velocity v and the wave speed of the helix v_w in the opposing direction. Since it is considered as a rigid coil the helix angle θ and pitch length λ are constant for the entire filament. Image is an adaptation of [30] where full details can be found.

Firstly the RFT is a crude approximation of how thrust is generated by a rotating helix, where several approximations are made. RFT essentially divides the flagellum into a series of small linear segments, which are approximated as a series of cylindrical rod with a length D and a radius r, *Figure.3.5*. This proposed theory neglects the hydrodynamic interactions between the cell body and the helix; and the localized hydrodynamic flagella-flagella interactions of each segment D. Rotating the helix about the x axis with an angular velocity ω; each segment D of the filament

is 'dragged' through the fluid with a rotational velocity and translation velocity producing a thrust force. It is precisely the summation of the generated drag force in the lateral direction (x direction) by each segment *D*, which provides the resultant thrust force to propel itself and the cell body [8]. This is shown in *Figure.3.*5 where swimming *E. coli* cells are often idealized as a prolate ellipsoid attached to a left-handed propulsive helix.

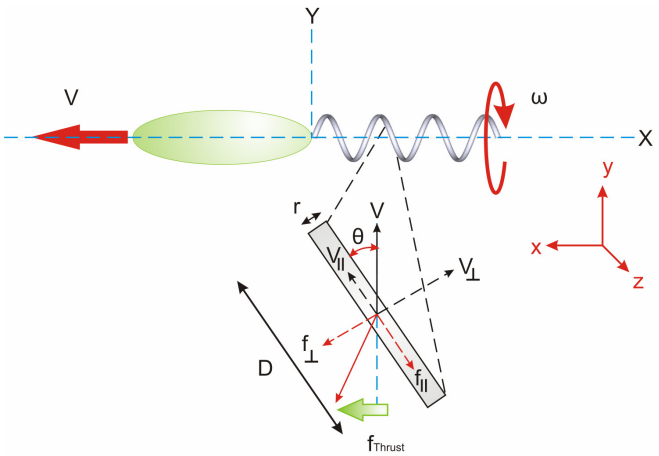

Figure.3.5: Schematic diagram modelling a swimming bacterium whereby the rotation of the helical coil generates forward thrust. The drag of a small segment of the rotating coil provides a mean thrust force perpendicular to the direction of actuation, propelling the cell towards the negative x direction with velocity v. Adaptation from [4].

Considering a small element of the helix *D*, to the first approximation it is a cylindrical rod. When this rod is actuated through a viscous medium with a velocity *v* in the vertical direction (similar to of a linear section of a helix as it is rotated about the x axis); the velocity can be resolved into two components, the perpendicular $v_{\perp} = v\sin\theta$ and parallel $v_{\parallel} = v\cos\theta$ therefore the drag forces per unit length of each components defined as: $f_{\perp} = -K_n v_{\perp} = -K_n v\sin\theta$ and $f_{\parallel} = -K_t v_{\parallel} = -K_t v\cos\theta$ respectively [6]. Where K_t and K_n are the tangential and normal drag coefficients respectively defined by: $K_t = 2\pi\eta/(\ln(2D/r) - 1/2)$ and $K_n = 4\pi\eta/(\ln(2D/r) + 1/2)$ for derivation see references [8, 23, 30]. Since the drag coefficients are $K_n \neq K_t$, an additional thrust force F_{thrust} component is generated,

which acts perpendicular to the motion of the element. Thus, the thrust force is defined as $F_{thrust} = (K_t - K_n)v \sin\theta\cos\theta$. To generate net propulsion both the variables V and θ must vary periodically in time [4]. This thrust mechanism *relies explicitly on the properties of Stokes flow, and in a world of isotropic viscous friction* ($K_t = K_n$), *locomotion would not be possible* [4]. Gray and Hancock argued that total thrust force generated to propel the cell is equal to the summation of the thrust force generated by each element *D*. Thus, the total thrust force exerted on the fluid by the rotating filament is the integral of the force generated by the each segment *D* over the entire length of the filament *L*. The full derivations of RFT is beyond the scope of this thesis, however further details of the derivation are found in references [9, 31].

Recently experiments with *E. coli* cells have been used to investigate the accuracy of the resistive-force theory [8, 10], and RFT has been compared to slender body theory [31] (not discussed here). Experimental data suggest the average thrust force of a swimming bacterium ranges between 0.25 - 0.85 pN [10], compared to RFT for a modelled flagella bundle one obtains a value ~ 0.57 pN [8]. The experimental data and theoretical predictions are consistent for the average thrust force. However, when calculating the torque for a single flagellum, RFT predicts a value which is significantly smaller than experimentally measured [10]. This discrepancy suggests that RFT may require further refinement. However, the comparison between RFT and slender body theory yields consistent results between the two theories, and RFT is accepted as a satisfactory for flagella analysis and modelling [31].

3.5 Conclusion

This chapter has introduced the fundamental ideas of self-propulsion on a micron length scale. It demonstrates in a low Reynolds regime only certain swimming modes generate net propulsion. It highlights the importance of the Navier-Stokes equations, the Reynolds number and Péclet number in regards to a swimming

microorganism and the use in simulations. In the low Reynolds regime it demonstrated that inertia has no effects and the inertia terms in the Navier-Stokes equations can be neglected. The Scallop Theorem highlights swimming modes which breaks reciprocal motion and time-reversal symmetry can only generate net displacements, thus permitting certain swimming modes. We discussed how flagellated bacteria such as *E. coli* escape the perils of the Scallop Theorem and introduce the propulsion matrix and the ideas of drag-based thrust by rotating flagella filaments. Finally we discussed the resistive force theory and how this is applied to model flagellated swimming bacteria.

Bibliography and References

[1] E. M. Purcell, *Life at low Reynolds number.* American Journal of Physics, **45**:3-11 (1977).
[2] H. C. Berg, *E. coli in Motion,* Biological and Medical Physical Series, Spring Verlag, (2003).
[3] J. Happel and H. Brenner, *Low Reynolds Number Hydrodynamics.* Springer, New York, 1st Ed, (1981).
[4] E. Lauga and T. R. Powers, *The hydrodynamics of swimming microorganisms.* Rep.Prog.Phys. **72**:096601, (2009).
[5] C. A Solari, J. O. Kessler, and R. E. Goldstein, *Motility, mixing and multicellularity*. Genet Programme Evolvable Mach, **8**:11-129, (2007).
[6] C. Dombrowski, L. Cisneros, S. Chatkaew, R. E. Goldstein, and J. O. Kessler, *Self-concentration and large-scale coherence in bacterial dynamics*. Phys. Rev. Lett. **93**:098103, (2004).
[7] E. M. Purcell*, The efficiency of propulsion by a rotating flagellum*. Proc. Natl. Acad. Sci, USA, **94**:24–29, (1997).
[8] S. Chattopadhyay, R. Moldovan, C. Yeung, and X. L. Wu, *Swimming efficiency of bacterium Escherichia coli*. Proc. Natl. Acad. Sci, USA, **103**:13712–13717, (2006).
[9] J. Gray and G. J. Hancock, *The self-propulsion of microscopic organisms through liquids*. J. of Exp. Bio, **32**:802–814, (1955).
[10] N. C. Darnton, L. Turner, S. Rojevsky, and H. C. Berg, *On Torque and Tumbling in Swimming Escherichia coli,* Journal of bacteriology, **189**:1756–1764, (2007).
[11] J. Adler, *Chemotaxis in Escherichia coli*, Quant.Bio, **30:**289-292, (1965).
[12] M. T. Madigan and J. M. Martinko, *Brock Biology of microorganisms.* Prentice Hall, Eleventh Edition, (2006).

[13] S. H. Larsen, J. Adler, J. J. Gargus, and R. W. Hogg, *Chemomechanical Coupling without ATP: The Source of Energy for Motility and Chemotaxis in Bacteria* Proc Natl. Acad. Sci, USA, **71**: 1239–1243, (1974).

[14] J. Henrichsen, *Bacterial surface translocation: a survey and a classification.* Bacteriol. Rev. **36**:478–503, (1972).

[15] R. M. Harshey, *BACTERIALMOTILITY ON A SURFACE: Many Ways to a Common Goal.* Annu. Rev. Microbiol, **57**:249–73, (2003).

[16] C. Brennen and H. Winet, *Fluid mechanics of propulsion by cilia and flagella*. Annu. Rev. Fluid Mech, **9:**339–98, (1977).

[17] E. H. Harris, *Chlamydomonas as a model organism.* Annual Review of Plant Physiology and Plant Molecular Biology, **52**:363-406, (2001).

[18] E. Lauga, Continuous *breakdown of Purcell's scallop theorem with inertia.* Phys. Fluids, **19**:061703, (2007).

[19] L. Quartapelle, '*Numerical solution of the incompressible Navier-Stokes equations*. Birkhäuser Verlag, (1993).

[20] L. H. Cisneros, R. Cortez, C. Dombrowski, R. E. Goldstein and J. O. Kessler, *Fluid dynamics of self-propelled microorganisms from individuals to concentrated population.* Exp. Fluids **43**:737-754, (2007).

[21] Y.C. Fung, *Biomechanics: Motion, Flow, Stress and Growth*. Springer-Verlag, New York, (1990).

[22] S. Childress. *Mechanics of swimming and flying*. Cambridge Studies in Mathematical Biology. Cambridge University Press, 1 edition, (1981).

[23] J. Lighthill J, *Mathematical Biofluiddynamics.* (SIAM, Philadelphia), 3rd Ed, (1989).

[24] H. C. Berg and R. A. Anderson, *Bacteria swim by rotating their flagellar filaments*. Nature, **245**:380-382, (1973).

[25] H. C. Berg, *The rotary motor of bacterial flagella,* Annu.Rev.Biochem, **72:**19-54, (2003).

[26] R. M. Macnab, *Bacterial flagella rotating in bundles: a study in helical geometry.* Proc.*Natl.Acad.Sci* **74**:221-25, (1977).

[27] H. C. Berg, *Random Walks in Biology*, Princeton Paperbacks, Princeton University Press, Princeton, New Jersey, (1993).

[28] G. I. Taylor, *The action of waving cylindrical tails in propelling microscopic organisms.* Proc R Soc London A, **211**:225-239, (1952).

[29] F. Roberts, JR and R. N. Doetsch, *Some Singular Properties of Bacterial Flagella, with Special Reference to Monotrichous Forms.* Journal of Bacteriology, **91**: 414-421, (1966).

[30] S. Chattopadhyay Thesis, *Study of bacterial motility using optical tweezers.* University of Pittsburgh, (2008).

[31] R. E. Johnson and C. J Brokaw, *Flagellar Hydrodynamics: A Comparison between Resistive-Force Theory and Slender-body Theory.* Biophys.J, **25**:113-127, (1979).

Chapter 4 : Investigating motility in spherical *E. coli*

4.1 Introduction

This chapter investigates the possibility of cellular motility in spherical mutant KJB24 *E. coli* cells. This provides an excellent introduction to the biological aspects of this PhD project. As a part of this chapter it will introduce a number of standard microbiology techniques and procedures regarding bacterial characterization and synchronization. Such as the standard motility protocol, growth curves assays and the semi-solid chemotactic agar plate assay. Moreover it discusses the basic microscopy techniques used to image bacteria in bright-field, discussing the two main types of microscope design and their limitations. The basic principles of fluorescence microscopy are discussed, which are utilized in subsequent experiments.

This chapter is primarily focused on determining whether spherical mutants KJB24 *E. coli* cells are actively motile, in comparison to wild-type cells HCB1 which demonstrate motility under specific growth conditions. KJB24 was incubated with a motility growth procedure promoting flagella synthesis and making cellular motility possible. KJB24 cells incubated with the motility procedure were observed with bright-field video microscopy and with force measurement optical tweezers[1] to explore the possibility of flagella synthesis and flagella motility in spherical mutants. Observations in bright-field microscopy of ~ 1 μm diameter spherical cells were compared to similar sized 1 μm diameter polystyrene beads. Subsequently, force

[1] Optical tweezers was constructed and calibrated by the author of this thesis as part of this PhD project, as a tool to non-invasively manipulate and examine bacteria in microfluidic devices.

measurement optical tweezers were implemented to examine the diffusivity and low frequency fluctuations of KJB24 cells in respect to colloids. Semi-solid chemotactic agar plate assays were conducted to examine both wild-type and spherical strains for signs of chemotaxis and cellular motility. For conclusive evidence of flagella synthesis in spherical cells, nanometer scale resolution microscopy is required. This led to the implementation of atomic force microscopy (AFM) where the advantages and disadvantages of these techniques are discussed along with the results obtained by AFM where normal wild-type *E. coli* cells and spherical mutants were imaged.

4.2 Motivation for studying spherical *E. coli*

For decades there have been numerous mathematical and hydrodynamic models which attempted to model the swimming behaviour of cells at low Reynolds number. These date back to the classical works of Taylor [1] which endeavoured to model the tail motion of spermatozoon cells from a hydrodynamic perspective; subsequently the work of Ramia *et al* [2] studied the swimming behaviour of bacteria using the slender body theory and produced a hydrodynamic model of a microorganism with a spherical body, propelled by a single helical flagellum. They also investigated how a microorganism would behave when swimming near a non-slip plane boundary, midway between two plane boundaries and in close proximity to neighbouring cell.

Research presented by Lauga *et al* [3] examined curved swimming trajectories of cells near a non-slip plane boundary. It is believed circular swimming trajectories are due to hydrodynamic interactions of the helical bundle with the interface. Lauga *et al* presents a force free and torque free swimming model based upon a spherical cell body ~ 1 μm above a non-slip surface. Furthermore, other research groups have explored the hydrodynamics of swimming bacteria in pairs or in groups. Ishikawa *et al* [4] evaluated the hydrodynamic interactions between a pair of swimming bacterium, where cells are modelled with a spherical body and single helical

flagellum. *Figure.4.1* is a schematic of a modelled spherical bacterium typical of numerous hydrodynamic models and simulations.

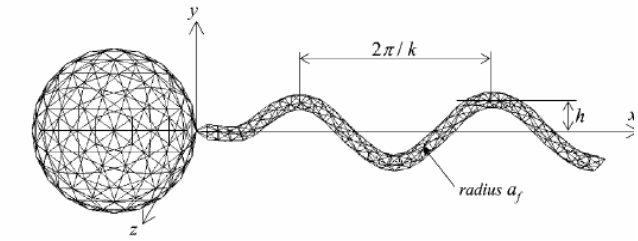

Figure.4.1: A spherical cell modelled by Ishikawa et al. They assumed the cell is neutrally buoyant with as single filament representing the bundle with a specific length, pitch, amplitude and helical radius. Image source from [4], reproduced with permission from the Biophysical Society.

Collective group swimming of bacterial is modelled by Cisneros *et al* [5], they studied the velocity flow field produced by a group of swimming bacteria by modelling each individual cell as a single sphere with a given radius and a cylinder representing the flagella bundle with a predetermined length and radius. With regards to hydrodynamic models and simulations, they all typically strive to simulate swimming behaviour of *E. coli* or *B. subtilis*. However one of the shortcomings is to model the cell body as an approximated simplified sphere, with an attached single helical filament. In reality however, the body of wild-type *E. coli* cells is typically rod shaped or considered by many as a prolate spheroid [6]; which has approximately 4 - 6 extracellular flagella filaments protruding from the outer cell membrane [7].

Due to the nature and complexity of studying bacterial locomotion, hydrodynamic models have proven to be extremely constructive in providing an insight into hydrodynamic interactions with surface, single cell-cell interactions and collective group hydrodynamics. To emphasize, without hydrodynamic models and simulations to understand bacterial locomotion one would rely exclusively on empirical data. Since empirical data tends to have a large associated uncertainty due to heterogeneities amongst cells [6]. It is often challenging to interpret empirical data without models. Therefore it is often the case that experimental data and models are used in conjunction to provide a comprehensive understanding of biological systems. Thus it would be constructive in the field if there was a strain of *E. coli*

which is spherical in profile and has been well characterized biologically. Swimming spherical *E. coli* cells would be an ideal candidate for further experimental investigation which will provide a better insight into bacterial locomotion; since the spherical cells are more representative of many hydrodynamic models. Moreover; spherical cells could be implemented in experiments to verify experimentally the claims made by hydrodynamic models and simulations.

For several decades optical tweezers have been deployed to study bacteria and microorganisms, from the pioneering work by Ashkin which trapped living cells for the first time [8], to Berg who studied the torque generated by flagella of *E. coli* [9]; and to more recent work by Chattopadhyay *et al* [6] which investigated the swimming efficiency of smooth swimming *E. coli* cells. In the latter reference they used optical tweezers to determine key swimming parameters such as the swimming velocity, body rotation rate and flagella bundle rotation rate. In modern designs of optical tweezers numerous research groups typically use backscattered interferometer technique to calibrate optical tweezers. This method relies on the interference of the backscattered light and the forwards scattered light, for details see [10, 11]. The method of optical tweezers characterization is performed with spherical beads since the diffusive behaviour of colloids is well documented [10, 11]. When trapping rod shaped bacteria the optical trap behaves somewhat differently from the well characterized bead. This is due to additional light scattering caused by the elongated geometry of the cell and the refractive index difference. It would be most beneficial if motile spherical cells were trapped rather than a rod shaped cells, since this will minimize scattering of the signal and makes it easier to examine the output signals (increase signal to noise ratio) and interpreting indications of cellular motility. Therefore it would be extremely advantageous if a spherical motile strain of *E. coli* is utilized to study motility, since it would provide a more precise measurement of the swimming force generated by flagella bundle.

The objective is to investigate the possibility of cellular motility in spherical mutant strain of *E. coli* KJB24 and to compare the findings to wild-type cells HCB1. Firstly

it aims to determine whether KJB24 are able to synthesize flagella filaments. Secondly this project explores the possibilities of KJB24 to demonstrate significant signs of meditated movement and cellular motility similar to wild-type cells. In summary if a motile spherical strain of *E. coli* is discovered, it would be a useful and beneficial in studying cellular motility. It will provide the bases for experimental examination of numerous hydrodynamic models, typically since these models approximate bacteria as spherical particles. Finally, optical trapping of bacteria can provide vital empirical data on the physical parameters of bacteria similar to the research of Chattopadhyay *et al* [6]. When trapping rod shaped bacteria larger amounts of light scattering occur on the quadrant photo detector increasing instrumental noise. Optical trapping of spherical motile cells may in result increased precision of the measured physical swimming parameters of bacterial motility.

4.3 Materials and Methods

This section describes the experimental techniques used to examine motility in spherical and in wild-type *E. coli* cells. This section will discuss the basic microbiology techniques utilized to characterize the bacterial growth rate, the number of cells in batch cultures using a viable plate assay and finally a basic method to synchronized batch cultures where cells are approximately in the same growth phase. Moreover, it will explain the methods used to determine motility and cellular morphology, discussing microscopy techniques such as bright-field microscopy, atomic force microscopy. Moreover it introduces an outlook of the techniques used to examine motility, such as optical trapping and semi-solid agar plates.

4.3.1 Wild-type (HCB1) and spherical (KJB24) *E. coli* cells

E. coli is the one of the most well understood microorganism where details of morphology, motility and chemotactic signalling path ways in wild-type *E. coli* cells

are discussed in *Chapter 2.* Typically, wild-type *E. coli* cells are rod shaped ~ 2 µm in length by ~ 1 µm in diameter and have 4 - 6 flagella filaments randomly distributed over the surface, *Figure.2.6*. The genetic mapping of HCB1 is beyond the scope of this thesis, however details can be found in [12, 13].

A derivative K-12 strain of *E. coli* has been genetically modified to retain a spherical cellular morphology. This was successfully performed by Begg and Donachie in 1998 [14], they deleted the proteins RodA and PBP. Further details can be found in references [14, 15]. When both of these proteins in wild-type cells are deleted spherical cells are formed. It is believed that other properties such as cellular growth rate, flagella synthesis and chemotaxis remain unaffected by the deletion of the two proteins [14, 15]. Typically, spherical KJB24 cells are ~ 1 µm in diameter, where cells divide via binary fission forming the septum in the centre of the cell, bisecting it into two cells, *Figure.4.2.*

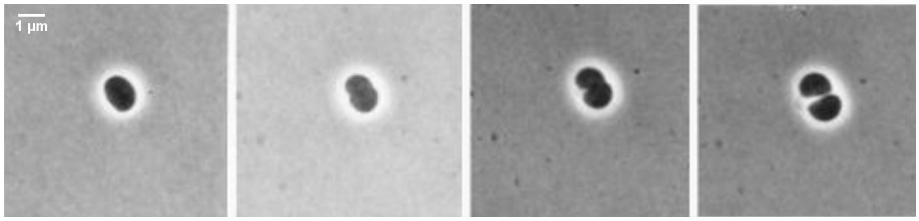

Figure.4.2: Several time lapse micrographs acquired using bright-field microscopy of spherical E. coli cells KJB24; illustrating the cellular division plane. It demonstrates the spherical morphology of KJB24 and depicts how spherical cells form the septum which bisects the cell into two. Images sourced from [14], reproduced with permission from the American Society of Microbiology.

In summary the cell strains used are either wild-type HCB1 or a spherical mutant KJB24 *E. coli* cells. Both strains are derivatives of K-12 strain, where in KJB24 cells two proteins have been deleted to induce a spherical morphology without altering life essential process. Moreover, both HCB1 and KJB24 should be comparable in terms of growth, flagella synthesis and chemotactic behaviour, with the only difference in cellular morphology.

4.3.2 Culture storage

The method of cellular storage and handling is adopted from standard microbiology protocol for producing a frozen stock [16]. This method is used throughout this project, which is suitable for storing either *E. coli* or *B. subtilis* cells. Initially the bacteria of interest (HCB1 or KJB24) are incubated to mid-exponential phase. These liquid cultures are then placed into freezing vials with 10 % DMSO (D2650, Sigma-Aldrich, St.Louis, MO) and stored in a – 80 º freezer. This method of storing cells worked effectively; prepared frozen stocks of cells can be stored in a frozen state for several years without deterioration [16]. Reviving cultures from frozen stocks consists of drawing 10 µl of thawed frozen stock and streaking onto nutrient LB agar plates. LB nutrient agar plates are made by adding 1.5 % agar (Sigma-Aidrich) w/v to LB broth. LB broth consists of 1 % tryptone (Sigma-Aidrich), 1 % NaCl and 0.5 % of yeast extract, made up into sterilized water. Streaked plates were incubated at 37 º C for 16 hours until single cell colonies grew to ~ 0.5 mm in diameter on the plate. Single colonies from this plate were selected via a loop to inoculate fresh LB media for day culture experiments.

4.3.3 The General motility procedure

The general motility procedure was developed to increase individual cellular motility, where swimming velocity can be increased by ~ 30 %; secondly it promotes flagella synthesis amongst cells where the majority ~ 90 % of wild-type cells are motile when incubated with this general procedure. The motility procedure involves incubating the cells under a stressed temperature condition which promotes the cells to synthesize flagella and become motile. For *E. coli* the optimal growth temperature is 37 ° C, incubation of *E. coli* cells at 37 ° C resulting in an average swimming of ~ 10 μms^{-1} since cells are not under stress. By stressing the cells via incubation at lower temperatures 25 – 30 ° C, the swimming velocity dramatically increases to an average of ~ 35 μms^{-1}. However, incubation at lower temperatures also reduces the

growth rate of cells, and prolongs the lag phase of growth. Typically incubation at 30 ° C yields extremely motile cells, yet the growth rate is reasonably fast, ~ 4 - 5 hours to reach exponential phase. Cells can also be stressed by the available nutrient concentration, where lower available resources can stress cells equally effectively as temperature. Varying the incubation temperature and the available nutrients dramatically changes the growth rate. The motility procedure has been optimized to provide both extremely motile cells and yet a reasonably fast growth rate.

The motility procedure is an adaptation of the motility procedure developed by Turner *et al* [17], which intensively study motility in *E. coli*. 10 µl of the frozen stock (either HCB1 or KJB24) is thawed, and subsequently streaked onto 1.5 % nutrient agar plates containing LB broth. Plates are incubated overnight (~ 16 hours) at 37 ° C until isolated colonies formed. A typical isolated colony was picked via a loop to inoculate 5 ml of fresh LB broth in a test tube. The inoculated batch culture was incubated in an orbital shaker (200 rpm) at 30 ° C overnight. The optical density ranged between ~ 1.2 - 1.7 at 600nm in stationary phase. 50 µl of stationary phase culture was utilized to inoculate a secondary test tube containing LB broth (5 ml) for ~ 4 - 5 hours, shaking at 200 rpm at 30 ° C. The optical density yielded ~ 1.2 at 600nm in mid-exponential phase ~ 1×10^{8} cells per ml. Harvested cells are washed and suspended in motility buffer (**MB**) consisting of (0.01 M KPO_4, 0.067 M NaCl, 10^{-4} M EDTA (ethylenediaminetetraacetic acid) [pH 7.0]) prior to experiments. Washing of the cells consisted of placing 1 ml sample in 2 ml Eppendorf (micro test-tube) and centrifuging at 2000 rpm for 5 minutes. The supernatant (old suspending fluid) was poured off, and the pellet was gently re-suspended in MB. The suspending volume was varied accordingly depending on the dilution factor, typically 1:100. This motility procedure was also used for incubating *B. subtilis* discussed in *Chapters 6*.

4.3.4 Characterization of *E. coli* cell cultures HCB1 and KJB24

Synchronization of batch cultures of bacteria is conduced with a standard microbiology procedure to ensure the majority of cells are synchronized in their growth phase; this ensures cells are homogenous in the growth cycle, where properties such as swimming velocity are approximately the same. Considering normal wild-type *E. coli* cells HCB1, the synchronization is produced by incubating a single colony from the working plate via a sterile loop. The colony is used to inoculate 5 ml of fresh LB broth in a test tube. Cultures are allowed to incubate for 16 hours at 30° C, shaking at 200 rpm to create the overnight culture. The overnight cultures are examined for cellular concentration, motility and normal cell length distributions, in the stationary phase. On average for wild-type cells 70 % are motile in the stationary phase, whereas KJB24 in identical growth conditions demonstrated no discernable motility. The procedure to produce an exponential phase culture entails taking 50 µl of the night culture and inoculating 5 ml of fresh LB broth in a test tube at 30 ° C shaking at 200 rpm. Liquid cultures were incubated for approximately five to six hours. Approximately 90 % of wild-type cells were motile after incubation period with a typical optical density $(OD)_{600nm}$ = 1.2. During the incubation period cells are roughly synchronized and this basic method described above produces cells with roughly in same growth phase [16]. However heterogeneities are always present ~ 10 % of cells in the sample, even with well established techniques cultures often have some level of heterogeneities, this is part of the nature of working with biological systems.

To investigate cellular motility accurately, one must first characterize the organism in terms of growth rate and cellular numbers in a given growth condition. During cellular synthesis in the exponential phase, the number of cells doubles over a given period of time. Knowing the doubling time is a clear indication of the growth rate, which is dependent of numerous environmental parameters such as growing medium, temperature and oxygen availability. One needs to characterize the culture under

experiment conditions in order to provide an accurate characterization of the growth curve, the growth rate and typical numbers of cells during experiments.

To characterize bacteria cultures is to conduct a viable plate count assays (for details of the method see [16]). This assay determines the number of cells in a growing culture and the growth rate. It is desirable to observe the growth rate of cultures over a life cycle, and to identify the characteristic time scales for the four distinct phases of the life cycle. This technique determines the number of cells per ml which can be calibrated to optical density measurements. Calibrating a graph of optical density verses number of cells is a convenient technique of determine the number of cells in a growing culture via reading the optical density (turbidity measurement), thus this technique is extremely quick and convenient.

E. coli cells are calibrated in experimental conditions using standard motility procedure discussed previously. An overnight culture is prepared and a 500 µl is used to inoculate 50 ml of LB broth in a conical flask. A 100 µl of the over night culture is then used to inoculate 50 ml of LB broth for the day culture. This was then incubated in experimental conditions where the growth of the culture is monitored throughout its growth cycle at 30 minutes time intervals for six hours. At each time point 100 µl of the sample is taken for a 10-fold serial dilution ranging between 10^{-3}-10^{-8} and then plated for the viable plate the count assays. An additional 100 µl of the sample is taken for an optical density reading at 600 nm. The viable plate count assay utilized 10-fold serial dilutions consisting of lab grade PBS (Phosphate Buffer Saline); these are prepared in aliquots in 2 ml Eppendorf with 0.9 ml of PBS in each. At each time point, 100 µl is taken and placed in the first Eppendorf for the first 1:10 dilution (making sure the sample is mixed homogenously). Subsequently taking 100 µl from the 1:10 dilution, and then mixing into second Eppendorf making the 1:100 dilution and so forth. This systematically dilutes the original sample so that individual growing colonies (from single cells) can be counted depicted in, *Figure.4.3.*

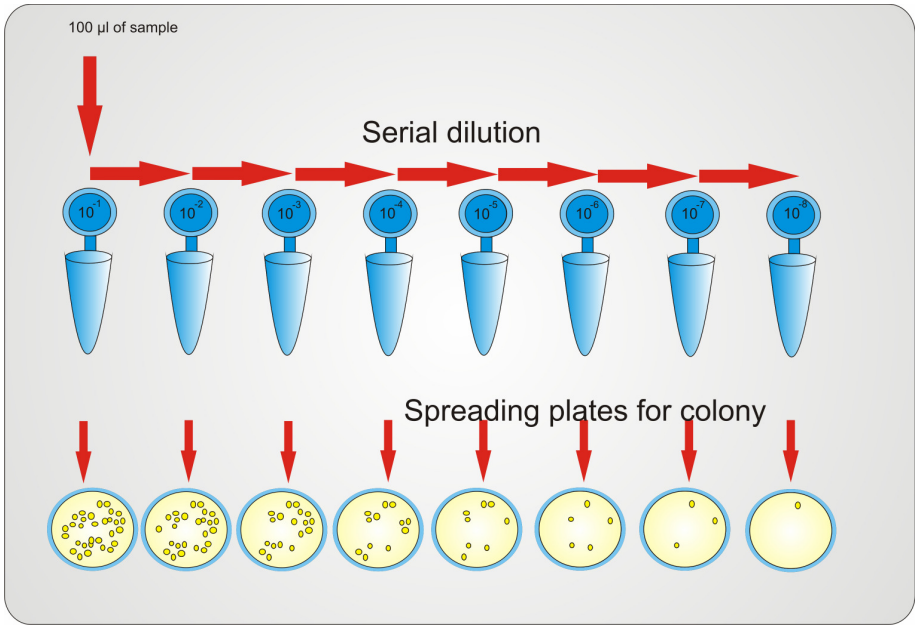

Figure.4.3: A schematic diagram to illustrate the method for 1:10 serial dilutions ranging from 10 $^{-3}$ – 10 $^{-8}$; where 100 µl of each dilution is taken from each Eppendorf and plated on to LB agar plates. Each plate is incubated for 16 hours at 37º C, the plates depicts a depleting number of colonies grown in each 1:10 dilution as expected.

It is important to select a large range of dilutions to determine an estimate of the number of cells required for viable plate counts. In the viable plate count assay dilutions ranged from a factor of 10 $^{-3}$ - 10 $^{-9}$. Each plate aims to achieve approximately 10 - 300 colonies for calibration and viable colony count calculations [16]. However, plates with more than 300 colonies on a single plate results in inaccuracies which are discarded from the calculations [16]; typical plates in the viable plate count assay are depicted in *Figure.4.4.*

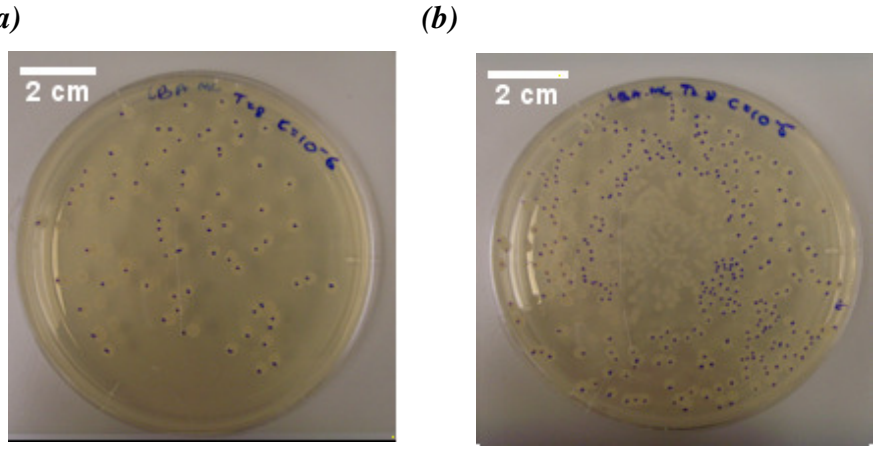

Figure.4.4: Representative photographs of wild-type E. coli cell HCB1 incubated on 1.5 % LB agar plates during the viable plate count assay. (a) A representative plate 7 hours into the growth of a new culture, at a suitable dilution factor of 10^{-6} where less than 300 colonies are counted. (b) Illustrates a respective plate with a dilution factor of 10^{-5}, more than 300 colonies are observed and is discarded from the assay.

Each viable plate at corresponding time intervals was produced by taking 100 µl of the each serial dilution and pipetting carefully onto freshly made LB agar plate. A sterilized plate spreader is used to evenly spread the liquid culture over the surface of the plate. Plates were incubated at 37 ° C for 16 hours until single colonies formed for counting. Incubated plates were examined for contamination and colony growth; the aim is to count each plate for the number of colonies which have grown corresponding to each dilution. The growth rate and the doubling time are calculated [16], and the results of the assay are presented in *Figure.4.5.*

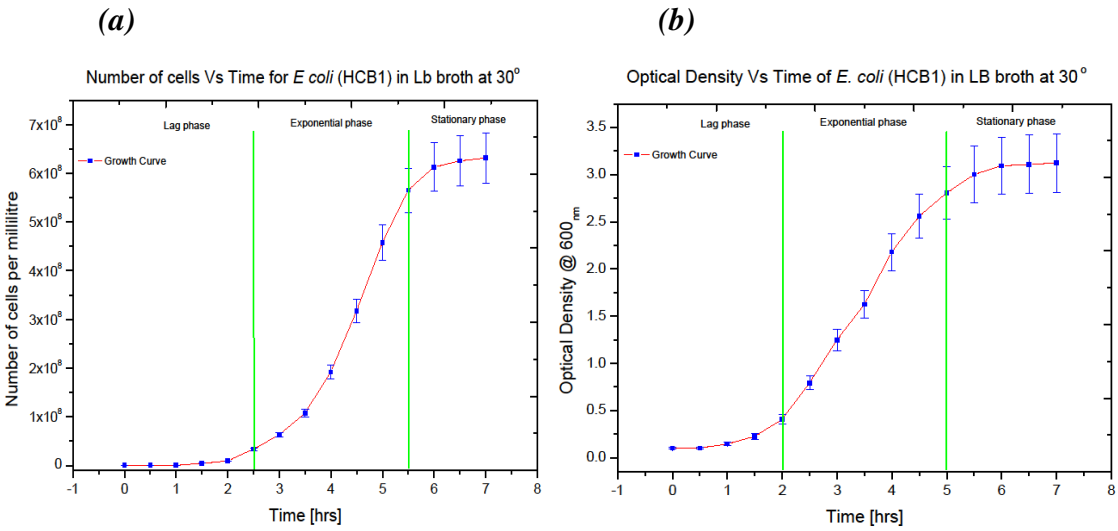

Figure.4.5: Growth curves of E. coli HCB1 (a) Depicts a plot of the averaged number cells per ml, where the lag and exponential growth phase are depicted by the green vertical lines. The lag phases last 2 hours and mid-exponential phase occurs between 4 - 5 hours. Beyond 6 hours incubation the culture enters the stationary phase which last for 10 - 15 hours. (b) Depicts the corresponding optical density readings, calibrating these two graphs provide a convenient method of extracting cell numbers during experiments. The exponential phase is determined by fitting the natural log of the growth curve, see reference [16] for details.

From the data obtained from the viable plate count assay the average doubling time is determined as 37 ± 10.1 minutes for our specific lab strain of *E. coli* (HCB1) incubated in our experimental conditions. Thus *E. coli* cells have been characterized for the specific experimental conditions using the procedure above, where it is possible to estimate the average number of cells for a given optical density. A similar viable plate count assay was conducted with KJB24 cells (data not presented) which yielded very similar results to the wild-type strain.

4.3.5 Microscopy techniques

This section briefly describes some of the physics of an optical microscope, and the microscopy techniques, evaluating the advantages and limitations. A microscope is an essential piece of equipment in microbiology, where microscopy techniques play

a significant role in this project. The basic mechanism of image formation, magnification and resolution are discussed, with additional comments on the operational procedures of a conventional optical microscope. Reviews on the mathematical details of image formation and optical microscopy can be found in references [18, 19] a more qualitative introduction to the practical and technical methods can be found in reference [20].

The human eye is nature's evolution of a lens system which allows us the ability of sight. Vision is a sophisticated process by which the eye lens forms an image onto the retina by rays entering the pupil. Moreover, the lens system in our eyes can focus by the contractions of the ciliary muscles. This allows the eye to focus on objects which are few centimetres to several meters away. Although, the human vision has a limited resolution; the smallest objects one can observe with the naked eye are in the order of ~ 500 µm. To achieve higher magnification, one brings the object closer to the eye. At very short distances the eye's magnification is limited; thus fine details become *'blurred'* when the object is too close to the eye therefore the resolution is limited. A solution would to devise a simple magnifying lens system where a single lens can achieve up to 10 × more magnification, depicted in *Figure.4.6.*

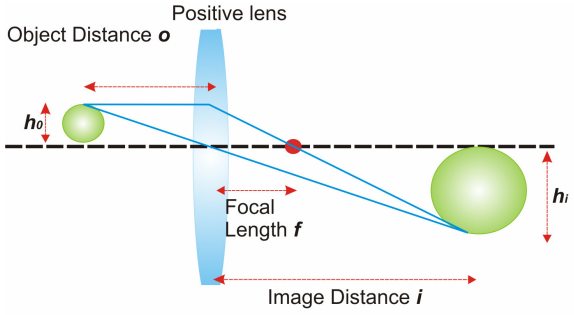

Figure.4.6: Using a ray diagram to highlight how a simple single lens system is capable of magnifying an object/image with a focal length f [18].

The useful magnification is defined as [18]: $M = h_i / h_o$ where h_o and h_i are the height of the original object and the image of the object respectively. Objects which appear on the single micron range are un-resolvable from a simple magnifying lens. To acquire significant magnification a series of lenses are required, i.e. an optical microscope. Microscopes provide high magnification of small objects with good

resolution which is limited to the hundred nanometer range [20]. The basic components of a microscope consist of an objective lens, a condenser lens, an illumination source and an eyepiece. These essential components of a microscope are depicted schematically in *Figure.4.7.*

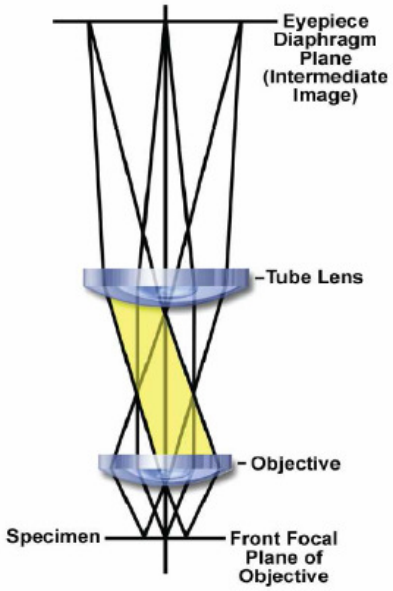

Figure.4.7: Schematic ray diagram of a compound microscope. The objective lens images the specimen and is projected onto the intermediate image plane via the objective and tube lens (condenser lens). The optimal separation distance of the objective and tube lens is considered to be between 200 - 250 mm reducing artefacts. Image acquired from [20].

The objective lens initiates the first stage of the magnification process in the microscope system. The lens generates a magnified image of the sample at an infinite distance and the role of the tube lens is to focus the parallel rays of the magnified image onto the intermediate image plane of the eyepiece lens depicted in *Figure.4.7.* Often the eyepiece lens offers an additional 10 × magnification. The secondary function of the tube lens besides focusing the parallel rays onto the eyepiece is to decouple the eyepiece from the objective lens, which provides independent control of the axial position of the objective when focusing the specimen. Thus focusing can be achieved by adjusting axial position independently. Without the tube lens, the objective lens and eyepiece positions, both require adjusting during refocus which is inconvenient, for further details consult [21,22].

There are two types of commonly used microscopes, the up-right microscope depicted in *Figure.4.8* and the inverted microscopy depicted in *Figure.4.9*.

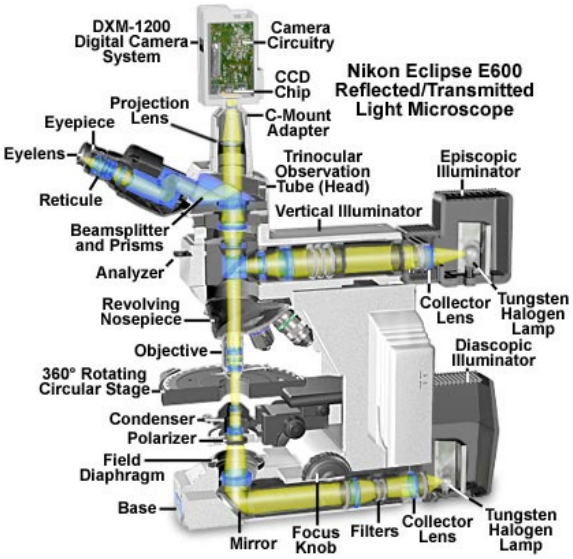

Figure.4.8: Schematic diagram of the light path of a Nikon eclipse E600 (similar microscope used in this project). In an up-right microscope the light source emerges from below the sample stages and illuminates the sample from under neither and projected onto the objective lens. Image is sourced from [20].

The up-right microscopes are the most common, typically a tungsten-halogen lamp is utilized as an illumination source propagating from beneath the stage. The emitted rays are collimated by a collector lens and are directed towards the main optical axis of the microscope located via a mirror at the base. The illumination source propagates through the field diaphragm and is focused by the condenser lens which is focus on the sample. The objective lens magnifies these propagating light rays and projects them onto a beamsplitter, either diverting the image to the eyepiece or to a camera port. The up-right microscope houses the sample on the stage which permits accurate positioning and focusing of the samples. The illumination and contrast is controlled by various apertures in the optical path. The upright design focuses the sample via controlling the distance of the stage in relation to the objective lens, thus the stage translates in the vertical axis.

An inverted microscope design is depicted in *Figure.4.9*. The key distinguishing features which separates this design from the up-right design is the optical light path and the location of the objective lens.

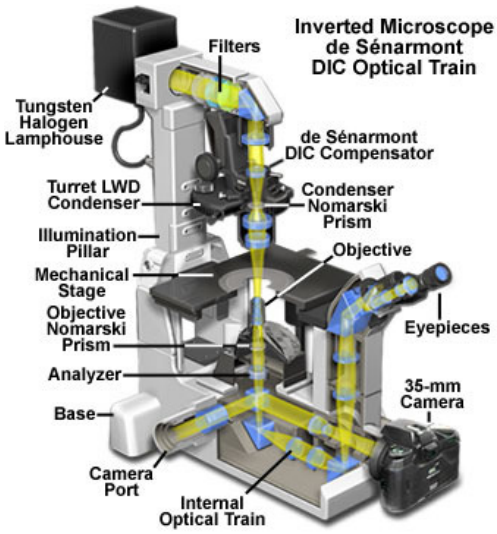

Figure.4.9: Schematic diagram of an inverted microscope depicting the optical light path. The illumination source is located above the sample stage along with the condenser lens. Note, the location of the objective lens is below the stage where samples are mounted. Image sourced form [20].

The inverted microscope design houses the illumination source above the specimen and stage. Light rays propagate through the field diaphragm and other filters, subsequently being deflected via a prism along the main optical path parallel to the optical axis. The light path is focused by the condenser lens onto the specimen; this achieves uniform illumination of the specimen. The objective lens is located beneath the stage on a revolving nosepiece pointing upwards (hence the name inverted design) onto the main optical axis of the microscope. The magnified image is then projected through the eyepiece or towards a camera port using a series of beam splitters and prisms.

The main advantage of using an inverted microscope rather than a conventional up-right, gives greater access to the sample stage area permitting physically larger specimens to be imaged from below. The inverted microscope is excellent at

observing motile bacteria at the bottom of Petri dish or in a container under a more natural environmental condition. The inverted design allows significantly easier access to the condenser lens where additional optical components can be inserted. However one of the limitations of the inverted design requires the bottom interface of the sample to be relatively thin ≤ 1 mm even with correction collars it often difficult to obtain good imaging with sufficiently thick samples. Overall both designs have their advantages depending on their specifics applications, for further details refer to [20].

When using a microscope (whether up-right or inverted) the image quality is determined by several factors such as the total magnification i.e. the magnification of the objective lens, tube lens and eyepiece combined. The more powerful the objective lens the higher magnification one can acquire; although high objective magnifications ≥ 500 × is meaningless if the resolution is not sufficiently high [18, 20 - 22]. This effect is referred to as empty magnification since no additional details are achieved with additional high magnification. Typically maximum possible meaningful magnification which can be achieved on an optical microscopy is ~ 1000 × [20]. To distinguish fine details one must *resolve* the image to identify minute features. The resolution or the resolving power *r* of a microscope is defined as minimal separation distance between two points which are still visibly distinct and separate. The main contributing factor which determines the resolution power *r* is given by light diffraction and refraction.

Figure.4.10, illustrates the effects of immersion fluid objective lenses which increased optical imaging quality and resolution power. *Figure.4.10 (a)* illustrates an air gap which separates the specimen from the objective lens. The propagating light has to travel through two media, glass and air where there is sufficient contrast in refractive index *n.* According to Snell's law the propagating light beam is deflected, $n_{air} < n_{glass}$ thus the exiting angle is larger [18] depicted in the ray diagram. Therefore less rays of the propagating light beam is collected by objective lens. However by inserting an immersion fluid such as oil or water to refractive index

match either the glass slides or the sample itself, *Figure.4.9 (b)* it reduces the amount of diffraction. By replacing the air gap with refractive index match fluid essentially removes refraction and more of the cone of light is collected by the objective lens.

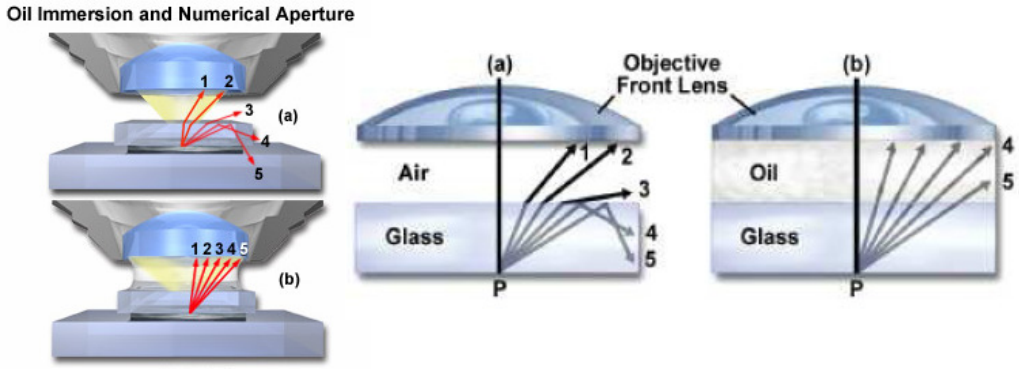

Figure.4.10: Ray diagram illustrating the effects of immersion fluid on the numerical aperture and resolving power. (a) Illustrate a sample without fluid where rays are refracted, (b) Shows a sample with oil which eliminates refraction and the majority of the rays are collected by the objective. Image acquired from [20].

The numerical aperture (**NA**) is defined as $NA = n \times \sin(\alpha)$, where n is the refractive index of the medium between sample and the objective lens, and α is the angle of the light cone in relation to the main optical axis. By using immersion fluid to reduce refraction, it essentially reduces optical aberrations and achieving higher **NA**, subsequently increasing the resolving power r. An optical instrument such as a microscope which is perfectly aligned and designed is referred to as diffraction limited meaning the converging light rays surrounding a focus point produces a diffraction pattern which is symmetrical about the microscope axis. The diffraction pattern is known as the Point-Spread-Function (**PSF**) when the PSF projected onto 2D it is referred to an Airy disk [18].

In every microscope the objective lens focuses on the sample creating a series of Airy disks which represents every point in the sample. When airy disks overlap one another it is an indication that the resolution of the microscope is at its limit. In this situation the points are indistinguishable; hence the resolution is not sufficient to resolve individual points in close proximity. To determine whether two points are

resolvable, i.e. being able to discriminate between them; one can invoke the *Rayleigh criterion* which states: '*Two points are only resolvable, when the centres of the one Airy disk lies within the first minimum of the second Airy disk.'* For lateral resolution i.e. in the x-y image plane the optical resolution is defined as [18]: $r = 0.616\lambda / NA$, where λ is the wavelength of illumination source, where typically for an optical microscope the optical resolution is limited to ~ 500 nm. Note – to achieve good quality images the contrast and the brightness of the final image are important. If the contrast of the object and the background is insufficient then it is extremely difficult to identify faint details. Varying the brightness levels of the final image can assist in the enhancement of faint objects, typical of bacteria. Maintaining minimal background illumination increases the contrast, where fainter objectives become more obvious. Microscopy techniques such as phase contrast, dark-field and differential interference contrast (DIC) have been developed to enhanced contrast of faint objects.

4.3.6 Bright-field microscopy — Köhler illumination

Köhler illumination is a method of optimizing bright-field imaging and was developed by August Köhler in 1893 [20]. This particular microscope configuration ensures that the microscope produces high quality images, which are sharply in focus and are uniformly illuminated in the field of view. *Figure.4.11* depicts the Ray diagram for Köhler illumination in an up-right microscope.

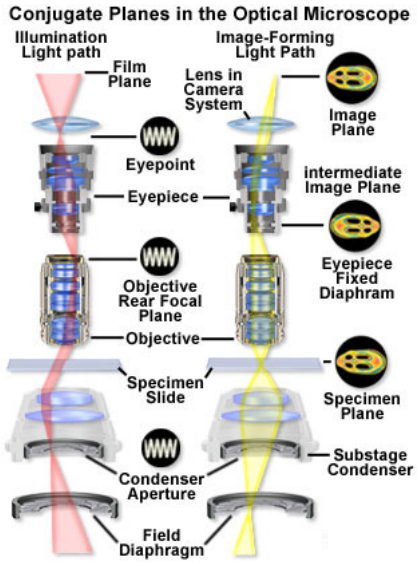

Figure.4.11: Schematic of the ray diagram depicting Köhler illumination and the locations of conjugate planes (a pair of image planes which are inverse to one another, i.e. when one plane is in focus, the other is out of focus) in the optical axis. Image sourced from [20].

By considering the rays from the illumination path, the left hand side of *Figure.4.11,* the light rays enter the back focal plane of the condenser lens and are transmitted onto the specimen. Thus the light rays propagate through the objective lens and are focused onto the back (rear) focal plane of the objective. Subsequently the light rays are transmitted through the eyepiece and are detected via the human eye or a CCD camera. This ensures a homogenous illumination is achieved when light rays appear in the observation plane of the detector (or eye). Considering the image-forming light path depicted in the right hand side of *Figure.4.11*, the rays which illuminates the specimen are homogenous and are focused tightly onto the front focal plane of the microscope. The consequence of this that is an intermediate image is produced, which is later projected onto plane of the eyepiece. Thus the image of the specimen is focused in the image plane and is detected by the user of the microscope. Details on practical procedure on achieving Köhler illumination can be found in [20].

4.3.7 Principles of fluorescence microscopy

This subsection describes the fundamental principles of fluorescence microscopy, it describes how this techniques works, and highlights the applications and the advantages/limitations. Moreover fluorescence microscopy is featured in later chapters in order to image flagella filaments. Fluorescence microscopy is a technique used to image selected areas of interest by using specimens which have been tagged with a fluorophore [20 - 22]. One of the advantages of using fluorescence microscopy is to overcome the effects of background illumination and interference; this is particularly useful when the contrast of sample is similar to that of the background. The sample tagged with fluorophore molecules absorb radiation at a specific wavelength band and becomes excited. During the excited state, the molecules dissipate a small amount of energy non-radioactively, causing it to emit radiation at a longer wavelength than the initial excitation wavelength. The illumination light source is then separated from the significantly weaker emitted fluorescence light via emission filters, hence only the emitted fluorescence radiation is detected. The typical components required for fluorescence microscopy are a high energy light source, typically a mercury or xenon arc lamp, an excitation filter, a dichroic mirror and an emission filter, the last three components can be combined into a convenient filter cube located in the optical axis of the microscope depicted in *Figure.4.12.*

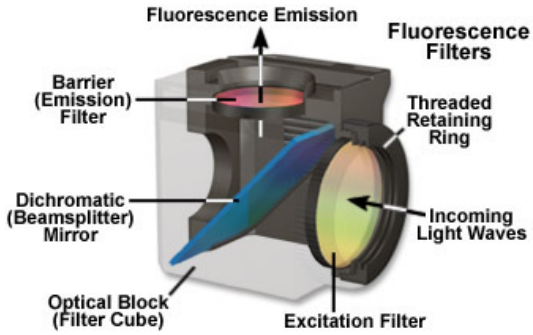

Figure.4.12: Schematic diagram of a typical Nikon filter cube; the cube houses three filters, the excitation filter, the dichromatic mirror and the (barrier) emission filter. Light from the arch lamp impinges on the excitation filter where the specific band of wavelength is selected, (unwanted wavelengths are blocked); selected wavelength radiation reflects off the dichromatic beamsplitter towards (downwards) the sample. Fluorescence radiation at longer wavelengths now propagating upwards passes through the dichromatic beamsplitter due to longer wavelengths, which passes a barrier filter and prevents other stray wavelengths being emitted. Image sourced from [20].

The main beam path of a fluorescence microscope is shown in *Figure.4.13*; it highlights the principles of fluorescence microscopy. The arc lamp is situated in focal point of the collector lens, where the incident light is collected through a lens system until it is finally projected onto the dichromatic beamsplitter (mirror). The property of a dichromatic beamsplitter ensures a narrow band of wavelength is transmitted, and incident light rays which are below the selected range (wavelength band) are reflected. It is essential for fluorescence microscopy that an appropriate dichromatic beamsplitter is selected with the correct wavelength band; such that it transmits the emitted light from the sample and reflects the illumination light (excitation radiation).

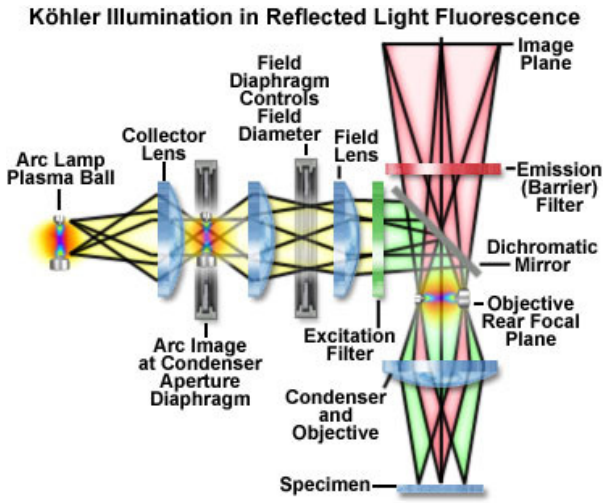

Figure.3.13: Schematic diagram of the beam path of conventional fluorescence microscopy, imaged sourced from [21].

The excitation filters and the dichroic mirror are specifically chosen to match the spectral excitation and emission characteristics of the fluorophore used to label the sample. For green fluorescent proteins GFP, typically excited with a wavelenghts of 470 - 490 nm and Emission wavelenghts of 510 - 530 nm. The differnace between the excitation and emission wavelengths is known as the Stokes shift. As the excitation radiation is shone upon the sample via the objective lens, the fluorophore molecule in the sample instantly absorbs this excitation wavelength and re-emits at a longer wavelength. The emitted radiation is collected by the objective lens in the conventional way, as in bright-field. Finally the re-emitted radiation is transmitted though the objective and through the emission filter to block any unwanted wavelengths. The emitted wavelengths are projected onto the image plane of the eyepiece/detector. The emission filter also referred to as the barrier filter to ensure none of the excitation radiation is backscattered and transmitted into the image plane. One of the limitations of using fluorescence microscopy is that the fluorophore molecules tend to lose the ability to fluoresce when exposed to high excitation intensities or for extended periods of time, this is known as photobleaching. Thus the intensity and the period of exposure is limited, therefore special attention is required to prevent bleaching. This can be achieved by minimizing the intensity of

illumination by using neutral density filters and restricting the field of view. Further details see reference [20 - 22].

4.3.8 Overview of optical tweezers

During this PhD project a force measurement optical tweezers (FMOT) were designed and constructed using optical components on an optical bench. This section briefly evaluates how optical tweezers work and how they can be used to detect subtle moments with nanometre precision; for detailed reviews of optical tweezers see references [8, 11, 23 - 28]. Optical tweezers use tightly focused laser beams to optically confine micron sized particles such as polystyrene beads and bacteria.

The fundamental principles of optical tweezers are based upon this simplistic fact that a photon carries momentum, $p = h/\lambda$, where, h is Planck's constant and λ is the wavelength of the light that is slightly altered during interactions with matter through refraction or scattering. As light rays propagate through transparent objects with contrasting refractive index n to its surrounding, photons interact with matter leading to subtle changes in momentum of the propagating photons. The change in momentum exerts a minute force on the particle. Due the laws of classical mechanics, momentum is always conserved. The rate of change of momentum is conserved via an equal and opposite force being transferred [23 - 25].

In the case of optical tweezers forces can be resolved into two essential components, a scattering force and a gradient force, where the former acts in the direction of wave propagation and the latter in the direction of gradient of the intensity, see reference [23]. A tightly focused laser beam is able to create a pair of optical tweezers, whereby sustainable trapping is achieved. Three dimensional stable trapping occurs when confined particle experiences a gradient force which is conserved by a scattering force. The most essential requirement for stable optical trapping requires is a tightly focused laser with a large N.A. to generate a sufficient gradient force [23 - 27].

To explain optical trapping there are several approximations to be considered concerning the wavelength (λ) of the trapping beam and the size of the particle. The approximations are two size approximations which are used to describe optical trapping; these are referred to as *Rayleigh* and *Ray Optics* approximations [29, 30]. The *Rayleigh* regime is when the wavelength (λ) of the trapping beam is larger than the radius (r) of the trapped particle ($\lambda > r$). Conversely at the other extreme, the *Ray Optics* is when the wavelength is considerably smaller than the trapped particle ($\lambda < r$) [28]. In this project we exclusively consider the *Ray Optics* regime since the wavelength of the laser is similar to that of the specimens. Typically we are trapping micron sized particles with a wavelengths λ = 1064 nm for its low absorption properties when working with biological samples [28], thus ($\lambda \sim r$). Arthur Ashkin was the first to demonstrate the fundamental theory of optical forces produced via light interactions with micron sized particles using the *ray optics* approximations [26].

The *Ray optics* model assumes the particle-like properties of light radiation [26]. The model considers light as a steady stream of particles, which can be explained by *Ray Optics* diagrams [23 - 26]. Light is composed of rays with a defined power; rays are normally represented with straight lines that obey Snell's Law of refraction and Fresnel's equation for reflection and transmission [18]. When they embark on a boundary with contrasting refractive indices, rays are refracted and a small fraction of the associated particle's momentum is transferred from the refracted ray to the confined object. The summation of change in momentum from every individual rays gives rise to the net momentum transferred, ultimately this results in a total net force being exerted on the particle. Arthur Ashkin demonstrated that light is able to exert sufficient force 1 – 100 pN to propel micron sized particles [23 - 26].

Considering a spherical particle (1 μm spheres), the change in momentum of the rays is due to refraction at the boundaries of the particle due to difference in refractive indices [23, 24, 26]. The differences in refractive index are the basis of light reflection and refraction at interface of a sphere and the surrounding medium. For sufficient trap strength the refractive index of micro sphere must be greater than the

suspending fluid, otherwise they are rendered invisible to the trapping beam [26]. The rate of change of momentum of photons caused by refraction is conserved via an equal and opposite force exerted on the confined particle. By definition Newton's second law verifies the rate of change of momentum equates to force $F = \Delta mv / \Delta t$. A resultant force is caused by the refracted rays acting in the direction of light intensity. Secondly the force of reflection produces a force that acts in the direction of light propagation. Since the incident photons refract at the interface of the micro sphere, the photons are deflected leading to a change in direction. This ultimately is a minute force being transferred to the micro sphere; which is sufficient to confine microns size particles [26 - 28].

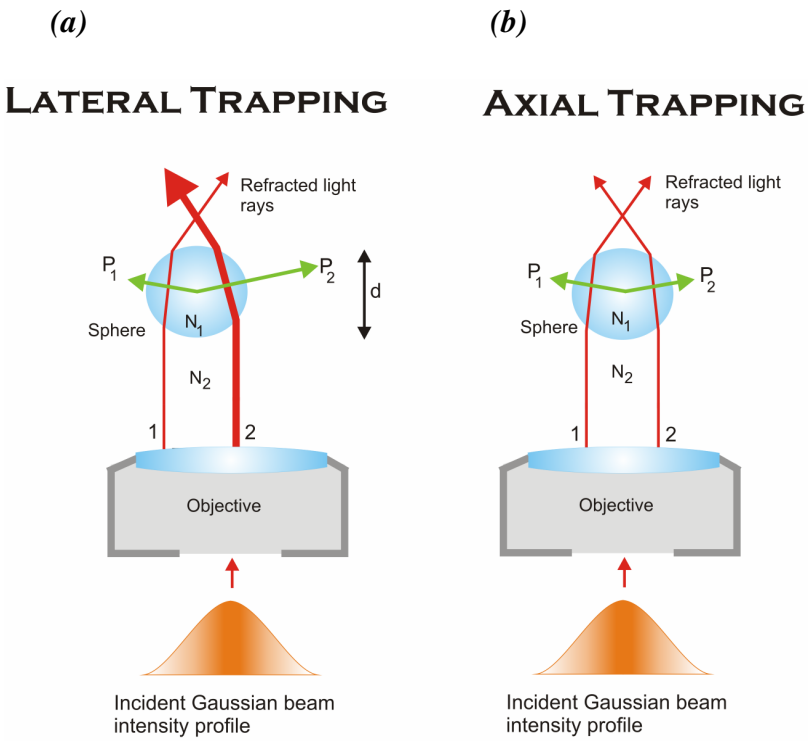

Figure.4.14: Schematic of lateral and axial trapping using a high numerical aperture objective lens to create a tightly focused beam using ray optics. (a) The width of the rays is proportional to the laser intensity of the ray provided by the Gaussian profile, thus the laser intensity is greatest at the centre. The green arrows represent the forces exerted on the bead by refraction of the rays, since ray 2 has a larger intensity it creates a larger restoring force to the right. (b) Here both rays retain the same intensity and refract the same amount, thus the restoring forces are equal enabling stable three dimensional trapping.

Lateral optical trapping is confining particles perpendicular to the direction of laser propagation i.e. in the x-y plane, presented in *Figure.4.14.* The gradient force is derived by a non-uniform intensity profile of the input Gaussian laser beam, thus creating a restoring force towards the geometric focus. The opposing force, i.e. the scattering force, is created via the reflections of light at the surface of the particle. This propels the particles away from the focus which counteracts axial trapping, for further details references [23 - 26]. *Figure.4.15* is a schematic diagram and a photograph of the optical tweezers design used in this project.

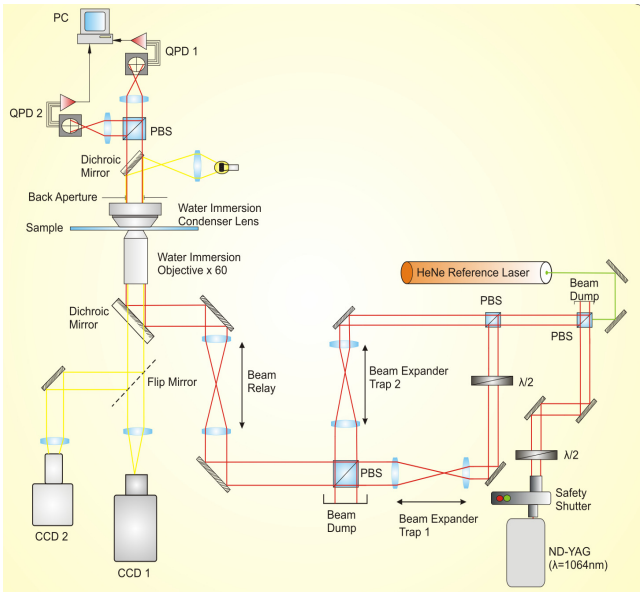

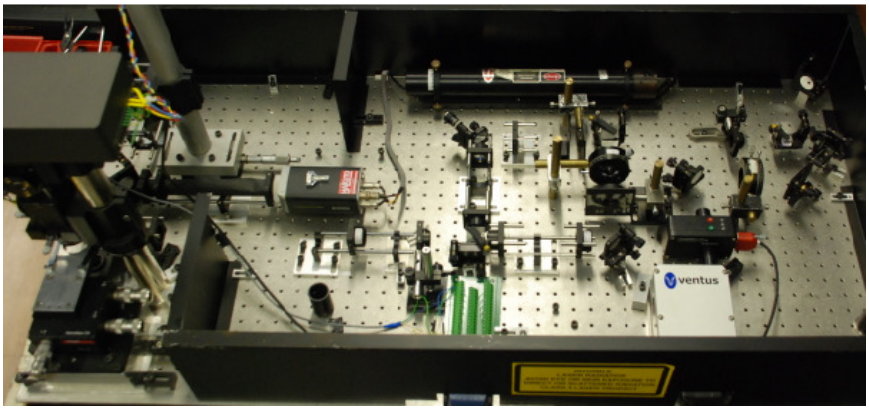

Figure.4.15: A schematic diagram of the force measurement optical tweezers set-up constructed for micromanipulation of micron sized particles. An Nd-YAG laser (λ = 1064 nm) propagates through a series of lens to manipulate the beam into the back focal plane of the objective lens, creating the tweezers. Forward scatted laser radiation is detected on quadrant photo diodes, which is sensitive enough to measure nanometer scale displacements.

This paragraph is a brief discussion of the back focal plane detection method used to calibrate force measurement optical tweezers, more details are found in [10, 11 31]. Back focal plane particle detection is based on the interference between forward scattered laser light produced from the trapped particle and the unscattered light [10, 31]. The quadrant photo detector is normally mounted along the optical axis approximately in the conjugate image plane of back focal plane of the condenser lens. As the scattered light from the particle and the unscattered light interfere, the interference pattern is projected on the quadrant photo detector and is converted into a series of voltages signals from each quadrant of the detector. The voltage signals can be normalized by the total intensity projected onto the four quadrants to reduce the dependence of the output on the total intensity. Furthermore, the total intensity information can be interpreted as the axial displacement of the beam, essentially summing the signals from all the quadrants. This leads to three dimensional interpretation of the particle positions as a function of time [10, 32]. Using the image of the back focal plane of the condenser to project the particles displacement onto the detector is beneficial since, the signal detected are no longer sensitive to relative displacement of the particle in the sample plane. Rather, it measures the relative displacements of the particle from the mean laser axial position [10]. Moreover, a major advantage of using this method of particle detection is that it only requires a single laser for particle trapping and position detection [10].

4.3.9 Principles of atomic force microscopy (AFM)

Atomic Force Microscopy (AFM) is an extremely versatile method of nanoscale surface characterization [33, 34]. This technique of visualising surfaces was first developed by Binning *et al* 1986 [35]. AFM can be used to visualize biological specimens [36], and is capable of operating in numerous environments ranging from substrates in vacuum to aqueous samples. We discuss the fundamental principles of AFM where one can consult references for details [35 - 39].

AFM is operated in three scanning modes either contact mode, non-contact mode and tapping mode. Contact mode and tapping mode AFM are only relevant in this project and are discussed. The main difference between contact mode and tapping mode AFM is the method in which the cantilever and tip is scanned over the surface of the sample, *Figure.4.16* shows a typical AFM device.

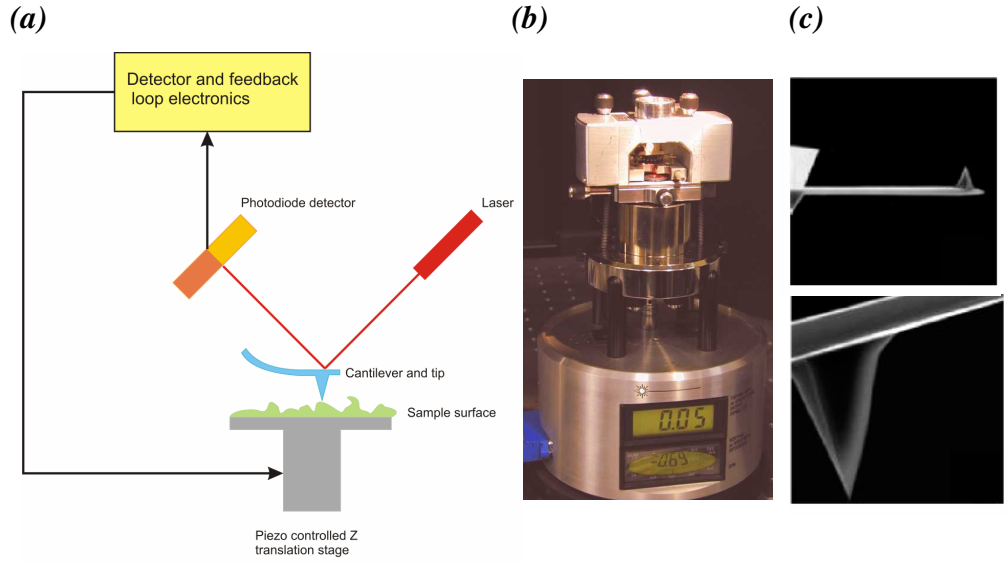

Figure.4.16: (a) Schematic illustration of an AFM device, a scanning tip is attached to a cantilever with a laser focused onto the back of the cantilever as it is scanned over a surface. (b) Photograph of the AFM device illustrating three main components: the optical block (housing the laser, cantilever, tip and photodiode), the piezo stage and scanner, and a digital display. (c) Micrographs of standard silicon AFM scanning tips. Image sourced from [39] with permission from the publisher.

Figure.4.16 (a) depicts a laser aligned to reflect off the rear of a semi-flexible cantilever, orientated at approximately 12 ° to the horizontal plane [40]. The laser reflection is then centred onto the quadrant photodiode. Each quadrant produces a photo-current which is proportional to the incident light intensity; these currents operate the feedback loop adjusting the height of the tip as it is scanned over the surface. Thus amplified measured deflections of the tip are used to create a surface map of the sample [38].

In contact mode AFM, the tip is scanned across the sample and is constantly adjusted to maintain a constant deflection, therefore a constant height above the sample. This is achieved by a positive feedback loop continually varying the height of the sample maintaining a constant deflection force. When the tip encounters a large protrusion from the surface the deflection of the cantilever is detected on the quadrant detector. The amplitude of the deflection is measured and recorded via the feedback loop amplifier. Via the feedback loop the sample is lowered to compensate for the protrusion to restore constant deflection of the cantilever, *Figure.4.17*. The laser reflection from the cantilever onto the quadrant detector records the height variations of the surface as it is being scanned, permitting accurate topography of the scanned surface. The cantilever is scanned in the x-y plane in a raster fashion [39], permitting relatively small areas to be mapped; typically ranging from 1 μm^2 - 30 μm^2.

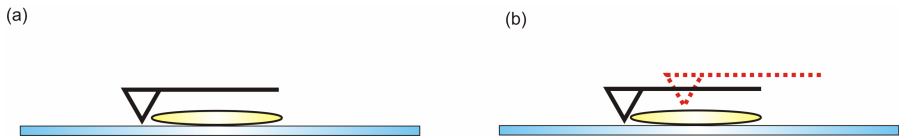

Figure.4.17: Schematic diagram of contact mode AFM, (a) Sample is scanned from left to right where a constant deflection force and tip height is maintained. (b) As the tip approaches an object the deflection force increases and the feedback loop alters the high of the stage accordingly to restore a constant deflection force.

In contact mode AFM the tip always remains in physical contact with the surface during scanning, hence the name. To a first approximation, the force exerted on the cantilever can be approximated to Hooke's Law, thus the resultant force on the cantilever is proportional to the displacement. The force exerted on the tip is equal to the defection multiplied the spring constant of the cantilever. It is vital when choosing a cantilever with an appropriate spring constant *k*, which is appropriate for the scanning mode and the sample. Cantilevers are typically 100 µm - 200 µm in length and the tips are ~ 10 nm in width, *Figure.4.16 (c)*. The typical spring constant *k* for cantilever ranges between 0.01 N m^{-1} - 100 N m^{-1} which permits force detection sensitivity to be as low as 10^{-11} N; where silicon based tips are most commonly used. Contact mode AFM exerts a continuous force ~ 50 - 100 pN on the specimen via the tip. Therefore contact mode is typically used for examining hard surfaces, and not suitable for delicate samples such as bacteria. These samples often become

damaged during imaging or the acquired image is significantly distorted. To avoid this, tapping mode AFM was developed for imaging fragile samples.

Tapping mode permits high resolution topography of delicate samples which is less invasive than contact mode AFM [39]. Tapping mode overcomes problems regarding friction, adhesion, electrostatic forces, and various other difficulties associated with conventional contact mode AFM imaging. Tapping mode achieves high resolution imaging of delicate samples by oscillating the cantilever at the resonance frequency ω_R, and the tip is lowered into contact with the surface. As the tip approaches the surface, the tip makes contact for brief period of time before the tip is removed. This cycle repeats itself as the tip is scanned across the surface; hence the tip gently 'taps' the surface as it is scanned, *Figure.4.18*. This significantly reduces the forces exerted on the sample and prevents dragging of the tip across the surface, thus avoiding permanent damage and image distortion [41].

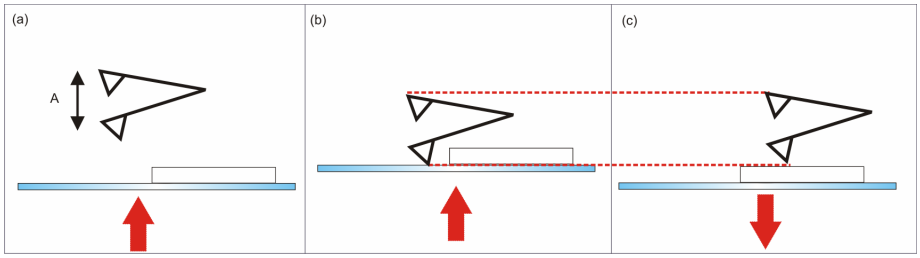

Figure: 4.18: Schematic illustration of tapping mode AFM (a) Shows the cantilever in free oscillation before scanning the surface. (b) Shows the cantilever lowered into contact with an area of relief prior to imaging a sample. (c) Demonstrates scanning of the tip as it approaches the sample and the stage is lowered to maintain constant deflection of the tip.

The oscillation of the cantilever is controlled via a piezo-electric ceramic plate which allows the cantilever to oscillate with high amplitudes or at specified amplitude *A*, which is typically greater than 20 nm whilst in contact with a surface. The oscillating tip is brought into contact with a surface such that the tip gently makes contact. This tapping of the surface operates at a typically frequency of 5 KHz – 500 KHz [38]. As the tip makes contact with the surface the amplitude of the oscillations is dampened. This reduction of amplitude is interpreted as features on the surface of

the sample. Prior to imaging, tuning of the cantilever is required such that mechanical interactions with the surface can be calibrated.

In tapping mode AFM the amplitude of the cantilevers is maintained at a constant predetermined value A_{set} via a feedback loop. As the tip scans across a protrusion in the surface, the cantilever has a reduced volume of oscillation thus the amplitude of tapping is decreased. Conversely, if there is a cavity there is more room for the cantilever to oscillate and the amplitude increases. These oscillations are measured via the quadrant photodiode which utilizes the feedback loop to vary the height of the sample to sustain constant amplitude and force on the surface of the sample. These variations in height, map out the surface of interests resulting in AFM images.

The limitations of contact mode and tapping mode of AFM are the associated dragging force/intermittent tapping force produced by the contact of the tip during surface scanning. This is most evident when samples are not sufficiently secured onto substrates or are extremely delicate. Insecure samples may lead to distortions in the final image due to the sample being dragged along with the tip, which can also damage the cantilever. Moreover with extremely fragile samples the slightest contact with tips can lead to permanent damage therefore a misrepresentative image is produced. The size and profile of the scanning tip has a significant importance on the lateral resolution in the final image. As a tip is scanned across a surface and approaches an extremely larger protruding feature, then the lateral resolution of the image is compromised. This is due to the feature's angle is greater than the angle of the tip which introduces artefacts and distortions, essentially tip broadening of the feature. This type of artefact is known as tip convolution or tip broadening, *Figure.4.19.* Ideally, a tip with the highest aspect ratio will give the best resolution [39] overcoming tip broadening; however these tips become blunt relatively quickly.

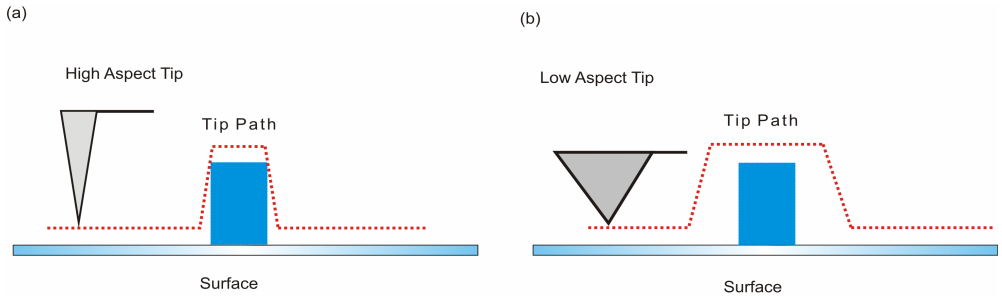

Figure.4.19: Schematic illustration of the scanning path taken for a high and low aspect ratio tips (a) high aspect ratio tip which provides good lateral resolution (b) is a low aspect ratio tip where the radius of curvature of the tip leads to tip convolution. However the overall height of feature does not change but the lateral resolution is broadened.

In summary atomic force microscopy is a powerful tool of imaging surfaces with nanometer precision. In contact mode AFM provides excellent resolution via lateral scanning of a tip over the surface. However, this mode often causes damage to delicate samples or even dislodges loosely fixed samples which ultimately cause distortions in the final image. Tapping mode AFM was developed to achieve high resolution imaging invasively to minimise sample damage. Tapping mode technique yields excellent images of soft and fragile samples, thus rendering tapping mode AFM an obvious choice for high resolution imaging of biological cells.

4.3.10 General protocols

Preparing specimens (plates and slides):

Bright-field experiments

We used coverslips (Menzel-Gläser, 22 × 50 mm, thickness 0.13-0.17 mm, MNJ-350-070 P) since the microscope was an inverted design allowing imaging from below. Slides were cleaned with absolute ethanol with a micro fibre cloth prior to a 5 µl – 10 µl sessile drops being placed on the surface for examination.

Optical tweezers experiments

Standard microscope slides (26 × 50 mm thickness 1.0 mm) and square coverslips were cleaned with absolute ethanol and a micro fibre cloth and left to air dry. Using double sided tape a small window section is cut out 5 mm × 5 mm, this section of tape is placed onto standard microscope slide. Subsequently 5 µl of desired sample is placed inside the double side window, where the coverslips is gently placed on top. Using optical glue, the coverslips edges were sealed such that the samples were air tight and flow free.

Semi-solid chemotactic agar plates

0.3 % w/v of noº 1 grade of bacteriological agar (Oxoid, UK) was made up with LB-broth (10 g tryptone, 5 g yeast extract, 5 g NaCl per L). Once set and cooled the semi-solid agar is prepared for pouring into sterilized Petri dishes. Prior to inoculation (with desired specimen), prepared plates were dried in a heating oven at 60 º C to remove condensation residue. 10 µl of exponential phase cultures (either HCB1 or KJB24) used to inoculation the semi-solid agar plates which were incubated at 37 º C for 18 hours.

Atomic force microscopy experiments

Glass coverslips (Agar Scientific, 13 mm diameter, no. 2 thickness) were chemically treated to adhere cells to the surface. Coverslips were cleaned in 96 % H_2SO_4: 30 % H_2O_2 (8:2 v/v) solution for 20 minutes, rinsed with distilled water and dried in a stream of nitrogen. Subsequently, they were immersed in a 0.1 % 3-aminopropyltriethoxysilane (Aldrich) solution (95:5 ethanol:water) for 20 minutes and then rinsed with ethanol. 10 µl of prepared cells were deposited onto the coverslip and left to settle for 5 minutes. Subsequently the coverslips were then rinsed gently twice with a motility buffer (**MB**) (0.01 M potassium phosphate, 0.067 M NaCl, 10^{-4} M EDTA; pH 7.0) to remove non-tethered cells and finally washed once with distilled water to remove salts. The substrates were left to naturally dry under ambient conditions prior to AFM imaging.

Acquiring images:

E. coli (HCB1 and KJB24) images were recorded at room temperature 23 º C with a Nikon Eclipse TE2000-U inverted epifluorescence microscope using a 60 × water immersion objective (Plan Apo, N.A 1.2 working distance 0.22 mm). Images were acquired from a monochromatic CCD camera (MARLIN F-14582, 17 fps). The microscope was configured with standard Köhler illumination using bright-field microscopy.

Analyzing images:

The videos were recorded as an avi format, which then later converted to an 8-bit grey scale (0 - 255) image using National Instrument Vision (Version 7.0, Austin TX). These individual images were then

converted into a virtual Tif stack using ImageJ (http://rsb.info.nih.gov/ij). Sequences of interest were manually selected and digitally enhanced in ImageJ before the sequential frames were converted back to avi format. Calibration of the camera was performed using a Richardson test slide (Generation 3, model 80302, Electron Microscopy Science).

AFM instrumentation

In this thesis, AFM images were acquired from tapping-mode atomic force microscopy (Multimode Veeco with a NanoScope IIIa controller equipped with a "J" scanner), with silicon cantilevers (Veeco, spring constant $k \approx 48$ N/m and resonance frequency between 130 – 250 kHz). Since fragile samples (bacteria) are being imaged, tapping mode was preferred to minimize tip-sample forces whilst still maintaining intermittent contact.

Experimental Results

4.4 Bright-field video microscopy

The initial experiment was to observe motile behaviour and mediated swimming of wild-type cells and spherical mutants in bright-field, incubated with the motility procedure to promote flagella synthesis. The objective was to observe indications of cellular motility after incubation, where run and tumble behaviour is expected for the wild-type cells [7].

Both HCB1 and KJB24 cells were incubated using the motility procedure to provide the maximum possibility of visualizing cellular motility. Incubated cells in the exponential phase where harvested at $(OD)_{600nm} \sim 1.0$. Samples were diluted down to typical concentrations of 10^2 - 10^3 cells per ml, where cultures were examined for cellular motility. Typically the produced samples are ~ 200 µm thick in the centre (thinner at the edges ~ 50 µm), and cells were imaged near the bottom interface ~ 10 µm. The results obtained for wild-type *E. coli* cells HCB1 yielded similar results to

previous reports and literature [7] as expected. Results depicted cells swimming with the classic run and tumble behaviour, where the morphology of cells are consentient with literature yielding a typical length of 2.3 ± 0.5 µm and diameter of 0.9 ± 0.3 µm depicted in, *Figure.4.20.*

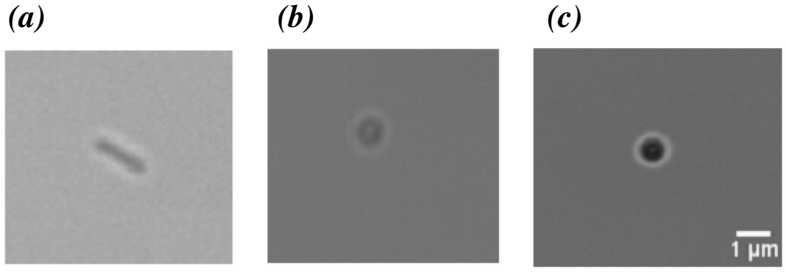

Figure.4.20: Micrograph of representative E. coli cells HCB1 and KJB24 incubated with the motility procedure and a 1 µm colloid. (a) Wild-type E. coli cells where the average length is 2.3 ± 0.5 µm and 0.9 ± 0.3 µm in diameter. (b) Representative mutant KJB24 E. coli cell incubated in identical conditions to the wild-type. The measured diameter is 1.3 ± 0.5 µm. (c) Micrograph of a 1 µm polystyrene bead suspended in water imaged with bright-field.

The average swimming velocity of wild-type cells (HCB1) in the bulk fluid was extracted as 29.6 ± 4.3 μms^{-1} for an average of 50 individual cells; the run and tumbles times extracted were 1.2 ± 0.3 s and 0.2 ± 0.1 s respectively. These swimming characteristics are in excellent agreement with previous experimental work reported by other research groups [7]. For the purpose of experiments conducted in this chapter, the wild-type cells HCB1 are considered as the control sample in respect to the spherical mutants KJB24. The initial observations of spherical mutants KJB24 incubated in identical conditions to the control strain yielded interesting results. The morphology of KJB24 cells were confirmed to be spherical in both stationary and exponential phase, except when dividing; the average extracted diameter is 1.3 ± 0.5 µm. Noticeably spherical cells do not perform the classic run and tumble behaviour. Instead our observations depict that KJB24 cells displays diffusive behaviour (Brownian motion) only. However, the diffusion observed for a typical KJB24 cells observed by eye was significantly slower approximately by an order of magnitude, compared to a colloid of a similar size (1 µm bead), *Figure.4.20.*

Unusual slower diffusive behaviour of KJB24 cells prompted further experimental investigation; with a working hypothesis that spherical cells retain additional extracellular appendages (suspected to be flagella at the time) creating additional drag, thus a larger effective hydrodynamic radius. A secondary hypothesis drawn from initial observations is that flagella filaments are present similar to wild-type cells, however flagella bundling does not occur due the symmetry of the spherical cell body (since bundles normally form at the poles). It is plausible that randomly distributed flagella filaments are rotating but non-cohesively where one can infer a coordinated bundle is not formed due to the lack of a designated bundling site such as a cellular pole. The latter case assumes spherical cells are active, but unable to form a propulsive bundle to swim.

Experiments were conducted to investigate both hypotheses above. An experimental investigation was conducted to examine the unusual smaller diffusivity of KJB24 cells, providing evidence of flagella synthesis in spherical cells. The latter hypothesis infers cells may synthesize flagella filaments which are 'actively' rotating, but do not form a propulsive bundle. An experiment was conduced to examine flagella rotation without directly visualising flagella filaments. KJB24 cells were incubated with the motility procedure to promote flagella synthesis and active motor rotation, thus these cells are rendered active. By observing a discernable difference in active cells and non-active (de-energized, discussed later) cells, one can deduce the presences of flagella motors activity. The term active and non-active cells in this experiment refer to the flagella motor activity.

To render cells inactivated one can simply starve the cells [42], although this varies the growth phases from an exponential phase culture to a stationary phase. This method is undesirable since there is no positive confirmation that cells are inactive. Moreover, without direct flagella visualisation one can only assume motors are not actively rotating. Heat treating has proved to be an extremely effective method for terminating cells (causing cell death). Incubating cell cultures at 60 ° C in a water bath for 30 minutes creates an inhospitable environment for *E. coli* cells to survive.

The disadvantage of this technique tends to denature the cells where proteins break down due to heating effects, including external appendages such as flagella, which is not suitable for our experiments. After much consideration the best method to render cells inactive is to use a cellular metabolic poison.

A cellular metabolic poison 2,4 Dinitrophenol (DNP, Sigma D198501) was used to de-energize cells. In the presences of DNP, *E. coli* cells are essentially paralyzed. DNP uncouples oxidative phosphorylation molecules resulting in a rapid consumption of energy without further generation of adensosine triphosphate (ATP) [43]. An associated side effect of using DNP generates heat as it consumes energy. To reduce heating effects a minimal amount of DNP was used to avoid excess heating effects. Cell cultures were treated with 1mM of DNP and were incubated for 1 hour to produce de-energized cells, which proved extremely effective by Berg *et al* [43]. A positive confirmation of the effectiveness of the poison was performed with motile wild-type cells. Motile cells were incubated with 1mM of DNP for 1 hour prior to examination in bright-field. Observations yielded DNP treated cells were all non-motile after chemical treatment, where cells were diffusive thus confirming the effectiveness of the metabolic poison.

The secondary objective is to compare the rate of diffusion of a polystyrene colloid 1 µm in diameter to similar size spherical *E. coli* cells; where previous observations illustrated an unusual slower rate of diffusion for its diameter. By evaluating the rate of diffusion for active spherical *E. coli* cells incubated with the motility procedure, in comparison to de-energized cells treated with DNP and a final comparison to a 1 µm colloid; one can determine the existence of flagella synthesis and flagella motility. In order to measure the rate of diffusion one can calculate the diffusion coefficient *D* by measuring the mean squared displacement (MSD) of a diffusing particle. The MSD is defined as the measure of the mean distance a particle travels and is quantified as:

$$msd(t) = \left\langle \Delta r(t)^2 \right\rangle = \left\langle \left(r(t) - r(0)\right)^2 \right\rangle \qquad \text{Eqn.4.1}$$

Where $r(t)-r(0)$ is the vector distance travelled over a given time interval t, and the square of the magnitudes of the vector is averaged over all the time intervals denoted by the angle brackets. The diffusion coefficient is derived from the gradient of MSD curve, defined below for the 2 dimensional case as:

$$\frac{d}{dt}\left\langle \Delta r(\Delta t)^2 \right\rangle = 4D \qquad \text{Eqn.4.2}$$

This expression for diffusion coefficient is related to the Stokes-Einstein's diffusion equation, permitting one to calculate the estimated hydrodynamic radius of the particle with a given diffusivity at a specific temperature T and viscosity η.

$$D = \frac{k_b T}{\gamma} = \frac{k_b T}{6\pi\eta a} \qquad \text{Eqn.4.3}$$

Where k_b is the Boltzmann's constant, T is temperature (room temperature 23 ° C), η is the viscosity of the suspending fluid and a is the hydrodynamic radius. The MSD of 1 µm diameter colloid, an active spherical *E. coli* cell and paralyzed spherical cells were all extracted using bright-field video microscopy. Measuring the MSD of these particles entails recording short video clips, ~ 1 minute in length of a single particle diffusing in the x-y image plane. Since particles are diffusing in the bulk fluid, they often appear in and out of focus i.e. diffusing in the z imaging plane. The microscope's focus was continually adjusted such that the particle always remained in focus. It was important to have a single particle/cell in focus and in the centre of the field of view to prevent the mismatching when extracting the MSD.

A particle tracking program written in LabVIEW[2] was used to analyze the short video clips. The particle tracking program is based on a pattern matching algorithm, where the user defines an in focus image of the particle to be tracked (whether a cell or a colloid). Subsequently the algorithm attempts to best fit the defined image to

[2] Programme written by Dr J. Arlt in LabView (Version 7.1, Austin TX)

each frame in the video; there is only one cell in the field of view which makes it easier for the algorithm to identify the particle. The program allocates an x and y coordinate and a time stamp Δt for each position which has recognized a match. Particle matching was an effective method of extracting x-y coordinates where the error in matching was only ~ 5 pixels corresponding to ~ 200 nm (23 pixels ≡ 1 µm). Mismatching arises when particles are significantly out of focus, where the algorithm is unable to identify the particle, thus unable to allocate x-y coordinates. This resulted in problems when extracting the MSD, when the algorithm is unable to identify the particle position it skips the frame. Skipped frames are programmed to indicate a zero in the x-y coordinates columns. Calculating the MSD of a non-complete tracks yielded discrepancies in the MSD calculations, where skipped frames resulted in zero displacements. To avoid such discrepancies complete tracks are necessary for accurate measurements of MSD. To acquire complete tracks, the focus of the particle was constantly adjusted such that that particle remained continuously in focus. Typical complete track lengths were on the order of 10 seconds sufficient to extract the MSD. 25 individual complete tracks where collected for respective samples and averaged, where results are presented in *Figure.4.21*.

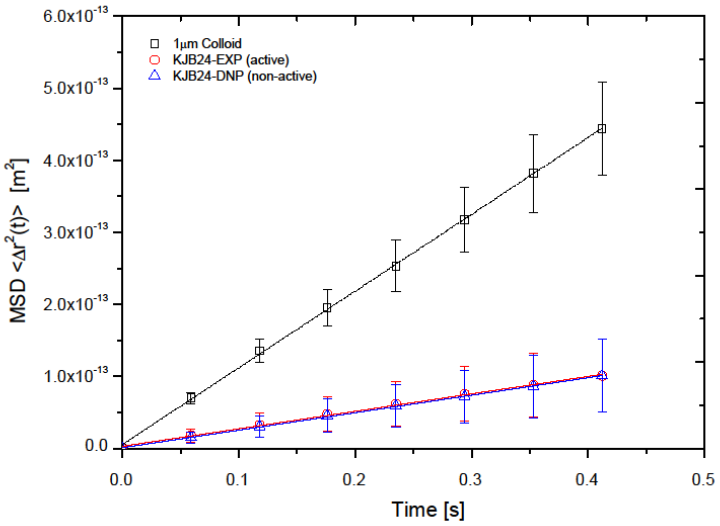

Figure.4.21: Graph of the average extracted MSD curves for a 1 µm polystyrene colloid, active KJB24 cells incubated with the motility procedure to the exponential phase and non-active KJB24 cells incubated with 1 mM DNP. Depicts the diffusion coefficient of a colloid to be an order of magnitude larger than spherical cells, secondly it shows the active cells have a consistent diffusion coefficient as non-active cells. Error bars are the standard deviation.

The diffusion coefficient is determined by calculating the gradient of each curve. The average diffusion coefficient D for the corresponding samples yielded $1.05 \pm 0.30 \times 10^{-12}$ $m^2 \cdot s^{-1}$, $2.34 \pm 0.36 \times 10^{-13}$ $m^2 \cdot s^{-1}$, and $2.43 \pm 0.33 \times 10^{-13}$ $m^2 \cdot s^{-1}$ respectively of a colloid, an active KJB24 spherical cell and paralyzed spherical cells incubated with DNP. From the theoretical calculations using the Stokes-Einstein's diffusion expression Eqn.4.3, the theoretically derived value of D yielded 1.73×10^{-12} $m^2 \cdot s^{-1}$ for a 1 µm sphere diffusing in water at $T = 23$ ° C. Thus this theoretical value is consistent with our measured experimental value; therefore independently verifying our method of extracting the diffusion coefficient D within experimental errors.

Figure.4.21 depicts both active and non-active spherical mutants are conclusively diffusing slower than a similar size 1 µm colloid, previously noted by eye via bright-field microscopy. To quantify the difference in the rate of diffusion one can compare diffusion coefficients of the colloid in respect to both active and non-active spherical bacterium. The comparison between the experimentally extracted diffusion coefficients D of colloid and spherical cells, illustrates spherical cells are diffusing approximately 80 % slower than a colloid of a similar size. The average diameter of KJB24 was measured to be 1.3 ± 0.5 µm, similar dimensions to a 1 µm polystyrene bead. Therefore one expects the rate of diffusion D of spherical bacteria and beads to be comparable, where the theoretical calculations from the Stokes-Einstein's diffusion Eqn.4.3 yields an expected $D \sim 1.33 \times 10^{-12}$ $m^2 \cdot s^{-1}$ for an average sized KJB24 cell. The experimentally acquired value yielded D as 2.34×10^{-13} $m^2 \cdot s^{-1}$ thus an order of magnitude slower diffusion discrepancy is observed. Due to the slight increased size of the bacterium, the expected discrepancy in diffusion rate should be ~ 20 % slower; however our experimental results reflect an order of magnitude differences.

The results yielded from *Figure.4.21* are highly suggestive that there are additional extracellular appendages protruding out of the membranes, which are beyond the resolution limit of bright-field microscopy. It is most likely that these suspected

external appendages increase the effective hydrodynamic radius and induces additional drag; resulting in cells diffusing slower than expected, reflected in our experimental results. The Stokes-Einstein's diffusion equation Eqn.4.3 was used to calculate an estimated effective hydrodynamic radius of spherical cells. Substituting typical values of D acquired from active and non-active cells, the estimated effective hydrodynamic radius r yielded 3.7 μm and 3.5 μm respectively. This result implies that the radius of the spherical cells ought to be seven times larger than what is experimentally measured. This obvious discrepancy in diffusion is mostly likely to be the results of extracellular organelles protruding from the outer cell membrane; where these appendages are highly suspected to be flagella [7].

In summary, an experimental investigation was conducted to examine the possibility of cell motility in spherical cells. Active cells incubated with the motility procedure were examined, as well as cells treated with the metabolic poison DNP to paralyze cell without associated cell damage. *Figure.4.21* illustrates the diffusion coefficients D of both active and non-active cells are consistent $D \sim 2.43 \times 10^{-13}$ $m^2 \cdot s^{-1}$. Since DNP cells are definitely non-motile, the results reflected in the experiment, imply active cells are also non-motile. The large discrepancy between the diffusion rates D, yielded from experiments and theoretically calculated, is highly suggestive that external appendages are protruding out of the cell surface. These appendages are suspected to be flagella filaments, by using the measured diffusion coefficients D, the hydrodynamic radius was estimated to be in the order of ~ 3.7 μm, 7.5 × larger than expected. Moreover this method of extracting the diffusion coefficients D is not as precise as other methods; where suspected flagella rotation may only subtly alter the diffusion coefficient D and is beyond the limit of detection with this method. However, results demonstrate from this experiment that the diffusion of spherical cells are significantly slower than expected.

4.5 Optical trapping of spherical bacteria

To probe bacterial motility further in spherical *E. coli* cells, both active and non-active cells were examined with force measurement optical tweezers (FMTO) discussed in

materials and methods. Optically trapping of cells permits precise measurements of diffusions with nanometer resolution, which is able to measure discernable differences regarding flagella motility. The experimental objective was to optically trap spherical cells with sufficient a trapping force to prevent cells from escaping, but weak enough to allows subtle movements caused by suspected flagella beating to be detected. *E. coli* cells consist of approximately 70 % water, where contrast in refractive index of bacteria is extremely similar to suspending buffer $n \sim 1.33$. This renders cells difficult to optically trap and image, thus slightly increased laser power compared to trapping colloids. The disadvantage of using increased laser powers to trap living cells increases the probability of causing photo-damage and heating of the cell [8, 27, 28]. To avoid these undesirable effects near infrared laser radiation is used (λ =1064 nm) where a minimal laser power setting is utilized to trap cells and short laser exposure times implemented ~ 1 minute per measurement.

Obtaining a suitable laser power was non-trivial since the laser power setting had to achieve sufficient trapping force such that bacteria is unable to escape, but sufficiently weak enough such that suspected rotating flagella filaments causes adequate deflection of the beam to be detected on the quadrant detector. To calibrate the laser power setting for optimum bacterial trapping and subtle force measurements consisted of trapping a typical spherical cell at relatively high power settings and subsequently reducing the power until the particle exhibits the effects of Brownian motion. Thus this laser power setting is sufficient to hold cells against Brownian motion, yet sufficiently weak to detect mediated movements. The optimal trapping power laser power in the back focal plane to confine spherical cells was extracted as 64.6 ± 0.4 mW. Using 1 µm spherical beads, trapped ~ 15 µm from the bottom interface and a 64.6 mW laser power setting was utilized to calibrate the optical tweezers for force measurements experiments. Prepared KJB24 cells, both active and non-active cells, were examined with optical tweezers where cells were trapped and their movements detected using the back scattered interferometer techniques [12, 33] in conjunction with a quadrant photo-diode. The yielded results are presented in *Figure.4.22.*

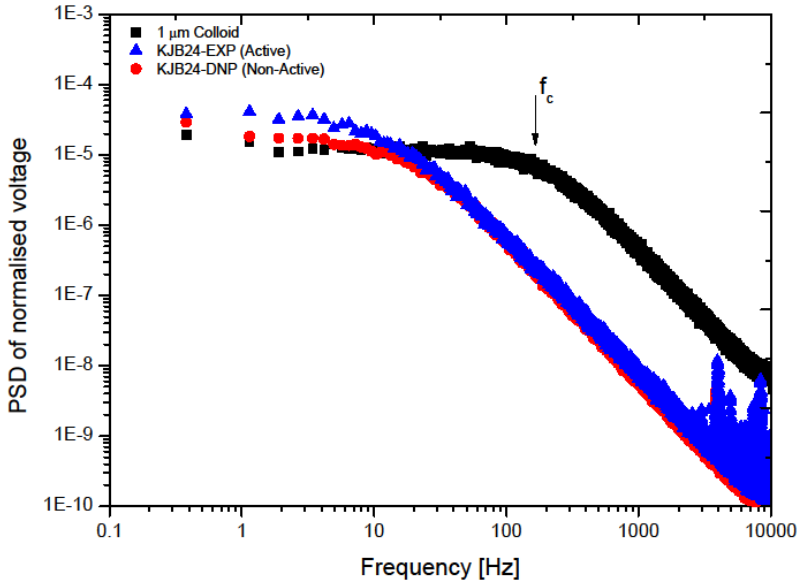

Figure.4.22: A Log-Log plot of the x component of the normalized power spectrum density obtained via optically trapping a 1 µm colloid, an active spherical cell (KJB24 - EXP) and a non-active spherical cell (KJB24 - DNP) 15 µm away from the lower interface. At high frequencies >1000 Hz instrumental noise occurs as aliasing where it is difficult distinguish between the trapping signal and noise.

Figure.4.22 depicts representative power spectrum obtained by optical trapping of spherical *E. coli* cells and 1 µm sphere. The filled square symbol represents the 1 µm colloid which was used to calibrate the optical tweezers. The theoretical behaviour of a passive colloid confined in an optical trap is well defined by the Lorentzian function [10, 11, 31] described as:

$$s_x(f) = \frac{k_b T}{\gamma \pi^2 \left(f_c^2 + f^2\right)} \qquad \text{Eqn.4.4}$$

The expression describes the behaviour of a trapped particle due to random thermal fluctuations over a range of frequencies f. Two distinctive regimes are noted, *Figure.4.22 (squares),* where the transition is denoted by the corner frequency f_c. At low frequencies the power spectrum is constant ~ 10^{-5}, representing the particle under confinement of the trap. At higher frequencies i.e. shorter time scales ~ 200 Hz, the slope declines with a curve of $1/f^2$ which describes free diffusion of the

colloid. *Figure.4.22*, for colloids illustrates a classic Lorentzian function verifying accurate alignment of the optical tweezers.

Figure.4.22, shows that the diffusion of a colloid behaves significantly different i.e. faster than spherically trapped cells as expected and demonstrated in the previous MSD experiment. The discrepancy between colloids and bacteria power spectra occurs for 2 reasons, firstly the noted slower diffusion, and secondly the tweezing properties of bacteria. Bacteria has a significant difference in refractive index to that of a colloid, which varies the trap sensitivity and trap stiffness, therefore measurements for colloids and bacteria are not quantitatively comparable. Qualitatively the power spectra are comparable providing information regarding the behaviour of the object in the trap. Noticeably, the measurements obtained from bacteria and colloids depict very similar Lorentzian profiles, which can be compared respectively.

Firstly all three curves at high frequencies > 500 Hz depicted a $-f^{-2}$ slopes as expected, representing diffusive Brownian behaviour at short times scale. However at low frequencies <10 Hz the curve for the colloid is constant as expected, since colloids are passive. Experiments conducted by Soni *et al* [44] demonstrated by trapping collides in various concentrations of bacterial baths, showed that low frequency power spectrum signals fluctuate linearly with bacterial concentration. The observed low frequency fluctuations were a result of bacterial collision/bombardments with the optical trapped sphere effectively displacing the colloid from the centre of trap resulting in low frequency fluctuations in the power spectrum. Thus trapping active motile cells, one also expects to observe low frequency fluctuations due to flagella beating, which causes minute displacements from the trap centre resulting in low frequency fluctuations.

Evidently from *Figure.4.22* we do not observed low frequency fluctuations in the active spherical cells (blue triangles), but rather the low frequencies signal is constant up to the corner frequency. The power spectra trace for active KJB24 cells is

consistent with treated DNP treated cells (almost identical), where flagella motility is certainly inhibited. Both bacteria power spectrum traces are reminiscent of the passive collide, although with a different diffusion coefficient *D* as expected (previous experiment). It is highly conclusive that 'active' cells are non-motile due to the power spectrum trace, which is almost identical to DNP treated cells where motility is inhibited. We expected to observe low frequency fluctuations due to minute displacements of active cells, however no such fluctuations were observed. This experiment has lead to the conclusion that spherical KJB24 cells do not exhibit motile behaviour, despite incubation with motility procedure. The finding presented strongly suggests spherical mutants *E. coli* cells only display diffusive behaviour, casting uncertainty to whether KJB24 cells synthesize flagella filaments. The presented results suggests spherical cells displays diffusive behaviour exclusively similar to passive colloids although with a significant slower diffusion *D,* however at the time it was still unclear why this was.

4.6 Semi-solid chemotactic agar plates

In microbiology there are well established technique for investigating chemotactic signalling pathways and motility in chemotactic mutants of *E. coli* cells, which often utilize semi-solid agar plates 0.2 % – 0.8 % concentrations [45, 46]. Wild-type *E. coli* are chemotactic [7] where a wild-type *E. coli* cell proactively explores its environment for improvements. Inoculating a semi-solid nutrient agar plate with wild-type *E. coli* cells, these cells divide and grow in the immediate vicinity of the inoculatant until nutrients are diminished. In a diminishing nutrient environment, chemotactic cells migrate outwards (utilizing flagella filaments) until cells establish an environment suitable for reproduction [45]. Typically wild-type cells replicate this process until the cells have completely exhausted nutrients in the environment. Deficiencies or mutations in the chemotactic proteins or intercellular chemotactic pathways generally resulted in catastrophic failure, where cells demonstrated little or no signs of migration but only cell growth. *Figure.4.23* shows results of a chemotactic plate assay sourced from Bibikov *et al* [46]. Bibikov *et al* investigated methyl-accepting chemotaxis proteins in *E. coli*

cells; moreover they explored the functions of CheR and CheB essential chemotactic proteins. In the wild-type *E. coli* both CheR and CheB are present, these cells propagated (migrated) outwards in concentric rings, typically in bands [46]. Deleting either one of the proteins resulted in inhibited chemotactic behaviour, where cells do not exhibit migration in concentric circles due to the lack chemical signal detection.

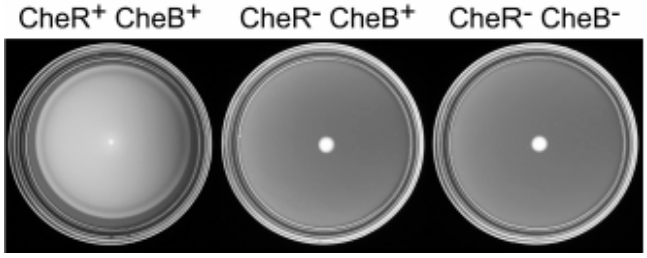

Figure.4.23: Depicts semi-solid agar plates which were used to investigate the role of CheR and CheB in chemotatactic wild-type E. coli. The left hand plate depicts the control wild-type strain, where both CheR and CheB are present, exhibiting chemotactic *migration. However, deletion of either CheR or CheB resulted in cell growth exclusively, where cellular migration is inhibited centre and right plate. Image from [46], reproduced with permission from the American Society of Microbiology.*

KJB24 are genetic mutants which are purely transcribed to alter cellular morphology (Rod A and PBP [14, 15]), therefore it is reasonable to assume that chemotaxis in KJB24 cells remains unaffected by the deletion of Rod A and PBP. Moreover, it is assumed that flagella synthesis in KJB24 cell remains unaltered. Semi-solid nutrient agar plates were utilized to examine motility and the existence of flagella filaments in spherical *E. coli* cells KJB24. The results presented in the optical tweezers experiments cast uncertainty as to whether flagella filaments are present in spherical cells.

In microbiology standard nutrient agar plates normally consist of 1.5 % agar which produces an excellent ridged gel to incubate bacterial colonies, typical pore size ~ 200 nm [47]. However, semi-solid chemotaxis agar plates consist of agar concentration ranging between 0.2 % - 0.8 % depending on the desired pore size and gel consistency. Chemotactic plates require large enough pore sizes permitting cell migration, but adequately rigid to support itself under its own gravity. 0.3 % agar concentrations are used for semi-solid chemotactic plates [46]. This experiment utilizes both wild-type HCB1 and spherical mutants KJB24 incubated with the motility procedure to verify chemotactic behaviour and motility on semi-solid chemotactic plates. It is expected that

both strains are chemotactic and retain flagella filaments, and should migrate across the semi-solid agar plate; possibly with a concentric ring pattern suggests by Bibikov *et al Figure.4.23*. Both wild-type and spherical mutants were incubated for 18 hours on semi-solid plates (described in material and methods). The following results are presented in *Figure.4.24.*

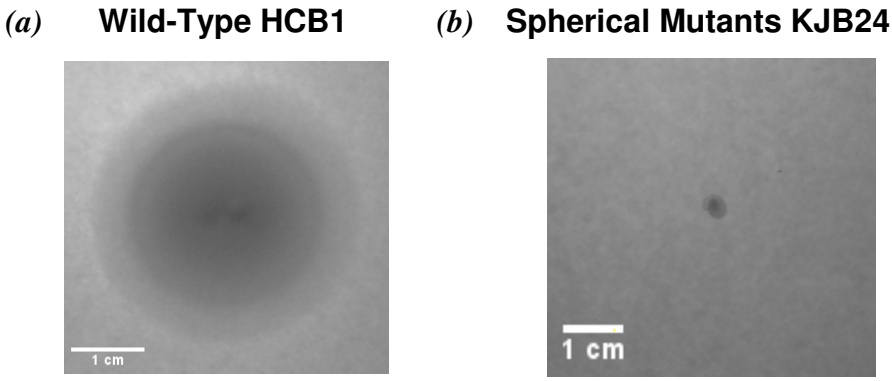

Figure.4.24: (a) Illustrates 10 µl of wild-type E. coli HCB1 inoculated in 0.3 % semi-solid agar plate for 16 hours at 37 º C. Evidently cells have migrated from the inoculate site outwards concentric ring pattern as predicted; indicating normal chemotactic response and flagella motility, where the measured diameter of the colony d = 52.3 ± 0.1 mm. (b) Depict E. coli KJB24 incubated in identical conditions which fails to demonstrate chemotaxis and motility, where the colony grows in the vicinity of the initial inoculation site typical d =3.6 ± 0.1 mm.

The results of the semi-solid chemotactic plate assay are presented in *Figure.4.24*, which clearly demonstrates wild-type HCB1 cells have migrated from the initial inoculation site as expected, demonstrating natural chemotactic behaviour and cellular motility. KJB24 sample remained in close proximity to the inoculation site which does not migrate outwards unlike HCB1. The typical measured diameter of an *E. coli* colony on standard 1.5 % agar plates is approximately 1.6 ± 0.4 mm. The diameters of cell colonies on semi-solid agar plates yielded 52.3 ± 0.1mm and 3.6 ± 0.1 mm for the wild-type and spherical cells respectively, *Figure.4.24.* The average growth rate of cells on semi-solid agar plates was calculated as 2.9 $mm \cdot h^{-1}$ and 0.2 $mm \cdot h^{-1}$ respectively. For HCB1 a ~ 25 fold increase in diameter size was observed on semi-solid agar plates, whereas KJB24 demonstrated an insignificant factor of 2 increase relative to normal sized colonies. The results presented provide strong evidence that KJB24 cells are not actively motile, where it is now strongly suspected

that these cells lack flagella filaments although this experiment does not conclusively demonstrate KJB24 cells are not chemotactic. KJB24 cellular colony did increase in size, but not significantly where the increase in colony size is due to the combination of cellular growth and diffusion in semi-solid plates (increased pours size ~ 500 nm).

The presented results from semi-solid agar plates illustrate wild-type HBC1 demonstrates motility and chemotaxis as expected, whereas KJB24 cells did not. However a conclusive explanation to address the lack of motility is still uncertain. There are two feasible explanations; firstly KJB24 cells do not have flagella filaments and thus are unable to migrate outwards. Secondly KJB24 cell do retain flagella filaments but beats incoherently (lack of a bundling site due to symmetry) similar to continual tumbling, thus cells do not migrate. In the latter case, optical tweezers experiments suggest that active beating of filaments are not present, thus the former case is more likely. Perhaps KJB24 cells do not synthesize flagella filaments, but rather a different category of extracellular appendages. To directly confirm these hypotheses a method of imaging nanometer scale structures is required to precisely verify the cell morphology and external structures in KJB24 cells.

4.7 Atomic Force microscopy

This experiment implements atomic force miscopy (AFM) to directly visualise the external morphology of both HCB1 and KJB24 *E. coli* cells. AFM provides accurate nanometer scale resolution images which can be achieved relatively quickly [35]. The advantage of using AFM is that it provides very accurate visualisation of surfaces topography with nanometer resolution which can be adapted to image most solid surfaces. Generally however AFM imaging requires dried samples[3] and the limitations regarding bacteria is that cells are dehydrated and adhered to coverslips. Thus the acquired images are of denatured *E. coli* cells which are not in their natural environment.

[3] Recent advancements can scan samples in aqueous environments, but it is significantly more challenging.

Moreover AFM was configured only to imaging flagella filaments which are in the nanometer range, images of the cell body becomes distorted due to large forces exerted by the tip during scanning.

Secondly cellular handling during preparation may introduce flagella/appendages shearing off as implied by Turner *et al* [42]; thus caution was taken during cell handling. Identifying flagella in wild-type cells verify our technique of visualizing flagella filaments, where this method is applicable to identify flagella in spherical cells if they are present. Cells were adhered to the surface because as the cantilever scans over lose cells they are dragged along with the cantilever. This causes damage to the cantilever and secondly the acquired images are often heavily distorted. Thus coverslips were treated with 3-aminopropyltriethoxysilane which renders the glass surface extremely positively charged[4]. Negatively charged cells were deposited on the glass coverslip and dried at ambient conditions 23° C which fixed cells to the surface.

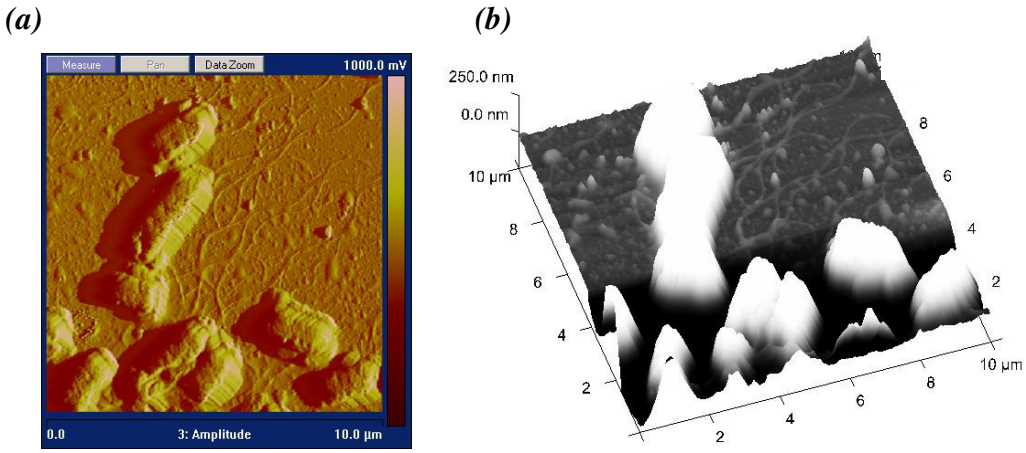

Figure.4.25: Acquired images of wild-type E. coli HCB1 from AFM imaging. (a) Illustrates a two dimensional scan of 10 µm^2 field of view. It depicts dehydrated E. coli cells on a surface with several flagella filaments as expected; each cell has ~ 4 flagella filaments. The cell body appears distorted due dehydration (hence the cell body has a significantly small body diameter) and the set-up of the AFM. (b) Depicts a three dimensional reconstruction of dehydrated E. coli cells to determine the diameter of the cell body and flagella; 0.8 ± 0.1 µm and 31 ± 5 nm respectively.

[4] Treatment of the coverslips was performed by Dr N. Pham, whom is also an expert on AFM imaging and supervised the AFM imaging process.

Figure.4.25 are representative AFM images of dehydrated wild-type *E. coli* cells, the extracted cell length and diameter yielded 1.7 ± 0.1µm and 0.8 ± 0.1 µm respectively consistent with bright-field imaging results. However the dimensions are slightly smaller due to cellular dehydration process, thus outer surface of the cell appears wrinkled also contributed to the AFM configuration. Images evidently depict flagella filaments protruding out of the cell membrane at random locations as expected. The typical length of a flagellum filament was extracted as 5.3 ± 0.1 µm, shorter than the expected value from literature ~ 7 – 8 µm [7]. The cause of flagellum truncation is highly likely to be the result of hydrodynamic shearing during cell handling and AFM preparation, where broken filaments are observed in the sample. These appendages were verified as flagella due to the pitch length ~ 2.5 µm and characteristic sinusoidal wave structure. Moreover the measured diameter of the filaments, typically 31 ± 1 nm are in excellent agreement to previous values ~ 25 nm [7], thus verifying that these structures are indeed flagella. The reason for marginally larger diameters measured is due to tip broadening effects during scanning.

(a) ***(b)***

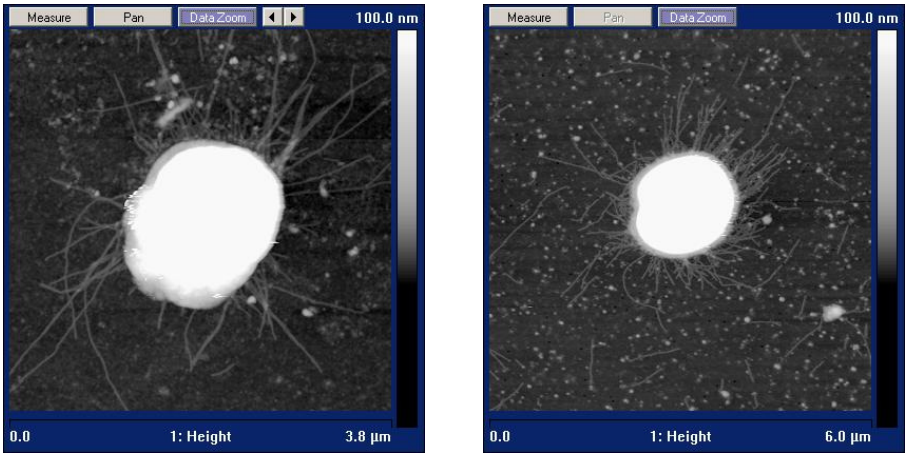

Figure.4.26: (a) Depicts a dehydrated spherical mutant KJB24 cell imaged using AFM, which highlights cells retaining short straight appendages protruding out of the cell membrane. The extracted diameter of the cell is d = 1.2 ± 0.4 µm consistent with bright-field measurements. (b) Highlights a typical spherical cell with numerous short (~ 2 – 3 µm*) appendages distributed over the surface. This image conclusively confirms the suspicions of extracellular appendages responsible for the observed slower diffusion.*

Figure.4.26 are representative images of dehydrated spherical *E. coli* KJB24, height measurements yield a cell diameter of 1.2 ± 0.4 μm consistent with bright-field measurements 1.3 ± 0.5 μm. The visualised extracellular appendages appear to be somewhat different from the characteristic sinusoidal wave structure of flagella observed in *Figure.4.25* obtained in an identical fashion. External appendages observed in KJB24 cells are relatively straight in structure and short ~ 2 - 3 μm, where the measured diameter of filaments yielded 3.6 ± 0.5 nm significantly smaller than the expected value of 25 - 30 nm for flagella. Moreover images of KJB24 cells highlight significantly more filaments, at least 6 times as many as those observed in HCB1 cells. AFM imaging is conclusive evidence to suggest observed appendages in KJB24 cells are not flagella filaments but rather KJB24 cells retained a different type of appendage possibly for cell adhesions, discussed in next section. Therefore, this experiment conclusively demonstrates that KJB24 cell do not retain flagella filaments which explains why these cells are not motile, moreover visualization of the cellular morphology depicts cells as having numerous short filaments 'hairy sphere' increasing the hydrodynamic radius of cells which explains the slower diffusion observed in bright-field experiments.

4.8 Discussion

From the four experiments conducted above it is evident that spherical mutants KJB24 cells are not motile, in comparison to the wild-type cells HCB1 which are known to synthesize flagella filaments [7, 42]. Initial experiments utilizing the motility procedure to promote flagella synthesis demonstrated that 95 % of wild-type cells were motile exhibiting the classic run and tumble behaviour [7] with a typical swimming velocity of 29.6 ± 4.3 μms^{-1} as expected. However, KJB24 cell did not demonstrate swimming but diffusive behaviour, although noticeably slower than expected for the given cell size d ~ 1 μm. The diffusion coefficient *D* was extracted for active cells (incubated with motility procedure), non-active cells (DNP treated cells) and 1 μm passive colloids, via extracting the mean squared displacement.

Figure.4.23 depicts the diffusion coefficients D of active cells and non active cells are consistent $D \sim 2.43 \times 10^{-13}$ $m^2 \cdot s^{-1}$, whereas a similar sized 1 µm colloid diffused an order of magnitude faster. The discrepancy in the diffusion coefficient, infer external appendages are presents most likely to be flagella. Using the Stokes-Einstein's equation Eqn.4.3, the theoretical hydrodynamic radius r was calculated from extracted diffusion coeffiecnt D of the spherical cells which yielded a theoretical hydrodynamic radius of 3.7 µm. KJB24 cells typically have a measured radius of r = 0.5 µm, but diffuses like a r = 3.7 µm passive colloid. This is 7.5 times larger, thus this initial experiment strongly indicates external appendages are present, but does not conclusively show they are flagella filaments.

Force measurement optical tweezers were designed and constructed during this project, which are capable of non-invasive micro manipulation of particles and detection of nanometer scale displacements. Optical tweezers were used to confine spherical cells and colloids to observed low frequency fluctuations corresponding to flagella motor actively. The results presented in *Figure.4.22* depict that active and non-active cells demonstrate a similar trace to colloids, where at low frequencies both traces are similar. This provides evidence to suggest KJB24 mutants diffuse identically to that of a passive collides but with a slower diffusion coefficient *D;* further evidence to show the lack of flagella filaments in mutants. Semi-solid chemotactic agar plates are often used in assays to investigate motility and chemotaxis mutants [46]. 0.3 % nutrient agar plates were used to examine flagella motility, results presented in *Figure.4.24.* Wild-type cells exhibited normal type behaviour where cells migrated outwards (25-fold expansion) as the cell colony grew and migrated, as expected [46]. The same experiment was conducted with KJB24 cells where the colony remains localized at the inoculation site. This experiment provides strong evidence that these cells do not have flagella filaments, but this does not necessarily mean KJB24 cells are not chemotactic.

To directly prove the existence of external appendages, atomic force microscopy was used to visualise the surface and external structures of HCB1 and KJB24 cells. The

AFM results are presented in *Figure.4.25* and *Figure.4.26*, HCB1 cells are positively identified as retaining flagella filaments (~ 4 filaments per cell) which are approximately 5.3 ± 0.1 µm in length and 31 ± 1 nm in diameter. Experimental observations of flagella are in excellent agreement with previous reports regarding flagella statistics in *E. coli* cells [42]. However, KJB24 cells appear to retain a different type of external structure, which is significantly shorter ~ 2 - 3 µm and does not have the distinctive wave like features of flagella. Moreover, the appendages are extremely small in diameter ~ 3.6 ± 0.5 nm, and there are significantly more of these appendages. From AFM it is evident that these appendages are not flagella filaments, which explains why spherical cells are non-motile and explains the slower observed diffusion in bright-field. These extracellular are most likely to be Fimbriae [7]. Fimbriae are very thin short hair like structures which are associated with surface adhesive and DNA transfer [48, 49]. The phyical dimensions of frimbera are 2 - 4 µm in length, with a diameter of 3 - 10 nm, in excellent agrement with AFM images [49]. Therefore, the results obtained from AFM imaging strongly stuggests external appendages in KJB24 are passive fimbriae. However this raises the question why KJB24 cells do not synthesize flagella, which we suspect is linked to the deletion of RodA and PBP proteins [14, 15]. The experimental investigation suggests that either RodA or PBP also regulates flagella synthesis and cellular morphology, and deletion of RodA and PBP forms spherical cells but also inhibits flagella synthesis. The genetics effects of deleting RodA and PBP proteins is beyond the scope of this project, but we have shown that spherical cells are not motile since they do not synthesize flagella but fimbriae instead.

4.9 Conclusion

The experimental research presented in this chapter primarily investigates a mutant spherical strain of *E. coli* to determine whether they are motile as this would considerably assist with mathematical and hydrodynamic modelling of swimming microorganisms. This chapter is a good introduction to the essential microbiological

techniques used to calibrate cell cultures and understand cellular handling. Moreover, it introduces the basic microscopy techniques which are heavily used in this project, in particular bright-field and fluorescence microscopy. The investigation demonstrates that spherical mutants KJB24 cells diffuse significantly slower than expected due to fimbriae protruding from the surface depicted by AFM imaging. Fimbriae are short protein structures which enable cells to transfer DNA and adhere to substrates. Therefore experiments have conclusively shown that spherical mutants do not retain flagella filaments, thus rendering cells non-motile. However the reasons why spherical cells do not retain flagella is a direct consequence of deleting the proteins RodA and PBP, which regulates both morphology and flagella synthesis. However it is still very beneficial to this field of study to find a strain of *E. coli* which is spherical in shape and motile, since numerous studies approximate cell bodies as swimming spheres.

Bibliography and References

[1] G. I. Taylor, *The action of waving cylindrical tails in propelling microscopic organisms.* Proc R Soc London A, **211**:225-239, (1952).

[2] M. Ramia, D. L. Tullock and N. Phan-hien, *The role of hydrodynamic interaction in the locomotion of microorganisms.* Biophys. J, **65**:755-778, (1993).

[3] E. Lauga, W. R. DiLuzio, G. M. Whitesides, and H. A. Stone, *Swimming in Circles: Motion of Bacteria near Solid Boundaries*. Biophysical Journal, **90**:400–412, (2006).

[4] T. Ishikawa, G. Sekiya, Y. Imai, and T. Yamaguchi, *Hydrodynamic interactions between two swimming bacteria.* Biophys. J, **93**:2217-2225, (2007).

[5] L. H. Cisneros, R. Cortez, C. Dombrowski, R. E. Goldstein and J. O. Kessler, *Fluid dynamics of self-propelled microorganisms from individuals to concentrated population.* Exp. Fluids **43**:737-754, (2007).

[6] S. Chattopadhyay, R. Moldovan, C. Yeung, and X. L. Wu, *Swimming efficiency of bacterium Escherichia coli*. Proc. Natl. Acad. Sci, USA, **103**:13712–13717, (2006).

[7] H. C. Berg and R. a. Anderson, *Bacteria swim by rotating their flagellar filaments.* Nature, **245**:380-382, (1973).

[8] A. Ashki and J. M. Dziedzic, *Optical trapping and manipulation of single living cells using infra-red laser beams.* J. Phys. Chem, **93:**254-260, (1989).

[9] S. M. Block, D. F. Blair, and H. C. Berg. *Compliance of bacterial flagella measured with optical tweezers.* Nature, **338**:514-518, (1989).
[10] F. Gittes, and C. F. Schmidt, *Interference model for back-focal-plane displacement detection in optical tweezers*. Optics. Letts **23**:7-9, (1998).
[11] J. R. Moffitt, Y. R. Chemla, S. B. Smith, and C. Bustamante, *Recent Advances in Optical Tweezers*, Annu. Rev. Biochem, **77**:205–28, (2008).
[12] H. C. Berg, *E. coli in Motion,* Biological and Medical Physical Series, Spring Verlag, (2003).
[13] J. B. Armstrong, J. Adler, and M.M. Dahl, *Nonchemotactic Mutants of Escherichia coli.* J. Bacteriology, **93**:390-398, (1967).
[14] K. J. Begg and W. D. Donachie, *Division Planes Alternate in Spherical Cells of Escherichia coli*. J. Bacteriol, **180**:2564–2567, (1998).
[15] K. J. Begg *et al*, *The Balance between Different Peptidoglycan Precursors Determines Whether Escherichia coli Cells Will Elongate or Divide.* J. Bacteriol, **172**:6697-703, (1990).
[16] K. Barker, *At the bench: a laboratory navigator.* Cold Spring Harbor, N.Y. Cold Spring Harbor Laboratory Press, (2005).
[17] N. C. Darnton, L. Turner, S. Rojevsky, and H. C. Berg, *On Torque and Tumbling in Swimming Escherichia coli,* Journal of bacteriology, **189**:1756–1764, (2007).
[18] E. Hecht. *Optics*. 4th Edition, Addison Wesley, San Francisco, (2002).
[19] M. Pluta, *Advanced Light Microscopy*, Volume 1. Elsevier Science, Amsterdam, (1988).
[20] Http://www.microscopyu.com
[21] Http://micro.magnet.fsu.edu
[22] Http://www.olympusmicro.com
[23] A. Ashkin, *Acceleration and Trapping of Particles by Radiation Pressure. Phys. Rev. Lett*,**24**:156-159, (1970).
[24] A. Ashkin*, Optical Levitation by Radiation Pressure*. Applied Physics Letters, **19:**283-285, (1971).
[25] A. Ashkin and J. M. *Dziedzic Optical trapping and manipulation of viruses and bacteria.* Science, **235:**1517-20, (1987).
[26] A. Ashkin. *Forces of a single-beam gradient laser trap on a dielectric sphere in the Ray Optics Regime*. Biophysical .J, **61**: 569-582, (1992).
[27] K. Svoboda and S. M. Block, *Biological Applications of optical forces. Annu. Rev. Biophys*, **23**: 247-85, (1994).
[28] K. C. Neuman and S. M. Block, *Optical Trapping*. Rev. Sci. Instrum, **75**, 2787-2809, (2004).
[29] A. Ashkin, J. M. Dziedzic, J. E. Bjorkholm, and S. Chu, *Observation of a single-beam gradient force optical trap for dielectric particles*. Optics. Letters **11:** 288-290, (1986).
[30] Y. Harada and T. Asakura, *Radiation forces on a dielectric sphere in the Rayleigh scattering regime,* Optics communications **124**: 529-541, (1996).
[31] M. W. Allersma, F. Gittes, M. J. deCastro, R, J. Stewart, and C. F. Schmidt, *Two-Dimensional Tracking of ncd Motility by Back Focal Plane Interferometry.* Biophysical. J*,* **74**:1074-1085, (1998).

[32] A. Rohrbach, H. Kress, and E. H. K. Stelzer, *Three-dimensional tracking of small sphere in focused laser beams: influence of detection angular aperture.* Optics Letters, **28**: 411-413, (2003).
[33] B. Drake, *et al*, *Imaging crystals, polymers, and processes in water with the atomic force microscope*. Science*,* **243:** 1586-9, (1989).
[34] C. Bustamante, C. Rivetti, and D. J. Keller, *Scanning force microscopy under aqueous solutions*. Curr. Opin. Struct. Boil*,* **7**:709-16, (1997).
[35] G. Binning, C. F. Quate, Ch. Gerber, *Atomic Force Microscopy*. Phys. Rev. Lett. **56**:930-933, (1986).
[36] D.G. Castner, B.D Ratner, *Biomedical surface science: Foundations to frontiers.* Suf. Sci. 500: 28-60, (2002).
[37] G. Binning, *Force Microscopy*. Ultramicroscopy, **7**:42-44, (1992).
[38] F. J. Giessible, *Advances in atomic force microscopy*, Rev.Mod **75**:949-83, (2003).
[39] A. Alessandrini and P. Facci, *AFM: a versatile tool in biophysics*. Meas. Sci. Technol**, 16:**0957, (2004).
[40] G. Meyer and N. M. Amer, *Novel approach to atomic force Microscopy*. Appl. Phys. Lett, **53:**1045-7, (1988).
[41] J. P. Cleveland, B. Anczykowski, A. E. Chimid, V. B. Elings. *Energy dissipation in tapping-mode atomic force microscopy.* Appl. Phys. Let. 72: 2613-5, (1998).
[42] L. Turner, W. S. Ryu and H. C. Berg, *Real-time imaging of fluorescent flagellar filaments.* J. Bacteriol, **182**:2793-2801, (2000).
[43] H. C. Berg and L. Turner, *Torque Generated by the Flagellar Motor of Escherichia coil*. Biophysical. J, **65**: 2201-2216, (1993).
[44] G. V. Soni *et al*, *Single Particle Tracking of Correlated Bacterial Dynamics.* Biophys .J, 84:2634–2637, (2003).
[45] J. Knut *et al*, *Chemotactic Signaling by an Escherichia coli CheA Mutant That Lacks the Binding Domain for Phosphoacceptor Partners.* Bacteriol .J, **186**: 2664–2672, (2004).
[46] S. I. Bibikov *et al*, *Methylation-Independent Aerotaxis Mediated by the Escherichia coli Aer Protein.* Bacteriol .J, **186**: 3730–3737, (2004).
[47] J. Narayanan, J.Y. Xiong and X. Y. Liu, *Determination of agarose gel pore size: Absorbance measurements vis a vis other techniques*. Institute of Physics, Publishing Journal of Physics, **28**:83–86, (2006).
[48] M. T. Madigan and J. M. Martinko, *Brock Biology of microorganisms.* Prentice Hall, Eleventh Edition, (2006).
[49] P. Klemm, *Frimbrial adhesion of Escherichia coli*. Rev Infect Dis, **7**:321-40, (1985).

Chapter 5: Examining filamentous *E. coli*

5.1 Introduction

This chapter primarily investigates the swimming behaviour of filamentous *E. coli* cells where wild-type *E. coli* cells are incubated with β-lactam antibiotics to inhibit cell division. Often filamentous cells forms naturally triggered by an SOS response, and it is scientifically interesting to examine how these cells remain motile. It initially discusses how β-lactam antibiotics inhibit cell division, with a brief literature review conducted to highlight the present understanding of filamentous *E. coli* cells. It reviews the effects of β-lactam antibiotics on well characterized cellular processes i.e. cellular growth, chemical signalling and flagella synthesis; and how these processes differ from that of normal dividing *E. coli* cells. We focused on motility in filamentous cells and experimentally exams the swimming mechanism despite significant elongation of the cell body.

With high speed imaging, filamentous cells at different lengths 4 - 30 μm were examined for cellular flexing at suspected division sites. We provide empirical evidence to suggest body rotation is sustained even in significantly elongated cells. Experiments examine how the swimming velocity varies as a function of cell length. Surprisingly the average swimming velocity to the first approximation remains constant despite additional drag of the elongated body. Moreover we investigated the swimming velocity of filamentous cells as a function of separation height above a non-slip plane boundary, the yielded results were unexpected.

Fluorescent staining of flagella filaments was performed in normal dividing *E. coli* and filamentous cells. Fluorescent labelling of flagella filaments is an excellent

method of visualizing flagella filaments in real-time. Imaging of de-energized flagella filaments allow quantitative parameters such as length, pitch length, and amplitude to be extracted. More importantly for filamentous cells the number of flagella filaments as a function of cell length was extracted. To understand motility, real-time fluorescent imaging of swimming cells was performed, which enables one to visualize the flagella bundling process in filamentous cells for the first time. The novel combination of dark-field imaging and high video accusation rates was implemented to extract the cell body Ω and flagella bundle ω rotation rates, by exploiting periodic wobbling of the cell body. This method extracts the average Ω and ω for large numbers of cells ~ 5×10^3 simultaneously from short videos ~ 10 s. Key swimming parameters were quantitatively extracted as a function of cell body length such as average swimming velocity *v,* number of flagella filaments per cell *n,* average angular body frequency Ω, average bundle rotation ω and the number of observed flagella bundles. We fitted our experimental results for normal cells to the standard Purcell model, and by scaling the model to fit filamentous cells shows reasonably good agreement with the experimentally measured values.

5.1.1 The effects of *β*-lactam antibiotics on *E. coli* cells

The experiments conducted in this chapter utilize wild-type *E. coli* cells (HCB1) which were incubated in the presence of *β*-lactam antibiotics. Administrating low concentrations (60 µg/ml) of *β*-lactam antibiotics such as cephalexin inhibits cell division, resulting in elongated cells known as filaments [1 - 4], *Figure.5.1* and *Figure.5.2.* Administrating minimal concentrations (< 100 µg/ml) of cephalexin inhibits cell division without affecting the growth rate [1] and it is irreversible process [5, 8]. In 1980 Rolinson [1] experimentally demonstrated that *E. coli* cells which have been treated with various *β*-lactam antibiotics including cephalexin form filaments. The growth rate of treated cells continued at a uniform exponential rate with an average doubling time of ~ 24 minutes similar to the growth rate of normal dividing cells [1]. Treated cells continued to grow for several generations without

cell division, yielding filaments ranging from 60 - 100 µm in length [1, 7] while their diameter remained unchanged, *Figure.5.2.* Cell death occurs suddenly due to the rupture of the cell wall causing lysis [1, 2, 4]. Prior to lysis the growth remains constant, often localized swelling is observed usually at potential division sites [1, 4, 8, 9]. Schwarz *et al* suggests lysis occurs as a direct result of localized effects regarding murein synthesis and murein hydrolysis at potential division sites [4] *Figure.5.1.* Administering ≤ 100 µg/ml of cephalexin has little effect on the growth rate [1], whereas administrating more than 100-fold of the inhibitory amount terminates cells instantly without further cell growth [1].

β-lactam antibiotic targets the cell wall (murein synthesis) and prevents the formation of the septum. Moreover *β*-lactam antibiotics bind to enzymes involved in cross-linking by the transpeptidase during murein synthesis and hydrolysis [4, 6]. In *E. coli* the role of the peptidoglycan layer is to provide the cell its shape and structural strength [4, 10]. *β*-lactam antibiotics such as penicillin, ampicillin and cephalexin all bind to these transpeptidases which mutate the synthesis of murein and the formation of the septum, therefore inhibiting cell division [1, 4]. Thus filamentous cells are formed with localized defects in the cell wall, occurring at the potential division sites [4]. Filamentous cells eventual lysis due to significant weakening of the cell wall and increasing turgor, *Figure.5.1.*

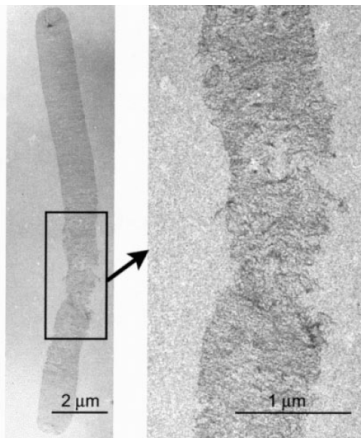

Figure.5.1: An electron micrograph of a filamentous E. coli exhibiting extensive cell wall damage due to lysis; demonstrating the rupture of the cell wall which results in instant cell death. Image sourced from [4], with permission from the Society for General Microbiology.

5.1.2 Chemotaxis in filamentous cells

Maki *et al* investigated the effects of cell size on the chemotactic signalling path ways [7]. Despite increased cell lengths (≥ 50 × larger than normal cells) this group demonstrated that the chemotaxis response in filamentous cells retains similar properties to normal dividing *E. coli* cells [7]. Electron micrographs depict filamentous *E. coli* exhibiting flagella filaments distributed randomly along the entire length of the cell, *Figure5.2.* Non-stimulated filamentous cells exhibit repeated runs and stopping behaviour, analogous to the runs and tumbles in normal cells [7].

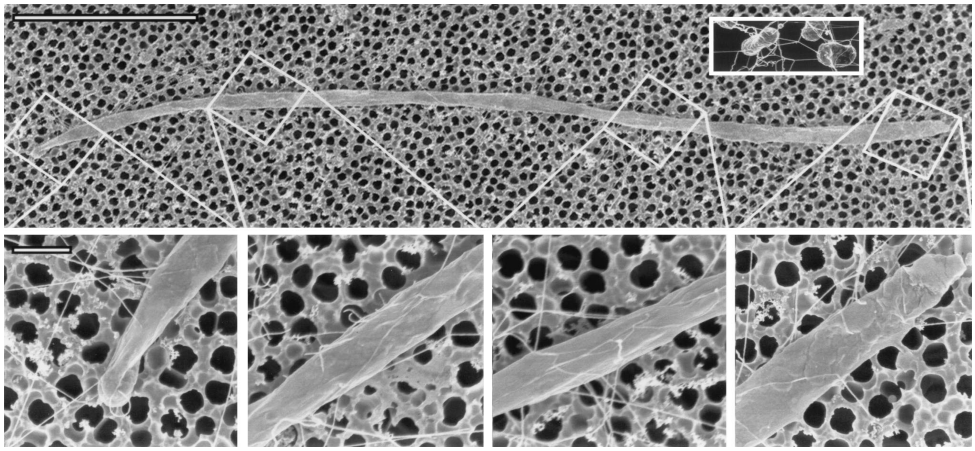

Figure.5.2: Electron micrograph of a 25 μm filamentous E. coli cell incubated for 6 hours with cephalexin (60 μg/ml). Inset is a normal E. coli cell. Bottom images illustrate higher magnification of the filament at various regions, illustrating flagella filament distributed randomly. Top scale bar 5 μm and bottom scale bar 0.5 μm. Image acquired from [7], reproduced with permission from the American Society of Microbiology.

Chemotaxis is a system of receptor signalling and signal transduction enabling *E. coli* cells to seek improvements to their living environment via detecting extracellular chemical signals (See *Chapter 2* and references [10 - 13]). Transmembrane chemoreceptors located at both poles in *E. coli* are known as methylaccepting chemotaxis proteins (MCP's) which regulate flagella motor direction. Thus mediated swimming modes enable cells to swim towards attractants and away from repellents. Flagella motor signalling transduction is regulated by a cascade of MCP's

phosphorylation and dephosphorylation, details in references [7, 11, 12]. In normal *E. coli* cells MCP's are located at the poles, and transport of proteins CheY-P to FilM is carried out by internal diffusion. This process of CheY-P binding to FliM induces **CW** motor rotation, and dephosphorylation of CheY-P results in **CCW** [7, 14, 15]. The internal diffusion of CheY-P is estimated to be 10 μms^{-1} [16], this is consistent with the calculated flagella motor rotational response times of ~ 0.1 s, measured by Segall *et al* for normal cells [17, 18]. Diffusion of CheY-P is likely to be a limiting factor of the chemotactic response times in filamentous cells due to body elongation if MCP's are at the poles only [7].

Segall *et al* induced a chemotactic response from filamentous *E. coli* cells using a micropipette containing a chemical attractant. They reported cells exhibiting altered motor spin bias (observing rotation of attached beads) near the tip of the pipette whereas motors significantly far way ~ 5 μm did not respond to the attractant [18]. They concluded that chemotactic signals are inactive as they diffuses through the cytoplasm which decreases in strength by one-third every 2 μm [7, 18]. This chemotactic signal, (CheY-P) dephosphorylates as it diffuses through the cytoplasm. Therefore it is unlikely that the signal reaches both poles in filamentous cells [7]. Maki *et al* experimentally visualized the location of MCP receptors in filaments cells by labelling the MCP's with a fluorescent anti-MCP serum and using immunofluorescence microscopy [7], *Figure.5.3.* Maki *et al* demonstrated how filamentous cells overcome the diffusion limitations of CheY-P, essential for cellular motility and chemotaxis.

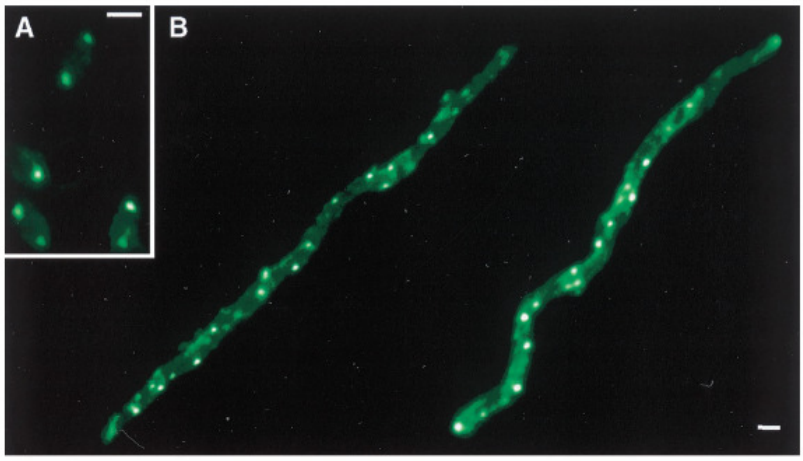

Figure.5.3: (A) Micrograph of normal wild-type AW405 E. coli cells which highlights MCP's located at either poles of the cell, scale bar 1 µm. (B) Illustrates cephalexin treated AW405 filamentous cells with MCP's distributed at the poles and also at various locations along the length of the cell. Image source from [7], reproduced with permission from the American Society of Microbiology.

Figure.5.3 demonstrates chemoreceptors in filamentous cells are localized at the poles and at random intervals along its length. The total amount of MCP located in small clusters along the length of the filament increased by 10-fold relative to the amount located at the poles [7]. It is not known whether MCP clusters are anchored at potential division sites or if they migrate. In normal cells diffusion of CheY-P is responsible for the chemotactic response, however in filamentous cells the discovery of MCPs at the poles and lateral positions enables sufficient diffusion of CheY-P, permitting a normal chemotactic response [7]. Therefore filamentous cells (10 - 30 µm) exhibit similar motility and chemotactic behaviour to those of normal sized *E. coli* cells due to the same molecular diffusion mechanism.

5.1.3 Flagella synthesis and motility in filamentous cells

Aizawa *et al* reported that flagella synthesis is independent of the cellular growth cycle and flagella length is believed to be regulated at the base of each flagellum [19]. However the number of flagella is dependent on the cell cycle [19 - 23]. The two defining factors of flagella synthesis are flagella length and flagella number.

Iino *et al* [20] measured the flagella contour lengths of *Salmonella* cells at various stages in the growth cycle. The results demonstrated that flagella number and length were widely distributed, which did not differ from the mid-exponential or early stationary phase [20]. Iino *et al* suggests the growth rate deceases exponentially with increasing flagella length due to reduction of the mechanical efficiency of transporting flagellin subunits through the central channel [19, 40] (*Chapter 2).* Therefore shorter filaments grow faster than longer filaments which are independent of cell cycle but are governed locally at the base [20].

Iino *et al* also illustrated that the number of flagella filaments per cell remains relativity constant throughout cell generations, implying flagella number is coupled to cell cycle [20]. Nishimura and Hirota demonstrated this also true in filamentous *E. coli* cells, and they believe that cells have a genetic regulatory mechanism which maintains the ratio of cell components (such as flagellin) during the cell division [21, 22]. The results presented by Nishimura and Hirota directly indicate that flagella regulon is under the control of a cell division regulatory mechanism, rather than DNA replication [21 - 23]. The dependence of flagella synthesis on cell division is essential for understanding flagella synthesis in filamentous cells. Filamentous cells can be considered as a series of single cells which are non-septated, therefore one would expect the flagella number per unit length to remain constant. This was confirmed by Nishimura and Hirota [21] which incubated *E. coli* cells with 2 units/ml of penicillin G, where flagella synthesis continues at a constant rate for three generations without cell division [21].

It is believed continual flagella synthesis enables the filamentous cells to continue to swim like normal *E. coli* cells despite the increased length. Maki *et al* investigated motility in filamentous cells and they reported that the behaviour of cells is similar to normal non-treated cells [7]. They experimentally showed that filamentous cells run and stop in a non-stimulated environment, equivalent to the run and tumble behaviour in normal cells. In the presence of chemical attractants filaments exhibited prolonged runs similar to normal cells. However prolonged stopping was observed

in the presences of chemical repellents, equivalent to a tumble in wild-type cells where suspected **CW** motor rotation occurs [7]. However, Maki *et al* did not address the mechanism which permits and sustains motility in filamentous cells.

The mechanism facilitating motility in filamentous cells is not well understood and we aim to investigate this further. The fundamental swimming properties of normal *E. coli* cells such as the average swimming velocity v, body rotation rate Ω, flagella bundle rotation rate ω and single motor torque N have been experimentally determined [10, 11 25 - 27]. These measurements are consistent with predictions from Purcell's model of a swimming cell [28, 29]. However, there are discrepancies between Resistive Force Theory (RFT) and measured torque values of a single flagellum [29] which require further investigation. Chattopadhyay *et al* investigated the efficiency of swimming *E. coli* using optical traps to examine the translational and rotational drag coefficients [28]. They derived the coefficients of the propulsion matrix from experimental values, which agree with RFT for a rigid helical coil. Interestingly they presented data regarding the rotational rates of body and flagella rotation as a function of cell body length L (for normal cells $L \leq 5$ μm), which showed a linear length dependence [28]. The swimming parameters v, Ω, ω, number of flagella filaments n and torque N have been extracted for longer cells > 5 μm where cell motility is often observed. It is interesting to observe the changes in these swimming parameters as a function of length and to see if extracted parameters agree with the accepted model by Purcell. This can determine whether Purcell's model is capable of predicting experimental extracted parameters or whether an alternative model is required. The following section describes the protocols used to produce and examine motile filamentous *E. coli* cells.

5.2 Materials and Methods

This subsection describes the material and methods used in experiments; it discusses growth of cells, the flagella staining technique, dark-field microscopy and sample preparation.

Growing Filamentous cells

A 5ml overnight culture of *E. coli* HCB1 was grown in LB broth at 30 ° C overnight (16 hours). A 10 µl sample was used to inoculate 5 ml of fresh LB in a conical flask. The culture was allowed to incubate for 5 hours until it reached an OD_{600} of 0.5 - 0.8, (1×10^{6} - 1×10^{8} cells per ml). Culture was then washed (centrifuged at 2000 rpm, in 2 ml Eppendorf for 5 minutes) once and re-suspended in LB broth and Cephalexin (60 µg/ml, sigma C4895) was administrated to inhibit cell division. This method yields bacterial filaments ranging in size depending on the period of administration. Samples where taken at hourly intervals. Harvested cells were washed and re-suspended in motility buffer. Typically, 20 µm long cells were observed after four hours of incubation, where the growth rate remained uniform.

Fluorescent labelling of *E. coli* cells

E. coli strain HCB1 was streaked onto 1.5 % nutrient agar containing LB broth, where cell colonies were grown overnight at 37 ° C. An isolated colony was used to inoculate 10 ml of LB broth in a 125 ml conical flask and the culture was grown in an orbital shaker (200 rpm) at 30 ° C. After overnight incubation a sample (100 µl) was used to inoculate a flask of fresh LB broth (10 ml) for approximately five hours until mid-exponential phase. Prior to staining a small sample of the culture was used to verify the motility in bright-field. The staining method used was similar to Turner *et al* [30]. Bacteria were washed twice at room temperature (2,000 × g, 10 minutes) in centrifugation vials, and re-suspended gently in 10 ml of pH 7.0 buffer (0.01 M $KP0_4$, 0.067 M NaCl, 10^{-4} M EDTA [pH 7.0]), and a final wash was carried out in pH 7.5 buffer. The sample was then concentrated to a 20-fold concentration into 0.5 ml, where only 125 µl of this sample was used for staining. A quarter of a pack (5 µl) of Cy3 (PA23001; Amersham Pharmacia Biotech, Newark, NJ) was inoculated with the 125 µl sample with additional 6.25 µl of 1.0 M sodium bicarbonate (to maintain pH neutral). The sample was allowed to stain for a period of 90 minutes at room temperature (23 ° C) with an orbital rate of 100 rpm. Subsequently excess dye was removed by washing the bacteria with MB+ (motility buffer containing 0.002 % tween [Sigma-Aldrich, St. Louis, MO] and 0.5 % glucose). The purpose of

the tween was to prevent fluorescently labelled cells tethering to the glass cover slips, during imaging, *Figure.5.12.*

Fluorescent labelling of filamentous *E. coli* cells

The procedure to fluorescently label filamentous *E. coli* cells is identical to the staining procedure of normal cells above. However the growth of filaments (also described above) was used, in conjunction with the staining method. Filamentous cells where incubated to the desired length, 100 µl of the sample was harvested and washed once (23° C, 2,000 × g, 10 minutes) to remove the antibiotics and re-suspended in the pH 7.0 buffer prior to staining protocol, *Figure.5.13*.

Preparing slides

Coverslips (Menzel-Gläser, 22mm × 50mm thickness 0.13-0.17mm, MNJ-350-070 P) were spin coated with 1 % agarose (*Sigma*-Aldrich) which renders the surface hydrophilic promoting motility and avoiding tethering of cells. A 5 µl sessile drop of the diluted culture (typically diluted 50-fold) was spotted onto the agarose surface prior to imaging.

Acquiring images

E. coli images were recorded at room temperature 23 ° C with a Nikon Eclipse TE2000-U inverted epifluorescence microscope; with a 60 × water immersion objective (Plan Apo, N.A 1.2 working distance 0.22 mm with collar correction). Images were acquired by a monochromatic CCD camera (MARLIN F-14582, 17 fps) or (Pulnix TM-6740CL, 200 fps). Fluorescently labelled cells were excited with a 100 W mercury arc lamp in conjunction with a filter cube set Nikon G-2A (Ex: 535/50 (510-560), DM:565 (LP), Em: 590 (LP)). The excitation intensity was measured as (3.5 10^{-3} $\mu W/\mu m^2$) when imaging cells. The microscope was configured with standard Köhler illumination in bright-field and a standard epifluorescence mode. An arc lamp shutter was closed to prevent unnecessary illumination onto the sample (to prevent photo bleaching), and opened when acquiring data.

Analyzing images

The videos where recorded in an avi format, which were then later converted to an 8-bit grey scale (0 - 255) image using National Instrument Vision Assistant (Version 7.0, Austin TX). These individual images where then converted into a virtual TIF stack using ImageJ (http://rsb.info.nih.gov/ij). Sequences of interest were manually selected and digitally enhanced in ImageJ before the frames were converted back to avi format. To track individual cells the manual tracking plugin was used to determine the average swimming velocity. Calibration of the camera was performed using a Richardson test slide (Generation 3, model 80302, Electron Microscopy Science). This allowed for

accurate measurements of cell length, flagella length, flagella diameter and swimming speed in the National Instrument software.

Dark-field configuration

Dark-field experiments utilized a Nikon Eclipse TE2000-U inverted microscope in conjunction with either a 40 × oil immersion objective (Plan Fluor, N.A 1.3, working distance 0.2 mm, DIC H) or a 10 × dry objective (Plan Fluor, N.A 0.3, working distance 16.0 mm, DIC L). An ultra high speed camera Mikrotron EoSen (MC1362 capable of recording at 3000 fps), was used to record dark-field images of bacteria typically at 500 fps; MotionBLITZ commercial software was used in conjunction. 10 µl of motile bacteria were observed on oxygen plasma treated coverslips, *see Appendix A*.

5.2.1 Fluorescent labelling of *E. coli* cells

This subsection outlines briefly a description of the molecular chemistry involved in flagella staining of *E. coli* cells (HCB1). Further details of fluorescent labelling of cells can be found in reference [29 - 31] and *Appendix F*. Flagella filaments are comprised of ~20,000 subunits of the protein flagellin [10, 11]. Flagellin proteins are made up of peptide chains that form short polymers of amino acids in a defined sequence. The amino acids of interest are the lysines. In the outer sub-domain structure of flagellin FliC there are three exposed lysine residues [29 - 31]. The lysine side-chain exposes a free NH_2 molecule. The exposed NH_2 molecule can be used as a non-specific binding site for fluorescent dyes, where Turner *et al* experimented with several different Alexa Fluor succinimidyl esters dyes [29]. Since there are several thousand exposed lysine's along the flagella filament, labelling the side-chain permits visualization of the entire flagella filaments. The fluorescent dye molecule used is Cy3 (PA23001, Amersham Pharmacia Biotech, Newark, NJ) which is extremely reactive and covalently binds to NH_2 molecules. This method of fluorescently labelling cells was extremely effective and real-time visualisation of flagella filaments were recorded with sufficient detail, presented in *Figure.5.12* and *Figure.5.13.*

5.2.2 Dark-field microscopy

Dark-field microscopy is often used to image transparent objects which have a similar refractive index to it's surroundings. *E. coli* is mainly composed of water thus the refractive index of a bacterium is almost identical to the suspending buffer. This renders *E. coli* cells difficult to visualise using standard bright-field techniques and dark-field or phase contrast microscopy methods are used to enhance the image contrast. This section discusses briefly the theory of dark-field microscopy and the advantages and limitations; and further details can be found in references [32, 33].

The principles of dark-field microscopy are based upon a unique method of illuminating the sample. Dark-field microscopy requires blocking out the light rays in the central region of the optical axis of the microscope forming an inverted hollow cone of light centred in the specimen plane [32]. Blocking centre regions creates emerging light rays propagating at sharp angles such that the effective numerical aperture is larger than the numerical aperture of the objective lens. The oblique propagating rays intersect each other and but do not enter the objective because of their sharp angles, thus the field of view appears dark [32], *Figure.5.4.*

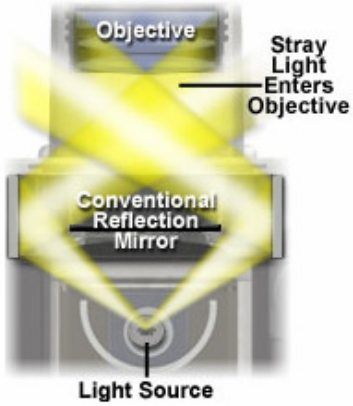

Figure.5.4: Depicts an upright microscope configuration, with a conventional dark-field condenser lens which obstructs the central light rays, forming a hollow cone of light. Thus the sample is illuminated with sharp angular light rays which intersect but do not enter the front of the objective lens, resulting in a dark background hence a dark-field. Image acquired from [32].

Moreover stray light which enters the objective lens results in a reduction of contrast relative to the background. When a specimen is placed on the stage, there is a significant enhancement of contrast of the object relative to the dark background. This is because the sample diffracts and reflects the intercepting light rays and scatters them. The scattered rays caused by the specimen are directed into the objective lens. Thus the sample appears as bright objects on a dark background and the contrast is increased by an order of magnitude, for further details see reference [32].

One of the disadvantage of this technique is that significant light scatting from foreign objects such as dirt in the sample plane obscures the image. Therefore this technique often requires meticulously clean samples, to avoid excess light scattering from dirt particles which saturates fainter objects[1]. Using dark-field microscopy colour is lacking and internal structures are also omitted due to light scattering. *Figure.5.5* depicts examples of dark-field microscopy used to image of *E. coli* cells.

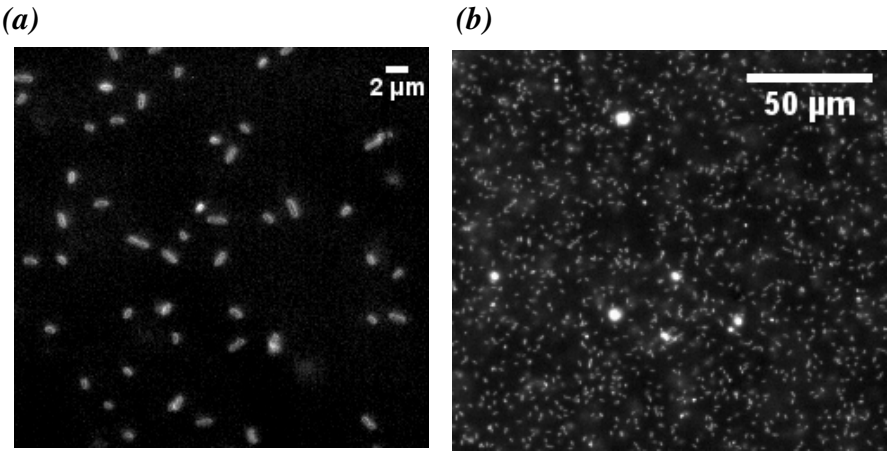

Figure.5.5: (a) Dark-field micrograph of E. coli HCB1 using a 40 × oil immersion objective lens, it illustrates bacteria as bright objects on a dark background. (b) Illustrates the same sample with a 10 × dry objective lens; here large dirt particles scattering additional light, obscuring the bacteria.

[1] Typically out of focus dirt particles can scattered significant amount of light which completely obscures the specimen.

Experimental Results

5.3 Cellular Growth of filamentous cells

Figure.4.5 and current literature demonstrates that, when *E. coli* cells are incubated in batch cultures they grow exponentially [10, 34]. Wild-type *E. coli* cells have well defined length distribution (2 - 4 µm) [34]. Rolinson demonstrated by inhibiting *E. coli* with minimal concentration of cephalexin (20 µg/ml) the cell growth rate remained constant. Treated cells yielded a doubling time of ~ 24 minutes consistent with normal dividing cells in the absence of antibiotics [1]. Rolinson's results also demonstrated inhibiting cells with higher concentrations up to 100 µg/ml did not differ from that of 20 µg/ml [1], we use a similar protocol to Maki *et al* [7] to incubate motile filamentous cells.

Experimental verification is presented in *Figure.5.6,* confirming the growth rate of cells is uniform when incubated with 60 µg/ml of cephalexin. Optical density readings were obtained as a function of time to determine the growth rate. The calculated doubling time for our strain of *E. coli* (HCB1) in our growing conditions from the viable plate count assay yielded an average doubling time of 37.1 ± 10.1 minutes, from *Chapter 4*, *Figure.4.5*. As a comparison the cell length of 100 individual *E. coli* cells at hourly time points of administration where measured. The cell body length is directly proportional to cell generations, where one expects the cell body length to increase exponentially as a function of time.

(a)

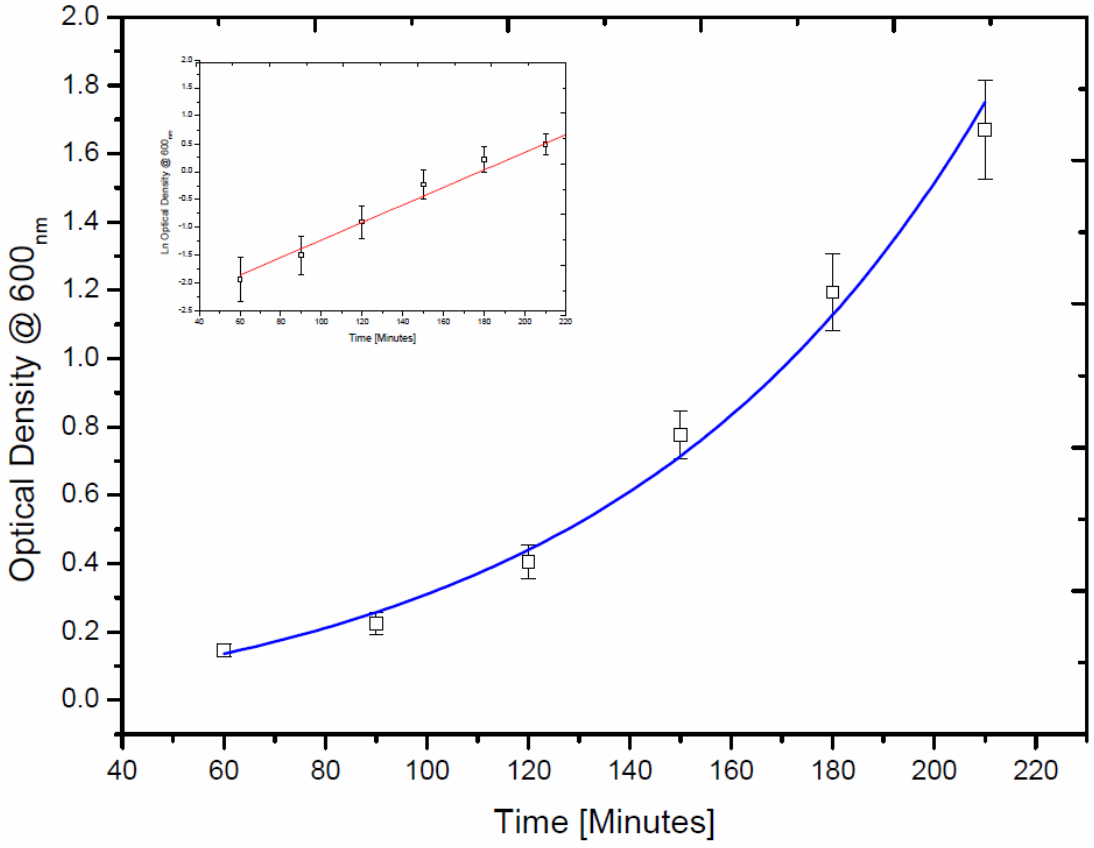

Figure.5.6: (a) Shows the optical density as a function of time for E. coli (HCB1) in experimental conditions, where the growth rate is exponential as predicated. The calculated doubling time is 37 ± 10.1 minutes. Insert illustrates the natural log plots of the exponential growth phase, demonstrating a linear trend as expected.

(b)

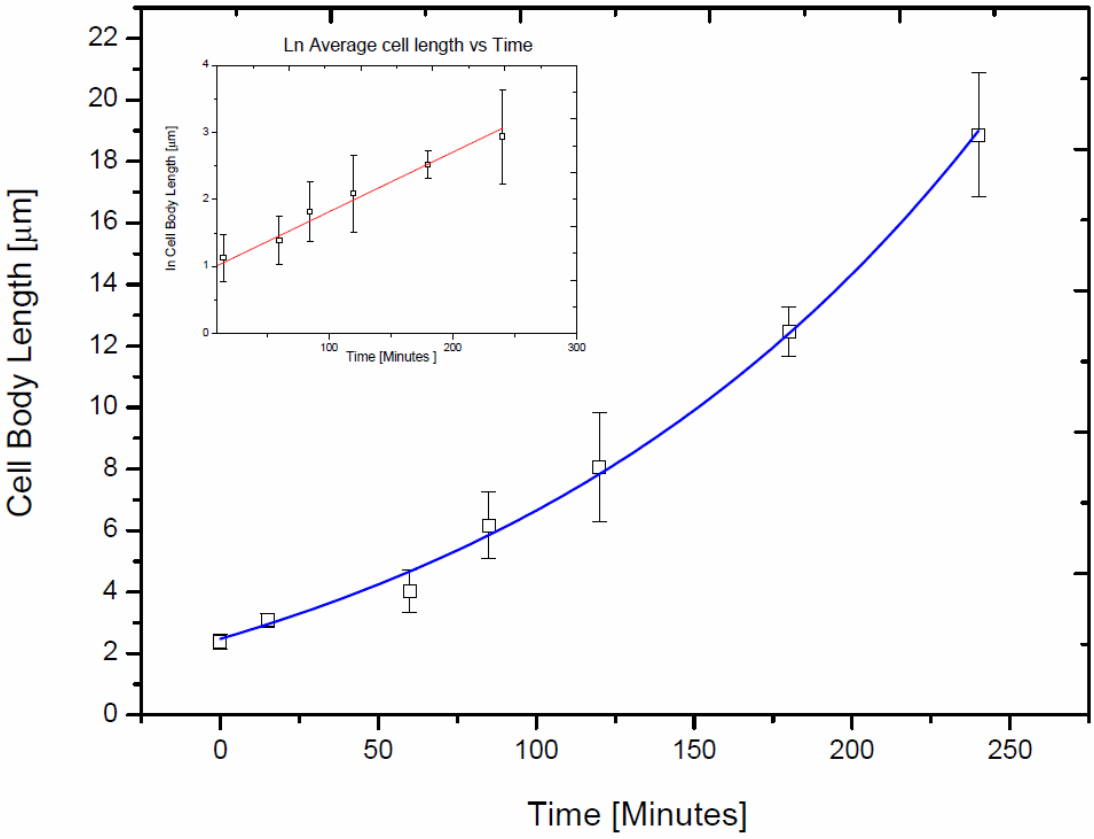

Figure.5.6: (b) Graph of average cell length as a function of time for average of 100 at each time point. The graph reflects a good exponential fit, where the error bars are the standard deviations. The calculated doubling time is 35 ± 5.2 minutes (from the inset), consistent with normal dividing cells. Similarly the inset illustrates the natural log plots of the exponential growth phase, demonstrating a linear trend as expected.

Figure.5.6 confirms that both graphs exhibit exponential growth rates; the doubling time for normal dividing cells was calculated to be 37.1 ± 10.1 minutes, whereas inhibited cells yielded a doubling time of 35 ± 5.2 minutes. Our findings are in excellent agreement with the results presented by Rolinson [1] suggesting cellular growth rate is uniform until the point of lysis. For the purpose of our experiments we investigated cells up to 30 µm in length, while the cells are still reasonably healthy. *Figure.5.7* shows the average cell lengths of bacteria at each hour time interval in respect to cephalexin administration.

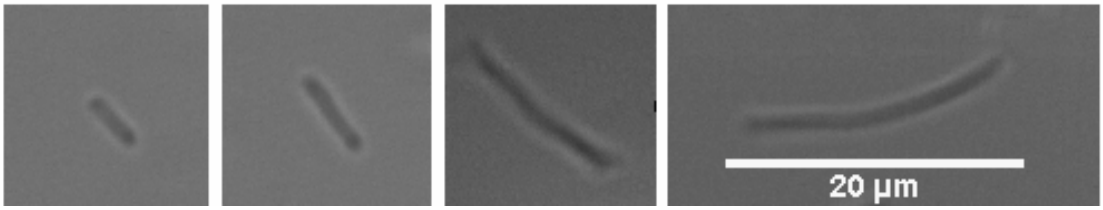

Figure.5.7: Representative micrographs of swimming filamentous cells incubated with cephalexin to inhibit cell division without altering the cellular growth rate. Samples were observed at hour intervals where the respective cell length are L = 4.37 µm, 6.63 µm, 14.08 µm and 19.13 µm; however cell diameter did not vary considerably ~ 1 µm.

In summary, inhibiting cellular division with 60 µg/ml of cephalexin does not alter the growth rate of cells which remains exponential until cell death via lysis[2]. The average doubling time for normal and treated cells is in the order of ~ 37 minutes. Moreover cells as long as 30 µm are relatively healthy indicated by sustained motility. However, filaments beyond 50 µm experienced body deformities (large angular kinks) and their motility is reduced significantly suggesting cells are no longer healthy.

5.4 Bending or Rotating?

Filamentous cells exhibit motility despite significant body elongation 10 - 50 µm. The cell body in normal *E. coli* cells rotates typically at 20 Hz, in the opposing direction of flagella bundle rotation to cancel out the total torque [10, 28, 35]. Observations of filamentous cells (15 - 30 µm) (*See movie: HCB1-Filament-rotating.avi)* at 17 fps showed that they appeared to flex their cell body back and forth periodically as they swam. This apparent flexing of the cell body was suspected as a possible alternative swimming mechanism to sustain motility, similar to the mechanism of non-flagellated cells, i.e. *Spiroplasma* which relies on body deflections to generate net motion [36]. By implementing a high acquisition rate

[2] Cell lysis was not observed at short cell lengths ≤ 60 µm where cells remained relative healthy.

CCD camera it is possible to slow down the motion of swimming filamentous cells and to verify if cells actually deflect their bodies in order to sustain motility.

The body deflections may occur due to the undesirable effects of using cephalexin, which produces localized weakening of the cell wall at potential division sites [4]. At these sites the weakening of the cell wall is due to the lack of septal murein synthesis (SMS) which is prone to lysis, see reference for details [4]. It is possible that this weakening of the peptidoglycan layer permits greater flexibility of the cell body; where possible body deflections may assist in sustaining motility. Evidently, *Figure.5.8* shows angular deformities > 15 ° of the cell body; these kinks are formed due to the lack of structural rigidity at potential division sites. These kinks where observed typically in longer cells 10 - 50 µm due to the deterioration of the cell wall occurring randomly along the cell. To determine whether filamentous cells ≥10 µm rotated like normal *E .coli* cell or whether cells performs body undulations, a high speed camera (≤ 200 fps) was implemented to record the swimming of individual filamentous cells, *Figure.5.8.*

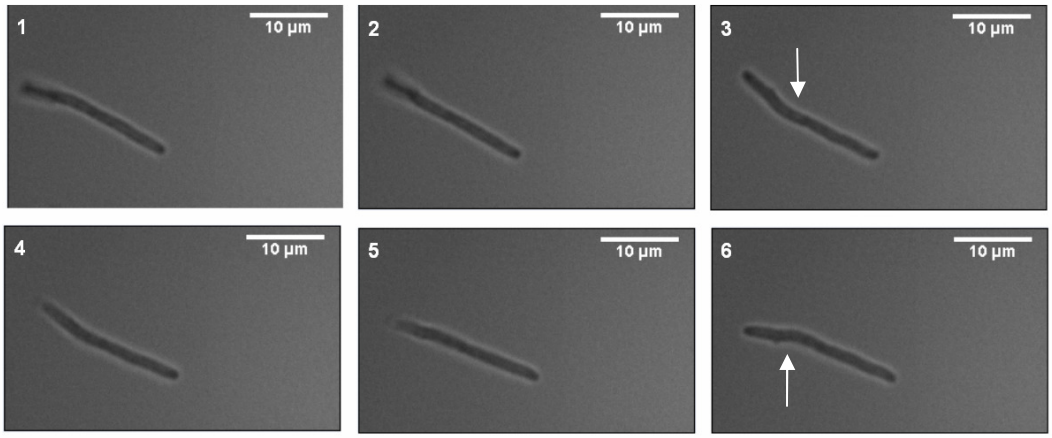

Figure.5.8: Shows consecutive frames (Δt = 0.014 s) of a filamentous E. coli cell ~ 15 µm which has been treated with cephalexin for 4 hours. The sequence illustrates the cell is still motile generating forward motion. It conclusively depicts that the cell is rotating about its longitudinal axis periodically by observing the location of a double kink in consecutive frames indicated by the arrow; body deformations were not observed, (see movie: HCB1-filament-rotating-5fps.avi).

Figure.5.8 provides conclusive evidence of a filamentous cell rotating about its longitudinal axis by the periodic axial rotation of the kink in consecutive frames. Moreover videos show the rear of the cell (kinked end) goes periodically in and out of focus, further supportive evidence of body rotation. The appearance of body deflection/undulations is due to the 2D imaging plane and the fast rotation rate of the cell body creates the optical illusion of body deflections. It is obvious from high speed imaging and frame-by-frame analysis that filamentous cells rotate about the longitudinal axis, similar to normal cells. A range of cell lengths 5 - 30 µm also demonstrated body rotation while body deflections were not observed. Therefore we consider filamentous cells as a rigid cylinder. However, minute body effects may occur beyond the detection limit.

In summary cephalexin incubated *E. coli* cells at typical body lengths of 5 - 30 µm demonstrated body rotation rather than suspected periodic body deflections. This was evident from high speed imaging, where observed kinks rotate periodically in and out of the focus plane. Frame analysis shows large body deflections are not observed, however we can not rule out small body deflections. Therefore we consider motile cells which are $\leq$ 30 µm in length as ridge rotating cylinders.

5.5 Swimming velocities of filamentous *E. coli*

Maki *et al* investigated the chemotactic response in filamentous *E. coli* cells, where it was demonstrated that cephalexin incubated cells remained motile despite the increase in cell body length [7]. They showed that filamentous cells were able to run, however tumbles were omitted. Instead, cells stopped for substantial periods of time in the presence of a chemical repellent. They demonstrated the chemotactic response mechanism remains identical to those of normal dividing cells. However, observed motility in filamentous cells does not necessarily swims with the accepted model of a swimming bacterium with a single flagellum bundle at the rear of the cell,

Figure.2.10 [11, 35], but the authors did not discuss the mechanism of motility in filamentous cells.

An experiment was conducted to examine the swimming mechanism of filaments cells by investigating the average swimming velocity (during run events) near a non-slip interface, and how the swimming velocity varies as a function of body length. We expected the swimming velocity of cells to decreases sharply due to increase in viscous drag of elongated bodies. *Figure.5.9* presents 500 individually tracked *E. coli* cells where the average swimming velocity was extracted for corresponding cell lengths, and also respectively of the administration period of antibiotics. Examining samples of inhibited cells shows non-uniform cell length distributions, these heterogeneities are due to cells being in various growth cycles[3] when cephalexin was administrated, (see *Figure.5.20* for length distributions at hourly intervals) as a result a broad length distribution is observed.

(a) ***(b)***

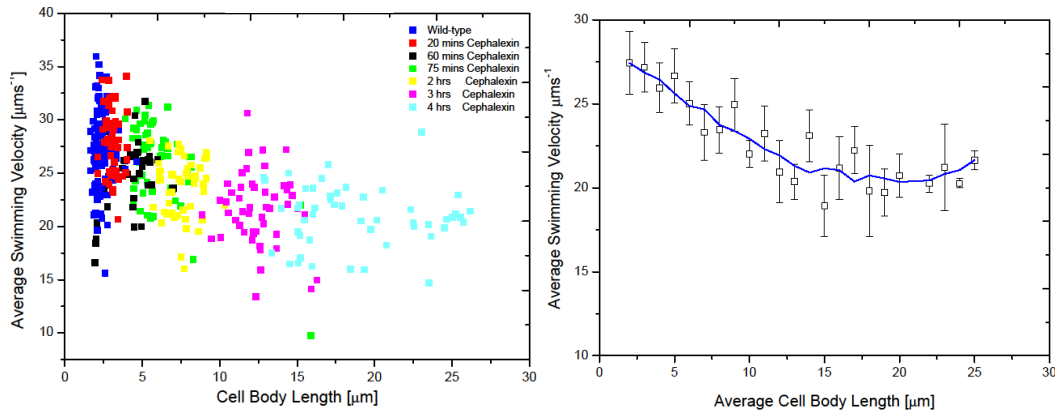

Figure.5.9: (a) Presents the swimming velocity of cells as a function of corresponding body length. The blue data set illustrates normal dividing wild-type cells; the data set is colour coded to respective incubation periods. The average swimming of cells in each sample was extracted as <v> = 27.1 ± 3.5, 27.3 ± 3.1, 26.0 ± 3.9, 24.9 ± 3.1, 23.7 ± 2.7, 21.5 ± 3.3 and 20.9 ± 2.8 μms^{-1} respectively. To first approximation the cellular swimming velocity is constant, where the velocity decays gradually with cell length. (b) Statistically binned data illustrating a 5 point average curve highlighting the decaying trend which remains relatively constant at approximately 10 μm and sustains a velocity of ~21 μms^{-1}.

[3] Where the extremes are when cells have just divided or about to divide.

Figure.5.9 (a) Shows that the swimming velocity of filamentous cells to the first approximation decreases slowly. In normal dividing cells the average swimming velocity is 27.1 ± 3.5 μms^{-1}; however when cells were five times their normal length ~ 10 µm the swimming velocity is reduced to ~ 21.5 ± 3.3 μms^{-1}, a 15 % reduction in swimming velocity. Cell lengths exceeding 10 µm illustrated a plateau with approximately constant swimming velocity of 20.9 ± 2.8 μms^{-1} highlighted by the 5 point average curve in *Figure.5.9 (b).* *Figure.5.9* raises interesting questions regarding the mechanism of thrust generation which sustains motility, and how this mechanism differs from normal dividing cells. The results suggest that swimming velocity in filamentous cells has a weak length dependence, and swimming velocity may depend on other properties such as flagella number.

We also considered how the swimming velocity varies at different separation heights above an interface where hydrodynamic interactions with the surface occurs [37 - 39]. Cells swimming close to a surface experience a larger viscous drag than in bulk due to the presence of the surface. The effects of this on the swimming velocity are not obvious. One would intuitively expect the velocity to decrease due to the increasing viscous drag on the cell body; however the thrust mechanism (rotation of flagella bundle) is based upon viscous drag recall *Chapter 3*, therefore an increase in localized drag near the surface leads to a larger thrust force being exerted on the fluid as the bundle rotates thus increasing the swimming velocity [37]. Since both the drag on the cell body increases, and the thrust forces generated by the flagellum bundle increases; this results in a very subtle affect on the average swimming velocity of the cell near a surface. It is been accepted that, at close proximity to a non-slip surface the swimming behaviour and velocity is hindered [38].

We extracted the swimming velocity of various lengths of cells at defined separation distances h above the surface. Moreover we investigated two types of surfaces, either an oxygen plasma glass surface or a spin coated 1 % agarose surface. The difference between the surfaces, is that glass is a non-slip interface, whereas agarose is porous (pores size of 200 - 230 nm and thickness of 150 - 200 µm) this enables the

fluid to pass through the pores, therefore it is not a non-slip surface [40]. Utilizing a piezo controlled objective lens mount the average swimming velocity of filamentous cells at separation heights $h =$ 0.5 µm, 2.5 µm, 4.5 µm and 6.5 µm on respective surfaces was extracted. Only cells which were in focus for substantial periods were collected to ensure accurate height measurements. The minimal measured separation height between the cell and the surface is 0.5 µm which was used as a respective off-set value $h = 0$. The results are presented in *Figure.5.10.*

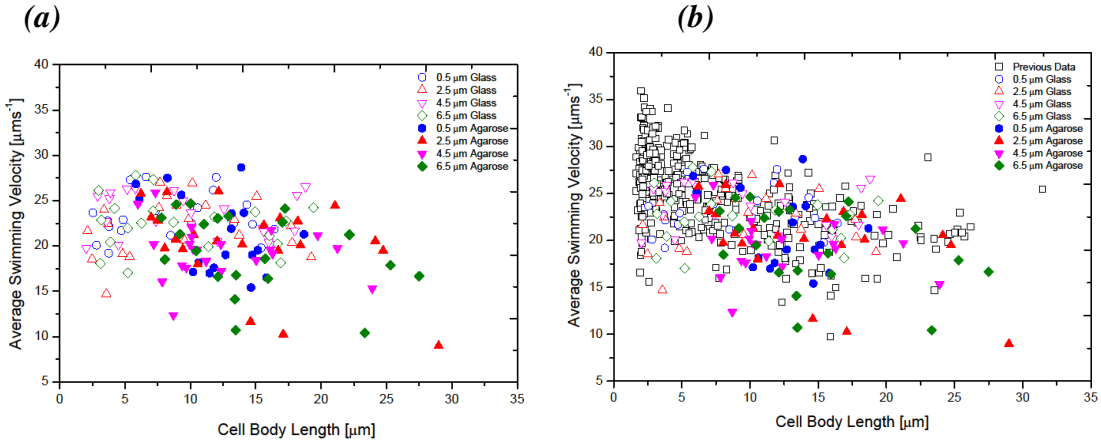

Figure.5.10: (a) Reports the averages swimming velocity of filamentous cells as a function of separation height on respective surface. The open symbols represent 100 filamentous cells on a non-slip glass surface at respective separation height $h = 0$, 2, 4, and 6 µm. Similarly filled symbols are 100 filamentous cells on an agarose surface at the same separation heights. The results show a negligible difference between surfaces and at various separations heights; moreover a correlation as function of separation height was not observed. (b) Illustrates a comparison between previous data set presented in (Figure.5.9) and newly acquired data set at different heights. It demonstrates both data sets are consistent where no obvious trend is observed.

The results in *Figure.5.10* illustrate no observable correlations between different separation heights and surfaces. Comparing these results to the previous data set presented in *Figure.5.9* indicates experimental consistency, where the effects of hydrodynamic interactions near the surface appear to be negligible. We conclude hydrodynamic interactions with the surface appear to have a negligible or a very subtle effect on the swimming velocity of cells despite their elongation. A secondary plausible explanation could be due to the heterogeneities in the cells despite being

incubated from a single colony. Heterogeneities in swimming velocities can arise due to several factors such as varying number of flagella. Thus these variations lead to differences in hydrodynamic interactions with the surface and therefore a correlation cannot be clearly observed. Moreover, hydrodynamic interactions may be extremely subtle where the effects on the swimming velocity are beyond the detection limit of our experimental methods.

Filamentous cells incubated beyond 6 μm in length exhibited run behaviour exclusively with tumbles completely omitted. Our observation supports the findings presented by Maki *et al* [7]. We examined the swimming velocity of '*smooth swimmers'* (*E. coli,* RP437, [12]) mutants which run continuously. We expected the velocity of smooth swimmer to be marginally faster than those of wild-type cells, since in normal cells flagella motor reversal causes additional drag.

In long filamentous cells it is possible for cells to run and to have several flagella filaments rotating **CW** simultaneously without initiating a tumble, since flagella filaments are regulated locally [7, 17, 18]. It is possible for flagella filaments at the front of a filamentous ($\geq$ 6 μm) cell to experience a chemical repellent such that the motor initiate **CW** rotation. However for flagella filaments at the rear of the cell the tumble response may not be elicited, since localized MCP's are only sensitive over a short range ~ 2 μm and do not sense the chemical repellent to initiate **CW** rotation. Thus filamentous cells continue to run despite **CW** motor rotation, whereas normal cells would tumble. In the scenario where few flagella rotate **CW** out of many filaments rotating **CCW,** it is unlikely for **CW** filaments to induce an effect except for causing extra drag reducing the swimming velocity slightly. It is unlikely for small minority of **CW** flagella filaments to cause a tumble event when there are majority of flagella rotating **CCW**. Moreover since the cell body has increased cell length, it requires a significantly larger toque to re-orientate the cell body or alter swimming trajectory, which is also restricted by the proximity of the interface. This explains why filamentous *E. coli* cell beyond 6 μm do not to exhibit tumbles. Furthermore when a filamentous cell is in the presence of a strong chemical repellent

all the flagella rotate **CW** and the cell stops swimming and remains stationary for prolonged periods without body re-orientation. This is because **CW** rotation of flagella are deployed in an incoherent direction exerting a force randomly which is insufficient to re-orientate the elongated cell body. *Figure.5.11* presents data of the swimming velocities of wild-type filamentous cells and smooth swimming filamentous cells.

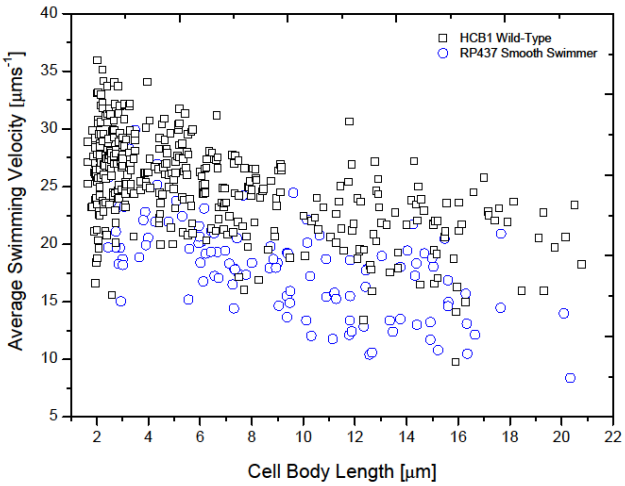

Figure.5.11: The squares represent the average swimming velocity of wild-type cells as a function of length, the circles represent the smooth swimmers (200 individual cells). There is a systematic shift in the swimming velocity of cells due to suspected heterogeneities between strains; however the swimming velocity as a function of length illustrates a similar trend, decreasing slowly as a function of length. The data sets are consistent suggesting CW rotation of 1-2 filaments in longer cells has a negligible effected on swimming velocity and cell trajectory.

Figure.5.11 illustrates the data obtained from smooth swimmers, plotted against previous data for wild-type cells. The graph indicates a systemic reduction in swimming speeds of smooth swimmers. The estimated reduction is ~ 20 %, most likely due to inherent differences between the wild-type and the mutant smooth swimmers strains. Both data sets are consistent with each other, supporting the conjecture that a minority of flagella filaments which rotate **CW** has a negligible effect on the swimming speed and trajectory for long cells, where tumble events are omitted. In summary the velocity of filamentous cells decays very slowly as a function of cell length, filamentous cell beyond 6 µm did not exhibit tumbles. Filamentous cell swimming near an interface illustrated subtle interactions with the

surface, where the swimming velocity of filaments are consistent whether 2 µm or 6 µm above the surface. Smooth swimming cells were examined and the velocity was extracted as a function of length which showed a similar trend to wild-type cells. **CW** flagella motors are present in wild-type cells (experimentally verified using real-time flagella staining, discussed in the section below), where in significantly long cells, **CW** rotation did not effect the swimming velocity or swimming trajectory, concluded by the consistency between smooth swimmers and wild-type data sets.

5.5.1 Imaging of flagella filaments

Fluorescent flagella labelling described earlier was used to image flagella filaments in normal and in filamentous cells. This section discusses the effects of fluorescent staining and presents data regarding the number of flagella filaments observed in normal cells and in filamentous cells. The average swimming velocity of 100 normal cells was extracted as 31.2 ± 3.1 μms^{-1} prior to fluorescent labelling. After staining the average swimming velocity was measured as 24.5 ± 2.7 μms^{-1} a noticeable 22 % decrease in swimming velocity. This reduction in swimming velocity is believed to be linked to presence of fluorescently dye molecules which bind to the exposed lysines rendering flagella filaments brittle [29, 30]. The increased brittleness of the flagella may hinder the effectiveness of the flagella bundling process resulting in slightly slower swimming velocities. Also flagella truncation during staining may result in slower swimming speeds [29]. Moreover, cells were deliberately mistreated (vigorous re-suspension) and the average swimming velocities of mistreated cells was 16.2 ± 3.5 μms^{-1}. Typically cells retained almost ¾ of the number of flagella[4] than gently handled cells where the length of flagellum is ~ 3 - 4 µm, *Table.5.1.*

[4] Surprisingly cells demonstrated normal swimming behaviour despite significant flagella loses, which suggest flagella filaments may have a duel purpose, such as assisting in bio-film formation.

Table 5.1

	Velocity ***(μms^{-1})***	***No° of filament*** ***(per cell)***	***Length*** ***(μm)***	***Pitch*** ***(μm)***	***Amplitude*** ***(μm)***
***E. coli (gentle)*:**	31.2 ± 3.1	4.2 ± 1.8	9.2 ± 1.5	2.4 ± 0.2	0.3 ± 0.2
***E. coli (mistreated)*:**	16.2 ± 3.5	2.9 ± 1.2	4.3 ± 2.7	2.1 ± 0.5	0.2 ± 0.8

Table.5.1: Presents the average statistics of 100 independent cells for gently handled and mistreated cells respectively. Generally the number of flagella and length is halved in mistreated cells resulting in a 22 % decrease in swimming velocity. The pitch and amplitude for respective cell treatments were similar, as expected. The results for gentle handling are in agreement with results presented by Turner et al [29, 30].

It is possible that despite gentle handling a small percentage of flagella truncation may occur. *Figure.5.12* presents representative images of fluorescently labelled wild-type *E. coli* cells using the protocol described previously. The staining of cells produced excellent results comparable to the work of Turner *et al* [29, 30], where flagella filaments are clearly visualized without causing photo-damage or altering cell swimming behaviour (See *Chapter 6* for further details).

(a) ***(b)***

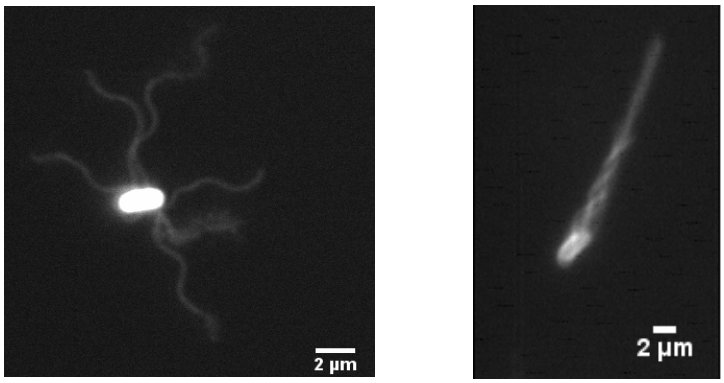

Figure.5.12: (a) Shows a fluorescently labelled cell E. coli cell (HCB1) which has been tethered to the glass coverslip. It shows a de-energized cell which has six flagella filaments distributed asymmetrically. (b) Fluorescently stained E. coli (HCB1) illustrating the formation of the propulsive flagella bundle by the co-rotation of flagella filaments. The flagella bundle consists of approximately six filaments which rotate at ~ 100 Hz. Due to the higher rotation, details of the polymorphic conformation are lost.

Figure.5.12 (a) shows a typical de-energized cell tethered to the glass surface enabling quantitative measurements of the flagella filaments and the cell body. *Figure.5.12 (b)* illustrates a snap-shot of a real-time imaging of an *E. coli* cell performing a run imagined with an excitation intensity of 3.5×10^{-3} $\mu W/\mu m^2$ which did not elicit a repellent response; where runs and tumbles naturally occurred. Excitation intensities significantly above this value demonstrated strong chemotactic response and at high intensities cells become instantly paralyzed (*Chapter 6* for full details). The fluorescent labelling technique was used to examine a number of flagella filaments in filamentous cells, but also used for real-time visualization of flagella filaments, shedding light on the swimming mechanism. Filamentous cells where stained at hourly intervals of the antibiotic administration period; the results are presented in *Figure.5.13.*

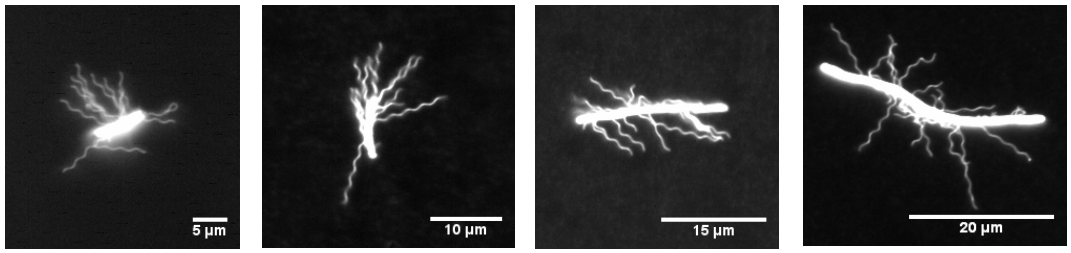

Figure.5.13: Presents fluorescently labelled cephlexin treated E. coli cells at various incubation time intervals. The observed flagella filaments are peritrichously distributed and they are identical to those from normal dividing cells. Less obvious is that the length of flagella increases subtly, where longer flagella filaments are typically found in older cells. The respective body length of each cell is L = 7.5 µm, 9.8 µm, 21.6 µm, and 35.62 µm.

Reports by Nishimura *et al* show that flagella synthesis continues in filamentous cells, while cell division is inhibited by administration of penicillin G [21]. Their report suggests flagella synthesis is regulated by the cell division process and not directly coupled to DNA replication [21]. In temperature sensitive mutant *E. coli* cells, cell division is inhibited at a non-permissive temperature forming filaments (See reference [21] for details) where flagella synthesis and the number of flagella per unit length decreased sharply. Nishimura *et al* showed by inhibiting cell division via administrating the antibiotic penicillin G (no genetic mutation in cell division), flagella synthesis continued. The rate of flagella synthesis in these cells was approximately constant for three generations, although a slight reducing trend is

observed (See reference [21] *Figure.2*). By analyzing images of fluorescently labelled cells, our results suggest the number of flagella filaments increases with cell body length for several generations. The initial trend is consistent with the finding presented by Nishimura, where the number of flagella filaments remains constant per unit length. However observations of significantly longer cells (additional generations) suggests the flagella number per unit length decreases as a function of generation time. To investigate we examined 500 independent images of fluorescently stained filamentous cells at various lengths, *Figure.5.13.* From each image we extracted the average cell body length and the corresponding number of flagella filaments, *Figure.5.14.*

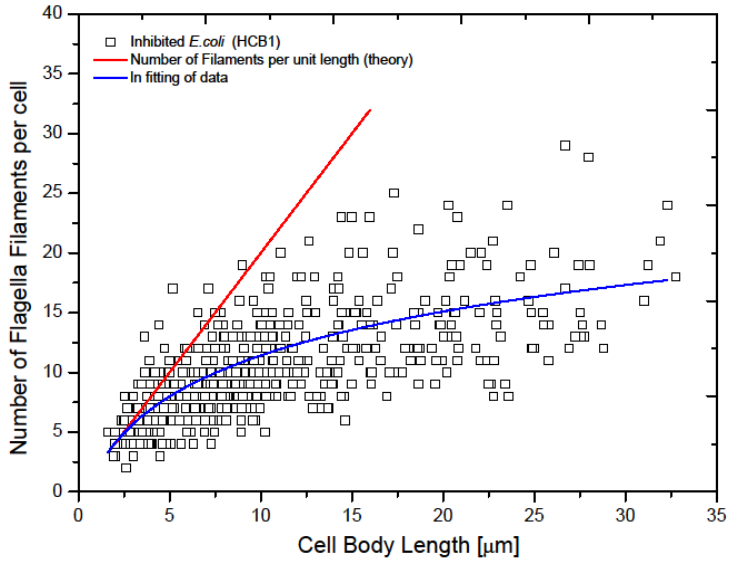

Figure.5.14: A plot of the number of flagella filaments observed in cephalexin treated E. coli cells plotted as a function of corresponding body length showing 500 data points. Each point represents an individual cell, the blue curve is a logarithmic fit for the data and the red line represents a linear theoretical curve.

The results presented in *Figure.5.14* are from 500 individual cells where the number of flagella and the corresponding cell length were recorded[5]. The results show that the number of flagella filaments is approximately constant per unit length up to 8 μm (3 generations). The observed constant number of flagella per unit lengths is

[5] Images of fluorescently stained cells were analysed by 4 independent people, to statistically reduced errors in the number of filaments in the images.

consistent with the results presented by Nishimura *et al* [21]; however they do not examine the number of flagella for much longer cells. Beyond three generations the number of flagella filaments per unit length decreases. The obtained data set suggests a possible logarithmic increase in the number of flagella filaments as a function of body length. We suspect the health of cells deteriorates as they become longer, thus the efficiently of flagella synthesis decreases since flagella synthesis is considerably costly in terms of energy and biomass.

One expects the flagella number per unit length to remain constant; however our results indicate this is not the case for significantly elongated cells. It was suspected that flagella truncation occurs during fluorescent labelling despite gentle handling [30] and this might be responsible for a reduction of observed numbers of flagella. Possible sheared cells may feature in the data set presented in *Figure.5.14*. These sheared cells are most likely to feature towards lower envelope of the graph. Since, they have fewer filaments whereas non-sheared cell would have more filaments with the same corresponding body length. There are strong arguments to suggest flagella truncation is not responsible for the reduction of visualized flagella numbers. Foremost, if the flagella number per unit length is constant for a typical 20 µm cells it would retain ~ 40 flagella filaments, we only visualized ~ 15 filaments and it is extremely unlikely to miss count 25 filaments. If we assumed flagella truncation did occur we would expected the samples to be saturated with truncated filaments and this was not observed in our specimens. Finally from *Table.5.1,* intentionally mistreating cells illustrated that 25 % of the filaments were truncated implying flagella filaments are fairly robust, but not as robust as *B. subtilis* cells see *Chapter 6*. If the flagella number per unit length was constant, for the extreme case of mishandling of cells we expect from a 20 µm cell to retain more filaments than what is visualized. Thus, it seems unlikely that the number of flagella filaments per unit length remains constant for longer cells. This is most likely due to the deteriorating health of cells as they become abnormally elongated, where we suspect the efficiency of manufacturing molecular motors decreases since flagella synthesis is extremely costly in terms of biomass.

Real-time visualisation of flagella filaments was conducted in filamentous cells. The natural swimming behaviour of filamentous cells was observed, illustrating the formation of multiple flagella bundles along the sides of the cell body (bundling of nearest flagella filaments) and at the pole generating propulsion. Short cells ≤ 4 µm swim with a single propulsive bundle at one pole similar to normal cells as anticipated. Although, the flagella bundle appears thicker in diameter due to twice as many flagella filaments, which seemed to be loosely bound. Larger cell lengths ≥ 6 µm, showed that thrust is generated by co-rotation of observed multiple bundles forming on the sides of the cell. The number of flagella bundles is correlated to the number of flagella filaments, thus longer cells retain more bundles, *Figure.5.15.*

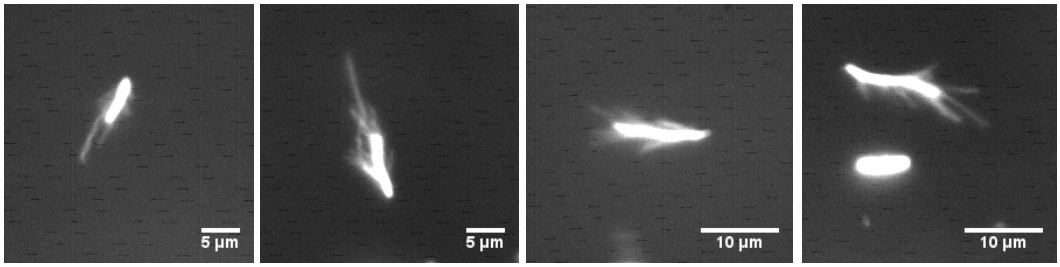

Figure.5.15: Micrographs of filamentous cells swimming in real-time near a glass interface, the micrographs are at hourly intervals of administration period. The cell lengths are L = 6.8 µm, 8.4 µm, 12.5 µm and 14.2 µm, where the corresponding typical number of flagella bundles observed for each respective cell length were 2, 3, 4, and 5. Moreover single flagella filaments were observed rotating independently outside of the flagella bundles. The number of bundles where directly proportional to number of flagella filaments as expect, where each bundle is believed to consist of at least of 3 flagella (See movie HCB1-Stained-swimming.avi).

Observations shows nearest neighbouring flagella filaments form into bundles when rotating **CCW**, observations also shows individual flagella contributing to thrust generation independently of the bundle, *Figure.5.15*. Occasionally flagella bundles are observed to disperse due to suspected **CW** rotation however chaotic re-orientation is not visualized for cells beyond 6 µm in length. For cell length beyond 6 µm, the dispersion of a single flagellum from the bundle has little or no effect on the overall run behaviour. In order to stop motility the majority of flagella filaments need to be rotating in **CW** direction, however cellular re-orientation is not observed for two reasons. Firstly elongated body length (larger viscous drag) requires a larger

torque to re-orientate the body in a viscous environment. Secondly it would also require a substantial number of flagella filaments to rotate simultaneously in the same direction, an unlikely event thus cells appear to run exclusively.

Observation illustrates flagella bundles disperse although the cell remains motile due to the thrust generated by the other bundles. Occasionally the formation of new flagella bundles occur incorporating different flagella filaments along the cell body, forming new bundles which can migrate along the cell length (i.e. different populations give new flagella bundle locations). The bundling process of flagella filaments is extremely complicated even in normal *E. coli* cells [29, 30] where bundling is often simplified as a rotating helix. The tumbling process in wild-type *E. coli* is still not fully understood [29, 30]. Therefore trying to explain the bundling and unbundling process in filamentous cells is challenging, where a full explanation is not yet at hand. Furthermore, visualizing flagella bundles provides supportive evidence of cell body rotation; as bundles clearly rotate about the swimming axis, *(See movie HCB1-Stained-swimming.avi)*. Thus flagella staining in filamentous cells have provided an insight into the swimming mechanism deployed to sustain motility, and several possible reasons are given to explain exclusive run behaviour in filamentous cells.

5.5.2 Measuring flagella bundle and body rotation rates

This sub-section described a novel use of dark-field microscopy and high speed imaging to extract the average body and flagella bundle rotation rates of swimming bacteria. In the literature, body and flagella bundle rotation rates for *E. coli* are estimated to be ~ 20 Hz and ~ 100 Hz, respectively [10, 28, 29]. The rotational parameters of swimming *vibrio alginolyticus* cells were simultaneously measured by laser dark-field microscopy by Magariyama *et al* [27]. They observed intensity signals when cells swim through a laser beam, where the intensity corresponds to the body and flagella bundle rotation rates [27]. More recently Turner *et al* used a high

speed imaging camera to visualize fluorescently stained *E. coli* cells which were stuck to a glass surfaces. Using video frame-by-frame analysis they derived the body rotation rate Ω = 24 ± 12 Hz and the bundle rate ω = 130 ± 40 Hz [29]. These values are consistent with Chattopadhyay *et al*, who used optical tweezers to extract the rotation frequencies of smooth swimming *E. coli* cells, implying the rotational frequencies have a linear dependence on cell body length [28]. These methods of extracting the rotational swimming parameters require single cell measurements, which is often time consuming and requires invasive techniques (fluorescent staining, using a laser, and artificial flow simulating run behaviour). The technique we used does not require a laser or fluorescent labelling and therefore non-invasive. This novel dark-field technique can extract the average rotation of larger number of cell (10^3 - 10^5) extremely quickly. The following section discusses details on how this method works and the results obtained for wild-type and filamentous *E. coli* cells. The combination of dark-field microscopy and high speed acquisition rates between 500 – 1000 fps makes it possible to extract motility parameters from short movie clips. This method can be used to extract the body rotation rate (Ω), the rotation rate of the flagella bundle (ω), and average swimming velocity (v) either near an interface or in fluid bulk. Previous measurements of v, ω and Ω are based on single cell measurements or particle tracking [11, 27, 28], where significant heterogeneities among different individual cells were observed despite incubation from a single colony [28]. The advantage of using high frame rates and dark-field microscopy enables one to extract Ω, ω and v for a larger population of cells ~ 5×10^3 in a single measurement, greatly enhancing current statistics. Individual measurements are typically time consuming whereas this method only requires a short video clip lasting ~ 10 s.

This dark-field technique considers swimming bacteria as a simple phase object in dark-field; the bacterium alters the amplitude of the incident wavefronts, and imposes a phase delay determined by the apparent optical thickness $\Delta\phi$, *Figure5.16,* see references [33] for details. For wild-type *E. coli* the cell body is considered as a prolate spheroid with a minor semiaxis a and a major semiaxis b, where flagella

bundle forms at the rear of the cells, *Figure.5.16*. During a run the major semiaxis *b* rotates about the swimming axis in the direction of $\vec{v}$ at an angle of α relative to the focal plane. The observed rotation about the swimming direction $\vec{v}$ is visualized as a '*wobbling*' motion[6], typical wobble angle are measured as 46 º ± 24 [29]. Here the optical thickness of the cell body $\Delta\phi$ is defined as vertical distance in the z plane multiplied by the refractive index of the bacterium. In dark-field microscopy the apparent intensity of the bacterium is proportional to optical thickness $\Delta\phi$. As the bacterium wobbles/revolves about the swimming direction $\vec{v}$ the optical thickness $\Delta\phi$ varies periodically, thus the observed intensity changes periodically (sinusoidal intensity fluctuation). It is precisely the changing angle of the bacterium α as it wobbles which is responsible for periodic intensity fluctuations, hence swimming cells appear to flash. The observed intensity fluctuations are periodic and have two frequency components. Principally the cell body rotation Ω corresponding to a frequency f_{body} ~ 20 Hz and a second less pronounced component from the flagella bundle rotation ω corresponding to f_{flag} ~ 100 Hz due to residual processional effects of the flagella on the cell body rotation. Thus the average body and flagella rotation rates are extracted for large number of cells ~ 5×10^3 freely swimming near the surface[7]. Cells which swims with a α angle smaller than 23 ° of the focus plane will produce a predominate first order frequency and also a second order harmonic frequency as the cell wobbles in and out of the focus plane. However this effect only occurs in a small percentage of cells within in the population, which may be linked to peak boarding effects, *Figure.5.22*.

[6] Due to asymmetric distribution of flagella motors, the flagella bundle often coalesces slightly off the main cell body axis causing the wobbling motion.

[7] Typically dark-field measurement was conducted near the bottom interface ~ 2 µm.

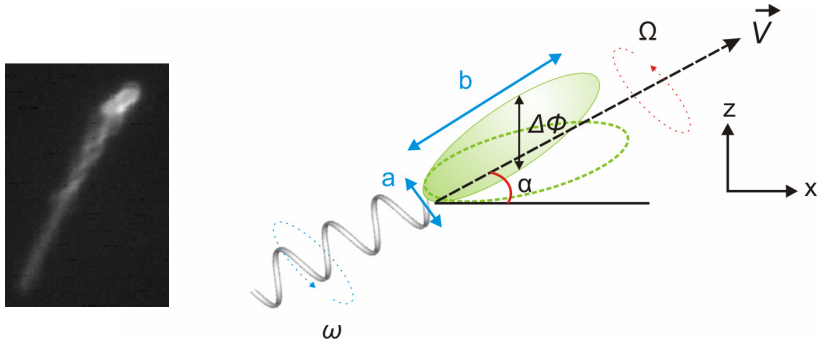

Figure.5.16: Simplified schematic representation of a swimming bacterium; a and b are dimension of the spheroid, where $\Delta\phi$ is the apparent optical thickness which is a function of α, the angle relative to the to the swimming direction and focal plane. Ω and ω are the body and bundle rotation rate respectively. Inset is a fluorescently stained swimming E. coli cell.

10 s videos clips were record at 500 fps at a resolution of 1280 × 640 pixels which corresponds to a sample area of approximately 960 µm × 480 µm. In a typical image there are approximately 5×10^3 cells with videos clips recorded in the centre of the sample. *Figure.5.17* shows a typical frame of cephalexin treated cells ~ 6 µm in length; where the cell concentration is slightly higher at the centre of the sample which later becomes uniform as cells disperse toward the peripheries of the drop.

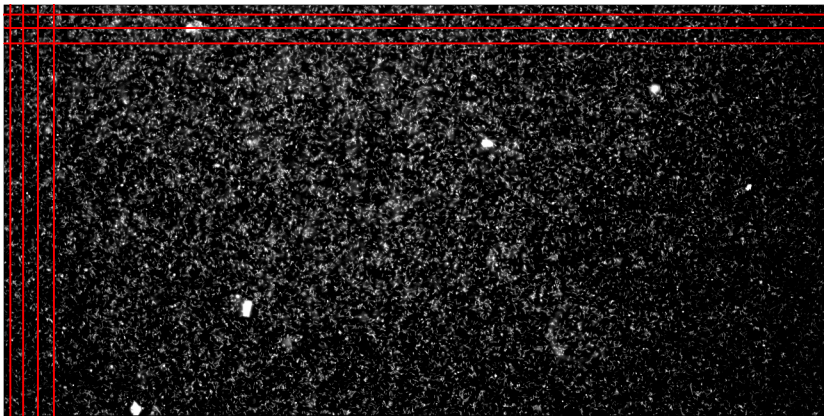

Figure.5.17: A typical dark-field frame taken from a 10 second video used to extract the body and flagella rotation rates. The bacteria appear as bright features on a dark background, where the intensity of bacteria periodically changes (flashes). The red lines indicate the tiling method used to analyze frames, where the entire image is divided into tiles and the intensity of each tile is measured discussed in text below. The larger bright specks are dirt particles in the imaging plane and not in the sample.

Videos were analyzed using an in house program written in LabVIEW[8] by Dr. L. Wilson. The program analyzes the dark-field movies by firstly converting the movie clip into an 8 bit grey scale image (0 - 255). Each frame is then divided into an integer number of square tiles of side length *l, Figure.5.17.* The tiles size is set to accommodate the length of the bacterium, (typically 5 pixels for normal dividing cells and the side length *l* was increased for filamentous cells accordingly). *Figure.5.19* demonstrates the effects of varying the tile sized *l* discussed later. The pixel intensity values in each tile are summed to provide a single intensity value for that particular tile, this was performed for every tile in that frame, which distils (condenses) individual pixel values into single tile values for each frame. The process was conducted for every tile in every frame of the video, thus acquiring the intensity as a function of time for each tile in the frame. The intensity fluctuate over a series of frames is obtained, i.e. extracting I_t(t), the intensity *I* for given tile as a function of time *t*. Thus the power spectrum $\left|FT\left[I_t(t)\right]\right|^2$ where *FT* is the fourier transform, is calculated from the intensity fluctuation as a function of time I_t(t) for each tile separately. The acquired power spectra in each tile is relatively noisy. To reduce noise the power spectra is averaged over every tile and over the entire video sequence increasing the signal to noise ratio and dramatically increasing the statistics, see [41] for details.

Figure.5.18 (a) Shows the results obtained from a calibration experiment[9] whereby actively swimming bacteria (normal dividing *E. coli* cells HCB1), non-motile bacteria (heat treated cells at 60 ° C for 30 minutes) and camera noise (without samples, displaying frequency independent white noise) were examined. The green curve corresponds to non-motile cells demonstrating a characteristic power spectrum of diffusing particles similar to those of passive colloids. The red curve illustrates

[8] LabView program was written by Dr L. Wilson, University of Edinburgh whom the author of this thesis is grateful for, see reference for details [41].

[9] The calibration graph was plotted by Dr L Wilson where he obtained the data for non-motile bacteria and camera noise, where the author supplied the data for motile bacteria using the dark field method.

motile cells, where the curve retains three distinct peaks in the power spectrum. These peaks become more obvious when the power spectrum is scaled by multiplying by frequency squared, f^2 i.e. removing the Brownian component, *Figure.5.18 (b).*

The peaks in the power spectrum where fitted to a log-normal distribution, where peak frequency is extracted as 0.7 Hz, 18.1 Hz and 105 Hz. The latter frequency corresponds to flagella bundle rotation rate; whereas the former frequency 2 frequencies correspond to the velocity coefficient and body rotation rate respectively. By extracting the velocity coefficient, it enables us to determine the average velocity of cells travels as they travel through a given tile size, see reference [40] for details. These measurements were in good agreement with previous experimental results [29, 30]. The same experimental data was analyzed using a range of tile sizes in order to observe their effects. By increasing the tile size the amplitude (intensity) of the raw power spectrum is shifted to a greater power [41]. However, varying the tiles does not vary the location of the observed peak values shown in *Figure5.19,* thus the measured frequencies are independent of tile size [41]. This is important when observing filamentous cells, since the cell length increases, thus tile size used to analyse the frames was increased accordingly to accommodate the entire cell, and this did not vary the pronounced peak frequency.

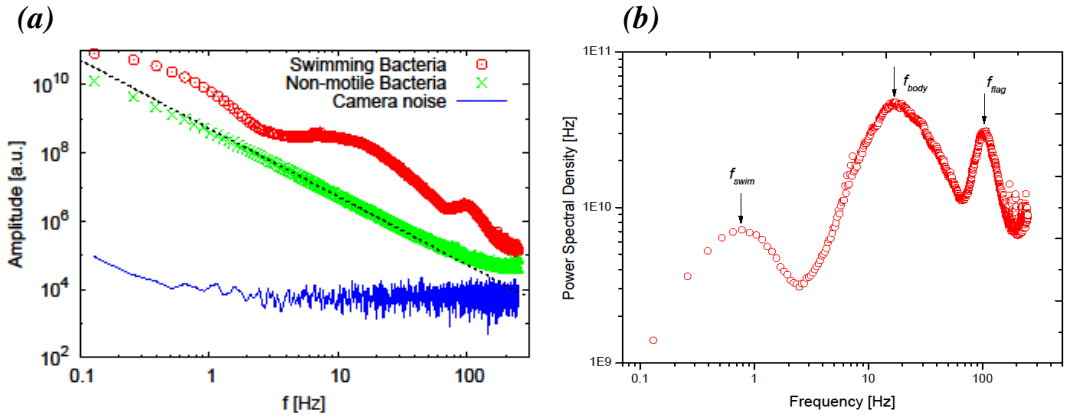

Figure.5.18: (a) The raw power spectra from motile cells, non-motile cells and camera noise; where the dashed line is the predicted Brownian contribution with a f^{-2} scaling to the observed signal, showing an excellent agreement for more than a decade. Beyond 200Hz the camera noise is observed in the signals and at very low frequencies where larger angular displacements are observed. (b) Data acquired from motile bacteria where the Brownian contribution is removed, scaled by f^2. By fitting of the three peaks with a log-normal distribution, the peaks yielded values of 0.73 Hz, 18.1 Hz and 105 Hz respectively. The latter two peaks correspond to the body Ω and flagella rotation ω.

Figure.5.19 (a) reports raw data acquired from a sample of *E .coli* cells incubated for 3 hours in cephalexin, where the average cell length was extracted as 5.7 ± 1.1 µm by measuring cells in bright-field with 60 × magnification lens. The red curve illustrates the tile size of 5 µm approximately the same size of the bacterium. The subsequent curves show the effects of increasing the tile size from 5 - 30 µm in increments of 5 µm. This showed that the curves are systematically shifted to higher power spectral density values, however the peak values are the same. *Figure.5.19 (b)* illustrates the normalization of curves illustrating curves collapse very well. Note with larger tile sizes we find that the results become slightly noisier; however the angular rotation rates of the cell body Ω and the flagella bundle *ω* remain unchanged with increased tile size. Since we were only interested in extracting the body and flagella rotation rates, we therefore neglect the first peak at low frequencies corresponding to a swimming velocity coefficient, where the average swimming velocity can be obtained [41].

(a) **(b)**

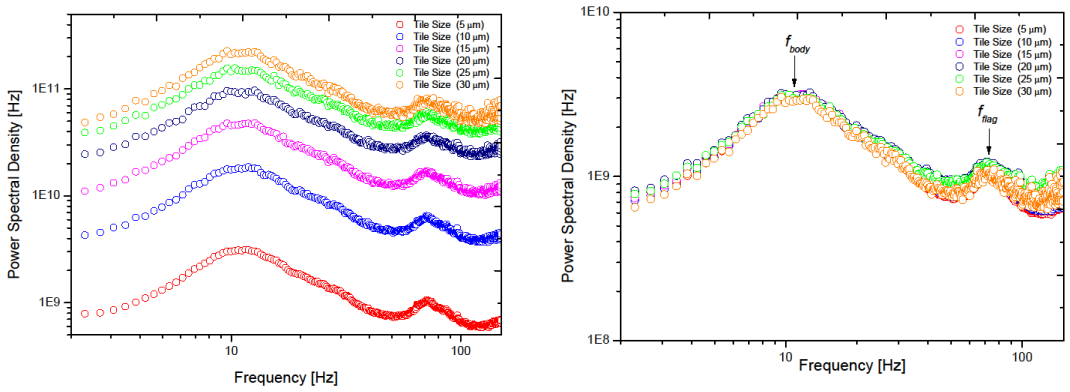

Figure.5.19: (a) Power spectrum density reading of E. coli cells administrated with cephalexin for 3 hours, where the average cell length in the sample was 5.7 ± 1.1 μm. The same data was analyzed using increased tile sizes. (b) The same results which have been normalized where the data collapses well, thus the peak values do not change.

The dark-field method was used to extract the body frequency f_{body} and the flagella frequency f_{flag}, corresponding to the body rotation Ω and flagella bundle rotation ω by fitting the peak values. Acquiring the power spectrum and extracting rotational parameters was conducted for several samples at hourly administration intervals of cephalexin, *Figure.5.22* discussed later. Administration of cephalexin inhibits cell division, but different cells in their growth cycle leading to heterogeneities in their length distribution, typically a range of lengths is observed. Dark-field recording utilized a × 10 objective (has a low N.A. for dark-field), determining the cell length accurately is challenging with low magnification. Thus a × 60 objective lens was used in bright-field to capture swimming cells sequentially on an independent camera. This enables us to determine the average length of the cells in the dark-field recordings accurately, where cells measured in bright-field are also present in dark-field videos. We extracted the average cell length for 100 individual cells in each sample and statistically analysed the data. Histograms where plotted and fitted with either a log-natural curve or Gaussian shown in, *Figure.5.20.*

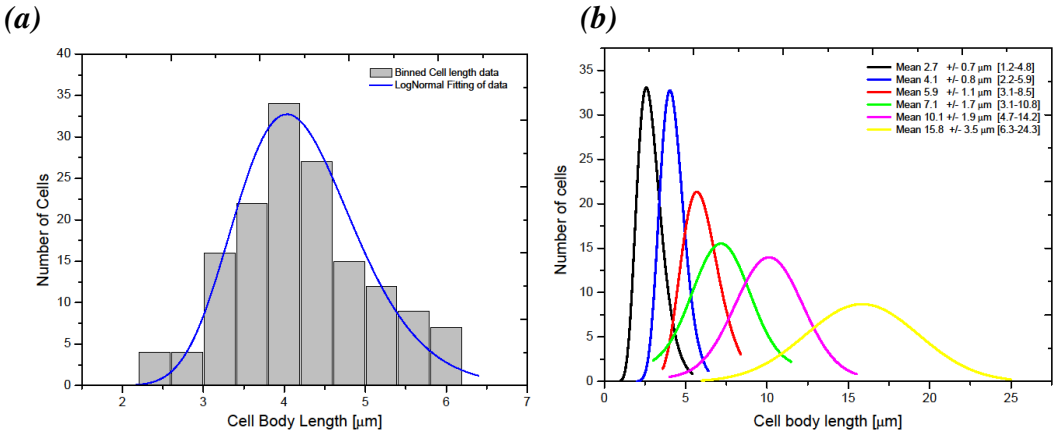

Figure.5.20: (a) Histogram of the cell body length for E. coli cells incubated for 2 hours with cephalexin. The blue curve is a good fit to a log-natural curve. The peak value was extracted as the mean length, and range was recorded i.e. longest and shortest cells observed in the sample. (b) Graph of the fitted histogram hourly samples, where the black curve is for wild-type cells with no antibiotics administrated, and the other curves are a function of administration time. The later curves are fitted with a Gaussian, while the former three curves are fitted with a log-normal.

Figure.5.20 (b) shows the fitted histograms initially show a log-normal fitted as expected [34], however by increasing the administration period the graph systematically shifts, and fits well to a Gaussian distribution. This is because a larger range of cell lengths is observed with longer administration periods, due to different growth stages, *Figure.5.21* illustrates representative images obtained in dark-field at various times. Since there is a larger possible range of cell lengths the peak frequency values becomes less pronounced when analysing the power spectrum. The peak values of the fitted curves in *Figure.5.20* are considered as the average cell length in each sample. These cell lengths correspond directly to the average cell lengths in dark-field recordings. The videos were analysed as described above and the average of three movies clips at different locations in the sample were measured and analyzed, and the average normalized power spectrum was obtained for each sample. By normalizing the power spectrum with the high frequency noise, the power spectrum collapse to respective values; where the two peak frequencies where fitted with a log-normal fit to determine peak frequencies, illustrated in, *Figure.5.22* and *Figure.5.23.*

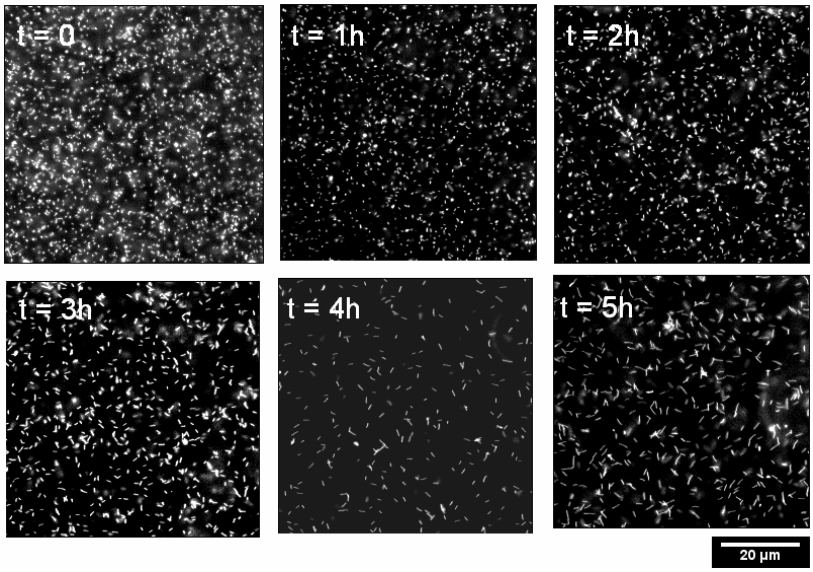

Figure.5.21: Snap-shot of cells imaged in dark-field microscopy at various times of antibiotic administration. t = 0 hr are wild-type cells, where in each micrograph the cell length becomes progressively longer. Cell wobbling was also apparent in longer cells, where the observed intensity varied periodically like the wild-type cell.

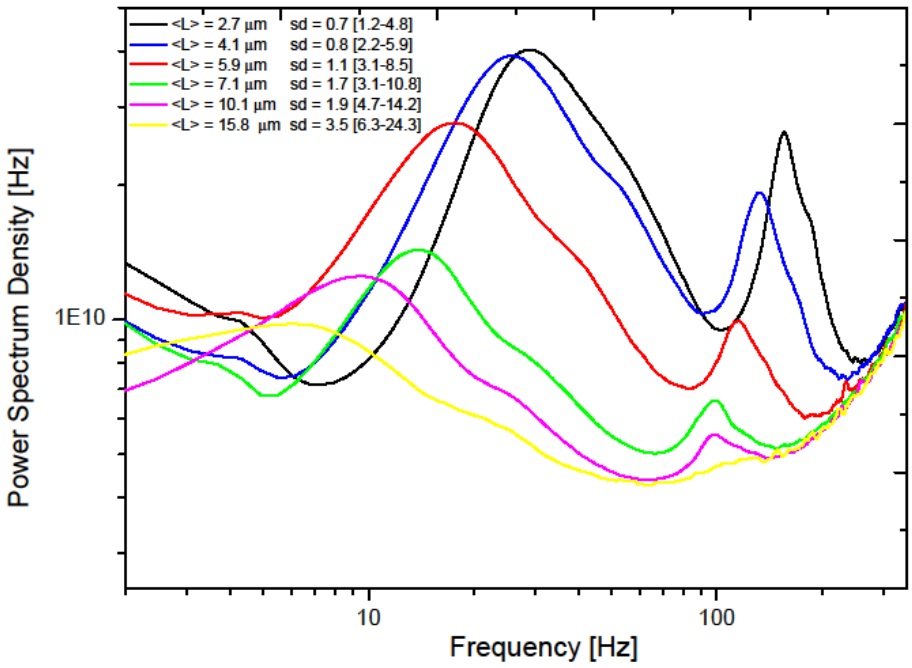

Figure.5.22: Shows the average scaled power spectrum (multiplied by f^2) which has been normalized. Normalization is required because each sample has a varying number of cells thus the intensity in each image varies; however the predominant frequency peaks are not shifted. Black curve represents wild-type cells and the subsequent curves correspond to the average increasing cell length <L>. The trend illustrates that the both body and flagella frequencies decrease with length L. Moreover the signal to noise ratio also decreases as a function of length.

Figure.5.22 shows the normalized power spectrum as a function of average cell length <*L*>. The results show both peak frequencies decrease as a function of increasing length *L*. The results also indicate that power spectrum density value decreases as a function of average length. The yellow curve (longest cells and largest cell distribution) highlights that the flagella peak frequencies are very small due to insufficient signal to noise signal ratio. This is primarily due to a broad range of cell lengths rotating at various frequencies, thus a single defining peak frequency becomes broadened and a single frequency becomes less apparent. Typically working with biological samples there are heterogeneities, where cell lengths and body rotation rates vary somewhat, therefore we measured a range of frequencies leading to peak broadening; however, the predominate peak frequency remains unchanged. *Figure.5.23* demonstrates the fitting of the peaks where the average body and flagella rotation rates were extracted for given <*L*>.

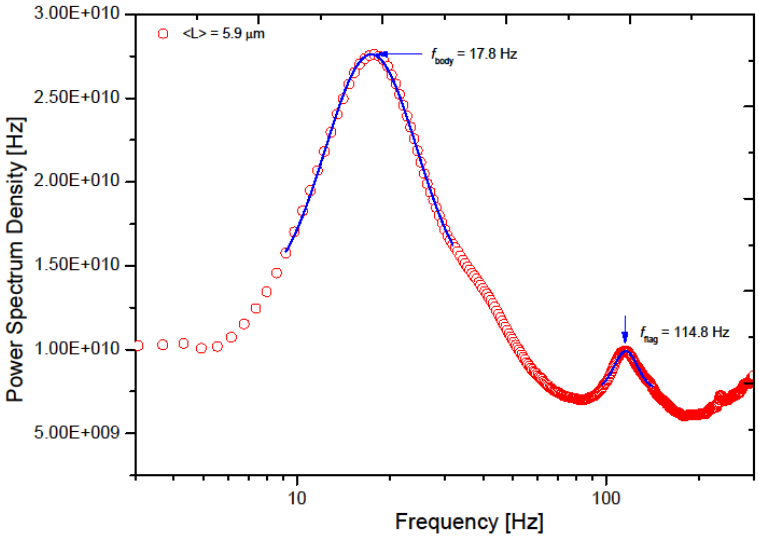

Figure.5.23: A log-linear plot of the data for average cell lengths <L> = 5.9 µm which has fitted to a log-normal distribution for both peak. The results show good fits to a log-normal distribution yielding peak values of f_{body} = 17.8 Hz and f_{flag} = 14.8 Hz.

The same fitting procedure was performed on all acquired power spectra extracting the peak frequencies at various cell lengths <*L*>, data presented in *Table.5.2.*

Table.5.2

	Length (μm)	f_{body} ***(Hz)***	Ω ***(rads^{-1})***	f_{flag} ***(Hz)***	ω ***(rads^{-1})***
(Wild-type)	2.7 ± 0.7	27.8 ± 1.8	174.7 ± 11.5	155.9 ± 2.4	979.8 ± 15.5
	4.1 ± 0.8	23.8 ± 2.4	149.5 ± 15.2	132.0 ± 3.0	829.6 ± 19.2
	5.9 ± 1.1	17.8 ± 2.2	111.8 ± 14.0	114.8 ± 3.2	721.4 ± 20.1
	7.1 ± 1.7	14.1 ± 2.3	88.6 ± 14.4	97.0 ± 2.6	609.5 ± 17.5
	10.1 ± 1.9	9.8 ± 2.7	61.6 ± 16.8	95.2 ± 2.8	597.8 ± 17.5
	15.8 ± 3.5	6.7 ± 2.7	42.1 ± 16.8	89.9 ± 3.8	565.4 ± 24.3

Table.5.2: The extracted peak values of the power spectrum for dark field measurements, where on average 5×10^3 cells where measured. The measured frequencies correspond to the angular velocities of the cell body $\Omega = 2\pi f_{body}$ and the flagella bundle rotation rate $\omega = 2\pi f_{flag}$.

The extracted body and flagella rotation rates for wild-type cells are in excellent agreement to measurements found in the literature [10, 27, 28, 29], with approximate values of $f_{body} \approx 20Hz$ and $f_{flag} \approx 100Hz$ respectively. Our results are consistent with both Turner *et al* [29] and Chattopadhyay *et al* [28]. The dark-field technique can analyse larger number cells (5×10^3) simultaneously, non-invasively and it is extremely fast. We present the results of the body rotation rate Ω and flagella bundle rotation rate ω extracted from of 5×10^3 cells, which decreases reasonably sharply as a function of body length *L*.

In summary this experiment illustrates use of dark-field microscopy and high speed imaging to determine the body and flagella bundle rotation rates of numerous cells. This method takes advantage of the intrinsic wobbling of the cell body, where in dark-field the intensity of the bacterium fluctuates periodically as the cell body revolves about the swimming axis. The average power spectrum was extracted and the peak values were fitted to obtain the average rotation rates. The disadvantage of this technique is that it requires a low numerical aperture objective lens typical of low magnification lens (× 10), where measuring the length of individual cells accurately is challenging. The yielded results for wild-type cells are consistent with previous measurements using different experimental techniques. By administrating

cephalexin (60µg/ml) the average cell body length <*L*> increases, and subsequently our results show both the average body and flagella bundle rotation rate decreases as a function of <*L*>.

5.6 Summary of experimental results

The experimental results acquired from investigating motility in filamentous *E. coli* cells are summarized in *Table.5.3*. The acquired data set now enables one to model the swimming of filamentous cells and to verify if the Purcell's model is applicable to filamentous cells.

Table.5.3

Length (µm)	***v (μms^{-1})***	***No° flagella (n) per cell***	**Ω ($rads^{-1}$)**	**ω ($rads^{-1}$)**	***No° of bundles per cell***
2.7	27.1	5.4	174.7	979.8	1
4.1	25.9	7.0	149.5	829.6	1.5
5.9	25.0	8.8	111.8	721.4	2
7.1	23.2	9.7	88.6	609.5	3
10.1	22.0	11.5	61.6	597.8	4
15.8	18.9	13.8	42.1	565.4	5

Table.5.3: Experimentally measured parameters for describing motility in filamentous E. coli cells. These values are the average measurements for a given average cell length <L>.

We have demonstrated that inhibiting cell division with cephalexin (60 µg/ml) does not alter the growth rate of cells where the doubling time is 35 ± 5.2 minutes, *Figure.5.6.* Filamentous cells retain localized weakening of the cell wall at potential division site, due to the method of inhibiting cell division [4]. Using a high speed camera our results indicates that body rotation is maintained despite significant body elongation; although possible small body deflections may occur which are beyond visual detection. The swimming velocities of these cells decrease subtly as a function of length, *Figure.5.9*, where tumbles events are omitted for cells longer than 6 µm in length. The average swimming velocity of cells longer than 10 µm was

approximately constant (~ 20 μms^{-1}), *Figure.5.9.* Our results indicated the separation height above an interface has a negligible effect on the swimming velocity. Fluorescent labelling of cells yielded the average flagella number as a function of length. Initially the number of flagella filaments per unit length appeared to be constant. Beyond three generations the number of flagella filaments increases logarithmically as a function of body length *<L>, Figure.5.14*. Real-time fluorescent flagella imagining depicted flagella bundles are formed at the pole and on the side walls of the cell to sustain motility shown in, *Figure.5.15*. The number of observed bundles is correlated to cell length, and flagella bundles form by hydrodynamic interactions between adjacent flagella filaments. Bundles occasionally form and un-bundle incorporating different flagella filaments at various locations along the cell. The angular rotation rates of the flagella bundle and cell body were extracted using a dark-field microscopy technique and both frequencies decreased as a function of length, *Figure.5.22*. With these experimentally extracted parameters it is possible to model how filamentous cells sustain motility and it can determine whether Purcell's model is capable of describing motility for filamentous cells. Furthermore, this data set is important because it can be used as a starting point for theorists to develop improved models of swimming bacteria.

5.7 A hydrodynamic modelling of swimming filamentous cells

This section attempts to fit the above experimentally measured parameters in *Table.5.3* to the existing Purcell model [35, 42], discussed in *Chapter 3*. We discuss whether Purcell's model is able to describe accurately motility for filamentous cells comparing the parameters F, N, Ω, ω and v. We explore whether if scaling the RFT coefficients A, B, and D in the Purcell model is able to predict accurately the experimentally measured values. Thus we compare the experimentally extracted results for filamentous cells, to values which have been theoretically calculated using the scaled Purcell's model.

Let's consider Purcell's model [35, 42] *Chapter 3*, the cell body is represented as a passive spheroid and the flagella bundle is simplified as a single rotating helix generating forward thrust, *Figure.3.5*. The model assumes a swimming bacterium is force and torque free [35, 42], such that the total torque of the flagella motor N_{fl} and the rotational viscous drag of the body directly balance. This implies that the total torque generated by the flagella bundle is equal to the rotational viscous drag of the cell body, hence $-N_{fl} = D_0\Omega$. Similarly the total thrust force F_{thrust} generated by the flagella bundle and the linear viscous drag of the cell body also directly balance, hence the expression $-F_{thrust} = A_0 v$ [28], *Figure.3.3*. From Purcell's model and the propulsion matrix we obtain the following expression for the thrust force and torque respectively, [28, 35, 42].

$$-F_{thrust} \equiv A_0 v = Av - B\omega, \qquad \text{Eqn.5.1}$$

$$-N_{fl} \equiv D_0\Omega = -Bv + D\omega \qquad \text{Eqn.5.2}$$

$A_0 = 4\pi\eta b/(\ln(2b/a) - (1/2))$ and $D_0 = 16\pi\eta a^2 b/3$ are the linear and rotational drag coefficients [28, 37], where a is minor semiaxis and b is the major semiaxis of the spheroid. The coefficients *A, B,* and *D* can be approximated from resistive force theory as [28]:

$$A = K_n l \frac{1-\beta}{\beta^{1/2}}\left(1 + \gamma_k \frac{\beta}{1-\beta}\right), \qquad \text{Eqn.5.3}$$

$$B = K_n l\left(\frac{\lambda}{2\pi}\right)\frac{1-\beta}{\beta^2}(1-\gamma_k), \qquad \text{Eqn.5.4}$$

$$D = K_n l\left(\frac{\lambda}{2\pi}\right)^2 \frac{1-\beta}{\beta^{1/2}}\left(1 + \gamma_k \frac{1-\beta}{\beta}\right), \qquad \text{Eqn.5.5}$$

where $K_n = \dfrac{8\pi\eta}{(2\ln(c\lambda/r)+1}$, $K_t = \dfrac{4\pi\eta}{(2\ln(c\lambda/r)-1}$ and $\gamma_k = \dfrac{K_t}{K_n}$

Here K_n and K_t is the longitudinal and transvers drag coefficients for a cylindrical rod with a defined radius r; and λ is defined as the wavelength of the flagellum, see *Figure.3.4*, *Chapter 3*. The coefficients *A*, *B* and *D* are directly related to shape and size of the helix, where *l* = flagellum length, λ = pitch length, ψ = pitch angle, β = $\cos^2 \psi$, and *r* is the flagella radius, for a flagella bundle r ~ 20 nm consisting of four flagella [28]. Using our acquired flagella parameters from *Table.5.1;* and by assuming the typical pitch angle as ψ = 41 ° determined by Turner *et al* [30], the radius as *r* ~ 20 nm and c as ~ 2.4 which was experimentally determined by Chattopadhyay *et al* [28]. Our calculated values for the coefficients *A, B* and *D* are consistent within errors[10] to the experimental values presented by Chattopadhyay [28]. For comparative purposes we also use the same resistive force coefficients *A, B* and *D* as Chattopadhyay *et al* which were also used by Darnton *et al* [28, 29]. The resistive force coefficients used are as follows: $A = 1.48 \pm 0.04 \times 10^{-8}$ N·s·m, $B = 7.9 \pm 0.2 \times 10^{-16}$ N·s and $D = 7.0 \pm 0.1 \times 10^{-22}$ N·s·m [28].

From the expressions Eqn.5.1 and Eqn.5.2 one can theoretically derive expressions for Ω, ω and *v*. These expressions are derived with respect to torque, N_{fl} since it is a fundamental characterization parameter in the Purcell model; where experiments have demonstrated that the torque of each flagella motor below the keen frequency remains constant [10, 26]. The total torque in our model acting on the cell body is equal and opposite in direction to the drag coefficient $D_0(L)$ multiplied by the body rotation rate Ω, and therefore Ω is equal to:

$$\Omega = -\frac{N_{fl}}{D_0} \qquad \text{Eqn.5.6}$$

[10] ~ 13 % differences, primarily due to the differences in flagella length *Table.5.1* which is strongly dependant on growth conditions [30] (Personal correspondence with L. Turner).

To derive an expression for ω, one can rearrange Eqn.5.1 and derive $v = -\frac{B\omega}{(A_0 + A)}$, by substituting into Eqn.5.2 an expression for flagella rotation frequency ω is obtained as:

$$\omega = -\frac{(A + A_0)N_{fl}}{B^2 - D(A + A_0)} \qquad \text{Eqn.5.7}$$

where *A, B*, and *D* are the RFT coefficients, N_{fl} is the calculated torque, and A_0 is the linear drag coefficients. An expression for *v* has already been derived as $v = -\frac{B\omega}{(A_0 + A)}$, however for consistency one can obtain an expression for *v* with respect to torque N_{fl}. Via substituting into Eqn.5.7 we derived the following:

$$v = \frac{BN_{fl}}{B^2 - D(A + A_0)}, \qquad \text{Eqn.5.8}$$

Using Purcell's model and the derived expressions above we can now begin to verify if this model is valid for filamentous cells. Previous reports have demonstrated that Purcell's model for normal sized cells agrees reasonably well with experimentally measured values [28, 29]. However it has been noted that this model predicts a torque value which appears to be smaller than expected[11] [29]. For normal sized cells in our experiments, we expect the Purcell model to hold showing good agreement between the experimental values and the theoretical values. For filamentous cells we know from experiments that there are several flagella bundles, which protrude randomly out of the cell body at a tangent, *Figure.5.15*. To the first approximation we assume each observed bundle is identical, thus having a well defined length *l,* and it generates a given thrust and torque. Since each flagella bundle is identical with the same RFT coefficients, as a very crude approximation we can model filamentous cells with a single effective elongated bundle at the rear of the

[11] This discrepancy is believed to be caused by an oversimplification of resistive force theory.

cell for simplicity, *Figure.5.24*. This model simplifies the complex swimming mechanism somewhat (neglecting the additional drag and torque cancellation), where each observed bundle is combined into a single effective bundle with the same pitch length and thickness. Although modelling filamentous cells with a single effective bundle is not what is observed experimentally, we are simply making adaptations (proportional scaling) to the Purcell's model in order to determine whether this model can be used to describe motility filamentous cells as an initially starting point.

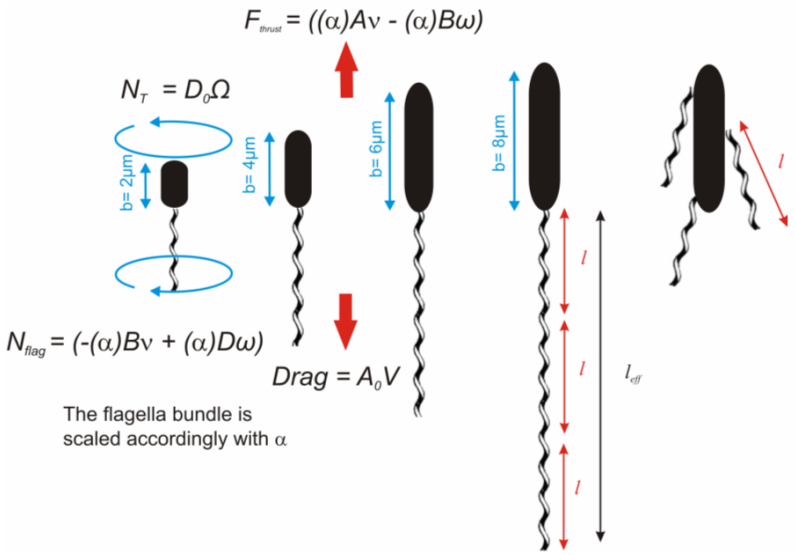

Figure.5.24: A schematic diagram which shows how we model and scale the RFT coefficients A, B and D which essentially scales the length of the flagella bundle l, accordingly since A, B, and D are flagella length dependant. We model multiple separate bundles as a combined single effective elongated bundle with the same pitch and thickness.

Since the thickness and pitch length of the effective bundle is fixed we only change one variable, the effective bundle length *l*. By adjusting the effective bundle length *l* essentially scales the RFT coefficients *A, B,* and *D,* since these coefficients are length dependant Eqn.5.3 - Eqn.5.5. Using the derived expressions for *F*, *N*, Ω, ω and *v* (above) we scale the RFT coefficients by factor of α, to fit the theoretically determined values to the experimentally acquired data. By using the same scaling factor α for *A, B,* and *D* we minimize the adjustment parameters, and only adjust the length *l* of the effective bundle in this scaled Purcell's model, hence *Figure.5.24*. We expect the scaling factor α to increase as a function of cell body length due to

the additional and increase of the linear and rotation viscous drag of the cell body, therefore the helix is required to generate a larger thrust and torque to sustain a constant swimming velocity as observed in *Figure.5.9*. If the scaling factor α does not increase with body length, we essentially fix the length of the flagella bundle and limit the amount of thrust the flagellum can produce. Fitting the theoretical values to the experimental data was conducted by adjusting the scaling factor α to obtain the best fit (within experimental errors) for the parameters *F*, *N*, Ω, ω and *v* simultaneously as a function of body length. By fitting the parameters *F*, *N*, Ω, ω and *v* simultaneously, the optimal scaling factor α for the scaled Purcell's model was determined. The required scaling factor α is presented in, *Table.5.4* with the corresponding scaled values of *A, B* and *D*.

Table.5.4

Length (μm)	***No° of bundles (Per cell)***	***Scale factor (α)***	***α (L) A (N·s·m)***	***α (L)B (N·s)***	***α (L) D (N·s·m)***
2.7	1	1	1.48×10^{-8}	7.90×10^{-16}	7.00×10^{-22}
4.1	1.5	1.64	2.44×10^{-8}	1.30×10^{-16}	1.16×10^{-21}
5.9	2	2.36	3.49×10^{-8}	1.86×10^{-16}	1.65×10^{-21}
7.1	3	3.10	4.59×10^{-8}	2.45×10^{-16}	2.17×10^{-21}
10.1	4	3.40	5.03×10^{-8}	2.69×10^{-16}	2.38×10^{-21}
15.8	5	4.60	6.81×10^{-8}	3.63×10^{-16}	3.22×10^{-21}

Table.5.4: Shows the acquired scaling factor α by fitting the graphs F, N, Ω, ω and v. It shows the corresponding values of the RFT coefficients as a function of length when scaled by α. The numbers of observed flagella bundles are presented for comparison purposes.

Table.5.4 shows that the required scaling factor α increases linearly with respect to the cell body length *L*, as expected. The scaling factor yielded from fitting the theoretical values to the experimental values is very similar to the number of flagella bundles in filamentous cells, *Table.5.3*. Comparing the scaling factor α to the number of observed bundles yielded a maximum discrepancy of ~ 15 %, shown in *Figure.5.25*.

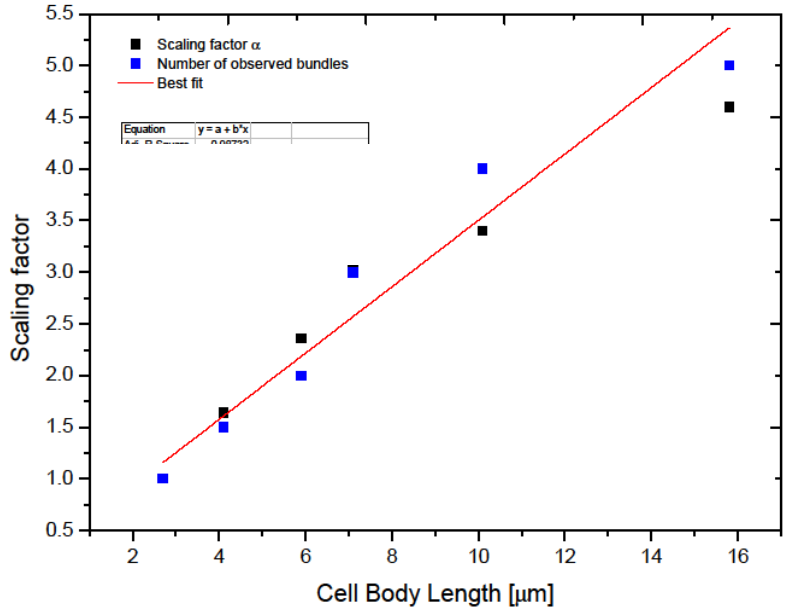

Figure.5.25: Shows the scaling factor α (black points) versus the number of observed flagella bundles (blue points) as a function of length. The scale factor increases approximately linearly with cell body length L, with an estimated gradient of 0.32.

Generally the scaling factor α is consistent with the number of observed flagella bundles demonstrating a linear trend, with an average gradient of 0.32. However for longer cells ≥ 6 μm the scaling factor α deviates from the number of bundles. Using the scaled RFT coefficients and the derived theoretical equations for F, N, Ω, ω and v, we examined how well the scaled Purcell's model, *Figure.5.24* agrees with experimental data. Thus determining whether Purcell's model is applicable to filamentous cells; the parameters F, N, Ω, ω and v must collectively be consistent with the experimental data if the model is to be valid. Considering the results from the scaled Purcell mode, we initially examined the total thrust force F and the total torque N with respect to the experimental results as a function of L, *Figure.5.26*.

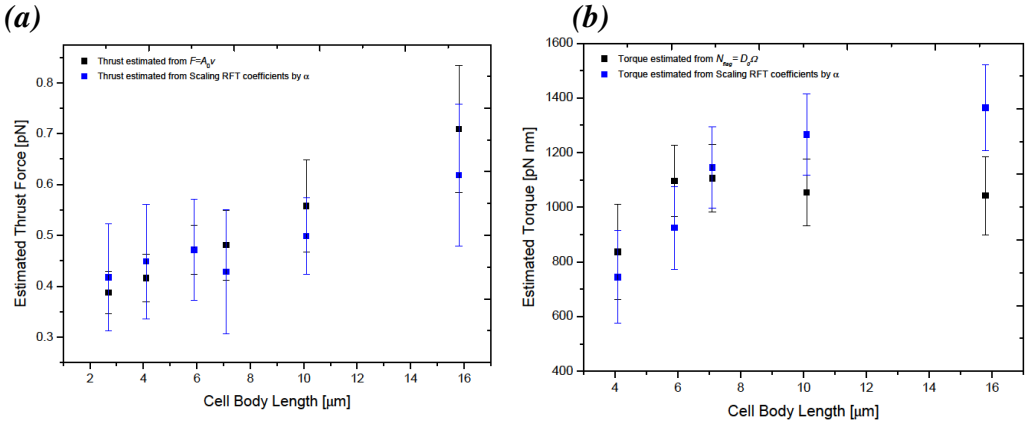

Figure.5.26: (a) The experimentally calculated thrust force $F_{thrust} = A_0(L)v$ *as a function of length (black points) versus the theoretically scaled thrust force* $-F_{thrust} = \alpha(L)Av - \alpha(L)B\omega$ *(blue points). (b) The experimentally calculated torque from* $N_{fl} = D_0(L)\Omega$ *(black points) versus the theoretically estimated torque* $N_{fl} = -\alpha(L)Bv - \alpha(L)D\omega$ *as a function of length.*

From *Figure.5.26 (a)* the thrust force is calculated in by two methods either experimentally using $F_{thrust} = A_0(L)v$ where we measured the swimming velocity v and multiple by the drag coefficient A_0. The theoretical thrust force is determined by the scaled Purcell's model, recall Eqn.5.1; where we used the measured values of v and ω (from Table.5.3). Similarly, the experimental values of the torque is calculated by using $N_{fl} = D_0(L)\Omega$, where we used the measured values of Ω. The theoretical torque values was extracted using the expression $N_{fl} = -\alpha(L)Bv - \alpha(L)D\omega$ derived from Purcell's model, again using the measured values of v and ω. The results determined by scaling Purcell's model depicts a good agreement with the experimental results for filamentous cells, within the majority of the error bars. The theoretical results for both thrust and torque (blue points) yielded consistent trends to the experimental data as a function of body length *L*. For normal size cells 2.7 μm we obtained a theoretical thrust force of 0.41 ± 0.1 pN, in good agreement to the experimental value of 0.38 ± 0.04 pN, also consistent with values presented by Chattopadhyay *et al*, 0.57 pN [28] and Darnton *et al*, 0.25 - 0.85

pN [29] as expected. For filamentous cells the experimental thrust force increases approximately linearly, and the predicted values from the scaled Purcell's model also illustrates a similar trend, depicting good agreement with the experimental values.

Figure.5.26 (b) illustrates the total torque for normal sized cells obtained theoretically yielding a value of 743 ± 169 pN·nm, consistent with the experimental value of 835 ± 174 pN·nm; and with previous reports [28, 29]. For filamentous cells the scale model, $N_{fl} = -\alpha(L)Bv - \alpha(L)D\omega$ predicts values which are in excellent agreement to the experiment data up to ~ 10 μm in cell length. Beyond 10 μm, the predicted torque values begin to deviate slightly, where the last data point is just outside the errors bars. The experimental values for torque are in fact an underestimate, since in this model we only consider the rotational drag coefficient of the body $D_0(L)$, which neglects the additional drag caused by protruding flagella filaments. This effect is more predominate in longer cells as they have more flagella filaments. By considering this oversimplification we may find a better agreement with the experimental data. The results from the thrust and torque graphs, *Figure.5.26* already suggest that the scaled Purcell's model is adequate for describing motility in filamentous cells, demonstrated by the good agreement between experimental and the predicted values.

To further verify that the scaled Purcell's model is accurate we examined how accurately the model predicts Ω, ω and v as a function of length. If the scaled model is valid then the predicted values of Ω, ω and v should all be consistent with the experimental values. From the expressions in Eqn.5.6 - Eqn.5.8 we calculated Ω, ω and v with the scaled RFT coefficients. *Figure.5.27* below shows the comparison between the theoretical values versus the experimentally extracted values as a function of length L.

(a)

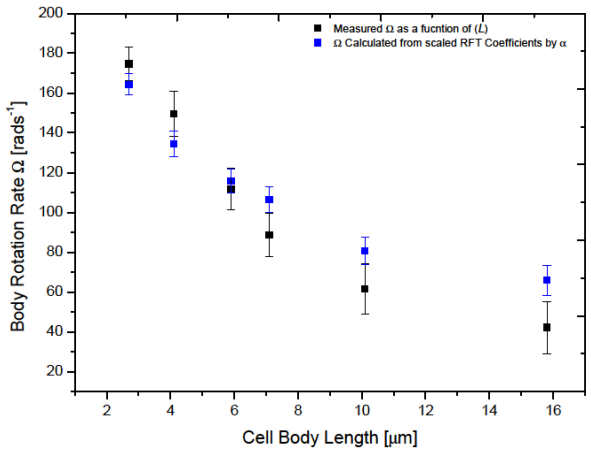

(b)

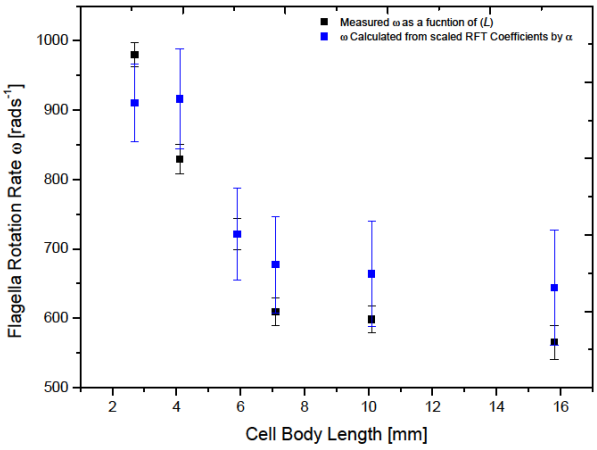

(c)

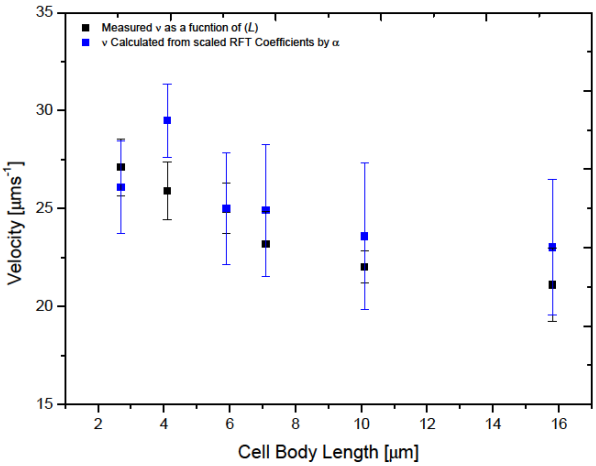

Figure.5.27: Shows the experimental measured parameters Ω, ω and v (black points) as a function of body length L versus the values predicted from the scaled Purcell's model (blue points). (a) Shows Ω as function of body length with an excellent agreement, illustrating similar trend. (b) Shows ω as function of length showing reasonable agreement, although the trend deviates for longer cells but

within the errors. (c) Shows v as a function of length where we also obtain a reasonably good fit.

Figure.5.27 shows for normal sized cells the data points in each graph all agree within the experimental errors as expected. This demonstrates for normal sized cells the Purcell's model can predict the experimentally measured parameters F, N, Ω, ω and v, accurately [28, 29]. *Figure.5.27* shows the results from the scaled Purcell model (blue points) versus the experimentally extracted data (black points). Generally the predicted values of Ω, ω and v as a function of length corresponds with the experimental values, depicting very similar trends. Thus results demonstrate that the scaled Purcell model despite its oversimplifications is also valid for filamentous cells where we do find an experimental and theoretical agreement within the errors. We find that the scaled Purcell's model yields surprisingly good fit to the experimental data, despite being a very simplistic model of how filamentous cells swim. By universal scaling the RFT coefficients *A, B*, and *D* (essentially elongated the flagella bundle) by a factor of $\alpha(L)$, the scaled Purcell model can describe accurately motility in filamentous cells. The scaling factor α is very similar to the number of observed bundles, *Figure.5.25* and by using the scaled RFT coefficients it is possible estimate the average effective bundle length l from equations Eqn.5.3 - Eqn.5.5, *Figure.5.26.* Dividing the effective bundle length by the typical number of observed bundles we obtained the average single bundle length. This yielded an average of 7.5 ± 0.6 μm which seems reasonable and consistent with fluorescent flagella staining experiments, *Table.5.1* as well as previous reports [11, 28, 30]. Hence scaling the RFT coefficients yields realistic flagella bundle lengths l, and this further substantiates the validity of the scaled Purcell's model to describe motility in filamentous cells.

5.8 Discussion

In summary we have independently verified that Purcell's model for normal wild-type cells is capable of describing the swimming parameters F, N, Ω, ω and v within the experimental errors [28, 29]. However there are minor discrepancies with

Purcell's model even for describing normal sized swimming bacterium. For example the model predicts a slightly higher torque value than expected to that of the experimental data points. The discrepancies become more discernable at larger cell lengths, *Figure.5.26 (b)*. These minor discrepancies are due to oversimplifications when modelling swimming flagellated bacteria. Resistive force theory only considers a single rotating helical coil, in actual fact the bundle is comprised of several rotating flagella filaments which causes internal friction. This internal friction between individual filaments in the bundle may lead to a reduction of total torque, which is neglected in resistive force theory [29, 35, 42] hence we observe a discrepancy between the experimental values and the theoretical values. Moreover, the theory also does not consider flagella bundle and cell body interactions which may also explain the higher torque values from the model [29]. Despite these oversights, the model predicts theoretical values which agree with the experimental data.

We used Purcell's model to predict the values of F, N, Ω, ω and v as a function of body length L for filamentous cells, by scaling the RFT coefficients A, B, and D appropriately. Since the RFT coefficients are proportional to l, Eqn.5.3 - Eqn.5.5 this effectively elongates the helical coil, *Figure.5.24,* without varying the thickness or pitch length. The scaled Purcell's model assumes that there is a single effective bundle positioned at the rear of the cell. This scaled Purcell's model is a substantial simplification of the actual swimming mechanism deployed by filamentous cells, where multiple bundles are observed protruding out of the cell body at random locations, *Figure.5.15*. Using the RFT coefficients A, B and D as variable adjustments parameters, the theoretically calculated values for F, N, Ω, ω and v was fitted to the experimentally measured values. From fitting the RFT coefficients we acquired a universal scaling factor α. The RFT scaling factor α increases linearly with cell body length; yielding similar values to the number of observed flagella bundles, *Figure.5.25*.

Using the scaled Purcell model, we theoretically calculated the value of F, N, Ω, ω and v and compared them to the experimental results, *Figure.5.26* and *Figure.5.27*. The result predicted by the scaled model showed a surprisingly good agreement with the experimental data and yields very similar trends. It is quite surprising that we observe such good agreement for a very simple model of how filamentous cells swim. We demonstrate by scaling Purcell's model it can adequately describe motility in filamentous cells predicting similar trends to the experimental data set. The trends for F, N, Ω, ω and v as a function of length predicted by the scaled model deviates slightly from the experimental values. These discrepancies are due to the shortcomings of the scaled Purcell's model used to describe motility in filamentous cells. We assume each observed bundle in filamentous cells are identical (given thickness and pitch length) which enables us to combine bundles into a single effective bundle at the rear of the cell. Observations show flagella bundles are not all identical, which vary in length l and in thickness, incorporating different number of flagella filaments. Ultimately this leads to noticeable discrepancies in estimating the thrust force and torque acting on the cell body which is overlooked in the model. Filamentous cells have multiple flagella bundles randomly located along the cell body, *Figure.5.15*. These bundles which protrude out of the cell body at a tangent generate additional linear and rotational drag. This has a direct consequence on both the total trust force and torque and ultimately varies Ω, ω and v, which was not considered in the model. Modelling multiple bundles which act at a tangent is challenging (also need to consider bundle-bundle interaction and bundle-cell body interactions), and it is not obvious how the torque from each bundle contributes to the total torque acting on the cell body. Since the bundles form on the sides of the cell body randomly, one would expect torque cancellation. This was not considered in the model since the bundle was modelled at the rear of the cell where all the torque is considered to balance the rotation of the cell body. Moreover, the model does not consider the thrust, drag and torque contributions of independently rotating flagella filaments which also play an important role. Despite these shortcomings of the scaled Purcell model, the results demonstrate by scaling the RFT coefficients by approximately the number of flagella bundles which can predict accurately the

swimming parameters F, N, Ω, ω and v for filamentous cells; which is surprising since it is a very basic and simplified model of how cells swim.

5.9 Conclusions

We have demonstrated that incubating cells with β-lactam antibiotics cephelexin, inhibits cell division without affecting the cellular growth rate, which remains uniform. Using a high speed imaging camera we found evidence that rotation rate of cell body continues similar to normal cells, and we found no evidence supporting cellular deflection as an alternative method of generating forward thrust. The observations shows that even with significantly long cells $\leq$ 50 μm, cells remain motile. Tumbles are only observed in relatively short cells ~ 6 μm. The results show cells beyond 6 μm exclusively run, and tumbles are completely omitted. We provide possible explanations why this occurs by flagella staining experiments; where it is believed that when the majority of flagella filaments rotation **CW** then cell stops generating forward thrust. However if only a minority of filaments rotate **CW** it is unlikely to initial cellular tumbling. This is due to the increase in cell body length; for longer cells the bacterium requires a larger torque forces to re- orientate the body. Secondly if the majority of flagella filaments are rotating **CCW** generating forward thrust, then a single filament rotating **CW** has a negligible effect on the majority, thus the cell continues to run. Observing the swimming velocity as a function of length, our results shows that the velocity of filamentous cells remains approximately constant, ~ 20 μms^{-1} even for significantly elongated cells.

By fluorescently labelling cells we extracted the number of flagella as a function of length, which yields a constant number of flagella filaments per unit length for approximately three generations. Beyond this, the number of observed flagella filaments begins to decrease in longer filamentous cells. Fluorescent staining of filamentous cells showed multiple flagella bundles forming on the side walls of the cell, which is the mechanism deployed to sustain motility. We utilized a dark-field

microscopy method to extract the body and flagella bundle rotation rates, where both rotation rates decrease as a function of cell length. Using these experimentally extracted parameters, we attempted to fit the acquired data to the Purcell model of a swimming bacterium. For normal sized cells we obtain reasonable values for *F*, *N*, Ω, ω and *v* which are consistent with experimentally extracted results (within experimental errors) and consistent with previous reports. Scaling the RFT coefficients and using them as adjustable parameters we fitted all the parameters *F*, *N*, Ω, ω and *v* and obtained the scaling factor α. By scaling the Purcell's model by α (i.e. scaling the RFT coefficients) we can explain motility in filamentous cells which shows a reasonably good agreement to the experimental data set, yielding similar trends. This demonstrates simplistic scaling of the Purcell's model is capable of predicting most of the experimental acquired parameters despite being a very simple model. This research has provided an insight into the mechanism which sustains motility in filamentous cells, where our experimental data set can be used by theorists to improve existing models, thus furthering our understating of this complex swimming behaviour deployed by filamentous cells.

Bibliography and References

[1] G. N. Rolinson, *Effect of β-Lactam Antibiotics on Bacterial Cell Growth Rate.* Journal of General Microbiology, **120**: 317-323, (1980).

[2] D. Greenwood and F. O'Grady, *Comparison of the responses of Escherichia coli and Proteus mirabilis of Seven β-Lactam Antibiotics.* Journals of Infectious Diseases, **182**:211-222, (1973).

[3] T. Oka and H. Fujita, *Effect of β-Lactam Antibiotics on In Vitro Peptidoglycan Cross-Linking by a Particulate Fraction from Escherichia coli K-12 and Bacillus megaterium KM.* Antimicrobial Agents and Chemotherapy, **14**:625-627, (1978).

[4] M. A. Pedro, J. Holtje and H. Schwarz, *Fast lysis of Escherichia coli filament cells requires differentiation of potential division sites.* Microbiology, **148**:79-86, (2002).

[5] K. Izaki, M. Matsuhashi, and J. L. Strominger, *Strominger. 1968. Biosynthesis of the peptidoglycan of bacterial cell walls. XIII. Peptidoglycan transpeptidase and D-alanine carboxypeptidase, penicillin sensitive enzymatic reactions in a strain of Escherichia coli.* J. Biol. Chem, **243**:3180-3192, (1967).

[6] T. Oka, *Mode of action of penicillins in vivo and in vitro in Bacillus megaterium.* Antimicrob. Agents. Chemother, **10**:579-591, (1976).
[7] N. Maki, J. E. Gestwicki, E. M. Lake, L. L. Kiessling, and J. Adler, *Motility and Chemotaxis of Filamentous Cells of Escherichia coli.* Journal of Bacteriology, **182**:4337-4342, (2000).
[8] P. Staugaard, F. M. van den Berg, C. L. Woldringh, and N. Nanninga, *Localization of ampicillin-sensitive sites in Escherichia coli by electron microscopy.* J. Bacteriol, **127**:1376-1381, (1976).
[9] A. Tomasz, *The role of autolysins in cell death. In Mode of Action of Antibiotics on Microbial Walls and Membranes*, Edited by M. R. J. Salton & A. Tomasz. New York: The New York Academy of Sciences, pp. 439-447, (1974).
[10] H. C. Berg, *E. coli in Motion,* Biological and Medical Physical Series, Spring Verlag, (2003).
[11] H. C. Berg, *The rotary motor of bacterial flagella,* Annu.Rev.Biochem, **72:**19-54, (2003).
[12] J. S. Parkinson, *cheA, cheB, and cheC Genes of Escherichia coli and Their Role in Chemotaxis.* J Bacteriol, **126**:758–770, (1976).
[13] J. S. Parkinson, *Bacterial Chemotaxis: a New Player in Response Regulator Dephosphorylation.* Journal of Bacteriology, 185:1492-1494, (2003).
[14] J. J Falke *et al*, *The two-component signaling pathway of bacterial chemotaxis: a molecular view of signal transduction by receptors, kinases, and adaptation enzymes.* Annu. Rev. Cell Dev. Biol, **13**:457–512, (1997).
[15] R. E. Silversmith, and R. B. Bourret, *Throwing the switch in bacterial chemotaxis.* Trends. Microbiol, **7**:16–22, (1999).
[16] M. B. Elowitz *et al*, *Protein mobility in the cytoplasm of Escherichia coli.* J. Bacteriol, **181**:197–203, (1999).
[17] J. E. Segall, M. D. Manson, and H. C. Berg, *Signal processing times in bacterial chemotaxis.* Nature, **296**:855–857, (1982).
[18] J. E. Segall, A. Ishihara, and H. C. Berg, *Chemotactic signaling in filamentous cells of Escherichia coli.* J. Bacteriol, 161:51–59, (1985).
[19] S. Aizawa and T. Kubori, *Bacterial flagellation and cell division.* Genes to Cells, **3**:625–634, (1998).
[20] T. Iino, *Assembly of salmonella flagellin in vitro and in vivo.* Journal of Supramolecular Structure, **2**:372-384, (2004).
[21] A. Nishimur and Y. Hirota, *A cell division regulatory mechanism controls the flagellar regulon in Escherichia coli.* Molecular and General Genetics, **216**:340-346, (1989).
[22] A. Nishimura, *A new gene controlling the frequency of cell division per round of DNA replication in Escherichia coli.* Mol Gen Genet, **215**:286-293, (1989).
[23] A. Nishimura, Y. Hirota , *Coordination of flagellar formation and cell division in Escherichia coli.* Annu. Rep. Natl. Inst. Genet. Mishima **32**:31-33, (1981).
[24] A. Samuel, and H. C. *Berg, Fluctuation analysis of rotational speeds of the bacterial flagellar motor. Proc. Natl. Acad. Sci,* **92**:3502–3506, (1995).
[25] R. M. Macnab, *How bacteria assemble flagella.* Annu.rev.microbiol, **57**:77-100, (2003).

[26] X. Chen, H. C. Berg, *Torque-speed relationship of the flagellar rotary motor of Escherichia coli. J. Biophys,* **78**:1036–1041, (2000).
[27] Y. Magariyama *et al*, *Simultaneous measurement of bacterial flagellar rotation rate and swimming speed.* J. Biophys, **69**:2154–2162, (1995).
[28] S. Chattopadhyay, R. Moldovan, C. Yeung, and X. L. Wu, *Swimming efficiency of bacterium Escherichia coli*. Proc. Natl. Acad. Sci, USA, **103**:13712–13717, (2006).
[29] N. C. Darnton, L. Turner, S. Rojevsky, and H. C. Berg, *On Torque and Tumbling in Swimming Escherichia coli,* Journal of bacteriology, **189**:1756–1764, (2007).
[30] L. Turner, W. S. Ryu and H. C. Berg, *Real-time imaging of fluorescent flagellar filaments.* J. Bacteriol, **182**:2793-2801, (2000).
[31] G. Kuwajima, J. Asaka, T. Fujiwara, K. Node, and E. Kondo, *Nucleotide sequence of the hag gene encoding flagellin of Escherichia coli*. J. Bacteriol, **168**: 1479–1483, (1986).
[32] http://www.microscopyu.com
[33] M. Born and E. Wolf, *Principles of Optics* (7th Ed), Cambridge Univ. Press, Cambridge, (1999).
[34] T. Åkerlund *et al*, *Analysis of Cell Size and DNA Content in Exponentially Growing and Stationary-Phase Batch Cultures of Escherichia coli.* Bacteriol. J, **177**: 6791–6797, (1995).
[35] E. M. Purcell, *Life at low Reynolds number.* American Journal of Physics, **45**:3-11 (1977).
[36] J. W. Shaevitz, J. Y. Lee, and D. A. Fletcher, *Spiroplasma Swim by a Processive Change in Body Helicity*, Cell, 122: 941–945, (2005).
[37] E. Lauga and T. R. Powers, *The hydrodynamics of swimming microorganisms.* Rep.Prog.Phys, **72:**096601, (2009).
[38] A. P. Berke, L. Turner, H. C. Berg, and E. Lauga, *Hydrodynamic Attraction of Swimming Microorganisms by Surfaces*. Phys. Rev. Lett, **101**: 038102, (2008).
[39] J. Happel and H. Brenner, *Low Reynolds Number Hydrodynamics.* Springer, New York, 1st Ed, (1981).
[40] J. Narayanan, J.Y. Xiong and X. Y. Liu, *Determination of agarose gel pore size: Absorbance measurements vis a vis other techniques*. Institute of Physics, Publishing Journal of Physics, **28**:83–86, (2006).
[41] L. Wilson, M. Li, J. Schwarz-Linek, V. A. Martinez, J. Arlt and W. Poon, *Darkfield Flicker Microscopy: Measuring Bacterial Swimming at High Speed* (in preparation).
[42] E. M. Purcell*, The efficiency of propulsion by a rotating flagellum*. Proc. Natl. Acad. Sci, USA, **94**:24–29, (1997).
[43] K. A. Fahrner, W. S. Ryu, and H. C. Berg, Bacterial flagellar switching under load. Nature 423:938, (2003).

Chapter 6 : Collective bacterial swimming

6.1 Introduction

This chapter is primarily focused towards research conducted with *B. subtilis* cells[1]; it examines the phenomenon of collective cellular dynamic behaviour. Large number of interacting cells (10^{9} - 10^{12} per ml) exhibit highly organized flocking behaviour, forming distinct patterns and vortices. These dynamically unstable patterns form and disintegrate reminiscent of turbulence; generating much scientific interest over the last decade. This chapter presents experimental research probing existing theories and providing further scientific evidence in support of current hypotheses. We present experiments which provide further insights into mechanism which facilitates collective flocking behaviour. We also introduce and discuss a novel experimental technique for examining collective behaviour in a sustainable monolayer.

Initial experiments utilize concentrated bacterial suspensions of *B. subtilis* cells (YB886) in sessile drop geometry. Observations show collective behaviour occurs near oxygen contact lines; often fluid flow caused by capillary forces and surface tension sterically aligned cells into self-organized domains at the peripheries. Observations illustrate close-packing of cells where steric alignment and hydrodynamic interactions contribute to the onset of collective swimming. An increase of cellular density at oxygen contact line was observed where collective behaviour originates. Time-lapse video microscopy was used to examine the onset

[1] Although there are experimental references to *E. coli (HCB1)* cells when stated, for comparative purposes.

of correlated motion and the role capillary forces. Video analysis highlighted the general phases leading up to the onset of collective behaviour. Over the last decade there have been several articles addressing collective behaviour of *B. subtilis* cells. Surprisingly, there is a lack of empirical data which directly addresses the mechanism of thrust generation, and the run/tumble statistics for swimming *B. subtilis* cells. The general accepted consensus assumes *B. subtilis* is analogous to *E. coli* cells in terms of the mechanism for thrust generation, where a single cohesive flagella bundle is formed. We directly investigate these assumptions by developing an experimental technique to image flagella filaments in real-time for *B. subtilis* cells. This experiment discusses the effects of fluorescent visualization and presents the extracted flagella filament statistics. Subsequently in this chapter it examines the swimming mechanism which yielded unexpected multiple bundle arrangements and evaluates the implications of these novel findings in respect to collective behaviour.

It has been reported that *E. coli* and *B. subtilis* cells reverse swimming direction without body reorientation when confronted by an obstacle. The asymptotic swimming velocities of *forwards* and *backwards* swimming respectively are indistinguishable. It was hypothesised that flagella filaments '*flip*' from one pole to the other during reversal; however flagella were not directly visualized in the study. Flagellum flipping was highlighted as a possible mechanism for facilitating *quorum polarity* and a likely candidate for sustaining collective behaviour in a close packed regime. Advancing this research a similar experiment was conducted, which directly visualize flagella filaments during reversal events for both *E. coli* and *B. subtilis*. Furthermore this chapter presents an investigation on the affects of removing flagella filaments on the reversal behaviour.

Finally this chapter presents research on a novel experimental method of suspending motile bacteria between two hydrophilic coverslips. This permitted excellent quantitative visualization of individual bacterium in the setting of collective behaviour, and is robust against fluid evaporation. Fluorescently labelled *B. subtilis* cells were suspended in a monolayer geometry permitting excellent visualisation of

individual cells and their flagella filaments in the setting of collective behaviour for the first time. This novel research is a significant advancement in understanding collective swimming and provides an insight into flagella interactions during collective swimming. It presents direct visualisation of quorum polarity and evidence to support recruitment of cells into cohesive domains. The combination of 2D geometry and fluorescently labelled cells allows reliable bacterial tracking. Tracking of actively swimming cells was conducted at various cellular concentrations (volume fractions φ), and the mean squared displacement was extracted. A similar experiment was conducted with fluorescent 4 μm diameter tracer particles for a comparative study and the results are discussed in reference to recent computational simulations work.

6.2 Correlated motion/collective swimming behaviour

Correlated motion is regarded as movement of large number of entities which migrate as a cohesive group in a polarized direction. Collective behaviour ranges from flocking birds, migrating bison to schools of fish [1 - 4], consisting of thousands of individuals moving collectively and exhibiting complex cooperative behaviour. This phenomenon can be extended to explain human crowding, panic behaviour in crowds, and even vehicular traffic flow [5, 6]. There are numerous reasons for collective movement amongst individuals; many of which are driven by benefits typical of predation avoidance, collective hunting or sustaining a suitable environment for reproduction [7, 8].

Collective behaviour is also observed at the microscopic level where concentrated self-propelled bacteria exhibit highly organized and large-scale vortices and jets, which are normally absent from passive systems i.e. colloidal suspensions [9 - 15]. In dilute suspensions cellular locomotion is characterized by runs and tumbles; and is regarded as an individual endeavour. But, *what happens when cellular concentration is increased significantly? And how does the run and tumble behaviour change?*

These are the types of questions which have generated much scientific interest, and we attempt to address some of these questions. Collective behaviour in *B. subtilis* is still under intensive study which is believed to be governed by the subtle interplay between buoyancy, hydrodynamic interactions, and mixing [7, 12].

At volume fractions $\varphi > 0.3$ [14], a transition occurs from individual swimming behaviour to non-equilibrium state collective behaviour; characterised by intermittent episodes of structural coherence and disorder [7, 9, 12 - 14], *Figure.6.1*. Self-organisation of self-propelled bacteria is believed to be via hydrodynamic and steric interactions between neighbouring cells [1, 13, 16]. The general consensus is that large-scale collective behaviour is driven by mechanical inputs of energy via the collective rotation of flagella, which exerts localized forces onto the surrounding fluid. As a consequence an ensemble of collective swimmers emerges which cascades from small length scales to large length scales, exceeding the lengths of single bacterium [14]. There is little understanding or reported studies regarding the location of flagella filaments in this collective setting, because it is experimental challenging to visualize even isolated cell due to the high cellular concentrations.

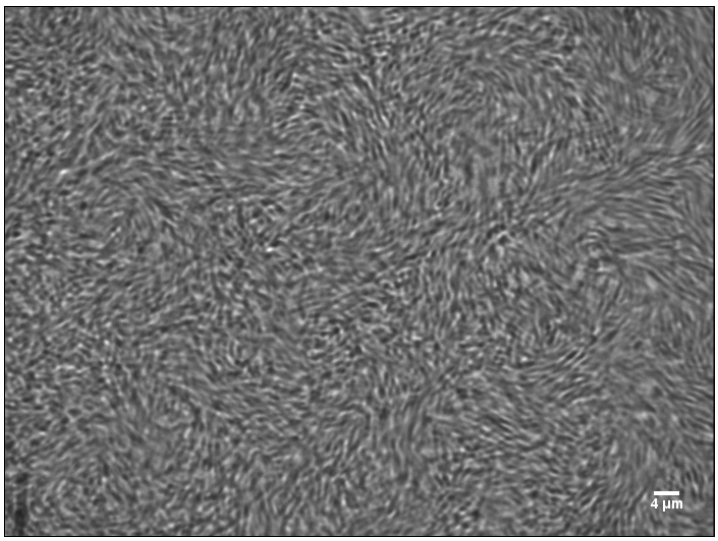

Figure.6.1: Concentrated (10^9 cells per ml) motile B. subtilis cells exhibiting large-scale collective behaviour, vortices are often observed persisting for several seconds before disintegrating and reforming. The typical vortex diameter is ~ 15 - 20 µm persisting for ~ 2 s (See Movie: YB886-Collective-swimming.avi).

Collective dynamics of swimming behaviour of mircoorganisms was initially reported by Kessler *et al.* [17, 18] who observed self-organized behaviour of swarming *B. subtilis* cells. Vicsek *et al* identified that collective dynamic behaviour of active particles, such as motile bacteria observed by Kessler *et al.* can be characterized by non-equilibrium dynamical system with numerous degrees of freedom [4]. This non-equilibrium system permits the phase transitions into self-organized dynamic behaviour. Vicsek *et al* provided a model to investigate particle clustering, transport and phase transition in these systems. This model exclusively used discrete particles; each self-propelled particle has several degrees of freedom following a single rule with additional noise. Each particle executes a new direction of motion after each time-step: *at each time step a given particle driven with a constant absolute velocity assumes the average direction of motion of the particle in its neighbourhood of radius r with some random perturbation added* [4]. This simplistic model was sufficient to demonstrate collective behaviour, where simulations exhibit transitions to cooperative behaviour analogous to experimental findings.

Subsequently, Toner and Tu identified that Vicsek's model is analogous to XY Heisenberg ferromagnetic model [2, 19]. Both models imply collective behaviour arises due to the cohesive movement of all particles in a cohesive direction. Since then there have been numerous simulations and models which investigate collective behaviour and its origin [20 - 24]. Recent work, [25 - 29] is directed towards simulating jets and swirls formation via hydrodynamic fluid flow in terms of dipole stress forces exerted on the fluid. Hardcore interactions such as collisions between rod shaped particles have been simulated, where hardcore interactions assist in the polar alignment providing structural coherence. These simulations attempt to model and reproduce empirically obtained velocity fields produced via particle image velocimetry (PIV) imaging analysis [14]. Ramaswamy *et al* were the first to make analogy between close-packed cooperative dynamic behaviour to aspects of nematic liquid crystals, stemming from the continuum models based on hydrodynamic equations [11, 30, 31]. They constructed hydrodynamic equations for self-propelled

particles with spontaneous orientation order which is purely nematic. These equations predict instability of self-propelled particles at small wave numbers, due to the interplay of hydrodynamics flow and fluctuations in the ordering direction and cellular concentration [31].

In terms of experimental work regarding collective behaviour in particular with *B. subtilis*, the Goldstein group have made several significant contributions providing invaluable insight to the cooperative swimming [7, 12 - 15, 32]. Prior to the research of Goldstein *et al*, correlated motion was reported by Mendelson *et al.,* who observed highly organized swimming behaviour at the leading edges of growing *B. subtilis* colonies [10]. This was the first attempt to characterize cooperative swimming experimentally. They describe cellular colonies to be highly structured where organized groups of cells travelled in *whirls* and *jets*. Colonies formed large correlated patterns that persisted until the suspending fluid had evaporated. Mendelson *et al.* showed by reintroducing a suspending fluid, cells immediately began collective behaviour. They demonstrated that cells undergo temporal-spatial changes; whirls covered an area of ~ 1000 μm^2 which were short lived, lasting ~ 1 s [10]. These vortices constantly disintegrated, and subsequently reformed in the opposing direction [10]. By seeding their colonies with passive tracer particles that align with direction of fluid motion, these cells generate localized fluid flow which facilities the formation of chaotic vortices [12 - 15]. The concept of tracking particles in bacterial suspension was continued by the research of Wu and Lichaber [9]. They designed a novel soap-film geometry where motile *E. coli* cells were suspended in a quasi-two-dimensional thin film. They extracted the mean squared displacement (MSD) $\left\langle \Delta r^2(t) \right\rangle = \frac{1}{N} \sum_i \left\langle \left[\vec{r}_i(\tau + t) - \vec{r}_i(\tau) \right]^2 \right\rangle_\tau$ of tracer particles (10 µm in diameter) in the bacterial films. *Figure.6.2* shows the results obtained via tracking particles for 5 minutes with increasing cellular concentrations *n*.

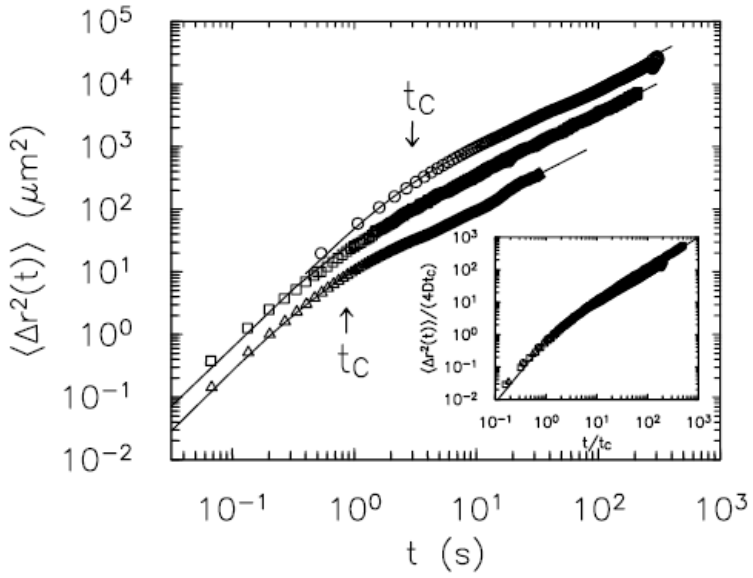

Figure.6.2: Graphical data of MSD of 10 μm beads with increasing bacterial concentrations n. The triangles, squares, and circles are, respectively, n = 0.67, 1.34, and 5.35 × 10 [10] cm^{-3}. The crossover time t_c, indicated by the arrows, increases with concentration n. The insert is the collapsed data, graph sourced from [9] with permission from the publisher.

The results yielded greatly enhanced diffusion of embedded tracer particles; where on short time scales $(0.03 \le t \le 1s)$, the motion of the tracer particles yielded super-diffusive behaviour, with $\left\langle \Delta \vec{r}^{\,2}(t) \propto t^{a} \right\rangle$ where $1.5 \le \alpha \le 2.0$. At longer time scales, typical of one decade $(10 \le t \le 300s)$ diffusive behaviour is restored, where $\alpha \sim 1.0$ [9]. The transition between anomalous diffusion to diffusive-like behaviour occurs at time t_c; this is directly correlated to the cellular concentration n. The ballistic motion on short time scales is due to correlated bombardment by bacteria, where correlated bacterial collisions are transferred onto the net motion of the tracer particles. The forces exerted on the beads are not random, but correlated over specific spatial and temporal scales. Such correlation corresponds to the formation of spontaneous swirls and jets [9]. In terms of hydrodynamic interactions this experiment provides insight into the long-wavelength velocity fluctuation, where the fluid is stirred by localized forces fields.

Recently the group headed by Goldstein has introduced some pioneering concepts and empirical results related to collective dynamical behaviour of *B. subtilis*. They associated cooperative swimming behaviour of cells to ideas of evolution, multicellularity and complexity [7, 12 - 15, 32 - 34]. A brief review of their research results is discussed, where one can refer to the references for additional details. In concentrated bacterial suspensions typically $n \sim 10^{11}$ cells per ml, *B. subtilis* cells occupy a volume of $\sim 1.5 \times 10^{-12}$ cm^{-3} [12] where cells collectively form non-trivial dynamics patterns which act over long ranges (several hundreds of microns). This collaborative swimming behaviour partitions cells into domains which manifest into vortices; where the physics of buoyancy, motility diffusion and mixing are intricately connected [7]. These vortices greatly enhance transport of molecular solutes essential for life processes such as oxygen. Goldstein *et al* attempt to gain an insight into fundamental biological questions, such as the emergence and origins of multicellular organism. Tuval *et al* [33] examined the self-organisation of swimming cells in a sessile drop geometry. *B. subtilis* cells actively swam towards oxygen contact lines facilitating vortex formation at the oxygen-liquid-glass contact line, *Figure.6.3.* This contributed to upwards swimming due oxygentaxis of cells and the Boycott effect [33] where cells form into distinctive plumes; where they present a mathematical model to simulate quantitative results, *Figure.6.3.*

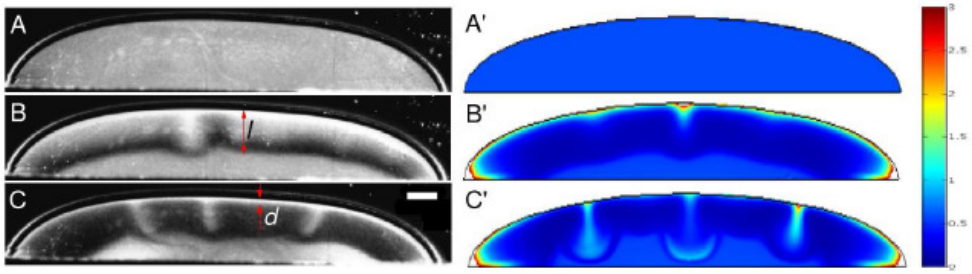

Figure.6.3: The phase transition of self-concentrated sessile drop of bacterial suspension in plane geometry configuration, where figures on the right represent a simulation of the experimental observation on the left. (A) Shows the initial sessile drop of homogenous bacteria, (B) Illustrates the formation of the depletion zone after 150 s, prior to appreciable fluid motion. (C) Demonstrate the migration of cells toward the drop edge, forming a vortex. Imaged sourced from [33], reproduced with permission from National Academy of Science, U.S.A, Copyright, 2005.

Further scientific contributions by Cisneros *et al.* developed a method to sustain cooperative swimming behaviour on a glass Petri dish; cells were visualized with an inverted microscope using a 20 × lens to maximise the field of view [12]. Cells were imaged near the oxygen contact lines where the drop geometry is approximately a thin film. The self-organisation mechanism trigged collective dynamic behaviour, and PIV was used to analyse acquired videos (The acquired results where similar to *Figure.6.1, (See Movie: YB886-Collective-swimming.avi*). PIV essentially estimates the most probable displacements between consecutive frames within a rectangular sampling region via implementing a pattern matching algorithm. It was used to measure characteristic length and time scales via recording collective motion of cells and extracting quantitative dynamical properties. However, the authors noted that the resolution of individual cells was challenging due to high cell numbers and rapid cellular displacements, and improvements to imaging may provide increased precision of PIV measurements [12]. *Figure.6.4 (a)* is a snap-shot of the velocity field estimated from PIV analysis; the results are reminiscent of turbulence, obvious vortex and jets formations are reported to occur intermittently. The authors extract the correlation function, where they define the correlation function as a vector field **V**(**x**, t) [7, 12] as:

$$J_v(\mathbf{x},t) = \frac{\langle \mathbf{v}(\mathbf{x},s+t)\cdot\mathbf{v}(\mathbf{x},s)\rangle_s - \langle \mathbf{v}(\mathbf{x},s)\rangle_s^2}{\langle \mathbf{v}^2(\mathbf{x},s)\rangle_s - \langle \mathbf{v}(\mathbf{x},s)\rangle_s^2} \qquad \text{Eqn.6.1}$$

And the spatial correlation function is defined as:

$$I_v(r,t) = \frac{\langle \mathbf{v}(\mathbf{x}+\mathbf{r},t)\cdot\mathbf{v}(\mathbf{x},t)\rangle_{\mathbf{x},\theta} - \langle \mathbf{v}(\mathbf{x},t)\rangle_{\mathbf{x}}^2}{\langle \mathbf{v}^2(\mathbf{x},t)\rangle_{\mathbf{x}} - \langle \mathbf{v}(\mathbf{x},t)\rangle_{\mathbf{x}}^2} \qquad \text{Eqn.6.2}$$

Where $\langle\cdot\rangle_s$ is the average over time frames, and $\langle\cdot\rangle_x$ indicates the average over space coordinates **x** = (*x, y*). In eqn.6.2, the first term is averaged over all angles θ of **r** where **r** is the change in position in the x,y plane**.** Thus $I_v(r)$ depends only on the

magnitude $r \equiv |\mathbf{r}|$ (see reference [12] for details). These extracted PIV correlation functions, J_v (**x**,t) and I_v (r,t) are plotted in *Figure.6.4 (b).*

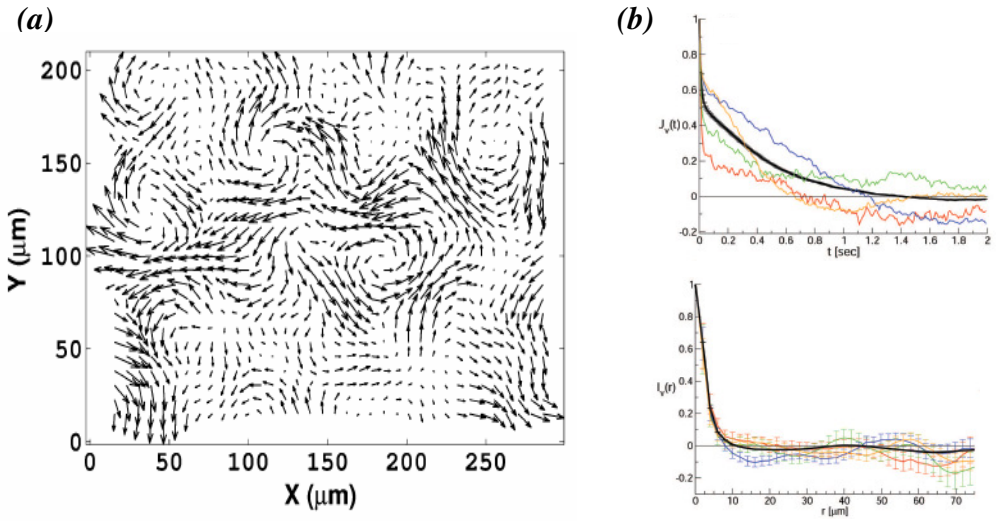

Figure.6.4: (a) The velocity field as a result from PIV analysis used to study collective dynamic behaviour in concentrated bacterial suspensions. (b) Extracted correlation functions from PIV analysis for a pendant drop. Top image is the average spatial correlation the various colours correspond to different times, where the black curve is the average. Illustrate the spatial correlation function of velocity $I_v(r)$, and the temporal correlation function of $J_v(t)$, error bars are the statistical fluctuations; images sourced from [13], reproduced with permission from Springer.

Results extracted from PIV analysis illustrate correlation length scales in the order of 10 μm, corresponding to the typical vortex radius. They observed strong correlation functions which extended up to 10 μm and a coherence time that persisted for at least a second [13], *Figure.6.4*. These quantitative measurements are consistent with Mendelson *et al.* [10]. Negative correlation function is evidence for collective behaviour, where it is now often accepted as a method to quantify the size and life times of vortices as well as collective swimming behaviour.

Recently, Sokolov *et al.* developed a suspending rig that permitted variable cellular concentration control. They examined spatiotemporal coherence of *B. subtilis* cells as a function of cellular concentrations [14]. Sokolov *et al.* demonstrated a novel technique to concentrate cells into condensed populations via a chemotatic response. A thin-film geometry was presented and individual cells were clearly visualized;

where the correlation lengths varied gradually and monotonically as a function of cell density, with no apparent sharp transition from individual to collective behaviour [14]. The onset of correlated swimming suggested by Sokolov *et al.* is a result of larger number of cells swimming in their respective orientation which leads to large-scale hydrodynamic chaotic flows. At a similar time Cisneros *et al.* published an article regarding collective swimming in domains and how individual cells are recruited, introducing the ideas of quorum polarity (unidirectional collective swimming requires polar alignment) [32].

Cisneros *et al.* investigated how '*wrong way*' orientated individuals join the majority of swimming cells hemmed in by neighbours in the setting of collective behaviour. They demonstrated reversal of bacterial locomotion without body reorientation, occurring with characteristic *'V'* trajectories when cells are obstructed by a wall. Their findings demonstrated that the inward and outward asymptotic swimming velocities where indistinguishable; therefore swimming of cells is symmetrical where the flagella bundle is capable of forming at either end. It was hypothesised reversal entails flipping the flagella bundle from the original rear polar end to the former front pole [32]. This was highlighted as a method of quorum polarity which facilitates the onset of collective behaviour. The emerging consensus in regards to experimental work, particular of flagellated bacteria (*B. subtilis* and *E. coli*) is that localized interactions (hardcore collisions) between neighbouring cells and hydrodynamic interactions are accountable for the collective behaviour amongst concentrate bacterial suspensions. Recent reports suggest steric interactions and hardcore collisions alone can also give rise to the emergence of collective behaviour and vortex formation [27].

To conclude flagellated bacteria such as *B. subtilis* and *E. coli* exhibit complex and non-trivial collaborative swimming behaviour where whirls and jets are often observed. These systems are governed by the subtle interplay between buoyancy, motility, hydrodynamic interactions and mixing [15]; where it is often challenging to separate the physics from the biology. Collective swimming behaviour typically

occurs at high bacterial concentrations (~ 10^{10} - 10^{12} per ml). Where cells swim in their respective swimming direction forming spontaneously patterns. These systems exhibit vortex formations and Eddies; thus giving rise to the appearance of turbulences even at low Reynolds number, and enhances cellular mixing and diffusion. The precise mechanism sustaining this non-equilibrium system is not obvious; collective behaviour arises from hydrodynamics interactions and localized cellular collisions. Flocking behaviour occurs due to localized mechanical input of energy via the collective beating of flagella filaments, generating fluid flow that cascades from small scales to large length scale, several orders of magnitude larger than a single cell. Real-time flagella imaging in the setting of collective swimming behaviour has not been successfully achieved. The research presented in this chapter directly tackles these experimental challenges.

6.3 Materials and methods

6.3.1 *B. subtilis* strains YB886 and DS1919

B. subtilis is an ideal organism for the study of correlated motion. The following experimental investigations utilized two strains of wild-type *B. subtilis*. Either *B. subtilis* (YB886) [35] or *B. subtilis* DS1919 (3610) provided by Professor D. B. Kearns[2] [36] both derivatives of *B. subtilis* M168. However, DS1919 (3610) was genetically modified by Kearns *et al.* in the flagellin peptide chain, where one of the non-essential amino-acids was modified to a cysteine residue [36]. This genetic modification enables the flagella filaments to be fluorescently labelled. *E. coli* (HCB1) was also utilized in experiments for comparative purposes when stated. The cellular storage of *B. subtilis* cells is identical to procedure discussed in *Chapter 4* [37]. *B. subtilis* (DS1919) requires the presences of antibiotics to maintain the

[2] Personal correspondence via e-mail. Professor Kearns (University of Indiana, Department of Biology, USA) supplied *B. subtilis* DS1919 (3610).

genetic mutation, these cells are stored and incubated with 100 µg/ml of spectinomycin (Sigma, S4014) [36]. See reference [36] for details on genetic mutation of *B. subtilis* DS1919. *B. subtilis* cells were incubated with the general motility procedure discussed previously in *Chapter 4* [38].

6.3.2 Characterization of *B. subtilis* cells

Viable plate count assays were conducted with both strains of *B. subtilis* cells incubated with the motility procedure, *Chapter 4*. This is a standard microbiology calibration technique, identical to method in *Chapter 4* used to characterize *E. coli* cells [37]. The number of cells per millilitre was recorded as a function of time (30 minutes time intervals) in three independent growing cultures. Results obtained were averaged and plotted as function of incubation time presented in *Figure.6.5*.

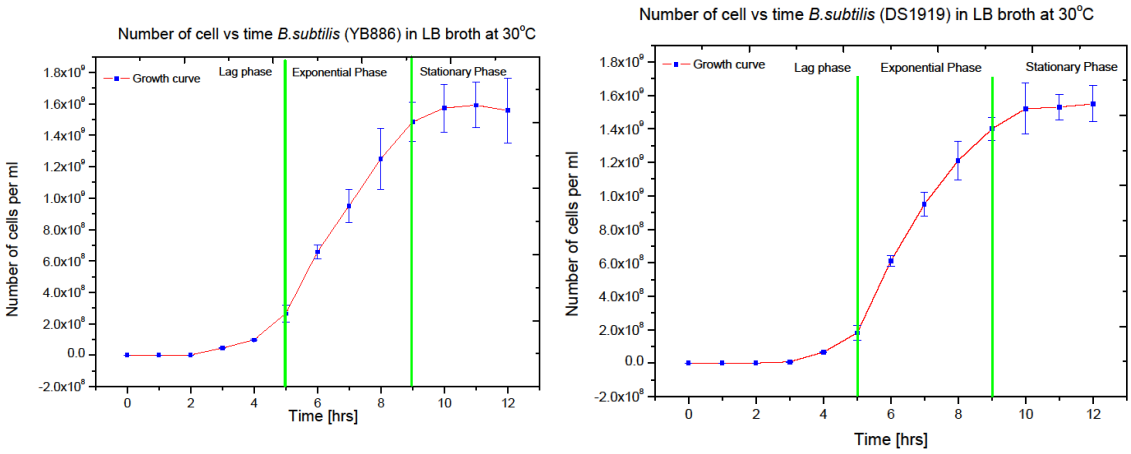

Figure.6.5: The average of three identical batch cultures (10 ml) of respective B. subtilis cells incubated at 30 º C in LB broth. Both curves depict the three distinct growth phases, lag, exponential and stationary indicated by the green horizontal lines, the exponential phase is determined by fitting the a linear trend to the log of the exponential phase. Mid-exponential phase occurs ~6 h in both cases, error bars are the standard error.

The growth rate constant in the exponential phase was calculated to be $g = 1.56\ \mathrm{h}^{-1}$ and $g = 1.49\ \mathrm{h}^{-1}$ respectively of YB886 and DS1919 *B. subtilis* cells. The doubling time derived from the growth rate constant was calculated as 26.6 ± 10.1 minutes and

27.9 ± 2.3 minutes respectively. The corresponding optical density in each growing culture was measured at each 30 minute time intervals. Utilizing the results obtained from the growth curves and optical density plots, one can correlate the average cell numbers to a given optical density. The obtained calibration graph provides a quick and convenient measure of cells numbers during experiments, via measuring the corresponding optical density. The growth curves in *Figure.6.5* indicate that after 6 hours of incubation cells are in the mid-exponential phase of growth and the typical cell numbers are ~ 10^8 cells per ml.

6.3.3 General samples preparation

Experiments were either conducted with standard microscope slides (75 × 25 mm and approximately 1 mm thick, Menzel-Gläser AA00000102E) or coverslips (Menzel-Gläser, 22 × 50 mm, thickness 0.13-0.17 mm, MNJ-350-070 P) where the surface is often treated. Depending on the experiment, microscope slides/coverslips where cleaned with ethanol using an ultra fine microfibre cloth. The slides were then spin coated with 1 % agarose (*Sigma*-Aldrich) rendering the surface hydrophilic promoting cellular motility and avoiding tethering of cells. Clean slides were placed in a spin coater device (Cammax Precima PR214E), 2 ml of liquid (heated) agrose was pipetted onto the centre of the microscope slide/coverslip prior to spin coating. The spin coater was set at 800 rpm for 15 seconds, this setting produced a thin (~ 150 - 200 µm) uniform coating of agarose on the surface of the slide. Many experiments in this chapter utilize very specific protocols, each adapted and optimized for a specific purpose. Therefore the above methods and materials are the general procedures used and specific details are provided in each subsection or appendix concerning a specific experiment when stated.

Experimental Results

The transition between individual swimming to large-scale collective behaviour in both *B. subtilis* and *E. coli* cells was investigated. The presented research aims to provide empirical evidence supporting current theories and to suggest new hypothesis concerning collective dynamic behaviour. Each experimental subsection is self-contained, providing a brief introduction to the experimental objectives, and a review of the results.

6.4 Sustaining correlated motion

The aim was initially to develop the microbiological techniques and methods to reproduce and sustain correlated motion with *B. subtilis* cells similar to references [7, 12, 14]. The objective was fundamentally to sustain continual collective flocking behaviour for substantial periods (in the order of minutes) to investigate this phenomenon and the boundary conditions which sustain it. Experiments utilized motile *B. subtilis* (YB886) cells incubated to mid-exponential phase (~ 8×10^{8} cells per ml) using the general motility procedure. A 10 µl droplet of bacteria was placed on a standard microscope slides. *B. subtilis* cells did not perform correlated motion at *'normal'* exponential phase concentrations, instead these specimens aggregated after 10 minutes. Cellular aggregation was the result of fluid evaporation and cell tethering, where samples show initial signs of biofilm formation. *Figure.6.6.* illustrate an experimental configuration to minimise these effects, promoting the onset of correlated motion.

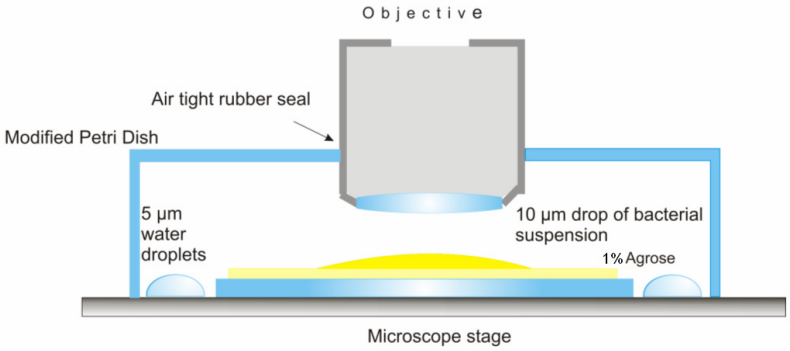

Figure.6.6: Schematic diagram of the experimental configuration used to observe concentrated bacterial suspensions on spin coated microscope slide. Several water droplets were placed inside the air tight chamber to maintain humidity.

The advantage of this configuration is that it minimizes the natural evaporation process, as a result reducing large scale hydrodynamic flow during extensive observation periods. Spin coating the microscope slide renders the surface extremely hydrophilic permitting cells to swim freely on the surface without tethering. Due to the hydrophilic surface the drop thickness decreases due to the fluid dispersion. This produces relative thin samples 5 - 10 µm at the drop peripheries, thus optically improving imaging. The drop thickness increases as a function of distance away from the oxygen contact line, where the typical thickness of the drop at the centre is ~ 150 - 200 µm.

Exponential phase samples were concentrated via centrifugation at low rpm to avoid cell damage. The results indicated that collective behaviour occurs at increased cellular concentrations from that of normal exponential phase batch cultures. Concentrated cellular suspensions ranging between $9 \times 10^{8} - 2 \times 10^{9}$ cells per ml exhibited collective behaviour after an average period of 13 ± 3 minutes. An identical experiment was conducted with motile *E. coli* cells (HCB1), which shows collective behaviour although at a marginally higher concentration ranging between 1×10^{9} - 3×10^{9} cells per ml. This is due to the differences in cell size, where *E. coli* cell require a higher concentration to achieve the equivalent volume fraction to that *B. subtilis* cells.

B. subtilis cells at concentrations of ~ 1.1×10^{9} per ml demonstrate initially that cells are drawn by fluid drift towards the peripheries (oxygen contact line) as the drop disperses. These cells remain at the oxygen contact line either due to presences of oxygen, or the contact line becomes a stiff no-slip boundary due to surface tension effects and the build up to solutes such as secreted polymers which immobilizes cells. In the latter case flagella motors are unable to produced sufficient torque to overcome the impeding yields stress. This was also noted in by Cisneros *et al* [12]. They believe excreted surfactants such as lipopeptides, glycolipids and polysaccharide-protein accumulate which trap and immobilize cells at the oxygen contact line. Observations illustrated cells swimming towards the contact lines (drop peripheries) is a direct result of oxygentaxis, creating a mean gradient influx of cells accumulating at the drop edge. This influx of cells manifests into self-organized cellular packing, where the concentration of cells at the leading edge increases steadily. Accumulation of cells at the oxygen contact line forms into well organized domains, where individual cells swim in their respective alignment and polarity, *Figure.6.7* [12, 13].

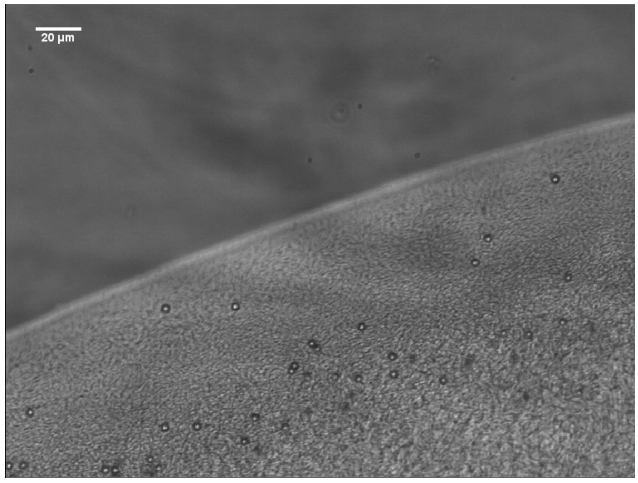

Figure.6.7: Micrograph of B. subtilis cells approximately 13 minutes after a 10 µl drop containing ~ 1.1×10^{9} cells per ml on a treated microscope slide. It highlights the close-packing of cell near the drop edge, where 4 µm polystyrene spheres emphasize the enhanced diffusion due to collective swimming. Cells at the oxygen contact line remain immobilized, whereas cell behind this layer exhibits large scale vortices ~ 20 µm in diameter (See Movie: YB886-Edge-Tracers.avi).

Collective swimming behaviour persisted for ~ 45 - 60 minutes until the suspending fluid evaporated. The characteristic length and time scales of vortices were extracted via video analysis which observed these structures over several minutes and took average values. This yielded length and time scales of 23.5 ± 2.3 μm in diameter and 1.2 ± 0.5 s, respectively. These length and time scales are in agreement with previous finding with similar experimental set-ups [9, 10, 12, 13]. Due to cellular accumulation at the peripheries, collective behaviour was mainly observed at the oxygen contact lines and subsequently expanded ~ 50 μm towards the centre of the drop. As a consequence of the influx of cells towards the peripheries, the centre of the drop did not demonstrate collective behaviour as a direct result.

In conclusion, a successful development of an experimental configuration and microbiological protocols to sustain collective behaviour of cells on spin coated coverslips was achieved. Collective behaviour of *B. subtilis* and *E. coli* cells were observed at higher than normal concentrations 9×10^{8} - 3×10^{9} cells per ml in bulk. Observed vortex length and time scales were extracted *B. subtilis* to be 23.5 ± 2.3 μm in diameter and 1.2 ± 0.5 s, respectively. Noticeably an influx of cells results in close packing of cells near oxygen contact lines where collective behaviour originates. This influx of cells is a direct result of chemotaxis (swimming up oxygen gradients), where cells self-organize in a well aligned polar direction. Cells at the oxygen-liquid interface were immobilized due to increased viscous shear, although cells may still generate fluid flow assisting in the onset of collective behaviour.

6.5 Analysing the onset of correlated motion

The previous experiment demonstrated that motile *B. subtilis* cells at high cellular densities (9×10^{8} - 3×10^{9} cells per ml) on a hydrophilic surface exhibit large-scale orientational coherence and spatial-temporal patterns. The experimental aim here was to probe the mechanism responsible for the onset of correlated motion in concentrated bacterial suspensions. The aim was to collect a time sequence of

evolving events leading to the onset of collective behaviour. We discuss and implement time-lapse video microscopy, as this technique enables interesting events which occur over substantial periods to be recorded in short videos. Therefore one can examine the progressive events leading up to collective behaviour.

An inverted microscope was used in this experiment, permitted imaging of cells from the bottom interface upwards. Slides where chemically cleaned and treated using oxygen plasma etching (*See Appendix A* [58]). This treatment renders the surface of substrates to be hydrophilic minimizing cellular tethering and reducing optical aberrations which improved imaging of cells. Measuring the thickness of the drop varied as a function of distance away from the oxygen contact line. At the contact line (region of interest), the estimated film thickness is ~ 2 - 4 µm; where film progressively became thicker due to the sessile drop geometry on a surface, *Figure.6.8*. At the centre of the drop the measured thickness is ~ 50 - 100 µm. Concentrated *B. subtilis* cells were examined on these substrates, where time-lapse video microscopy was implemented. *Figure.6.8* is a schematic diagram illustrating the experimental configuration used to enhanced image quality via use of a water immersion objective lens (reducing light scattering and increasing the numerical aperture, discussed in *Chapter 4*, *See Appendix A for protocols*).

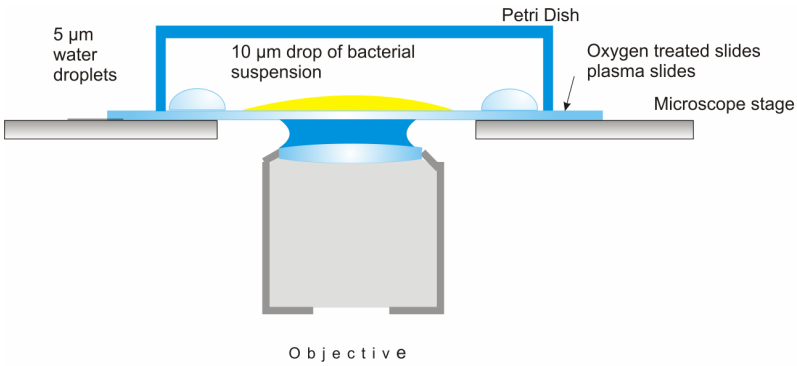

Figure.6.8: Schematic diagram illustrating the experimental configuration to visualize bacteria near the bottom interface. A 60 × water immersion objective was utilized to improve contrast and imaging of individual cells; a humidity chamber was used to prevent fluid evaporation of a concentrated 1 × 10 ^{9} per ml (10 µl) drop of motile B. subtilis.

Time-lapse videos were recorded in three independent drops[3] of motile *B. subtilis* suspensions at ~ 1×10^{9} per ml on oxygen plasma treated coverslips. The experiment primarily focuses on events occurring at the oxygen contact lines where collective behaviour appears to originate, *Figure.6.9.*

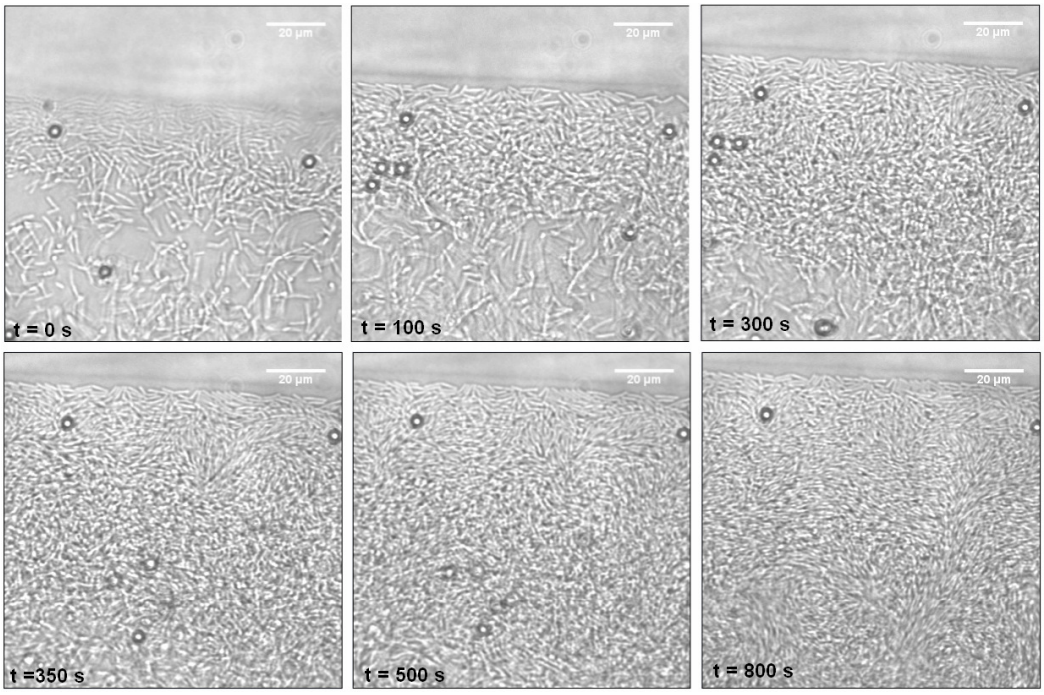

Figure.6.9 (A): Representative and sequential frames from a time-lapse recording of motile B. subtilis cells concentrated at 1 × 10 ^{9} cells per ml on oxygen plasma treated coverslips. Typical film thickness estimated at the edge ~ 2 - 4 µm, although increase to ~ 10 µm towards the bottom of the image. This illustrates the progressive accumulation of cells at the oxygen contact line which initiates the transition to collective behaviour (See Movie: YB886-Time-Lapse-onset.avi).

[3] To reduced statistical fluctuations due to inherent physiological and environmental fluctuations.

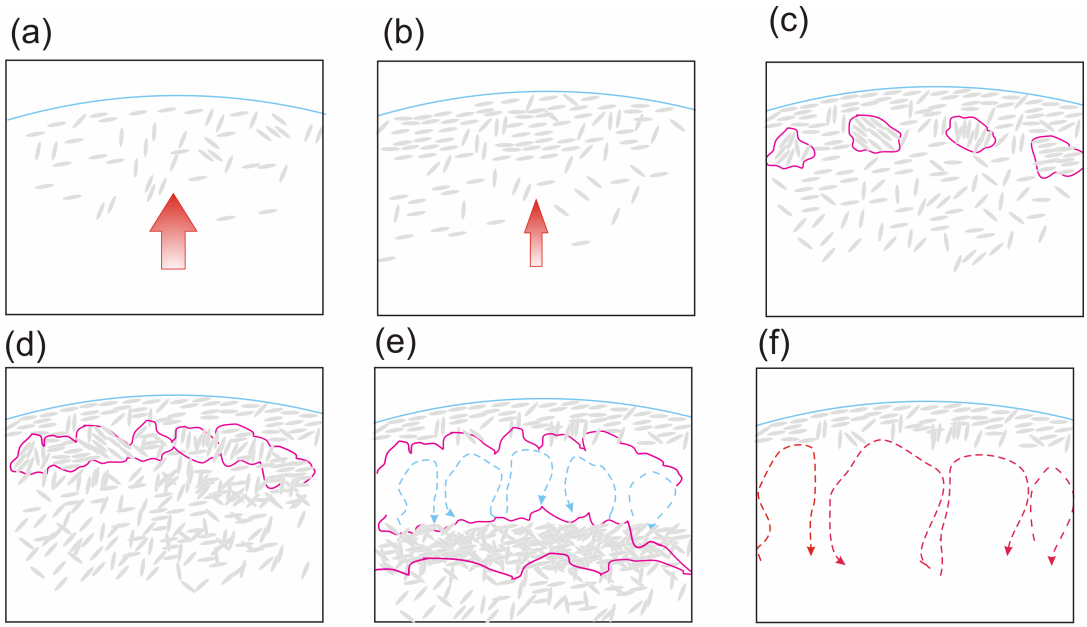

Figure.6.9 (B): Schematic representation of the key events which occur progressively initiating the onset of collective dynamic behaviour, corresponding to frames above. (a) Cells are drawn to the leading edge via large scale hydrodynamic fluid flow due to drop dispersal and via chemotaxis drawing the cells to the oxygen contact line (similar to the coffee stain effect, depositing particles at the edge as the fluid evaporates). (b) Influx of cells permits self-organisation and steric alignment leading to localized interactions. (c) Small groups of cells form into domains which swim in a cohesive direction, a possible mechanism for quorum polarity. (d) Expansion of domains occurs recruiting new cells to polar align with established domains. (e) Formation of large scale whirls and jets due to hydrodynamic interactions indicated by the blue arrows, where cell collisions and mixing occurs. The red band indicates highly compacted cells which subsequently disperse. (f) The red arrows shows the formation of vortices occurs where collective dynamic behaviour of cells establishes itself.

A qualitative approach is adopted to analyze the obtained time-lapse videos since this progressive phenomenon is non-trivial and is based on interplay between several effects such as hydrodynamics interactions, and steric repulsion, diffusion and mixing. *Figure.6.9 (A)*, at T = 0 s, influx of cells drawn to the oxygen contact line as the initial drop spreads outwards over the wet substrate. The measured influx flow rate is ~ 15 - 20 μms^{-1} where the contact line shifts forwards in the subsequent frames; hydrodynamic flow is caused by the dispersion of the drop rather than active swimming of cells. In the subsequent frame (T = 100 s) fluid flow subsides and cells

self-organize, demonstrating polar alignment providing empirical evidence of quorum polarity. Steric interactions occur near the contact line due to close packing of cells; mechanical beating of flagella filaments stirs the suspending fluid which facilitates localized hydrodynamic interactions between cells. An influx of cells continues approximately 80 µm behind the contact line, although at a slower influx rate ~ 5 μms^{-1}. At T = 300 s, a noticeable transitions occurs where highly organised cells at the leading edge manifests into small cluster/domains, typically 5 - 10 µm in diameter. Domains consist of 6 - 7 highly polar aligned cells moving cohesively in a single direction, typically perpendicular to the contact line. Between domains are cells with no apparent cellular alignment. Observations of several isolated cells indicated rapid movements away from the leading edge, presumably because of hydrodynamic interaction inducing cellular reversal. Relatively short times later T = 350 s, rapid expansion of domains occur expanding from a diameter of 5 µm to 15 µm. Expansion occurs via actively recruiting randomly aligned cells into these domains. There is supportive evidence of merging of domains, resulting in non-localized and large-scale fluid flow (indicated by tracer particles). Collective swimming is limited to a small region within a thin narrow band ~ 20 µm behind the leading edge, although the rest of the sample remains relative static. At T = 500 s cellular concentration becomes uniformly close-packed, subsequently fast moving domains gradually expand forming well defined whirls which completes the transition to collective swimming. These whirls temporally form and disintegrate usually opposing direction, where whirls are localized near the oxygen contact line. Several minutes later global expansion of whirls and jets occurs, and spontaneous formation of vortex appears. Vortex diameter ~ 25 µm, observations illustrate unaligned cells either integrates into a domains or forms new domains. Advective mixing was illustrated by the rapid velocities of the tracer particles, suggesting oxygen and nutrients are also mixed homogenously.

Time-lapse videos demonstrated that the cellular concentration increased as a function of time; cells are initially concentrated at the oxygen contact line where an influx of cells was evident. The density profile of each frame in *Figure.6.9 (A)* was

measured as a function distanced from the contact line. Since films are relativity thin ~ 2 - 4 µm, it was approximated as a quasi-2D film [9]. We measured the filling fraction of bacteria ρ (where, $0 < \rho < 1$), i.e the ratio of bacteria coverage in a given area of 5 × 5 μm^2 along the centre of the frame at key times (using digital thresholding), *Figure.6.10*.

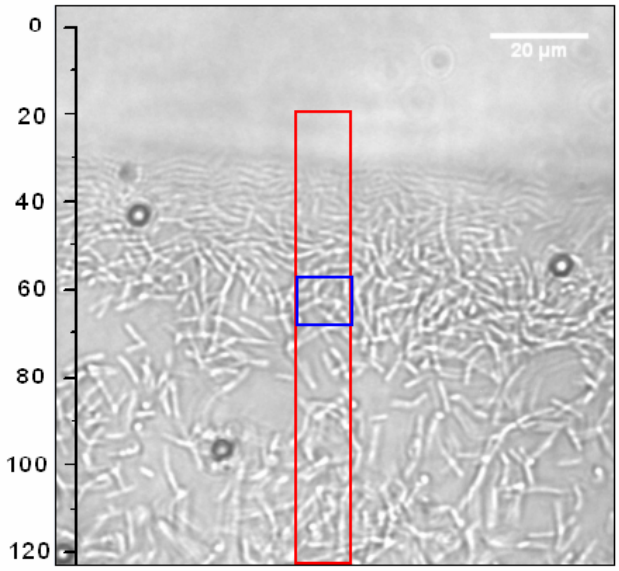

Figure.6.10: The first frame acquired from time-lapse video, the scale represents the distance from the final position of oxygen contact line. The red box highlights the section where the density profile was measured, the blue square is the 5 × 5 μm^2 area where ρ was extracted at 10 µm intervals.

The results of measuring the bacterial density fraction ρ at key points in time corresponding to frames in *Figure.6.10* are presented in *Figure.6.11*.

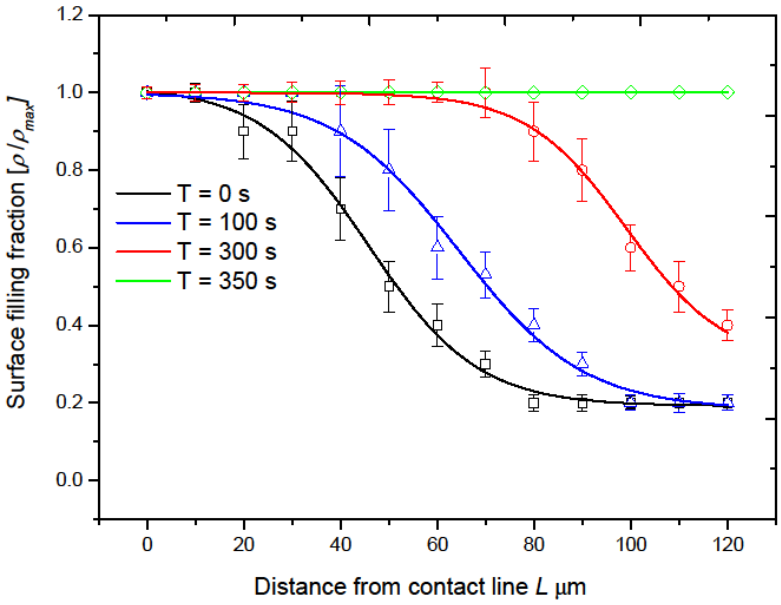

Figure.6.11: Presents the results obtained by measuring the filling fraction ρ in the centre region of each frame as function of time T =0 s, T =100 s, T =300 s and T =350 s respectively. The acquired density profile increases monotonically and smoothly becoming constant during the transition to collective swimming. The initial of value of ρ = 1 due to close packing of cells which decays gradually to ρ = 0.2 due to influx of cells.

Figure.6.11 shows the initial concentration at the contact line is closed packed due the influx of cells caused by the initial drop dispersion *(See Movie: Time-Lapse-onset-YB886.avi).* Increasing the distances from the contact line, cell concentration ρ decreases gradually to ρ = *0.2.* As time progresses we observed an influx of cells thus increasing ρ depicted by the blue curve; this illustrates an initial constant concentration ρ ~ 20 µm behind the relative contact line the concentration begins to decrease smooth and monotonically. At significantly longer periods T = 350 s where structured domains are present a constant close packing density was observed throughout the field of view, green curve. These smooth phase transition are in agreement to anticipated results, since the onset of collective behaviour requires substantial periods of time (~13 - 15 minutes) to initiate. During which numerous processes occur introducing noise masking the phase transition; these conclusions are in accordance to similar experiments performed by Sokolov *et al* [14, 15]. Such sources of noise may arise from observed spontaneous orientation fluctuations as

cells tumble, localized hydrodynamic fluctuations occur as a result of flagellum rotation etc. Although from this experiment we are unable to determine the source of the noise leading to a smooth onset of collective behaviour.

In conclusion this experiment illustrates collective behaviour originates from cellular alignment of cells forming into domains which rapidly expands. These domains initially consist of ~ 10 cells which interact with one another by steric interactions. Localized hydrodynamic interactions occur between neighbouring cells, facilitated by mechanical rotation of flagella filaments. These localized mechanical inputs of energy cascades into large-length scales, manifesting as highly organized collective swimming. Experimental evidence suggests correlated motion arises from highly organized domains, which subsequently expand by recruiting misaligned cells. Adjacent domains merge as they expand; the emergence of domains is believed to be the trigger for the onset of collective swimming. Cohesive swimming of cells in domains is the most likely cause of sustained vortices. Our experimental observations using time-lapse video microscopy have shown how a sample of concentrated bacteria evolves into large scale flocking behaviour. Analyzing the acquired video suggests the density profile of each sample increases gradually towards the oxygen contact line *Figure.6.10,* until the sample becomes close-packed. Our findings suggest a smooth and gradual transition to collective behaviour where numerous processes such as cellular tumbles introduce noise masking the phase transition. The onset of correlated motion occurs due to a number of localized interactions. These localized exchanges of energy and interactions ultimately lead to the onset of collective behaviour which occurs smoothly as the concentration increases. Moreover, observations of active cellular recruiting and reversal of swimming direction provides evidence for quorum polarity. Due to high cellular concentrations it is difficult to resolve individual cells in the setting of collective dynamics. This experiment has raised fundamental questions regarding the location of flagella filament, and how flagella interact with one another. To investigate the flagella interactions in this setting, we developed a technique of visualising flagella filaments in *B. subtilis* cells.

6.6 Fluorescent flagella labelling in *B. subtilis* cells

The aim was to develop a convenient and rapid method to image flagella filaments of *B. subtilis* cells in real-time with minimal side effects to the natural swimming behaviour. Ultimately, fluorescently labelled cells can be used in the setting of collective behaviour; where imaging flagella filaments can provide an insight into the localized mechanical inputs of energy which sustains collective swimming [14, 15]. It was important to visualize flagella filaments during natural swimming events such as runs and tumbles, to acquire an initial insight into the mechanism of thrust generation and cellular reorientation in *B. subtilis* cells[4], since real-time flagella imaging of *B. subtilis* has not been previously conducted with sufficient resolution. Real-time flagella visualization permits quantitative measurements of the morphology of filaments such as length and pitch, moreover permitting observations of flagella interactions and polymorphic transitions where comparisons can be drawn to *E. coli* [38, 39]. Fluorescent labelling of flagella filaments has proved to be an extremely effective technique of visualizing flagella in real-time [39]. Visualizing intact flagella filaments in living cells has permitted extensive investigations in polymorphic transitions of filaments in fundamental events such as run and tumbles [38, 39]. This provides accurate measurements of flagella parameters, essential for simulation work regarding motility. Thus, real-time visualisation of flagella provides a significant insight into the mechanisms that leads to net propulsion and cellular reorientation. *B. subtilis* cells are commonly utilised to study collective swimming behaviour [7, 12 - 13]; in spite of this, little is known about the precise mechanism of thrust generation. By fluorescently staining *B. subtilis* cells we investigate the natural bundling and unbundling of flagella filaments during runs and tumbles.

[4] Remarkably there are substantial studies in regards to the collective behaviour of *B.subtilis* cells; however characterization of run and tumble behaviour and thrust generation is almost non-existence.

Flagella filaments of *B. subtilis* have been imaged previously with several techniques, gram staining, electron microscopes [12] and purified in vitro [40]. These techniques provide empirical data regarding static morphology of filaments, recall *Figure.2.7 Chapter 2*. These protocols require cells to be dried onto substrates prior to imaging, thus visualized cells are not in their natural state. Live-cell video microscopy enables one to investigate the flagella interactions during runs and tumbles [38, 39]. The general accepted conjecture assumes *B. subtilis* cells swim in an analogous method to *E. coli* cells, whereby flagella rotate synchronously forming a single propulsive bundle [7, 12] due to the lack of real-time flagella imaging in *B. subtilis*.

Recently, flagella filaments in *B. subtilis* cells have been fluorescently labelled successfully [36]. Blair *et al* investigated the idea of a molecular clutch used to disengage flagella filaments in *B. subtilis* cells during biofilm formation. They successfully engineers a wild-type strain of *B. subtilis* to incorporate a genetic mutation in DS1919 (3610) cells. The genetic mutation modifies one of the non-essential exposed amino acids on the outer sub-domain present on the surface of the flagellin protein. The side chain (residue) of the mutated amino acid (*amyE::Phag-hag*^{T209C} see reference [36]) was specifically allocated as the target for specific binding for a fluorescent dye molecule (Alexa Fluor 488 C5 maleimide, Molecular Probes) [36]. Due to high density of exposed residues in the flagallin peptide chain, binding of the dye molecules is sufficient to visualize the entire length of the flagellum.

The supplementary online material in reference [36] demonstrates visualization of flagella filaments in *B. subtilis* cells where flagella rotation was deliberately inhibited. However, visualization of rotating filaments was not successfully achieved, the authors reported rotating filaments as '*blurs*'; due to the rapid rotation rates ~ 100 Hz. The motivation for the following research is to justify the conjecture that the prolusion mechanism in *B. subtilis* is analogous to *E. coli* (i.e. single bundles), where we investigate how *B. subtilis* cells swim.

The initial attempt to stain flagella filaments in *B. subtilis* cells was to implement the staining protocol for *E. coli* cells, *Chapter 5* using Cy3 monofunctional succinimidyl ester, *Figure.5.12*. The results were unsuccessful[5] for *B. subtilis* cells, less than 5 % of Cy3 labelled *B. subtilis* cells demonstrated motility; prior to staining ~ 90 % of cells were motile. Motility is inhibited presumably due to the cells lack the outer membrane, where the cell wall is permeable to the staining reagents [39]. Therefore Cy3 is not suitable for staining Gram positive cells. Alternatively we adopted the method developed by Blair *et al* [36], and by improving optical imaging, real-time flagella imaging can be achieved. We acquired *B. subtilis* DS1919 (3610), which is genetically modified such that flagella filament are stainable using Alexa Fluor 488 C5, maleimide [36]. A comparative assay was conducted to verify the biological properties of DS1919 are similar to YB886 (both strains are derived from 168 Marburg [35]).

Bright-field observations illustrate DS1919 cells are extremely motile after incubation using the motility procedure similar to YB886 cells. The cellular body lengths and diameters of 100 swimming cells were measured respectively. The average length and diameters was measured to be 5.47 ± 1.07 μm and 1.11 ± 0.4 μm respectively for YB886; where the error is the standard deviation. The averaged body length and diameter was measured to be 5.64 ± 1.34 μm and 1.29 ± 0.24 μm respectively for DS1919. Thus the morphology of both cell species is consistent within experimental errors. The length distribution of cell strains was extracted in exponential phase. We expect the length distribution to be reasonably broad, ranging from 4 - 8 μm; since the population of cells lengths are distributed between cells which have immediately divided and cells which are about to divided. *Figure.6.12* illustrates the cell body length distribution of each cell population respectively. As expected the majority of cells are distributed among the intermediate phase indicating cellar growth.

[5] Due to the lack of exposed lysines present in the flagellin peptide chain.

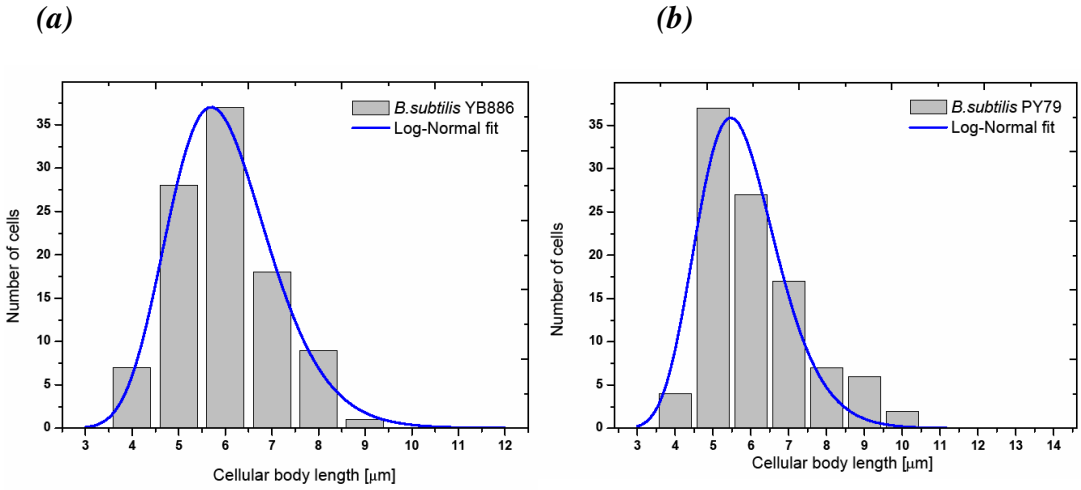

Figure.6.12: (a) histogram of the cell length distribution of 100 YB886 cells, the average cell 5.47 ± 1.07 μm. *(b) Histogram of the cell length distribution of 100 DS1919 cells, the average cell length* 5.64 ± 1.34. *Both histograms demonstrate a characteristic single peak which corresponds to the average cell length, where both histograms are fitted to a log-normal distribution curve.*

The histograms fits well to a log-normal distribution, at the lower boundary cell lengths are well defined after cell division. At the upper boundary the distributions have broad tails, corresponding to ~ 20 % of the population are in the final phase of cell division. These distributions are typical of a growing cluster [41]. *Figure.6.12* demonstrates the length distributions between strains are consistent. Useful parameters were extracted using particle tracking, such as the average swimming velocity, the run and tumble times and angle change during tumble events and are summarized in *Table.6.1*.

Table.6.1

Strain	***Velocity*** ***(μms^{-1})***	***Run Time*** ***(s)***	***Tumble Time*** ***(s)***	***Angle Change*** ***(°)***
B. subtilis (YB886):	25.7 ± 2.6	1.75 ± 0.31	0.77 ± 0.21	39.6 ± 26.5
B. subtilis (DS1919):	27.9 ± 3.9	1.92 ± 0.20	0.73 ± 0.18	34.3 ± 17.3

Table 6.1: Shows the averaged statistics of 100 motile cells, incubated under the motility procedure of B. subtilis YB886 and DS1919 respectively. Both strains of B. subitlis demonstrate analogues swimming behaviour, errors are the standard deviations.

To conclude, the presented results suggest the acquired *B. subtilis* strain DS1919 is physically equivalent to YB886 in terms of swimming characteristics and physiology, due to the fact that both strains are derived from 168M.

6.6.1 Immobilized flagella labelling in *B. subtilis* cells

Development of fluorescent flagella labelling techniques was successfully established using an adaptation of Blair *et al* [36] protocol *(See Appendix B).* This method of specific binding of dye molecules to the modified flagella filaments in DS1919 cells yielded excellent results. *Figure.6.13* depicts representative images of de-energised cells, which have been naturally tethered to the surface where individual flagella filaments are clearly visible with fluorescence microscopy at relatively low excitation intensities $< 22.3 \times 10^{-3}$ $\mu W/\mu m^2$.

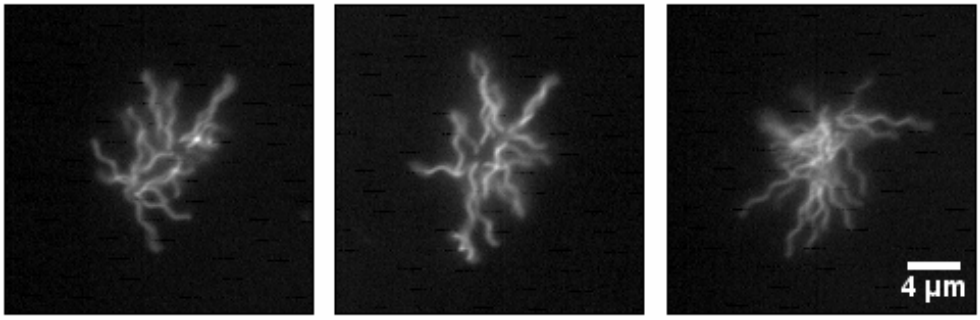

Figure.6.13: Shows the representative micrographs of fluorescently labelled DS1919 cells. Cells were imaged in bright-field prior to fluorescent imaging to verify single cells. Cells were de-energized via starvation subsequently tethering them to the surface; cells demonstrate numerous filaments with a normal left-handed conformation.

We extracted quantitative flagella parameters such as the number of filaments per cell, averaged length, pitch and amplitude; which were measured in an identical fashion to those of *E. coli* cells in *Chapter 5*. The *E. coli* data is also presented for a direct comparison.

Table.6.2

Species	***No of filament (per cell)***	***Length (µm)***	***Pitch (µm)***	***Amplitude (µm)***
B. subtilis (DS1919):	14.5 ± 3.5	8.5 ± 0.2	2.1 ± 0.4	0.4 ± 0.3
E. coli (HCB1):	4.2 ± 1.8	9.2 ± 1.5	2.4 ± 0.2	0.3 ± 0.2

Table.6.2: The averaged collected data of 100 independent measurements of the number of flagella per cell, the average flagella length, the pitch and amplitude for fluorescently labelled de-energized DS1919 cells. The data obtained from E. coli cells HCB1 is presented for comparison.

Noticeably on average *B. subtilis* cells have approximately four times more filaments than those of *E. coli* cells. The length, pitch and amplitude of respective bacterial species are consistent with finds with *E. coli* [39]. Flagella filaments are not only used for thrust generation, but also for alternative uses such as a bio-film formation and tethering to substrates [39].

To conclude images of flagella filaments of *B. subtilis* cells are physically similar to *E. coli* cells regarding morphology. Although the number of flagella filaments is significantly different between species they swim with similar velocities ~ 30 μms^{-1}. We have successfully developed a rapid and convenient method of visualizing flagella filaments with good resolution in *B. subtilis* cells, permitting us to investigate filaments during runs and tumbles.

6.6.2 Investigating the effects of the fluorescent labelling protocol

Two calibration experiments were conducted to evaluate the effects of the fluorescent staining on cells. These calibration experiments are critical to ensure the fluorescent labelling and the visualization method does not significantly interfere with the natural swimming behaviour of cells. Despite gentle handling of cells it is inevitable that hydrodynamic shearing occurs [39]. To assess the effects of the staining protocol the swimming velocities of cells were measured as an indication of cellular health and flagella truncation in three scenarios. The first scenario, incubated cells in the exponential phase, secondly applying the staining protocol without the fluorescent dye; and finally the full staining procedure.

The average swimming velocities of 50 individual cells were recorded in each case. The first case yielded an average swimming velocity of 25.3 ± 2.4 μms^{-1} consistent with previous measurements, (errors here and in the following are the standard deviation). The second case yielded an average velocity of 24.8 ± 2.2 μms^{-1}. In comparison to natural cells, washed cells yielded a ~ 2 % reduction in swimming velocity, not a significant difference and thus consistent with natural swimming cells. We interpret this result as minimal flagella truncation since gentle handling of cell has a minimal effects on swimming velocities. However, the average swimming velocity for stained cells was extracted to be 21.7 ± 2.3 μms^{-1}; a noticeable reduction of ~ 15 % in comparison to the natural incubated cells. These three measurements of the swimming velocity are consistent within the spread of populations.

The conclusions drawn from this study demonstrates a reduction of swimming velocity in stained cells primarily due to the presence of the dye molecules; rather than the effects of cell handling. Washed cells indicated a 2 % reduction in swimming velocities whereas the addition of dye molecules reduces swimming by 15 %. A 15 % reduction is not significant to suggest swimming of stained cell is dramatically different from normal cells if one also considers the heterogeneities when working within biology [45], where cellular variations are relatively broad. Also examining the run and tumble behaviour showed no noticeable differences in stained cells. It is likely that the general health of cells is affected during the staining period (15 minutes) where cells are incubated in the presence of Alexa Fluor 488 C5, maleimide. Obviously this is not an ideal environment, where cells are sensitive to subtle changes in conditions which effects motility [42]. Alexa Fluor 488 C5 is a relatively large molecule (molecular weight 895.07) which does not appear to cross the cellular wall. Binding of the dye molecule to the filament may affect the hydrodynamics of flagella filaments due to increased viscous drag. Moreover the dye molecules may affect the structural properties, with reports of similar dyes render filaments brittle [39] affecting the bundling process. We conclude this staining produces does not have a significant effect on the swimming behaviour and health of cells.

6.6.3 Investigating the effects of fluorescent excitation and imaging

Previous studies highlight the affects of short wavelength radiation (excitation wavelenghts ~ 450 - 490 nm) on *E. coli* cells which elicits a strong repellent response inhibiting cellular motility temporally. This can cause permanent photo-damage and in the severe cases cell death [39, 43]. We investigate the effects of short wavelength illumination and deduced acceptable levels of excitation intensity prior to altering the natural swimming behaviour of cells. Fluorescently labelled *B. subtilis* cells were subjected to increasing levels of excitation intensities to asses the effects. Systematically increasing the excitation intensity we obtained the upper limit prior to

cells eliciting a repellent response. Imaging cells below the threshold intensity ensures cells are not influenced by the excitation radiation.

Neutral density filters are used to attenuate the illumination power of the mercury arc lamp. Reducing the field stop aperture in the optical path of the microscope produces a circular region in the field of view which is illuminated by excitation (wavelength 450 - 490 nm) only. Within this circular region (~ 80 µm in diameter, *Figure.6.14.*) cells are exposed to the excitation radiation and outside this central region cells are illuminated by bright-field only. Events of most interest are the initial exposure and cells swimming into the excitation region. Variations in the swimming behaviour of cells in the excitation region indicate a phototaxis response, *Figure.6.14*.

(a) ***(b)***

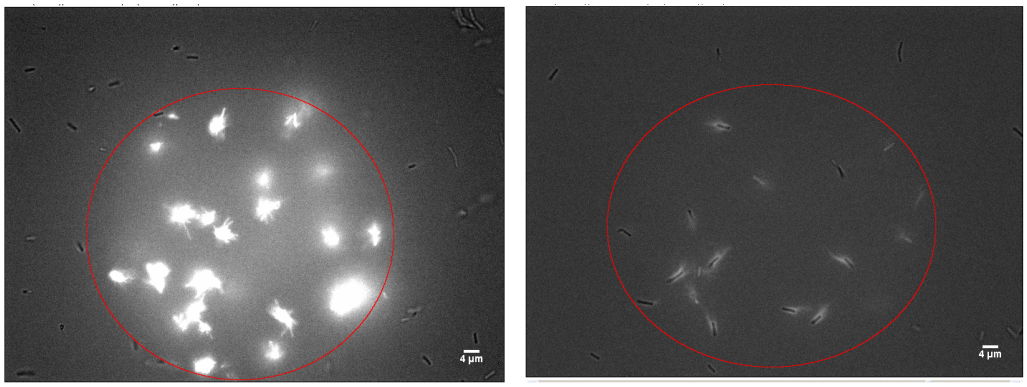

Figure.6.14: (a) Micrograph of stained DS1919 cells exposed with 22.3 × 10 $^{-3}$ µW/µm^2 of excitation intensity within the circular region. Cells within the exposed regions are permanently immobilized; whereas outside of the exposed regions cells remain motile. (b) Micrograph of cells exposed to 2.86 ×10 $^{-3}$ µW/µm^2 of fluorescence where cells remain motile and unaffected by fluorescence indicated by tight flagella bundles. Cells appear to swimming freely in and out of the exposed regions without discernable changes in their swimming trajectories.

The following illumination intensities, 22.3 × 10 $^{-3}$, 6.05 × 10 $^{-3}$, 2.86 × 10 $^{-3}$ and 9.13 × 10 $^{-4}$ µW/µm^2 were measured in the sample plane. Cells exposed to 22.3 × 10 $^{-3}$ µW/µm^2 demonstrated an obvious repellent response. The initial exposure causes cells to tumble and they become paralyzed within ~ 0.3 s. Cells entering the exposed region also became immobilized, at this excitation intensity the camera becomes

saturated, *Figure.6.14 (a).* After 10 s of continuous exposure the excitation illumination was turned off. Exposed cells did not recover motility. This conclusively shows that this intensity caused permanent photo-damage and motility in cells is permanently inhibited. At moderated intensities 6.05×10^{-3} $\mu W/\mu m^2$ the initial exposure induces a tumble response and the average swimming velocity ~ 25 μms^{-1} was reduced by approximately half. This response occurs relatively quick ~ 0.4 s of the initial exposure, cells demonstrated a strong repellent response by swimming and tumbling out of the excitation region. After 10 s of continuous exposure, the excitation radiation was turned off and cells recovered swimming after ~ 2 s; swimming at approximately the same velocity prior to exposure. Excitation at 2.86×10^{-3} $\mu W/\mu m^2$ indicated cells were not affected by the presence of excitation, where an elicited tumble response was not observed, *Figure.6.14 (b).* These cells demonstrated normal swimming behaviour indicated by tight flagella bundles and consistent swimming velocities. Tumbles and trajectories changes where observed due to natural occurrence as expected. At 9.13×10^{-4} $\mu W/\mu m^2$ no discernable difference between swimming behaviour in bright-field or in fluorescence microscopy. However, visualization of flagella filaments is more challenging at this intensity. As a further precaution a synchronized mechanical shutter was used to strobe the excitation illumination to prevent unnecessary exposure whilst recording.

In summary these experiments demonstrate that cells are extremely sensitive to high intensity short wavelength radiation (450 - 490 nm) [39, 43]; where at high intensities exposure $\geq 22.3 \times 10^{-3}$ $\mu W/\mu m^2$ cells became paralyzed within milliseconds ~ 0.3 s and they did not recover motility. At $6.05 \times 10^{-3} \mu W/\mu m^2$ cells elicit a strong chemotactic response; where cells tumble out of the exposed region, with approximately half the natural swimming velocity. At low intensities $\leq 2.86 \times 10^{-3}$ $\mu W/\mu m^2$ exposed cells showed no evident signs of phototaxis (photophobic reaction) or discernable variation in swimming velocity and behaviour in the exposed region. *Figure.6.15* depicts stained *B. subtilis* cells exposed with 2.86×10^{-3} $\mu W/\mu m^2$ with optimal camera settings. Observations via the eye pieces illustrate

vivid and detail images of flagella bundles[6]; unfortunately due to the limitations of the CCD camera some details were lost.

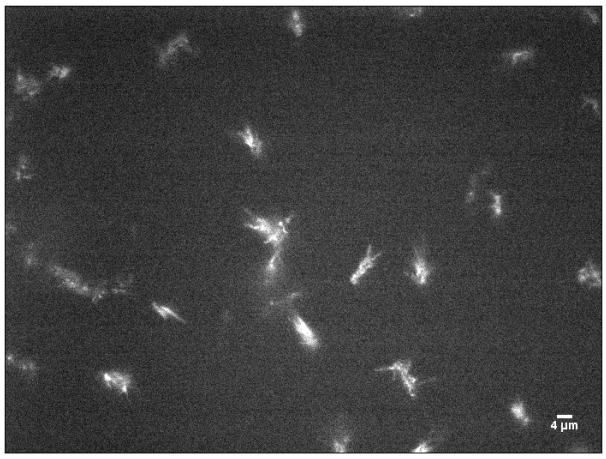

Figure.6.15: Micrograph of fluorescently labelled DS1919 cells swimming ~ 2 - 5 µm above a glass interface, illuminated with 2.86 × 10 $^{-3}$ µW/µm^2 without affecting the natural swimming behaviour of cells.

6.7 Real-Time flagella visualization: Unique bundle arrangements

Fluorescently labelled *B. subtilis* cells lead to the discovery of a novel and unexpected flagella bundle arrangements. Visualized bundles do not align along the central axis of the cell, but at a tangent, contradictory to the general accepted conjecture [7, 13 - 14]. Our findings provide direct evidence that the assumption that *B. subtilis* cells swimming with a single bundle similar to *E. coli* cells is incorrect, *Figure.6.16*. Instead real-time flagella staining showed *B. subtilis* cells swimming with multiple flagella bundles, similar to filamentous *E. coli* cell in, *Chapter 5*. The number of retained filament between *B. subtilis* and *E. coli* differ considerably, *Table.5.4* already suggesting a different swimming mechanism. We directly examine how *B. subtilis* cells generate thrust and change swimming trajectories, which is essential for understanding more advanced behaviour such as collective swimming.

[6] Observations by eye were significantly more detailed than those captured by a CCD camera, demonstrating the effectiveness of the human eye.

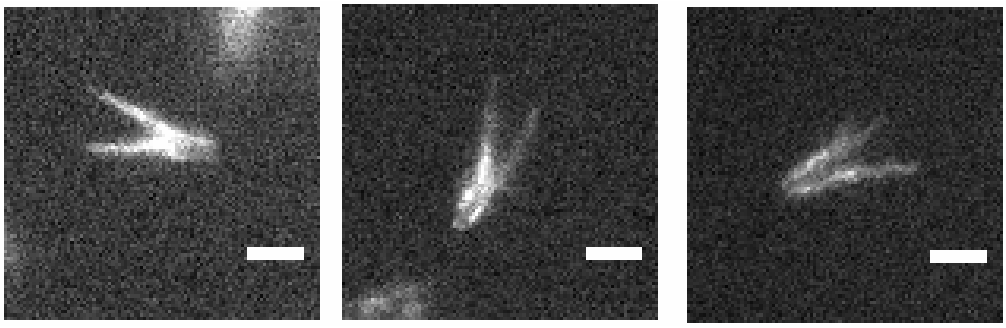

Figure.6.16: Digitally enhanced micrographs of fluorescently labelled B. subtilis cells swimming freely. Micrographs demonstrate cells swims with multiple bundles which do not align axially with the cell body. Scale bar 4 µm.

Figure.6.17 illustrates consecutive frames (Δt = 0.058s) of fluorescently labelled *B. subtilis* cells performing a run, (run length ~ 1.5 s). Due to the rapid flagella rotation rates individual flagella filaments and their polymorphic conformations could not be sufficiently resolved. The first frame shows all the flagella filaments swept towards the rear of the cells, aligning ~ 10 ° off axis to the cell body unlike *E. coli*. The number of flagella rotating in bundles is not obvious, however *Table.6.2* suggest ~ 14 filaments which rotate in two bundles evident from frames 5, 8 and 10. It is challenging to establish the precise number of filaments in each bundle we estimate it to be ~ 4 - 6 filaments per bundle. Some filaments are not bound to a bundle but rotate **CCW** independently generating thrust outside of the bundle [39], similar to filamentous *E. coli* in *Chapter 5*. Multiple bundles are not visualized in every frame due to body rotation estimated as ~ 15 Hz consistent with *E. coli* cells, where bundles eclipse one another as they rotate, *See Movie: DS1919-Labelled-run/tumble-5fps.avi*.

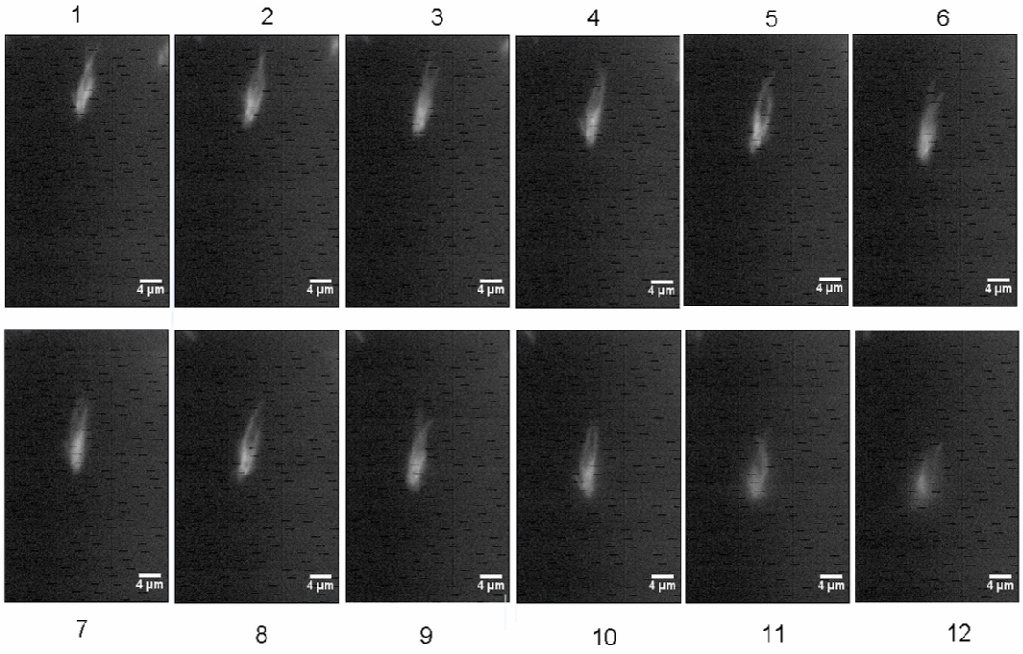

Figure.6.17: Consecutive frames of fluorescently labelled B. subtilis cell swimming freely. The cell is propelled by formation of two flagella bundles indicated in frames frame 5, 8 and 10. Frames 11 and 12 illustrate the cell initiates a tumble as it begins to go out of focus. (See Movie: DS1919-Labelled-run/tumble-5fps.avi).

Figure.6.18 shows consecutive frames of a tumble event lasting 0.58 s. Frame 1 illustrates the cell with two bundles in the run mode; in the subsequent frame the bundle initiates dispersal most likely due to the counter rotation of the flagella motor [38, 39]. Turner *et al* demonstrated with *E. coli* cells that a single reversal of motor direction can induce polymorphic transitions[7], initiating bundle dispersion and the tumble event discussed in *Chapter 2* [39, 42]. *Figure.6.18* supports this conjecture of polymorphic transitions[8] where a single filament is identified as changing configuration. The sequence shows the initial dispersion of one bundle and subsequently the secondary bundle which re-orientation the cell.

[7] Most likely from normal left handed to curly 1, which propagates rapidly from the cell body outwards [39].

[8] The lack of resolution makes it challenging to distinguish the polymorphic changes. However, digital enhancement and slow play-back of clips strongly suggests polymorphic transitions occur.

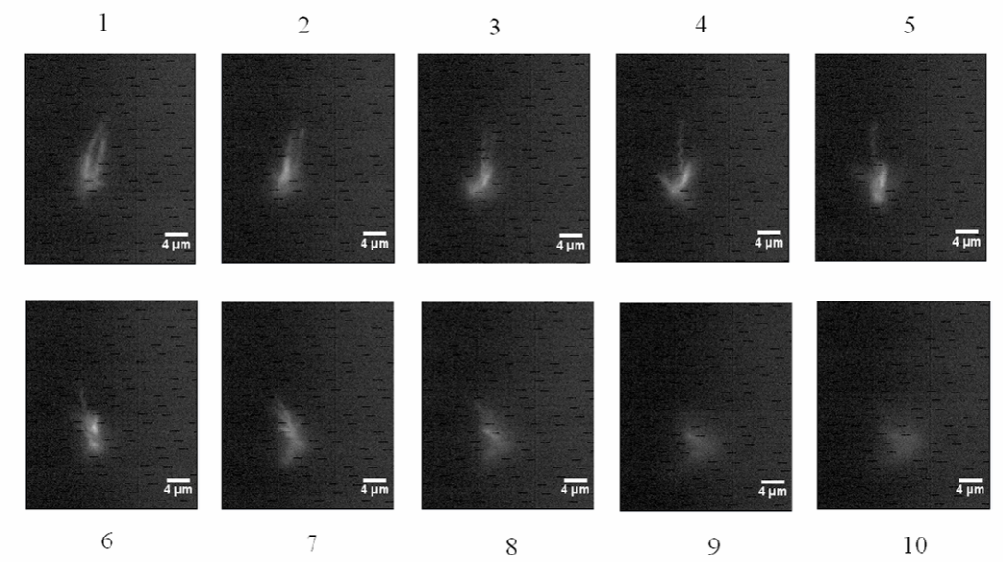

Figure.6.18: Consecutive frames of a fluorescently stained B. subtilis cells during a tumble event, lasting 0.58 s. Frame 1 illustrates the cell is propelled by multiple bundles, where frames 2 - 7 shows suspected ***CW*** *rotation and polymorphic transition. Changes in conformation disperse both flagella bundle, chaotically re-orientating the cell body into a new swimming direction (See Movie: DS1919-Labelled-run/tumble-5fps.avi).*

In summary the mechanism of propulsion in *B. subtilis* cells is obviously more complicated than *E. coli* illustrated by *Figures.6.17* and *Figure.6.18*. *B. subtilis* cells form multiple propulsive bundles which incorporate numerous flagella filaments (approximately 6 in each bundle during runs), which is still not fully understood. These propulsive bundles generate sufficient thrust to propel the cell, where the cell body rotates to conserve torque with an estimated frequency of ~ 15 Hz similar to *E. coli* cells [44, 45] discussed in *Chapter 3*. It is interesting to investigate the mechanism of propulsion in *B. subtilis* cells further, although it has certainly changed our perspective and a shift in paradigm in regards to the analogy between *B. subtilis* and *E. coli* cells. Polymorphic transitions are highly likely to be responsible for cellular re-orientation, due to a lack resolution this was not fully confirmed. Further developments in fluorescent imaging are required for an extensive investigation into polymorphic transitions in *B. subtilis* cells. We speculate that this novel multiple bundle ability may assist in the onset and sustaining of collective behaviour, enabling cells to alter swimming trajectories more readily.

6.8 Visualisation of flagella during bacterial reversal in isolation

Cisneros *et al* have quantitatively shown individual *B. subtilis* cells spontaneously reverse swimming direction without body re-orientation when confronted with an obstacle [32]. Collective group swimming behaviour requires unidirectional and polar alignment of cells, *Figure.6.9*. The authors highlighted bacterial reversal is a possible method of *quorum polarity*, permitting '*wrong way*' orientated cells to swim with the majority of cells in an established domain, discussed previously. They asked *what happens when cells are impeded by obstacles such as a wall, perhaps a group of cells or even a large number of cells swimming in the opposing direction* [32]. They quantitatively measured the '*inward'* and '*outward*' swimming velocities of *B. subtilis* cells during reversals. The results were symmetrical implying swimming forwards or backwards are intrinsically indistinguishable [32, 46]. Without direct visualization of flagella filaments Cisneros *et al* hypothesised bacterial reversal entails unbundling the original bundle, and '*flipping'* the filaments to the opposing polar end, and reforming a new bundle. Reversing trajectories are considered as an efficient method of changing swimming direction without body re-orientation; convenient in a spatially limited regime i.e. in close-packed domains. Quorum polarity is highlighted as the mechanism supporting collective behaviour facilitated by cell reversal events [32]. The authors also reported reversal behaviour in *E. coli* cells occurs less frequently but does not comment on why. Our previous experiments illustrate *B. subtilis* cells swimming with multiple bundles. This may be the cause of the increased reversal behaviour in *B. subtilis,* discussed and addressed in the following section.

The objective of the following experiment is to provide empirical evidence to verify the hypothesis of flagella flipping in both *E. coli* and *B. subtilis*, and to provide an explanation to why reversal is less frequent in *E. coli* cells. We present experiments that examine and explore how flagella numbers affect reversal behaviour, by

conducting analogous experiments to Cisneros *et al* [32] and applying flagella staining techniques to gain a further insight into the reversal mechanism *(See Appendix C for protocol).*

The experimental configuration here is analogous to the experiment set-up discussed by Cisneros *et al* [32]. This consisted of imaging the contact area of 700 µm glass sphere place gently on the spin coated coverslip with 1 % agarose imaged with an inverted microscope, *Figure.6.19 (a).* We collected the statistics of bacterial reversal in both species analyzing the velocity profile during reversal analogous to reference [32]. We also report no non-trivial swimming trajectories depicted in, *Figure.6.19 (b)* highlighted by several categories which was statistically analyzed.

(a)

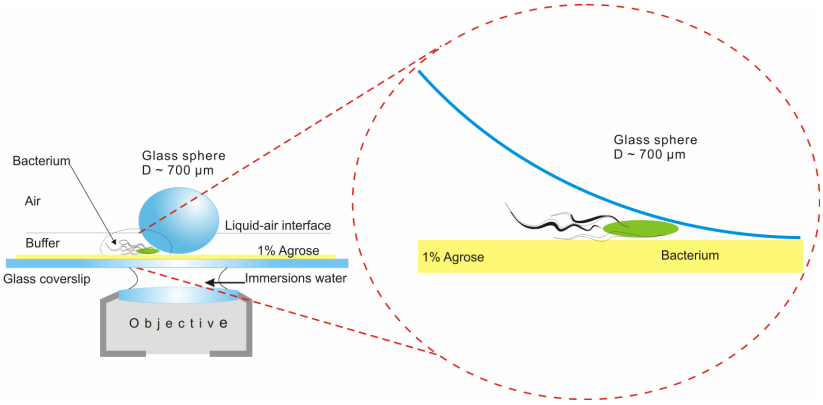

(b)

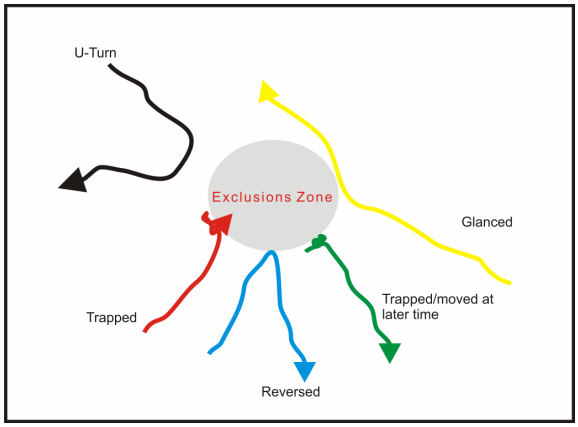

Figure.6.19: (a) Schematic diagram depicting the experimental configuration used to observe bacterial reversal events. A 700 µm diameter glass sphere is placed on the base of an agrose spin coated coverslip in a bacterial suspension. It highlights the convex-wedge shape creating the obstacle where cells reverse, adaptive image from [32], not to scale. (b) Diagram illustrating five categories of cellular trajectories observed when approached the obstacle. The exclusion zone for the cell body is the contact area of the bead ~ 50 µm.

Reversal events are defined as a single cell swimming towards the exclusion zone approximately perpendicular to the obstruction. Upon contact with the obstacle the cell remains relatively stationary for about 1 s. During this so called '*docking period'* [32] observations show that cells pivot typically 20° about the point of contact prior to cellular reversal without body reorientation. Typical reversal trajectories are highlighted in *Figure.6.20, (a).* Reversal events have a distinctive "*V*" shaped trajectories, where the angle varies considerably 5 - 60 degrees, which is independent of docking time [32, 13], *Figure.6.18 (b).* Observations illustrate cells decelerating from an asymptotic swimming velocity ~ 30 μms^{-1} to rest, when approaching the obstruction. The deceleration is due to the increasing viscous drag as the height between the upper and lower boundaries decreases when approaching the narrowest section of the wedge-shaped cavity [32].

(a) ***(b)***

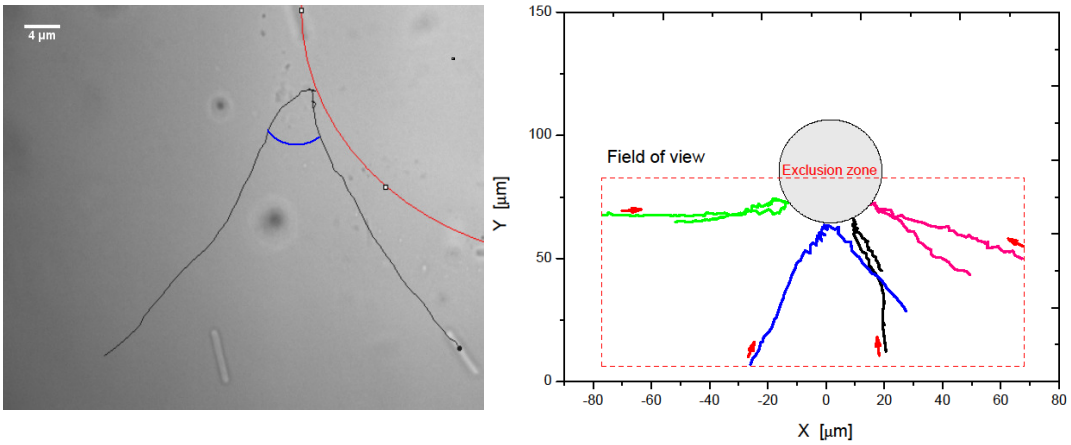

Figure.6.20: (a) Highlights a representative trajectory of B. subtilis (YB886) cells performing a reversal manoeuvre. The red curve indicates the contact line representing the exclusion zone; cells are unable to swim beyond this line. Interloper in the back ground did not interfere with cell reversal manoeuvre (See Movie: YB886-Reversing-Bright-field.avi). (b) Graphical illustration of collected reversing trajectories highlighting the 'V' shaped profile where the angles are broadly distributed, analogous to reference [32]. Similar trajectories were seen with E. coli cells.

A '*glance*' is whereby a cell swims near the vicinity ~ 5 µm of the exclusion zone at relatively large angles (≥ 30°) to the normal. These swimming trajectories are deflected and diverted around the obstacle; maintaining a constant velocity without

noticeable tumbles although small angle changes may occur. '*U-turn*' is defined as cell trajectories swimming close to the exclusion zone ~ 2 μm which performs a sharp turn avoiding the obstacle. On average U-turns are biased towards turning right-wards; which is possibly linked to the hydrodynamics coupling near plane boundaries, where cells often exhibit circular trajectories [47, 48]; although reversal events are uncorrelated. Finally, there were observations of two similar events; cells became immobilized at the obstruction and cells which become immobilized for a substantial period, ~ 2 - 3 minutes before escaping. The former is classified as '*trapped*' where cells remained in the cavity; the latter is classified as '*temporarily trapped*', where cells remained stationary for long periods before escaping. These cells where able to free themselves; either by beating its own flagella or with the assistance of a near by swimming/reversing cells. The statistical results are presented in *Figure.6.21*, where 150 random inward swimming *B. subtilis (YB886)* and *E. coli (HCB1)* trajectories were collected and classified.

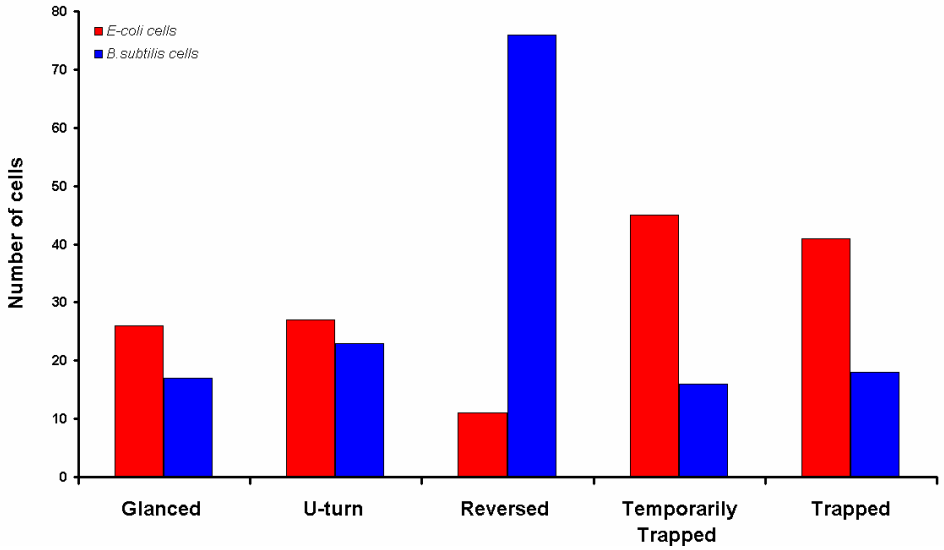

Figure.6.21: 150 randomly collected and categorized cell trajectories respectively. The graph shows 7.3 % of E. coli cells reversed and 50.6 % of B. subtilis cells reversed in comparison. E. coli cells are 60 % more likely to be immobilized or temporally confined, whereas U-turns and Glances are comparable between species.

Our results show *B. subtilis* cells perform cellular reversal manoeuvres more frequently than *E. coli* cells. 50 % of *B. subtilis* cells trajectories demonstrated bacterial reversal in comparison to 7 % in *E. coli* cells. A small percentage of the

cellular trajectories became immobilized, 12 % and 11 % respectively of trapped and temporally trapped for *B. subtilis*; whereas 30 % and 27 % respectively for *E. coli*. U-turn and Glance manoeuvres occurred slightly more often in *E. coli,* implying *E. coli* cells avoids the obstacle more often than *B. subtilis* cells.

Since *B. subtilis* cells inherently retain more flagella filaments, *Table.6.2* which form multiple bundles, *Figure.6.16;* we believe this assists the reversal behaviour when compared to *E. coli* cells shown above. We infer having more flagella distributed randomly over the surface increases the probably of flagella bundling at either end. Reports have shown *E. coli* cells are capable of swimming with both poles, although with a minor bias [46]. Biasing bundling formation at one pole limits the probability of reversal, evidently shown in *Figure.6.21*. It is most likely that there is a less tendency for biasing between polar ends in *B. subtilis* due to the increase of flagella filaments. Examining the reversal trajectories of *B. subtilis* cells, the average velocity profile of 50 trajectories was extracted *Figure.6.22*. The results of isolated reversing trajectories are in excellent agreement with previous findings [32].

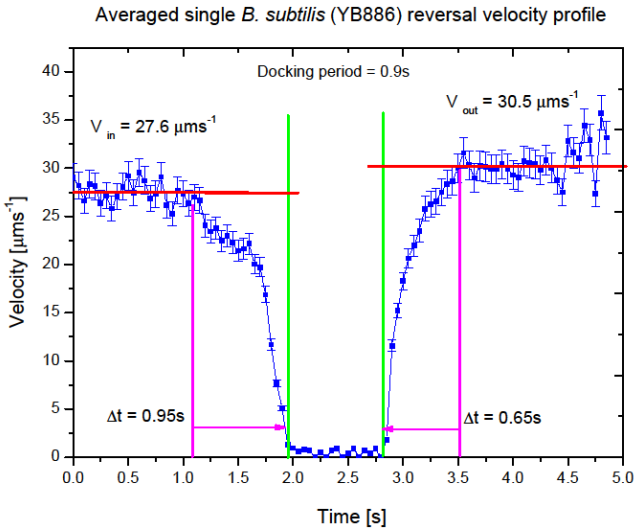

Figure.6.22: The average[9] velocity profile of 50 individually tracked B. subtilis cells during cellular reversal in the isolated geometry. The red lines represent the averaged asymptotic swimming velocities; green lines indicate the docking period and magenta averaged acceleration/deceleration times.

[9] Averaging was performed by dividing the trajectory into three segments, de-acceleration period, docking period and acceleration period, prior to averaging over all collected trajectories.

The average free swimming velocity in bulk was extracted as 31.4 ± 4.3 μms^{-1} approximately ~ 10% faster (within errors) than the values in *Table.6.1* due to heterogeneities of working with bacteria. The average asymptotic inward swimming velocity was extracted as 27.6 ± 5.3 μms^{-1}. The velocity decreased as cells enter the narrowing gap due to increased viscous drag, caused by the reduction of the upper plane boundary [32]. On average it takes ~ 0.96 ± 0.5 s for cells to decelerate to rest[10]. The average docking time was measured as 0.9 ± 0.3 s; hypothesized as the period for the flagella bundle to flip and form at the opposing end. The newly formed bundle accelerates the cells out of the wedge shaped gap and into bulk fluid. The time taken to accelerate into bulk is noticeably faster than time taken to decelerated due to the differences positions of the flagella bundles in each case. For the inbound trajectories, the flagella bundle are at the rear of the cell which is directed towards the wider bulk region. However, outbound trajectories the flagella bundle forms at the opposing end where the bundle points towards the bead and the contact area. The asymmetry of the flagella bundles results in different viscous forces and propulsive efficiency [32]. The averaged outward asymptotic swimming velocity was measured as 30.5 ± 7.2 μms^{-1} consistent within experimental errors[11]. The docking period varies between cells, ranging from a few milliseconds to a second; which is uncorrelated to the angle change during the reversal events. Our findings reflected those published by Cisneros *et al* [32]; independently verifying their results.

We present novel results using real-time flagella imaging to verify and provide evidence to the hypothesis of flagella flipping and we examine and discuss the reversal mechanism. We used fluorescently labelled *B. subtilis* (DS1919) cells discussed above, to directly visualized flagella filaments for the first time during isolated reversal events[12]. *Figure.6.23* shows for the first time, consecutive frames

[10] Consistent with pervious reports by Cisneros *et al* [32].

[11] Since *B. subtilis* cells are peritrichous and are capable of swimming at both poles analogues to *E. coli* [46] one would expect the asymptotic swimming velocity to be similar. However due to the random distribution of flagella filaments it is likely that there is a differences in the swimming efficiency at different poles, caused by the asymmetric distribution of filaments.

[12] In an identical geometry to previous experiments depicted in *Figure.6.19*.

of a single fluorescently labelled *B. subtilis* cells performing reversal manoeuvre in isolation.

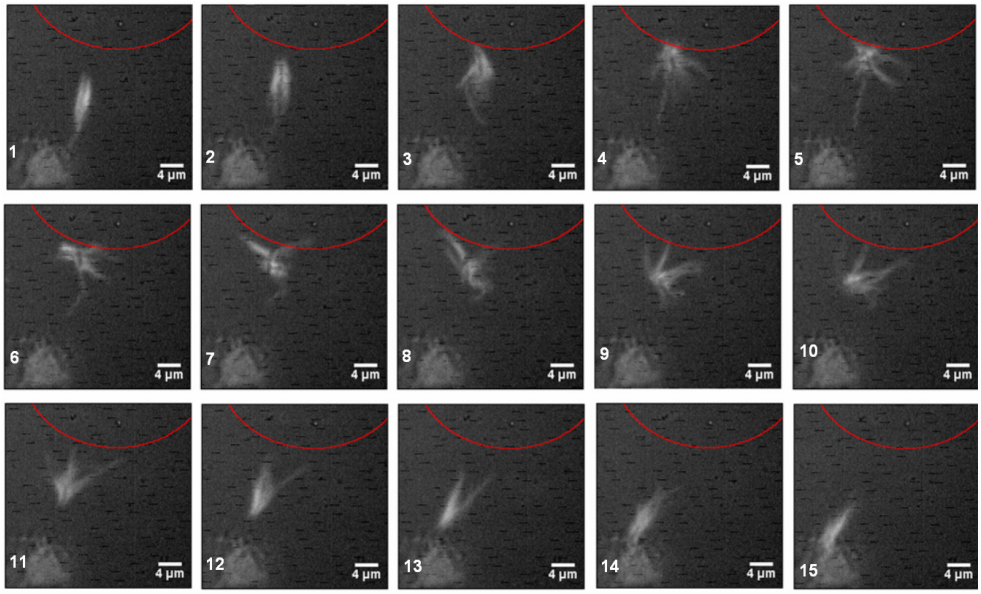

Figure.6.23: Consecutive frames of a single B. subtilis cell undergoing a reversal event. Every third frame is displayed the acquisition rate is 17 fps and the total time of event 2.5 s. Frames 1 and 2 shows multiple bundles at the rear of the cell, frame 3 - 6 illustrates complex bundle dispersion; subsequently bundles are reformed in frames 7 - 13 and finally the cell forms 2 new bundles at the opposing end. Red curve highlights the contact/exclusion area. (See Movie: DS1919-Labelled-Reversing-10fps.avi).

Figure.6.23: shows representative flagella arrangements in fluorescently labelled *B. subtilis* (DS1919) cells during cellular reversal. Reversal trajectories are analogues to *Figure.6.20* and *Figure.6.22. Figure.6.23* provides direct evidence supporting the hypothesis of flagella flipping. Reversal events are reminiscent of tumbles [38, 39], from *E. coli* studies; only **CCW** motor rotation causes filaments to bundle and **CW** results in polymorphic transitions and tumbling, (*Chapter 2).* We suspect individual flagella motors switching direction and introducing polymorphic transitions during reversal events which enables flagella filaments to re-orientate themselves over the cell body. However, it is also possible that the flagella motor continues to rotate in the **CCW** direction. It is still unclear whether polymorphic transitions are necessary for cellular reversal, however our observations strongly suggest they play a vital role.

Due to camera limitations polymorphic transitions are not clearly resolvable since they occur briefly and the flagella often still rotate extremely rapidly. However stationary filaments are distinguishable from rotating ones due to obvious left-handed conformation reminiscent of de-energized cells, *Figure.6.13*. The first two frames in *Figure.6.23* shows the cell swimming towards the obstruction with two obvious bundles located at the '*rear'* of the cell where we suspect all motors to be rotating **CCW**. Termination of **CCW** rotation in one or more filament is observed in frame 3 – 5, this termination of **CCW** rotation is suspected to be the cause of flagella bundle dispersion and suspected to be involved with the initial stages of flagella flipping. We suspect 1 - 2 flagella filaments initiates **CW** rotation and observation of polymorphic transition occur but not fully resolvable here. During frames 6 - 12, it appears that the majority of motors rotate **CW** or not all, analogues to tumble events [38, 39]. We suspect **CW** motor rotation produces a force along the filament which positions it to the opposite end to establish a new bundle. This highlights the extremely flexible nature of the hook and filament assembly, where filaments are capable of rotation despite significant deflections. In frame 8 the cell body has moved ~ 0.5 µm away from the obstacle during the reorientation of the filaments, typical of reversing cells. We observe the flipping of the filaments which creates a viscous drag force enabling the cell body to move slightly away from the obstruction. This creates a cavity to form the new bundles, depicted in frame 9. Frames 9 - 11 the cell begins to form the new bundles at the opposite end where **CCW** motor rotation is restored; initiating rotation of the body to conserve angular momentum and to form tight flagella bundles [49].

'*V*' shaped reversing trajectories are reported and *Figure.6.20* highlights a broad angle distribution range 5 - 120º. These are not correlated to the docking period but occur randomly [32]. Flagella visualization shows large angle distributions occur due to the random and asymmetrical distributions of flagella filaments. Frames 6 - 10 illustrate unbundling and a varying number of filaments performing a '*swooping*' like motion along either side of the cell body *(see Movie: DS1919-Labelled-Reversing-10fps.avi*). The asymmetry of the number filaments re-bundling at the

opposite end of the cell leads to more viscous drag force being exerted on one side (an asymmetrical biasing), hence the cell initiates pivoting due to asymmetrical flipping of filaments. Asymmetric distribution of filaments on either side of the cell increases the probability of bundling on that particular side of the cell first. Thus a larger lateral drag force is generated on the side which has more flagella filaments giving rise to '*V*' shaped trajectories. Since flagella distribution is random and flipping is asymmetrical, this gives rises to the observed large angle distributions during reversal. Supportive evidence is shown in frames 9 - 11, where the bundle appears to form on the right side first. A number of reversing stained cells supports the above conjecture implying asymmetric distribution of filaments is the primary cause of '*V*' shaped trajectories. *E. coli* demonstrates similar reversal behaviour but less frequently ~ 7 % *Figure.6.21*; due to suspected reduction of flagella in comparison to *B. subtilis* cells. To verify our hypothesis, flagella filaments in reversing *E. coli* cells were analyzed for the first time[13]. Due to the reduction of flagella numbers ~ 6 per cell, individual filaments are observed clearly *Figure.6.24*.

[13] Fluorescently stained using method discussed in Chapter 5.

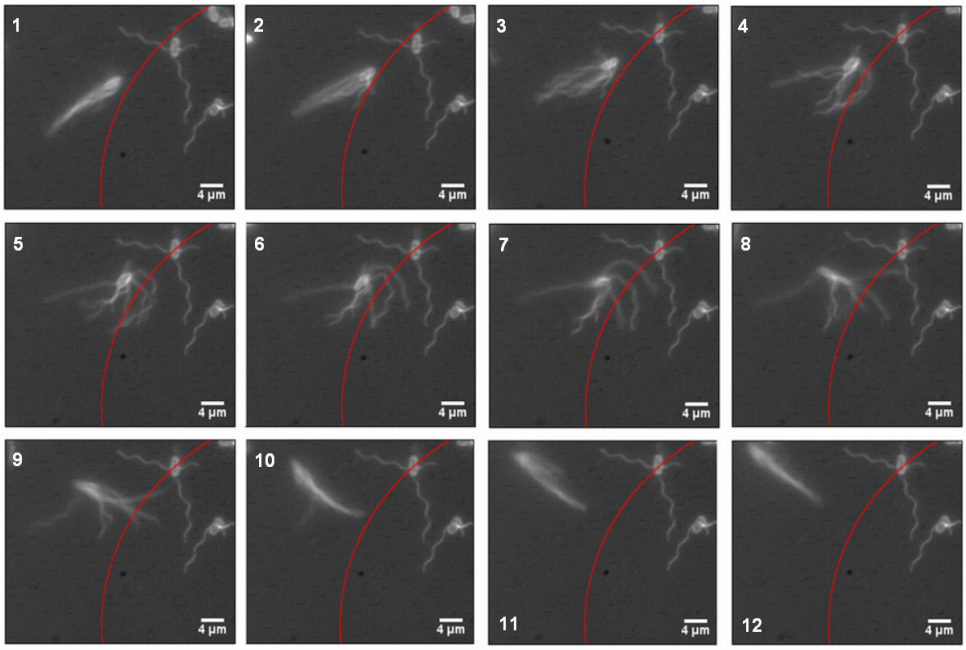

Figure.6.24: Consecutive frames of fluorescently stained E. coli cells undergoing reversal. Every fourth frame is displayed, acquisition rate 17 fps, total time take for reversal is 2.6 s. Red curve indicates the exclusion zone. A single cell approaches the contact area with a well defined single bundle which reverts to the opposing end during reversal. Also shows two immobilized cells which are compressed by the glass bead which does not interfere with the reversal event (See Movie: HCB1-Labelled-Reversing-10fps.avi).

Figure.6.24 shows the events of a reversing *E. coli* cell. Frame 1 visualizes the cell approaching the obstacle, where a single tightly formed propulsive bundle is rotating in the **CCW** direction. Frame 2 is the instigation of bundle dispersion where two identified filaments terminate **CCW** rotation. Frame 3 shows the full dispersion of the bundle where we suspect several filaments to be rotating **CW** reminiscent of a tumbles [39]. Frame 4 shows the filaments are in a normal left handed-configuration, except one filament which appears to be rotating either with a straight or curly-2 configuration, *Figure.2.11*. Most of the flagella are not rotating but appear stationary with a normal left-handed conformation, similar to de-energized cells, *Figure.5.12*. We suspect, either the motor has stalled due to large viscous loads [50,] or the motor is not generating rotational torque. Subsequently frames 4 - 7, illustrate the filaments dispersing and clearly flipping to the opposing end of the cell. The three most right handed filaments in frames 4 - 7 undergo large angular deflections as they move to the opposing end as a result of the viscous drag forces.

The forces produce by the flagella motor in both species enable filaments to translate to the opposing end, however it is not obvious how these forces are generated. We suspect either the motor generates torque introducing a force which translates these filaments to the opposing end. A second possibility might be due to the extremely flexible nature and the low modulus of rigidity of the hook assembly [51]. This is sufficient to re-orientate and repositions the flagella filaments such that it protrude naturally out of the cell membrane with minimal tensional load on the hook assembly. In frame 7, the top right filament initiates **CCW** rotation which hydrodynamically induces surrounding filament to rotate **CCW** forming the new bundle. However, the filament which remained rotating **CW** switches motor direction seen in frames 8 - 10 and rejoins the newly formed flagella bundle. The swooping action of the filaments creates significant viscous drag forces to move the cell body away from the obstacle, this could also be attributed to some filaments are still rotating in the **CCW** direction, generating thrust. This subsequently creates a small cavity to form the flagella bundle been fully established and body rotation is restored. Frames 6 - 7 are an excellent example of asymmetric distribution of flagella filaments, where four filaments moves toward the right side and only one filament moved toward the left during the reversal event; this was typical of observed *E. coli* and *B. subtilis* cells although due to number of filament in *B. subtilis* is was challenging to identify the precise number of filaments. This asymmetric flipping is a strong evidence to suggest *'V'* shaped trajectories are due asymmetry distribution of filaments as they form at the opposing end of the cell. This is more obvious in *E. coli* due to the fewer number of flagella filaments. Measuring the angle of deflection of the filament, it was possible to determine the Young's modulus; which was estimated as $3.9 - 4.9 \times 10^{10}$ N/m^2 consistent with the lower range of accepted values [51].

To evaluate, bacterial reversal occurs five times more often in *B. subtilis* than *E. coli* *Figure.6.21.* This discrepancy is believed to be due to the inherent differences in the number of flagella filaments. We have shown direct visualization of flagella filament during reversal events with both *B. subtilis* and *E. coli* cells experimentally

verifying flagella flipping. We suggest that the cause of typical '*V*' shaped trajectories is due to the asymmetry of flagella flipping on either side of the cell; finally we attempted to explain the flipping mechanism where we suspect **CW** motor rotation is responsible for polymorphic leading to cellular reversal events.

The following experiment was designed to examine how bacterial reversal is correlated to the number flagella filament. We infer *B. subtilis* reverses more frequently because it has more flagella distributed asymmetrically, while *E. coli* has less and therefore reverses less frequently, *Table.6.2* and *Figure.6.21*. We investigated how the reversal statistics change when we remove flagella filaments in *B. subtilis* cells. We analyzed reversal events in normal and hydrodynamically sheared cells. Aggressive pipetting of cells partially truncates filaments or completely removes them from the hook. Quantifying the amount of truncation is challenging as shearing cells can vary considerably, even when conducted systematically. *Figure.6.25* shows representative micrographs of samples where we define normal cells, lightly sheared cells and heavily sheared cells.

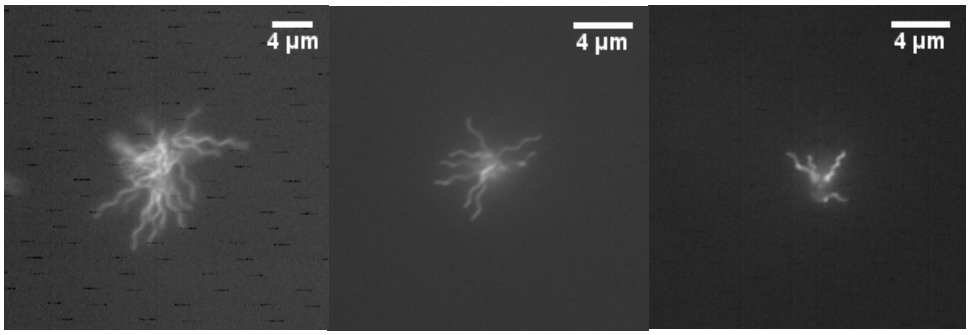

Figure.6.25: Representative micrographs of fluorescently stained de-energize B. subtilis cells which has been subjective to light and heavy shearing. Left image is a non-sheared cell with an average of 14.5 ± 3.5 flagella; centre image is of lightly sheared cell with an average of 5.96 ± 2.7 flagella and right image is heavily sheared cell with an average of 3.83 ± 1.5 filaments.

Figure.6.25 illustrates the micrographs of non-sheared, lightly sheared and heavily sheared cells. The micrographs demonstrate that hydrodynamic shearing is an effective method of reducing flagella number and length. We collected and

examined the average swimming velocity, flagella number, and flagella length in respective samples which are presented in, *Table.6.3*.

Table.6.3

Type	No° of filaments (μm)	Average Length (μm)	Swimming velocity (μms^{-1})
Non-sheared	14.5 ± 3.5	8.51 ± 0.2	22.6 ± 2.0
Light-sheared	5.96 ± 2.7	2.46 ± 0.9	15.9 ± 2.5
Heavily-sheared	3.83 ± 1.5	2.11 ± 0.6	11.6 ± 2.51

Table.6.3: Average statistics of the number of filaments per cell, filament length and swimming velocity of 50 individual cells. The results show that the swimming velocity decreases by 27 % and 47 %, respectively in comparison to the control sample.

The results suggest hydrodynamic shearing of filaments significantly reduces the average swimming velocity, 27 % and 47 % respectively of lightly and heavily shearing. The control sample which was not deliberately sheared indicated an average swimming velocity of 22.6 ± 2.0 μms^{-1} consistent with fluorescently stained cells. The results show 59 % decrease in flagella number and 71 % decrease in length resulted in a ~ 27 % decrease in velocity between non-sheared and lightly-sheared cells. The difference between light and heavy shearing is 35 % in the number of filaments, 14 % in the average length and also ~ 27 % in the average velocity respectively. Our results suggest that the average swimming velocity is strongly correlated to the number of filaments; but also correlated to flagella length. Surprisingly, with more than 80 % of filaments removed or truncated cells are able to maintain motility relatively effectively; supporting the conjecture that peritrichous cell only requires ~ 4 flagella filaments in order to swim [38, 39]. Cells with only 3 filaments and quarter of the original length are capable of swimming at half the normal swimming velocity — which is remarkable considering the viscous drag forces at low Reynolds number. Truncated cells were used to investigate the

correlation between flagella number[14] and reversal behaviour of cells, *Figure.6.26* and *Figure.6.27*.

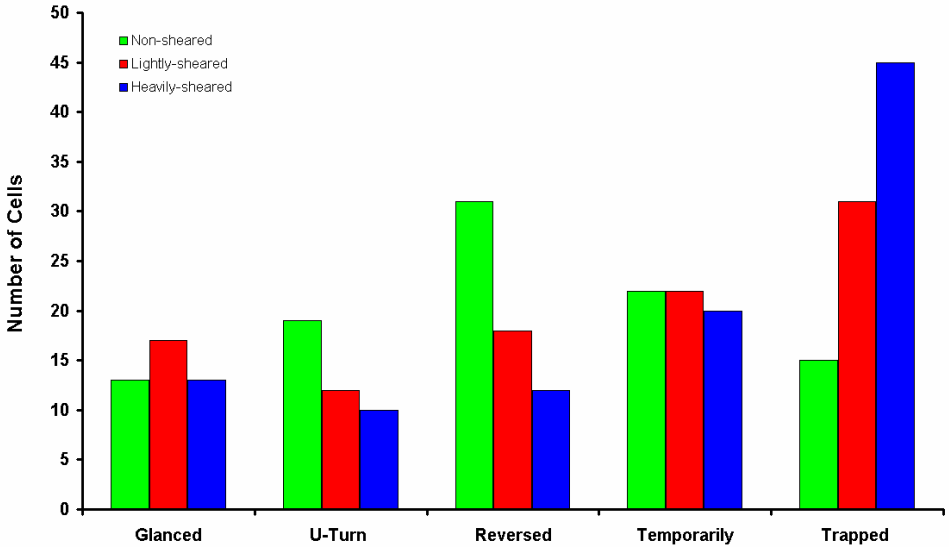

Figure.6.26: Bar chart of the statistics of events which occurred in 100 incoming individual cells in the isolated glass bead geometry. It categorizes 5 events which were recorded, respectively of flagella truncation treatment.

The general trend from *Figure.6.26* suggests that the increase in flagella shearing decreases the probability of cellular reversal events and increases the probability of cells become trapped. The control sample indicates a 31 % of cells performing bacterial reversal and 15 % of observed cell remained trapped. Noticeably the reversal behaviour in fluorescently stained cells is reduced compared to wild-type *B. subtilis* cells imaged in bright-field, *Figure.6.21* where 50 % of cells reversed. This was anticipated since the staining introduces artifacts such as filaments becoming brittle [39], discussed previously. The comparison between the control and lightly-sheared cells demonstrated a 13 % decrease in reversible behaviour, where lightly sheared cells become trapped by 50 % more. Heavily sheared cells in comparison to non-sheared cells depict a 33 % decreased in reversal behaviour and are ~ 3 times more likely to become trapped, *Figure.6.26*. The presented results show supportive evidence of decreasing reversal probability as a direct result of both flagella truncation and removal. The average velocity profiles of reversing cells were

[14] As well as flagella length, this was unavoidable.

extracted, depicting analogues profiles which shifts systematically according to the cell treatment, *Figure.6.27.* The typical trend shows a decreasing asymptotic swimming velocity and a prolonged docking time as more flagella are truncated and removed.

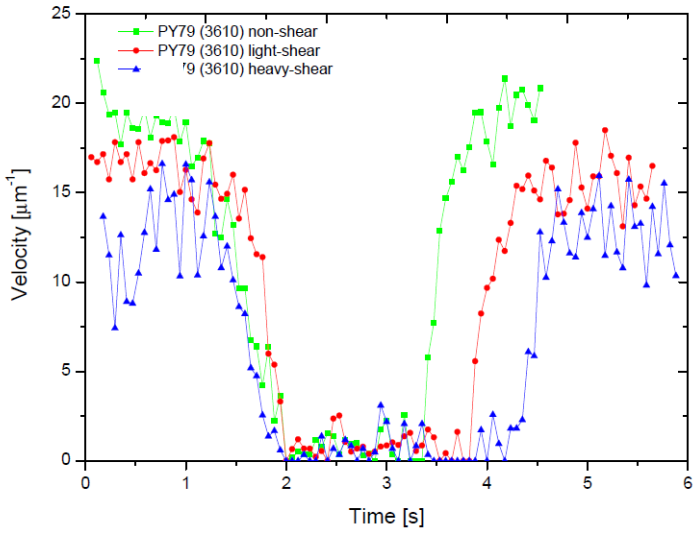

Figure.6.27: The average velocity profiles of reversing B. subtilis cells respectively of cell treatment. These are the statistical averages of 10 recorded trajectories. It is evident that the swimming velocity is correlated to number and length of flagella, moreover the average docking period increases as filaments become more sheared.

The green curve shows non-sheared cells, the average inward and outward swimming velocity was measured as 19.7 ± 2.5 μms^{-1}. Reducing the number of flagella filaments, the average swimming velocity of these cells decreased to 16.1 ± 4. 2 μms^{-1} and 12.3 ± 4.6 μms^{-1} respectively of cell treatment. The docking period increased systematically from ~ 1 s for non-sheared cells to ~ 2.5 s for heavily sheared cells. We infer a prolonged docking period is observed due to fewer available filaments to establish the new bundle at the opposing end. The deceleration and acceleration times where measured, generally we observed an asymmetry in the swimming profiles. This is due to the different position of the flagella bundle in reference to the bead increasing the propulsion efficiency [34]. In non-sheared and lightly-sheared cells the acceleration times are twice as fast as the deceleration times. Whereas heavily sheared cells depicts a symmetrical acceleration and deceleration

times, implying the position of flagella bundle has less of an effect when heavily truncated, results are summarized in *Table.6.4*.

Table.6.4

Type	docking period (s)	No° of filament (per cell)	de-acceleration time (s)	acceleration time (s)
Non-sheared:	1.35	14.51 ± 3.5	0.88	0.47
Light-sheared:	1.82	5.96 ± 2.7	1.09	0.52
Heavily-sheared:	2.17	3.83 ± 1.0	0.76	0.92

Table.6.4: Comparison of docking time, number of flagella filaments and acceleration times of cell treatments respective. Decreasing the number of flagella directly decreases the probably of reversal, also prolonging the docking period.

The results obtained from the truncation experiment demonstrate bacterial reversal is correlated to flagella number and length. Utilizing stained cells and intentionally truncating flagella filaments demonstrated that reversal behaviour becomes less probable and the time taken to reverse increases noticeably. The statistics demonstrate an increase in probability of becoming trapped with shortened and fewer flagella filaments. However, this method of flagella truncation varies both length and number simultaneously, hence interpreting results becomes more challenging and the results are not fully conclusive. Therefore, further study is required to determine fully whether reversal behaviour depends on the number of asymmetric distributed flagella filaments.

In conclusion we have demonstrated that both *B. subtilis* and *E. coli* cells are capable of bacterial reversal. 50 % and 7 % of incoming trajectories reversed swimming direction without body reorientation respectively, *Figure.6.21*. We present a novel study of direct visualization of flagella during reversal events, demonstrating a range of complex unbundling processes when confronted with an obstacle. This provided empirical evidence to verify the hypothesis of flagella flipping during reversal manoeuvres for the first time [34]. Our results suggest **CW** motor rotations and

termination of motor rotation are responsible for the unbundling and subsequent flipping of the flagella filaments. This is reminiscent of tumbles where we strongly suspect polymorphic transitions occur. During this process we suspect the motor produces a torque force which enables the filament to re-bundle at the opposing end, *Figure.6.24*. Our results show broad angular '*V*' shaped trajectories which occur due to an asymmetric distribution of flagella filament sweeping down either side of the cell during reversal events. We investigated the correlation between flagella number and statistics of reversal events by hydrodynamically truncating filaments and examiming the frequency of reversal events respectively. Generally the results suggest the reduction of flagella number and length reduces reversal probability and the swimming velocity, also prolonging the docking period. The results are not fully conclusive due to the flagella truncation method which varies length and number simultaneous, although the results strongly suggest reducing the number of flagella filaments, reduces the probability of reversal events.

6.9 Bacterial reversal behaviour among groups of cells

An experiment was designed to explore how the reversal mechanism changes when approaching a group of cells rather than a passive wall (bead). In the context of collective behaviour, a cluster of oppositely swimming cells is more natural occurring obstacle for a '*wrong way'* swimmer [34]. A cluster of cells as obstacle is significantly more complex than a passive wall. Firstly cells create hydrodynamic flow, secondly steric interactions hem in cells into a polar alignment, therefore flagella filaments are limited spatially. Fluorescently staining of flagella filaments in the setting of collective have not been achieved yet, primarily because it is extremely challenging to image individual cells due to rapid swimming speeds and high cellular concentrations. At the time when this experiment was conducted flagella labelling had not been successfully developed, thus we only discuss reversal behaviour in respect to bright-field microscopy. However in later experiments we present successful flagella imaging in the setting of collective behaviour for the first time.

The objective is to compare how the reversal behaviour changes when cells are in an ensemble or approaching a cluster of cells. We analyze the difference in reversal behaviour in the group scenario where cell-cell interactions occur and the isolated case discussed previously. It was noted in isolated reversal behaviour that immobilized cells are able to regain motility via cell-cell hydrodynamic interactions of a secondary swimming cell. We believe cell interactions assist in reversal behaviour, and we developed a method of suspending cells between agrose treated coverslips at semi-dilute concentrations (volume fraction $\varphi \leq 0.1$ in a monolayer) to examine reversal behaviour in clusters of cells. This experimental method permitted excellent imaging of individual cells[15] in the setting of collective behaviour. The advantages of this novel geometry allows the samples to be preserved for longer periods (without rupturing), which are easier to handle and are robust against evaporation processes unlike soap films [9] *(See Appendix D)*. Cells are suspended in a monolayer where the spacing between coverslips is approximately 3 - 4 μm preventing tumbling in the z - plane, but not in the x-y plane, *Figure.6.28*.

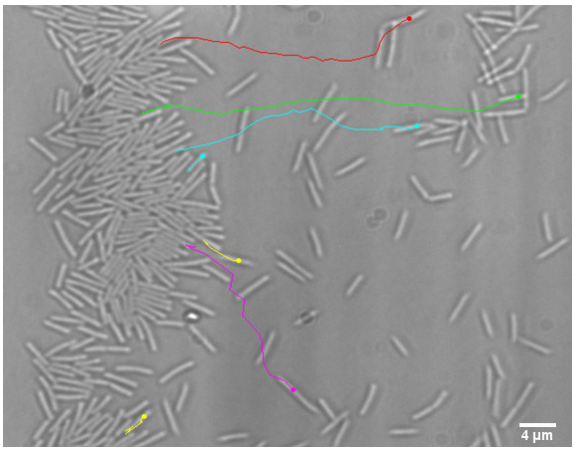

Figure.6.28: Snap-shot of B. subtilis cells at semi-dilute volume fraction $\phi \sim 0.06$ *measured at the centre of the drop. The sample geometry is uniformly in thickness ~ 3 - 4 μm in height where a monolayer of bacteria is achieved. Cells congregate at the oxygen contact line; trajectories show cellular reversal without body reorientation (See Movie: YB886-Group-Reversal.avi). Demonstrates cell reversing from the oxygen-liquid contact line, where weak correlated motion is observed in the centre of the sample.*

[15] This enabled one to clearly resolve individual cells providing an insight to cell collisions, where cell are traceable in the setting of collective behaviour.

Observations depict cells swim in small clusters (~ 2 - 4 cells) showing supportive evidence of quorum polarity [12, 13]. The oxygen contact line is a natural barrier where cells congregate into a close packed and self-alignment regime reminiscent of collective behaviour, *Figure.6.1*. Initial observations shows individual cells reversing and frequently small clusters of cells reversed. *Figure.6.29* shows the average velocity profile of 50 manually tracked individual cells swimming toward the oxygen contact line, docking for ~ 0.5 s and reverse. These cells interact via hydrodynamics and hardcore collisions

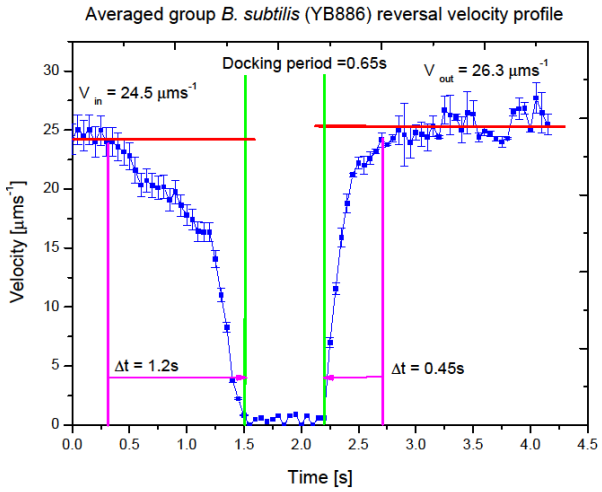

Figure.6.29: Average velocity profiles of 50 cells trajectories which reversed at the oxygen-liquid contact line. The red lines represent the averaged asymptotic swimming velocities, green lines indicate the docking period and magenta averaged acceleration/ deceleration.

The average inward/outward asymptotic swimming velocities where measured to be 24.5 ± 4.6 μms^{-1} and 26.3 ± 5.3 μms^{-1} respectively. The average swimming velocities of cells are impeded by the hydrodynamic interactions of the non-slip plane boundary which increases the viscous drag [47, 48, 51]. Moreover the increase of cells create complex fluids flows and regions of high/low viscous shear as well as cell collisions which impeded the swimming velocity. The inward and outward swimming velocities are symmetrical within experimental uncertainties. However the docking period of hemmed in cells is shorter in comparison to the isolated case, *Figure.6.22* which last several milliseconds. The deceleration and acceleration times

for hemmed in cells are asymmetric, similar to the isolated case. *Figure.6.30* illustrates a comparison between reversals events in the two regimes.

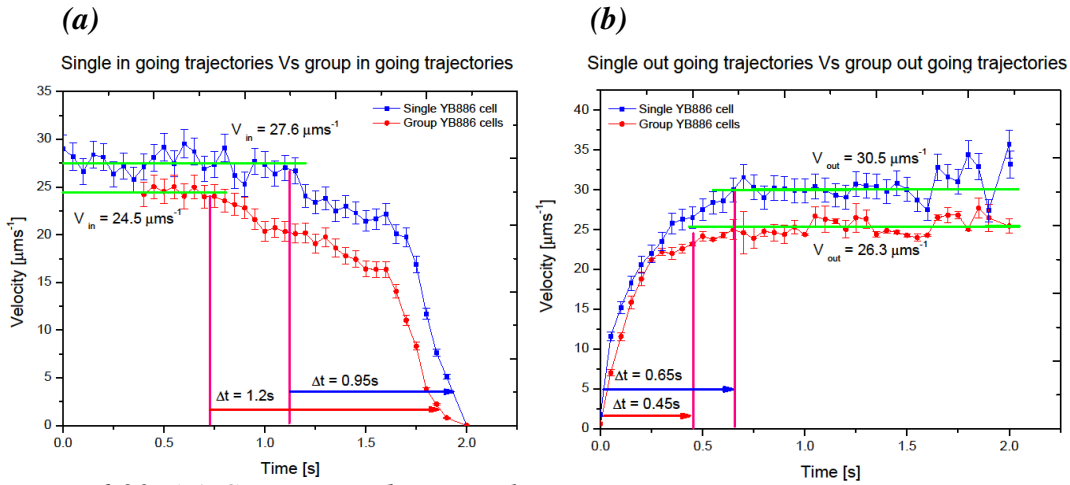

Figure.6.30: (a) Comparison between the average inbound swimming trajectories of cells in the two stated regimes. The average decelerations time from their respective asymptotic value to rest, yield 0.95 s and 1.2 s respectively. (b) Graph of the time taken for cells to reach the maximum swimming velocity respectively of geometry. The time taken for cell to accelerate from rest is 0.65 s and 0.45 s respectively.

Figure.6.30 (a) shows isolated cells decelerations ~ 20 % faster than the group case. In the isolated case cells approach the obstacle and the swimming velocity decreases due to increased in viscous drag [34]. This is also true for the group case as cells approached the oxygen contact line where suspending fluid diminishes. Since cells congregate at the peripheries, incoming cells experience complex circulating fluid due to immobilized cells beating their flagella. These complex fluid flows were also noted by Cisneros *et al* [59], which examined unexpected flagella bundle bipolar flagella arrangements near a solid surface. We infer this fluid flow acts like a '*head wind*', impeding the swimming velocity where cells take longer to reach the oxygen contact line due to the impeding flow and increased viscous drag[16] as one possibility. *Figure.6.30 (b)* shows the averaged time for cells to accelerate to the asymptotic velocity in respective cases. Cells in groups accelerate faster than cells in isolation by 30 %, possibly due to the circulating fluid flow acting as a '*tail wind*' (i.e. cells are pushed by the fluid flow) resulting in an increase of rate of acceleration. Moreover, the docking period is also reduced by 25 % in the group case, suggesting

[16] *B. subtilis* cells have been reported to swim towards regions of high shear [12, 13]

reversal occurs more readily and rapidly in groups. Occasionally we observed individual cells triggering multiple and simultaneously reversal events, typically the nearest neighbours. Generally 10 % of cells trajectories which reversed also demonstrated simultaneously reversal behaviour with nearest neighbours.

Our results highly suggest that fluid flow and cellular interactions assist in bacterial reversal events, indicated by a significant 25 % decrease in docking time. Individual hemmed in cells can initiate multiple cellular reversal events amongst its nearest neighbours, providing strong evidence of quorum polarity [12, 13]. Localized hydrodynamic coupling between the reversing bacterium and neighbouring hemmed in cells influence the nearest neighbours to simultaneously reverse; these cells actively recruit cells to swim in the same direction. Here we raise an interesting question, *how do the flagella filaments flip from one end to the other in restricted spaces by other hemmed in cells?* In the isolated case, *Figure.6.23* and *Figure.6.24* there is ample space for flagella flipping, unlike in the group case which is spatial restricted by neighbouring cells. Our findings demonstrate bacterial reversal is enhanced by hydrodynamic flows and cell interactions. Occasionally cells reverse simultaneously in groups, providing strong supportive evidence of quorum polarity and the recruitment of cells.

6.10 Novel quantitative visualization of flagella filaments in concentrated bacterial suspensions

The objective of this experiment was to directly visualize the rotation of flagella filaments in the setting of collective cellular behaviour, for the first time. Visualization of flagella filaments in this setting is a significant advancement in gaining an insight into collective behaviour [12 - 14]. It is generally accepted that collective behaviour is sustained by localized mechanical inputs of energy facilitated by rotation of flagella [12 - 15]. It is also assumes that these mechanical inputs cascade from the small scale to the large length scale [14, 15]. Currently there are no

published articles or experimental data to support these theories. This thesis presents for the first time, real-time imaging of flagella filament in the setting of collective behaviour. With novel experimental techniques, we fluorescently labelled flagella filaments and suspended bacteria in a semi-dilute regime. Here we visualized flagella-flagella interactions in the setting of collective behaviour, extracting quantitative information regarding mean squared displacement and the mean run length of cells in dense suspensions. We present particle tracking of active cells and passive tracer particles undergoing collective motion at various bacterial concentrations; our empirical results are then discussed in reference to recent simulation studies [50].

The following section discusses a particle tracking algorithm, this programme enables accurate particle identification and particle tracking. Moreover it can extract accurately and quantitatively the MSD from particle trajectories. This particle tracking method is based on works by Crocker and Grier [53] which was later refined by Weeks [54]. These tracking routines are written in IDL designed primarily to track fluorescent colloid imaged with confocal imaging[17]. These routines were used to track fluorescently labelled bacteria and they proved to be extremely effective.

There are three basic requirements for successful particle tracking. Tracked features must be bright objects on a dark background, typical of confocal and fluorescence microscopy. The algorithm is programmed to track spherical particles assuming the maximum intensity of the feature corresponds to its centre. The algorithm was specifically written to track fluorescent beads, *Figure.6.32*; however fluorescent rod shaped bacteria can also be tracked accurately. The concept of particle tracking is the same for fluorescent bacteria but requires further discrimination steps[18], (for details see reference [53]). Particle tracking was conducted in monolayer sample, i.e. a quasi-2D slice; therefore features are tracked for the 2D case only. Movies file

[17] IDL routines are freely downloadable from reference [54].

[18] The routines use several discrimination steps to isolate the desired features we did not modify the routines but used specific tolerances to discriminate and track rod shaped bacteria.

were loaded into the programme and features were found via a filtering process to reduce noise and to enhance the contrast of the features relative to the background. The centre of each identified features of interest was identified by discriminating the intensity, pixel size and eccentricity. The coordinates of each identified feature of interest are extracted in every frame; the trajectories are obtained describing the motion of the particle in the x-y image plane. Each recorded trajectory is given an identification '*tag*' where one can superimpose the trajectory over the track particle to establish the accuracy of the tracking by eye. Additional algorithms written by E. Week can extract quantitative information from acquired trajectories such as the average MSD, describing the diffusive behaviour of tracked features and further details can be found in [54]. Motile bacteria were suspended between two oxygen plasma treated coverslips permitted extremely thin suspensions and excellent imaging of individual cells *(See Appendix E)*. The combination of monolayer geometry and flagella staining allows novel real-time flagella imaging in the setting of collective behaviour, *Figure.6.31*.

(a) ***(b)***

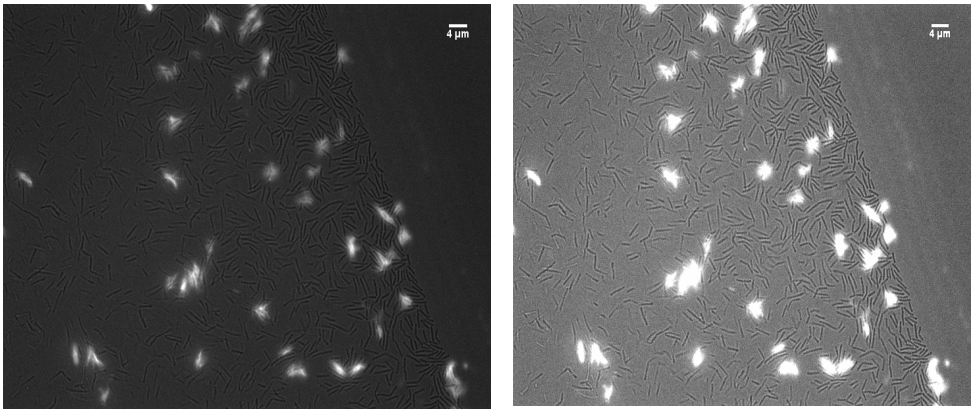

Figure.6.31: (a) Illustrates a snap-shot of collective behaviour of B. subtilis cells suspended between two oxygen treated coverslips the estimated volume fractions ~ $\varphi_e = 0.09$ *where ~ 5 % of cells have been fluorescently stained. From the image it is possible to identify the swimming modes of cells, where flagella dispersion indicates cellular tumbling. Moreover it is possible to identify cells swimming in jets or vortices, these videos were typically used for particle tracking due to contrast in background (b) Digital enhancement of the same image to highlight background cellular concentration which demonstrated collective behaviour (See Movie: DS1919-Lablled-Collecitve-swimming.avi).*

Figure.6.31 and movie *DS1919-Lablled-Collecitve-swimming.avi* demonstrates collective behaviour even in dilute bacterial suspensions $\varphi_e \sim 0.09$ where flagella filaments are observable. The volume fraction was estimated by counting the number of cells in the central region of the sample (25 µm × 25 µm), and calculating the respective surface coverage where one cell has an area of approximately 1 µm × 4 µm, *Chapter 2*. This experimental configuration enables identification of cellular swimming modes (running/tumbling) in the setting of correlated motion, via visualising bundle dispersion. Flagella conformation is not resolvable due to low magnification, however a large field of view enables one to observe collective behaviour and to track individual cells over large distances extracting the MSD.

Initially cellular concentrations were increased from the dilute limit to a semi-dilute regime. Cellular volume fractions, φ_e = 0.034, 0.066, 0.092, 0.116 were investigated, approximately 5 - 10 % of cells in these samples were fluorescently stained acting as tracers. The MSD of cells was extracted via particle tracking $\left\langle \Delta r^2(t) \right\rangle = \frac{1}{N} \sum_i \left\langle \left[\vec{r}_i(\tau + t) - \vec{r}_i(\tau) \right]^2 \right\rangle_\tau$ [10, 54]. Initially 4 µm fluorescent beads at a dilute concentration (~ 1 particle per 30 µm^2) were suspended between two treated coverslip without bacteria, beads demonstrated a diffusive behaviour due to thermal fluctuations as expected. Using the particle tracking algorithm, the diffusion coefficient D was extracted from MSD calculations, hence $\left\langle \Delta r^2(t) \right\rangle = 4Dt$ as D = 0.421 ± 0.01 µm^2·s^{-1}. Theoretical calculations from the Stokes-Einstein's equation $D_t = k_b T / 6\pi\eta r$, yields D = 0.536 µm^2·s^{-1} for freely diffusing 4 µm spheres. The theoretical curve and measured curve of MSD are illustrated in *Figure.6.34* discussed later. The results indicated a 20 % discrepancy between measured values and calculated values, as expected. This is due to the proximity and the separation distance of the plane boundaries which increases the viscous drag as a function of separation high; our samples are typically ~ 5 µm in separation distances [47, 55]. The hydrodynamic interactions with the plane boundaries hinder the beads

displacements caused by increased drag; therefore one expects a slower measured diffusion coefficient *D*.

Subsequently 4 μm passive tracer particles were suspended in bacterial bath of motile *B. subtilis* at increasing concentrations, from the dilute limit to a semi-concentrated regime $\varphi_e = 0.03 - 0.09$. *Figure.6.32* shows fluorescent tracer particles suspended in a bacterial bath of *B. subtilis* undergoing collective swimming behaviour. The correlated behaviour of bacteria influences the motion of the tracer particles, where the passive tracer particles mimic the fluid flow created by swimming bacteria and from bacterial collisions with the bead [9, 10, 56]. The motions of the particles are directly correlated to the motion of the bacteria, due to bombardments of bacteria transferring kinetic energy to the particles [9]. *Figure.6.32* illustrates the centre of fluorescent particles have been identified by the particle tracking algorithm where the X, Y coordinates are rerecorded in each frame. The identified features are highlighted by a white circle around the centre of the identified feature. Normally for tracking bright-field illumination is turn off, increasing contrast and the accuracy of particle tracking. Non-stained bacteria are not observed in this setting, *Figure.6.32*. Each identified feature is recorded and tracked continuously for a minimum of 90 seconds.

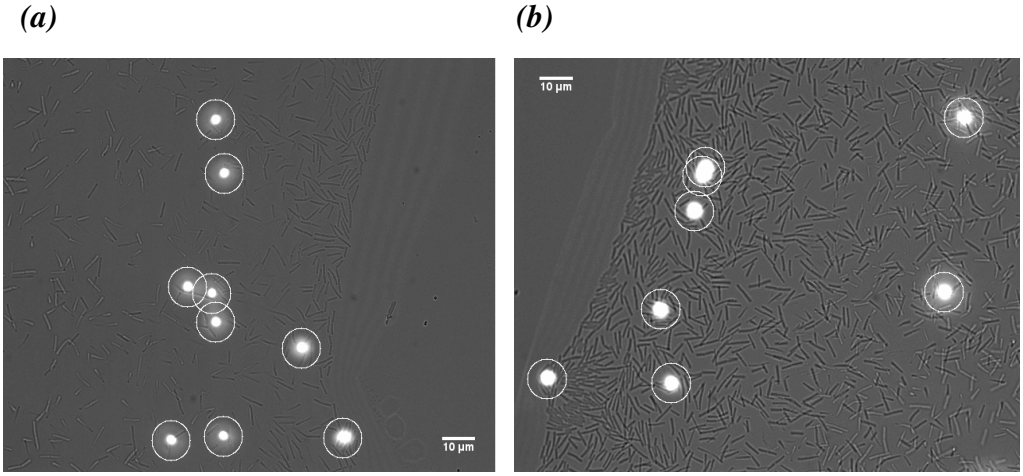

Figure.6.32: (a) non-stained B. subtilis cells suspended between treated coverslips at the dilute limit where collective behaviour was observed at relatively low volume $\varphi_e = 0.03$. *4 µm fluorescent beads are suspended in the sample, and particle tracking was conducted using IDL [54]. The particle tracking algorithm indicates identified features by highlighting them with a circle. (b) B. subtilis cells suspended between coverslips at a higher volume fraction* $\varphi_e = 0.09$, *collective behaviour was extremely obvious. Both images were digitally enhanced to illustrate the background cellular concentration; during particle tracking the background is dark to maximise tracking efficiency, excitation intensity 2.86 × 10 $^{-3}$ µW/µm^2 intensity.*

The results of passive particle tracking are shown in *Figure.6.34* discussed in detail later. Fluorescently stained *B. subtilis* cells were suspended in identical conditions to that of the beads. Fluorescently labelled cells were examined in extremely dilute suspension to ensure cellular interactions are absent. Naturally occurring run and tumble were examined; runs appeared to be extended in this geometry also reported by Cisneros *et al* [32] in a similar confined geometry. Tumbles were observed which changed cellular direction in the XY plane due to height restrictions. Stained cells were continually tracked for > 90 seconds, *Figure.6.33 (a).* Fluorescent tracer cells were tracked during collective behaviour at increasing concentrations ranging from $\sim \varphi_e = 0.03 - 0.09$ similar to the beads, *Figure.6.33 (b).* Tracking 4 µm beads and actively swimming cells at increasing concentrations was performed, the MSD was extracted in each case and the results are presented in, *Figure.6.34.*

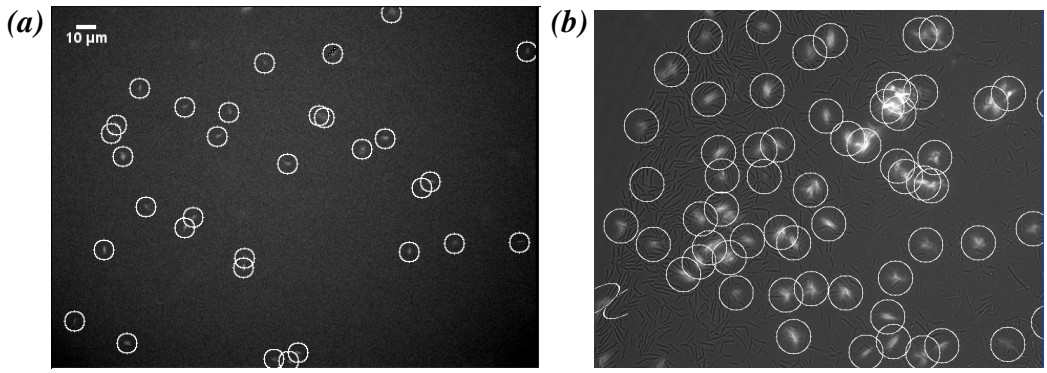

Figure.6.33: (a) illustrates fluorescently stained B. subtilis cells at a dilute concentration where runs and tumbles were observed, typically low magnification is required to observed 'naturally' occurring runs and tumbles. Circles highlight identified centres of the fluorescently labelled cells using the particle tracking algorithm. (b) Fluorescently labelled cells at a semi-dilute concentration $\varphi_e = 0.09$ *where collective cell behaviour is observed. ~ 20 % of motile cells were fluorescently labelled and tracked indicated by the circles. Higher magnification was used to observe flagella interactions.*

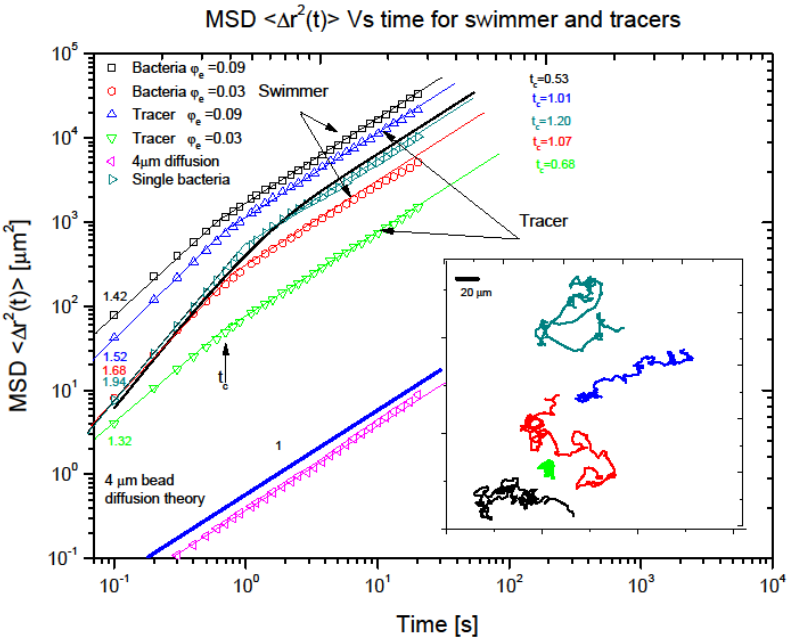

Figure.6.34: The extracted MSD curves as a function of time representative of tracers and swimmers at the high and low bacterial concentration. Graph demonstrates how diffusive behaviour of respective particle in isolation behaves in comparison to theoretical calculations. All the MSD curves illustrate a cross-over of regimes from super-diffusive regime at short time scales to a diffusive regime at longer times. The cross-over time is extracted by fitting the ballistic regime and the diffusive regime in a similar method to ref. [10]. Dilute 4 µm tracer particles remain diffusive as expected. The inset highlights the representative tracks obtained and analysed; it shows five colour coordinated trajectories corresponding to the respective MSD curve.

The MSD was theoretically calculated for a freely swimming bacterium that swims at constant velocity v with an exponentially distributed mean run length τ, and the cell re-orientates randomly. The expression which defines the diffusion coefficient for a swimming bacterium described above is given by $D = v^2\tau/3$ where τ is the mean run time and v is average swimming velocity [57]. We estimated the diffusions coefficient D for an average bacterium as D ~ 200 $\mu m^2 \cdot s^{-1}$. Using this theoretically estimated diffusion coefficient of a swimming bacterium, it is possible to derived an estimated MSD by substituting D into $\left\langle \Delta r^2(\Delta t) \right\rangle = 4D\Delta t\left(1 - e^{-\Delta t/t_c}\right)$ for each given time Δt [9]. The crossover time t_c corresponds to the average time during a run, estimated as ~ 1.5 seconds *Table.6.1*. The theoretical estimated MSD for a swimming bacterium is plotted as a solid line in *Figure.6.34*. One expects the behaviour of bacterium to be super-diffusive over short times scales $(0.1 < t < 1s)$, due to run events, thus the diffusion is anomalous $\left\langle \Delta r^2(t) \right\rangle \propto t^{\alpha}$ where $1.5 < \alpha < 2.0$ [9]. Since the swimming mode alternates between runs and tumbles, one expects normal diffusion to be restored at longer times $(1 < t < 10s)$, where the crossover time is equal to the average run length [9, 56]. Tracking of fluorescently labelled cells in the absence of cellular interactions yields an excellent agreement between theoretical and experimental curves, *Figure.6.34*. At short time scales swimming cells shows super-diffusive behaviour with a gradient of 1.94, consistent with the theoretical curve. The transition between the super-diffusive regime to the diffusive regime occurs at ~ 1.2 s, consistent with the average run length. The corresponding swimming trajectory depicted in the inset (dark green) are representative of runs and tumbles [42, 57]; where cells swim in relatively straight lines prior to randomly altering its swimming trajectory during which they remain relatively stationary. Particle tracking of swimming bacterium experimentally verifies the theoretical expression $\left\langle \Delta r^2(\Delta t) \right\rangle = 4D\Delta t\left(1 - e^{-\Delta t/t_c}\right)$ is valid. Using this as a reference/calibration curve the characteristics of correlated swimming behaviour were investigated as a function of cellular concentration. *Figure.6.34* generally depicts that the MSD curves all have a similar characteristic profile. The MSD curves are characterised by

switching from the super-diffusive regime on small time scales to diffusive regime at larger time scales; the details are disused in the following paragraphs.

Examining tracers particles at the dilute limit $\sim\varphi_e = 0.03$ the results demonstrate tracers are influenced by the presence of the bacteria, giving rise to super-diffusive behaviour and the distinctive crossover between regimes in comparison to a purely diffusive system, *Figure.6.34*. The initial gradient is greater than normal free diffusion, a slope of 1.32 suggesting correlated bacterial collisions 'pushes' the tracers such that they exhibit super-diffusion like behaviour [9]. The MSD of tracers is increased by an order of magnitude, compared to a passive sample of pure tracers undergoing Brownian motion. Increasing the cellular concentration to semi-dilute regime, $\sim\varphi_e = 0.09$ and observing the behaviour of tracers, two distinct features are observed. Firstly super-diffusive behaviour becomes more rapid, increasing by more than 10 %. Secondly the super-diffusive regime is prolonged i.e. the crossover time increases, by ~ 30 % in respect to dilute concentration $\varphi_e = 0.03$. *Figure.6.34* depicts that for higher cellular concentration an increase in diffusion by approximately two orders of magnitude, whereby the diffusion coefficient *D* is also significantly enhanced; D = 18.5 $\mu m^2 \cdot s^{-1}$ and D = 286.6 $\mu m^2 \cdot s^{-1}$ respectively. This is also highlighted by the corresponding trajectories blue and light green curves respectively in the inset of, *Figure.6.34* where displacement is obviously increased. Our findings for passive tracers suggest that increasing cellular concentration *n*, tracers become more energetic due to the additional correlated bombardments and collisions. Thus the ballistic motion increases leading to enhanced diffusion by several orders of magnitude [7, 9, 12]. The crossover time t_c is proportional to the increase in concentration which is directly linked to the characteristic length scales and vortex size. Whereby increasing concentration *n* results in larger correlated length scale. These results are consistent with other research groups that track passive particle in bacterial baths [9, 56].

Similarly actively swimming bacteria yielded MSD curves which display the typical crossover between super-diffusive regime to a diffusive regime. However, at cellular

concentrations $\sim\varphi_e = 0.03$ the gradient of short time super-diffusive behaviour is shallower 1.68; approximately 14 % in comparison to single swimming cells. Moreover the extracted diffusion coefficient *D* for $\varphi_e = 0.03$ concentration yielded *D* = 104.2 $\mu m^2 \cdot s^{-1}$ which shows a 30 % slower diffusion coefficient than a single swimming cells, where *D* = 152.3 $\mu m^2 \cdot s^{-1}$. Moreover the cross-overtime t_c is reduced by ~ 10 % in comparison to freely swimming cells, strongly suggesting the average run length of cells are truncated in semi-dilute concentrations in comparison to freely swimming cells, *Figure.6.34*. We expected to observe enhanced diffusion of the tracer cells, as the cellular concentration *n* increases, similar to what was observed with tracer particles [9, 12, 56]. However, our results reflect the opposite trend for actively swimming cells in the dilute limit regime. The diffusion coefficient *D,* cross-over time t_c, and the initial super-diffusive behaviour of cells decreased noticeably, most likely hindered by the presence of neighbouring cells. We believe this is due to additional cellular collisions which induced tumbling, therefore the free mean path length is reduced i.e. the average run length of a cell is truncated [50]; thus observing a reduced crossover-time and diffusion coefficient. In the semi-dilute regime $\varphi_e = 0.09$, the MSD curve for actively swimming cells has increased by an order of magnitude, where the initial slop yields 1.42, a reduction of 15 % and 25 % respectively of $\varphi_e = 0.03$ regime and freely swimming cells. Similarly the crossover time t_c yielded 0.53 s, a significant decrease of ~ 56 % in comparison to freely swimming cells, although the diffusion coefficient *D* increases massively as a function of concentration *n.* Novel tracking of swimmers in this setting demonstrated a decrease in ballistic behaviour illustrated by the decrease in cross over-time t_c in contrast to tracers. One possible explanation for the reduction in cross-over time t_c for swimmers, is the fact that cells become more spatially restricted which considerably reduces the run length (also hydrodynamic interactions and cell collisions induced cellular tumbling), while the formation of vortices increases diffusivity. Cohesive structures actively recruit cells into domains via strong hydrodynamic interactions between neighbouring cells enhancing diffusion due the increased velocities of individuals in these structures [12 - 15, 50], *Figure.6.34*.

Our experimental results reflect those of recent computational simulations of active swimmers presented by Hernandez-Ortiz *et al* [50]. They simulated collective behaviour from the dilute limit to a semidilute regime $\varphi_e = 0.1 - 0.3$, similar to our experiments; where they varied the separation height *h* and examined the effects on collective behaviour. Their MSD results presented for swimmers and tracers illustrated remarkable similarities to our experimental results. At short times the MSD for swimmers was ballistic reflecting straight line motion and decreases as function of concentration *n*; illustrating the same trends observed experimentally, *Figure.6.34*. At longer times the diffusive behaviour of swimmers is restored. Increasing the cell concentration *n* decreases the diffusive behaviour of swimmers, due to increased perturbations as a result of hydrodynamic interactions and cell collisions [50]. Simulated results for tracers yielded the opposing trend to swimmers also observed in our experiments where the ballistic regime increases as a function of cell concentration. This is due to the increase in correlated cell collisions with the tracers particles as the concentration of cells increase [9]. Our experimental results, in *Figure.6.34* verify and support the findings in the model presented by Hernandez-Ortiz *et al* [50]; where our results confirm that their simulations are representative of experiments. Moreover, with our experimental techniques we can further examine the affects of the separation height *h* of a wall on the collective behaviour. Verifying and testing the predictions made by simulations is important and may provide a further insight into collective behaviour near surfaces.

The MSD curves in *Figure.6.34* for tracers and swimmer at semi-dilute concentrations $\varphi_e = 0.09$ are remarkably similar. This suggests collective behaviour is not regulated by individual and localized movements of cells; but by a global hydrodynamic coupling between large ensembles of interacting cells. This result supports the conjecture that hydrodynamic interactions generated by flagella beating are responsible for spontaneous formation of cohesive structures [9 - 15]. In concentrated suspensions individual cells generate thrust but does not maintain independent movement (velocity and direction) but are influenced and governed by the collective behaviour of multiple interacting cells which manifest itself into

coherent structures. Tracer and swimmer are almost indistinguishable at $\varphi_e = 0.09$, highlighting the fact that this statistical behaviour is purely a collective phenomenon; extending over large distances and independent of localized individual displacements. Since the MSD curves for tracers and swimmers are very similar at high concentrations, this justifies the use of passive particles to trace the fluid flow during collective behaviour since the MSD curves are almost identical. This experimental verification also rationalizes the use of tracers in previous experiments [9, 10, 56]. MSD curves for tracers and swimmers are clearly distinguishable at low concentrations where collective behaviour is weakly observed. This was expected since swimmers actively generate thrust whereas tracers rely on external collision to generate net motion.

We finally examined how the run and tumble distribution changes as a function of cellular concentration during collective behaviour. Fluorescently labelled cells enable one to identify flagella bundle arrangements in the setting of collective behaviour. We define here run as the period in which the flagella are in a bundle and a tumble as the period in which the flagella are dispersed. This is subtlety different from the tumbles observed in bright-field where tumbles are defined as reorientation of the cell body, *Chapter 2*; here tumbles are defined as flagella dispersion. With flagella imaging we have extracted the mean run length distribution of 100 individual cells as a function of cellular concentration *n*. Observations of the bundle arrangements indicate whether cells are in a run or tumble mode respectively. The average time interval of flagella bundling was extracted as the mean run length. Observations verified that dispersion of the bundle resulted in termination of net motion, although cell collisions and hydrodynamic interactions with neighbouring cells may also produce net motion. The average run length of *E. coli* cell have been previously investigated by Berg and Turner [46], their findings demonstrate that the run length of cells is exponentially distributed [46, 57]. Statistically analyzed and fitted results of measuring the average run length of the *B. subtilis* cells under the conditions of collective behaviour is presented in *Figure.6.35*.

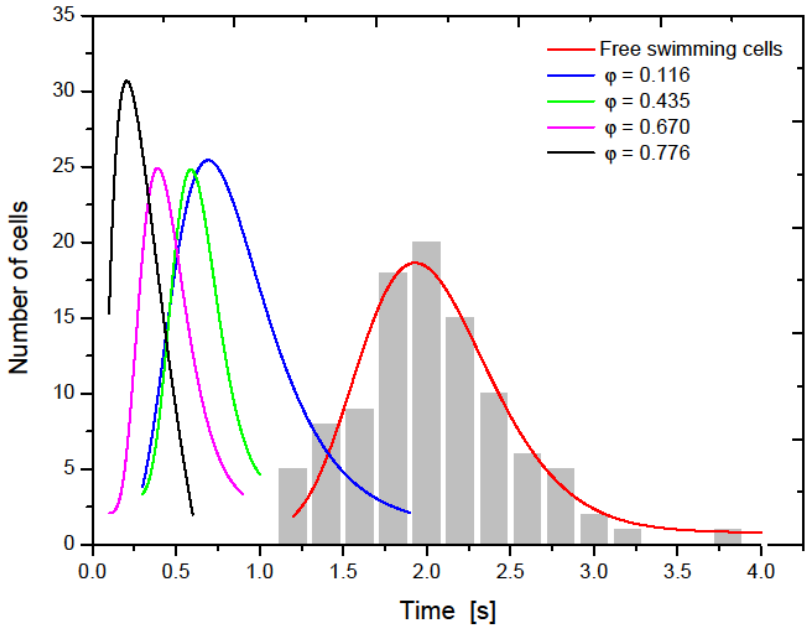

Figure.6.35: The run length distribution of 100 individual cells for each curve at increasing volume fractions. The obtained histograms were fitted with log-normal showing a good fitting, where the peak value indicates the average run length. The average run length of cells were 1.93 ± 0.31, 0.70 ± 0.18, 0.58 ± 0.08, 0.39 ± 0.07, and 0.20 ± 0.06 respectively.

Freely swimming cells between plane surfaces yielded an average run length of 1.93 ± 0.31 s. The run length distributions is slight different to the exponentially profile presented by Berg *et al* [46]. Our results fit well to a log-normal distribution where we define a run event as period of flagella being in the bundle, different to Berg's definition [42]. A possible explanation for this discrepancy is that we are investigating a mircoorganism which swims differently, *Section 6.7*. Secondly it is certainly influenced by the non-slip boundary condition which introduces hydrodynamic interactions and coupling between the cell and the surface [47, 48, 50, 52]. Cisneros *et al* mentioned in restrictive suspensions *B. subtilis* run behaviour are extended [12, 32]. Our observations indicate that the run lengths of *B. subtilis* cells are inherently longer than those of *E. coli* cells by ~ 40 %. *Figure.6.35* highlights the changes in the run distribution as function of cell concentration. The results shows as more cells are present the average run length is truncated due to cellular collisions and interactions.

At the semi-dilute regime the presence of other cells hinders the diffusion of cells due to collisions, also highlighted in *Figure.6.34.* As self-organization and structures form the average run length decreases since cells become spatially restricted reducing the mean free path to several micrometers. However since there are hydrodynamic interactions between groups of cells and the spontaneous formation of organised structures, the velocity of cells is significantly enhanced by several orders of magnitude, *Figure.6.34*. Despite decreasing run time, the mean distance a cell travels is significantly enhanced due to the massive increase in swimming velocities; hence the mean squared displacement is enhanced as a function of cell concentration, *Figure.6.34* [9]. Tracking of individual cells also revealed that they often remain trapped in several vortices for 2 - 3 s where a single cell can travel extraordinarily larger distances ~ 500 μm at enhanced diffusion by at least an order of magnitude [7, 9, 10, 12]. The majority of cells experiences bursts of acceleration when entering a vortex street also known as a jet (in between two formed vortices [10, 12, 13]) or vortex. When ejected from the vortex street or vortex cells often remain relatively stationary, hemmed in by neighbour cell until they are recruited into a subsequent vortex, *(See Movie DS1919-Lablled-Collecitve-swimming.avi).* We extracted quantitative parameters of observed vortices at increasing concentrations, such as vortex size, life time and average number of cells. Analyzing the videos, 25 independent vortices where examined for a given concentration. *Figure.6.36,* are snap-shots of representative vortices taken from each specimen. The blue circle indicates the estimated periphery of the vortex, used to extract the diameter and number of cells.

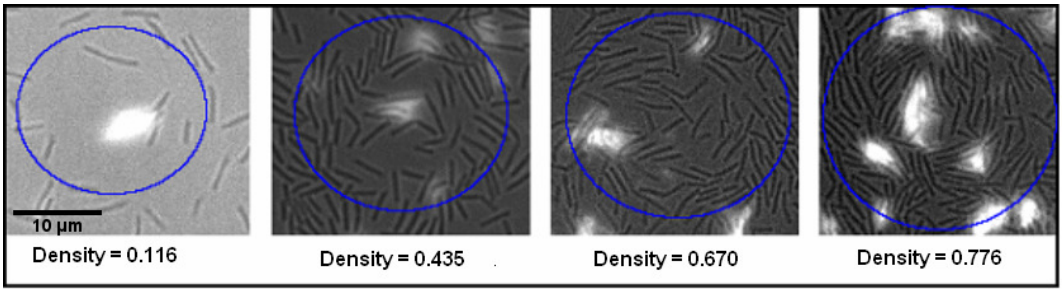

Figure.6.36: Snap-shots of vortices observed at increasing cellular volume fractions, where the average cellular density steadily increased from the dilute limit to a close packed regime. The vortex diameter and the number of cells within the vortex increase noticeably. The blue circle is an estimate of the average vortex diameter via the supposition of several frames, and we also averaged over several different vortices to extract the vortex parameters.

Table.6.5

Average Area fraction ***(φ)***	***Vortex diameter*** ***(µm)***	***Vortex life time*** ***(s)***	***Number of cell***
0.116	23.3 ± 2.3	1.04 ± 0.4	12.4 ± 2
0.435	25.9 ± 3.4	1.19 ± 0.4	57.3 ± 2
0.670	27.7 ± 3.2	1.30 ± 0.4	101.4 ± 3
0.776	30.9 ± 2.7	1.33 ± 0.4	145.6 ± 3

Table.6.5: The average statistics of 25 vortices observed with increased volume fractions, where the errors are standard errors.

The acquired results illustrate that the vortex diameter, life time and number all indicate a positive trend which appears to increase with cellular concentration φ, in accord to previous finding [8]. The characteristic length scale of vortices is linearly dependant on cellular concentration *n*, thus the vortex size is weakly dependant on φ. Our results reflect a weak correlation since an 80 % increase in volume fraction resulted in a 30 % increase in vortex size. These results suggest that the vortex properties are not strongly influenced by concentration, but by other parameters of the bacterium; i.e. cells size and swimming speeds [56]. Moreover, computational simulations have shown that surface interactions also play a role, where separation of the swimmer and the interface alters the vortex properties [50]. Further experimental investigations are required to fully understand collective cellular behaviour and what

regulates the vortex size, whether it is the size of the bacterium, swimming speeds, or separation between the surfaces.

6.11 Conclusion

The work presented in this chapter (whilst no by means exhaustive) has demonstrated that larger number ($9 \times 10^{8} - 2 \times 10^{9}$ cells per ml) of self-propelled rod shaped microorganisms such as *B. subtilis* and *E. coli* exhibits collaborative swimming patterns, often originating near oxygen contact lines. Observed vortices in drops of concentrated bacterial suspensions are typically 23.5 ± 2.3 μm in diameter and temporally stable for 1.2 ± 0.5 s. This collective dynamic behaviour can be sustained for up to an hour until the suspending fluid has evaporated. Seeding specimens with 4 μm tracer particles highlighted enhanced diffusion of solute molecules and the increase of swimming velocity of cells. This work demonstrates self-alignment of cells into a close-pack regime, permitting steric and hydrodynamic interactions that facilitate collective behaviour. Collective motility enables groups of cells to swimming on length scales and velocity scale larger than a single bacterium can achieve, thus enhances transport of essential molecules such as oxygen which influence viability of cells throughout the population [7, 12, 13]. Utilizing time-lapse video microscopy, the onset of collective behaviour in concentrated bacterial suspensions was investigated. This experiment observed how single a drop of concentrated *B. subtilis* cells evolves and undergoes several transitions leading to the onset of collective behaviour. This experiment showed bacterial concentration increase as a function of time, where cells become self-organised at the oxygen contact line. Subsequently, cells formed into domains and rapidly expanded and recruited cells; these are highly organized cells (~ 10 cells) swimming in a cohesive direction. It is precisely the close packing of cells and hydrodynamic interactions which facilitate the onset of collective swimming. Sustained vortices enhance the diffusion of tracer particles by several orders of magnitude. The measured density profile at critical points during the onset of collective behaviour showed a gradually

decrease in density ρ as a function of distance L from the oxygen contact line. At longer periods where samples become self-organized and closely packed, the density profile remains constant throughout the field of view. Our experimental findings suggest a smooth and gradual transition to collective behaviour, where the numerous processes such as cellular tumbling and hydrodynamic interactions introduce noise masking the transition from single cell swimming to collective behaviour.

A convenient and rapid method to image flagella filaments of *B. subtilis* cells in real-time, with minimal side affects was successfully established. Fluorescent labelling of *B. subtilis* cells (DS1919), demonstrated cells retained multiple flagella filaments typically 14.5 ± 3.5 per cells with an average length of 8.5 ± 0.2 μm. The side effects of the staining protocol reduced the swimming velocity of cells by ~ 15 % in comparison to non-stained cells, although the run and tumble behaviour did not change. High fluorescence excitation intensities elicited a tumble response, whereas intensities $\leq 2.86 \times 10^{-3}$ μW/μm^2 demonstrated normal swimming behaviour. Real-time visualisation of flagella filaments in freely swimming *B. subtilis* cells revealed unexpected flagella bundle arrangements, similar to filamentous *E. coli* discussed in *Chapter 5*. Generally *B. subtilis* cells form two propulsive bundles which incorporate ~ 7 flagella filaments in each co-rotating bundle. Real-time visualisation provided scientific evidence to suggest *B. subtilis* swims in a more complex manor than previously thought. It also sheds light on the assumption that *B. subtilis* cells swim in a similar fashion to *E. coli* cells. The research presented here suggests this assumption may not be strictly accurate. We suspect and our results indicate that **CCW** rotation of a single motor is sufficient to trigger polymorphic transitions which disperse the bundles during tumble events – analogues to *E. coli*. However without sufficient optical resolution to accurately observe defined polymorphic configurations and transitions, our understanding remains relativity limited leaving room for further fruitfully studies.

Reversal of bacterial locomotion when approaching an obstacle was observed with *B. subtilis* and *E. coli* cells. This was hypothesized as a method of quorum polarity

facilitating collective behaviour. The investigation examined the reversal behaviour of cells in isolation, where both cell species demonstrated a broad range of manoeuvres as they approached the obstacle. The statistics showed on average 7 % of *E. coli* cells reversed their swimming direction, in comparison to 50 % of *B. subtilis* cells. The use of fluorescently stained *B. subtilis and E. coli*, empirically verified the hypothesis of flagella flipping suggested by Cisneros *et al* [34]. It is believed from our findings that the flagella motor generates sufficient torque force to enable flagella filaments to rapidly translate to the opposite end. Reversing cellular trajectories highlighted a broad range of '*V*' shaped trajectories. Imaging of flagella filaments during such events suggests asymmetric distribution of flagella filaments is likely to be the cause. The noticeable difference between reversal statistics between bacteria species is believed to be associated with the number of flagella filaments and their distribution over the cell surface. Reversal statistics of hydrodynamically sheared *B. subtilis* cells demonstrated flagella truncation in length and number which systematically lead to a reduction of the swimming velocity and the probability of reversal behaviour. This method of flagella truncation reduces both flagella number and length making it difficult to interpret results, making them not fully conclusive. *B. subtilis* cells were suspended between two coverslips in a monolayer geometry where single cells are observed reversing in groups. The results show hydrodynamic interactions between neighbouring cells assisting in reversal behaviour. It was shown that hydrodynamic and flagella interactions between neighbouring cells induced multiple reversals of cells simultaneously providing evidence of quorum polarity and recruiting of cells.

Finally we developed a new method of suspending cells between oxygen plasma treated coverslips. This was able to sustained collective swimming behaviour, which was in a monolayer ~ 5 μm thick where individual cells are accurately resolved. Introducing fluorescently labelled cells to sample undergoing collective behaviour at the dilute limit $\varphi_e = 0.03 - 0.09$ permitted us for the first time flagella observations in real-time in the setting of collective dynamic behaviour. Observations of flagella reversal was visualised, as well as complex flagella interactions. Particle tracking

was implemented to analyze our videos and to extract the mean squared displacement. We examined how the MSD curve varies as function of concentrations *n,* for both passive tracer particles and active swimmers respectively. The results for passive tracers indicated an increase in cellular concentration enhanced diffusion by several order of magnitude due to cellular bombardments. The crossover times increased proportionally with increased concentration, consistent with previous finding, even in such dilute samples. MSD of swimmers illustrated the opposite trend, with the crossover time decreasing as a function of concentration. This is due to the reduction of the average cell run lengths, showing in *Figure.6.35,* reflecting strong hydrodynamic interactions and cellular collisions which truncate the free mean paths of cells.

The extracted MSD curves for tracers and swimmers were very similar at concentrations $\varphi_e = 0.09$ or higher, where collective behaviour is strongly pronounced. This lead to the conclusion that individual displacements created by actively swimming cells have little influence on localized movements, but rather cells are governed by collective global behaviour of the suspension. Moreover, this experiment justifies the use of tracer particles in such experiments since passive tracers and swimmer behave similarly in densely populated suspensions. This can not said about extremely dilute suspensions where collective behaviour is not so pronounced. Measuring the average run length as a function of increasing concentration appears to be anticorrelated, although the average velocity of cells increased with concentration. Observed vortices were analyzed extracting quantitative parameters such as the typical diameter and persistence time and how these parameters vary as a function of cellular concentration. The results indicate a subtle increase in vortex size and life times despite significant increase in concentrations. Therefore it was concluded these parameters are insensitive to concentration, presumably vortices properties are related to the cell size, swimming velocities and separation height which requires further experimental investigation.

Bibliography and References

[1] B. L. Partidge, *Strucutre and function of fish schools.* Scin. AM, **246**:114-137, (1982).

[2] J. Toner, Y. Tu, *Long-range order in a two-dimensional dynamical XY model: how birds fly together.* Phys. Rev. Lett, **75**:1326-4329, (1995).

[3] J. K. Parrish and W. M. Hammer, *Three Dimensional animals groups.* Cambridge University Press, Cambridge, England, (1997).

[4] T. Vicsek *et al, Novel type of Phase transition in a System of Self-Driven Particles.* Phys. Rev. Lett, **75**: 1226-1229, (1995).

[5] D. Helbin, *Traffic and related self-driven many-particle systems.* Rev. Mod. Phys, **73**:1067-1141, (2001).

[6] D. Helbing, I. Farkas, and T. Vicsek, *Simulating dynamical features of escape panic*. Nature, **407**:487-490, (2000).

[7] C. A Solari, J. O. Kessler, and R. E. Goldstein, *Motility, mixing and multicellularity*. Genet programme evolvable mach, **8**:11-129, (2007).

[8] J. T. Bonner, *On the origin of differentiation.* J. Biol, **293**: 523-528, (2003).

[9] X. L. Wu and A. Libchaber, *Particle Diffusion in a Quasi-Two-Dimensional Bacterial Bath.* Phys. Rev. Lett, **84**: 3017-3020, (2000).

[10] N. H. Mendelson *et al, Organized cell swimming motion in Bacillus subtilis colonies: Patterns of short-lived whirls and jets.* J. Bact, **181**:600-609, (1999).

[11] R. A. Simha and S. Ramaswamy, *Statistical hydrodynamics of ordered suspensions of self-propelled particles: waves, giant number fluctuations and instabilities.* Physica. A, **306**:262-269, (2002).

[12] L. H. Cisneros, R. Cortez, C. Dombrowski, R. E. Goldstein and J. O. Kessler, *Fluid dynamics of self-propelled microorganisms from individuals to concentrated population.* Exp. Fluids **43**:737-754, (2007).

[13] C. Dombrowski, L. Cisneros, S. Chatkaew, R. E. Goldstein, and J. O. Kessler, *Self-concentration and large-scale coherence in bacterial dynamics*. Phys. Rev. Lett. **93**:098103, (2004).

[14] A. Sokolov, I. S. Aranson, J. O. Kessler and R. E. Goldstein, *Concentration Dependence of the collective dynamics of swimming bacteria.* Phys. Rev. Lett, **98**:158102, (2007).

[15] A. Sokolvo, R. E. Goldstein, F. I. Feldchtein, and I. S. Aranson*, Enhanced mixing and spatial instability in the concentrated bacterial suspensions*. Phys. Rev. Lett, **80**:031903, (2009).

[16] J. P. Hernandez-Ortiz, C. G. Stoltz, and M. D. Graham, *Transport and Collective Dynamics in Suspensions of Confined Swimming Particles.* Phys. Rev. Lett, **95**:204501, (2005).

[17] J. O. Kessler, M. F. Wojciechowski, *Collective behaviour and dynamics of swimming bacteria.* In:Shapiro J.A. Dworking M (eds), *Bacteria as multicellular organisms*. Oxford University Press, New York, PP 417-450, (1997).

[18] J. O. Kessler and N. Hill, *In Physics of Biological Systems: From Molecules to Species.* Edited by H. Flyvbjerg *et al,* Springer, Berlin, Lecture Notes in Physics, **480**:325-340, (1997).

[19] J. M. Kosterlitz and D. J. Thouless, *Ordering, metastability and phase transitions in two-dimensional systems.* J. Phys. C: Solid State Phys. **6**:1181-1203, (1973).

[20] E. V. Albano, *Self-organized collective displacement of self-driven individuals.* Phys. Rev. Lett, **77**: 2129-2132, (1996).

[21] N. Shimoyama, K. Sugawara, T. Mizuguchi, Y. Hayakawa, and M. Sano, *Collective motion in a system of motile elements*. Phys. Rev. Lett, **76**:3870-387 (1996).

[22] A. Czirók, A. L. Barabási, and T. Vicsek, *Collective motion of self-propelled particles: Kinetic phase transition in one dimension*, Phys. Rev. Lett. **82**:209-212, (1999).

[23] A. Czirók, H. E. Stanley, and T. Vicsek, *Spontaneously ordered motion of self-propelled particles*. J. Phys. A: Math. Gen, **30**:1375-1385, (1997).

[24] R. Kemkemer *et al*, *Nematic order-disorder state transition in a liquid crystal analogue formed by oriented and migrating amoeboid cells*, The European Physical. Journal E, **3:**101-110, (2000).

[25] M. Nagy, I. Daruka, and T. Vicsek, *New aspects of the continous phase transition in the scalar noise model (snm) of collective motion*, Physica A, **373**: 445-454, (2007).

[26] B. Szabó, G. J. Szöllösi, B. Gönci, Z. Jurányi, D. Selmeczi, and T. Vicsek, *Phase transition in the collective migration of tissue cells: Experimental and model,* Phys. Rev. E **74**:061908, (2006).

[27] N. Sambelasvili, A. Lau, and D. Cai, *Dynamics of bacterial flows: Emergence of spatiotemporal coherent structures*, Phys. Lett. A, **360**:507-511, (2007).

[28] V. Mehandia and P. R. Nutt, *The collective dynamics of self-propelled particles.* Journal of Fluid Mechanics, **595**: 239-264, (2008).

[29] C. W. Wolgemuth, Colle*ctive swimming and the dynamics of bacterial turbulence.* Biophysical Journal, **95:** 1564-1574, (2008).

[30] R. A. Simha and S. Ramaswamy, *Hydrodynamic fluctuations and instabilities in ordered suspensions of self-propelled particles*. Phys. Rev.Lett, **89**:058101, (2002).

[31] S. Ramaswamy, R. A. Simha, and J. Toner, *Active nematics on a substrate: Giant number fluctuations and long-time tails.* Europhysics Letters **62**:196-202, (2003).

[32] L. Cisneros, C. Dombrowski, R. E. Goldstein and J. O. Kessler, *Reversal of Bacterial Locomotion at an Obstacle.* Phys. Rev. E, **73**: 030901, (2006).

[33] I. Tuval, L. Cisneros, C. Dombrowski, C. Wolgemuth, J. O. K and R. E. Goldstein, *Bacterial swimming and oxygen transport near contact lines.* Proc. Natl. Acad. Sci, 102:2277-2282, (2005).

[34] M. B. Short, C. Solari, S. Ganguly, T. R. Powers, J. O. Kessler, and R. E. Goldstein, *Flow driven by flagella of multicellular organisms enhance long-range molecular transport,* Proc. Natl. Acad. Sci, **103**:8315-8219, (2006).

[35] R. E.Yasbin, P. I. Fields, and B. J. Andersen, *Properties of Bacillus subtilis 168 derivatives freed of their natural prophages*. Gene **12**:155–159, (1980).
[36] K. M. Blair, L. Turner, J. T. Winkelman, H. C. Berg, D. B. Kearns, *A Molecular Clutch Disables Flagella in the Bacillus subtilis Biofilm.* Science, **20**:1636-1638, (2008).
[37] K. Barker, *At the bench: a laboratory navigator.* Cold Spring Harbor, N.Y. Cold Spring Harbor Laboratory Press, (2005).
[38] N. C. Darnton, L. Turner, S. Rojevsky, and H. C. Berg, *On Torque and Tumbling in Swimming Escherichia coli,* Journal of bacteriology, **189**:1756–1764, (2007).
[39] L. Turner, W. S. Ryu and H. C. Berg, *Real-time imaging of fluorescent flagellar filaments.* J. Bacteriol, **182**:2793-2801, (2000).
[40] M. L DePamphilis and J. Adler, *Fine structure and isolation of the hook-basal body complex of flagella from Escherichia coli and B.acillus subtilis*. J. Bacteriol, **105**:384-395, (1971).
[41] T. Åkerlund, K. Nordström, and R. Bernander, *Analysis of Cell Size and DNA Content in Exponentially Growing and Stationary-Phase Batch Cultures of Escherichia coli.* J. Bacteriol, **117**: 6791–6797, (1995).
[42] H. C. Berg, *E. coli in Motion,* Biological and Medical Physical Series, Spring Verlag, (2003)
[43] K. C Neuman, E. H. Chadd, G. F. Liou, K. Bergman and S. M. Block, *Characterization of photodamage to Escherichia coli in optical traps*. Biophys. Journals, **77**:2856-2863, (1999).
[44] E. M. Purcell, *Life at low Reynolds number.* American Journal of Physics, **45**:3-11 (1977).
[45] S. Chattopadhyay, R. Moldovan, C. Yeung, and X. L. Wu, *Swimming efficiency of bacterium Escherichia coli*. Proc. Natl. Acad. Sci, USA, **103**:13712-13717, (2006).
[46] H. Berg and L. Turner, *Cells of Escherichia coli swim either end forward.* Proc. Natl. Acad. Sci, USA, **92**:477- 479, (1995).
[47] E. Lauga and T. R. Powers, *The hydrodynamics of swimming microorganisms.* Rep.Prog.Phys. **72:**096601, (2009).
[48] A. P. Berke, L. Turner, H. C. Berg, and E. L, *Hydrodynamic Attraction of Swimming Microorganisms by Surfaces*. Phys. Rev. Lett, **101**: 038102, (2008).
[49] R. M. Macnab, *Bacterial flagella rotating in bundles: a study in helical geometry.* Proc.*Natl.Acad.Sci* **74**:221-25, (1977).
[50] J. P. Hernandez-Ortiz, P. T. UnderHill, and M. D. Graham, *Dynamics of confined suspensions of swimming particles*. J. Phys. Condens. Matter, **21:** 204107, (2009).
[51] T. C. Flynn and J. Ma, *Theoretical Analysis of Twist/Bend Ratio and Mechanical Moduli of Bacterial Flagellar Hook and Filament.* Biophys. Journals, **86**:3204-3210, (2004).
[52] E. Lauga, W. R. DiLuzio, G. M. Whitesides, and H. A. Stone, *Swimming in Circles: Motion of Bacteria near Solid Boundaries*. Biophysical Journal, **90**:400-412, (2006).

[53] J. C. Crocker and D. G. Grier, *Methods of digital video microscopy for colloidal studies*. J. Colloid. Interface. Sci, **179**:298-310, (1996).
[54] http://www.physics.emory.edu/~weeks/idl/
[55] J. Happel and H. Brenner, *Low Reynolds Number Hydrodynamics.* Springer, New York, 1st Ed, (1981)
[56] H. P. Zhang *et al*, *Swarming dynamic in bacterial colonies.* EPL, **87**:48011, (2009).
[57] H. C. Berg, *Random Walks in Biology*, Princeton Paperbacks (Princeton University Press, Princeton, New Jersey, (1993).
[58] S. M. Hong, S. H. Kim and J. H. Kim, H. I. Hwang, *Hydrophilic Surface Modification of PDMS Using Atmospheric RF Plasma.* Institute of Physics Publishing Journal of Physics: Conference Series **34**:656–661, (2006).
[59] L. H. Cisneros, J. O. Kessler, R. Ortiz, R. Cortez, M. A. Bees, *Unexpected Bipolar Flagellar Arrangements and Long-Range Flows Driven by Bacteria near Solid Boundaries.* Phys. Rev. Lett, **101**:168102, (2008).

Chapter 7 : Conclusions & Future work

This chapter summarizes and reviews the achievements presented in this thesis. This project has raised several fascinating questions with some of them answered. Unanswered questions can provide the foundations for further research regarding cellular motility and collective flocking behaviour.

7.1 Investigating spherical *E. coli* cells

Chapter 4 presented an investigation regarding active motility in spherical mutant *E. coli* cells. The motivation to conduct this investigation was to provide a strain of *E. coli* which is motile and spherical [1]. Motile spherical cells can be used experimentally to validate predictions from hydrodynamics models, which often models cells as a sphere [2, 3]. The investigation compared the motility of wild-type *E. coli* HCB1 to a spherical mutant KJB24 cells. The extracted diffusion coefficient D for spherical cells yielded an order of magnitude lower than a similar sized diffusing sphere. We examined spherical cells with force measurement optical tweezers, which demonstrated that spherical cells behave very similar to passive colloids. The semi-solid chemotatic plate assay showed that spherical cells do not migrate outwards, but remain localized at the inoculation site. These two experiments raised doubts of the existences of flagella filaments in spherical cells. We subsequently implement AFM imaging to directly visualize external appendages in both HCB1 and KJB24. The results conclusively showed numerous external organelles distributed over spherical cell which were identified as fimbriae [4, 5] rather than flagella. This explains why KJB24 cells diffused significantly slower due to the increase in effective hydrodynamic radius and that they do not actively swim.

The reasons why spherical cells do not retain flagella filaments is not obvious, it is believed to be a direct consequence of deleting PBP. One can investigate further as to which protein regulates flagella synthesis in KJB24 cells and determine if it is possible to change the cell morphology without effecting flagella synthesis. Or one can find alternative means of creating spherical *E. coli* cells without deleting either RodA or PBP. Recently a paper published by Freire *et al* [18] shows that *E. coli* cells which over express the gene BolA (a stress response gene) induce a spherical morphology. They demonstrate that by increasing the levels of BolA, it can inhibit the cellular elongation mechanism, resulting in spherical cells (pTK512 strain). Thus this method of producing spherical cells is less invasive than deleting proteins. Further studies can acquire the strain pTK512 and examine motility in these spherical cells with the techniques developed in this project; and subsequently compare motility in spherical cells to hydrodynamic models. This would be very beneficial to the field of biophysics as cells are often modelled as spheres.

7.2 Examining filamentous *E. coli* cells

In *Chapter 5* we investigated cellular motility as a function of cell body length in filamentous *E. coli* cells. When *E. coli* cells are stressed they trigger an 'SOS' response and grows into filaments [6], but often remaining motile. We investigated how these cells remain motile despite the increased in cell lengths and addressing the mechanism of thrust generation. We experimentally demonstrated that cells incubated cells with 60 µg/ml cephalexin does not change the growth rate verifying G. Rolinson [7]. High speed video-microscopy showed supportive evidence that filamentous cells rotate periodically about central body axis similar to wild-type cells. The swimming velocities were measured as a function of cell length in bright-field, demonstrating that they are motile up to ~ 50 µm. The average swimming velocity was extracted as ~ 20 μms^{-1} for a range of cell lengths up to 30 µm. Tumbles events were omitted in filamentous cells beyond 6 µm in body length. Real-time flagella imaging enables one to visualize the flagella bundle arrangements

in filamentous cells at various body lengths for the first time. This showed that filamentous cells form multiple bundles at random locations along the cell body as an adaptive method to sustain motility. The number of flagella filaments per unit length was measured as a constant for three generations consistent with Nishimura *et al* [8].

Using dark-field microscopy and a high speed camera, the average body and flagella rotations rates was determined. The experimentally measured swimming parameters *v,* and Ω were used to estimate average thrust forces *F,* and torque *N.* Purcell's model was used to describe motility in normal sized cells where the model agrees with the experimental data reasonably well [9, 10]. The Purcell model was used to predict the experimental data-set for filamentous cells, where the RFT coefficients were scaled to fit the experimental values of F, N, Ω, ω and v simultaneously. Thus a scaling the RFT coefficients *A, B* and *D* by a factor α (very similar to the number of observed bundles), demonstrates that the scaled Purcell's models can describe motility in filamentous cells surprisingly well demonstrating similar trends to the experimental data. Thus Purcell's model with appropriate scaling can estimate the experimental values of F, N, Ω, ω and v with reasonable accurately; despite being a very simplistic model of swimming filamentous cells.

Fluorescent staining experiments showed flagella bundles forming on the side walls of the cell to sustain motility. Often flagella bundles would disperse and reformed with different a population of flagella filament thus flagella bundles can form at different locations along the cell body. Due to insufficient camera sensitivity and acquisition rate it was not possible to analyze these events. With a more sensitive and faster camera it might be possible to examine these interesting events in more detail. This may provide a better understand why filamentous cells beyond 6 μm do not tumble. Moreover, it may lead to more complex polymorphic transitions and may shed light on how flagella filaments interact with each other. A useful parameter which we did not measure was the flagella motor torque in filamentous cells. By measuring the torque in filamentous cells can provide an additional fitting parameter in the Purcell's model, which can be used to improve hydrodynamic

models. Moreover, it would be very interesting to observe if the motor torque is consistent between different motors along the filamentous cells. Finally, although the Purcell model fits the experimental data reasonably well there are still discrepancies. The current model significantly oversimplifies how filamentous cells swim, and further work can develop more realistic models and our data-set can be used as starting point for theorist. Such improvements to the models can incorporate the additional drag caused by extra flagella filaments and modelling flagella bundles which act at a tangent to the cell body. This can provide a further insight into the motility, especially the effects of swimming near surfaces or in groups.

7.3 Investigating collective bacterial swimming

Chapter 6 presented research focused on collective swimming behaviour of *B. subtilis* cells, where concentrated suspension of self-propelled particles (~ 2×10^{9} cells per ml) exhibit collaborative swimming patterns. We experimentally observed and maintained collective swimming and we determine the typical vortex length and time scales which where consistent with previous reports [11 - 14]. Seeding samples with 4 µm tracer particles highlighted the enhanced diffusion and transport properties of collective flocking behaviour of cells. The onset from single cell behaviour to collective behaviour was investigated using time-lapse video-microscopy. This showed concentrated cell suspensions undergo several distinct phases before vortex formation was initiated. Typically we observed a gradual influx of cells towards the oxygen contact line where they self-organize into domains. Cells in these domains are highly organised and swim in a cohesive direction, and these domains rapidly expand from a few microns to ~ 20 µm recruiting misaligned cells as they expand. During the smooth and gradual transition numerous processes occur such as tumbling, collisions and collective beating of flagella which facilities the onset of collective swimming and is believed to originate from hydrodynamics and cell collisions.

We introduced for the first time flagella visualisation in *B. subtilis* cells with high resolution. Results show cells swimming with multiple flagella bundles which contradict the general conjecture that *B. subtilis* swim like *E. coli* cells [13 - 15], *Figure.5.12 and Figure.6.16*. Subsequently, we examined the locations of flagella filaments during bacterial reversals when approaching an obstacle. Cellular reversal is hypothesized as a method of quorum polarity facilitating collective behaviour [16]. The use of fluorescently stained *B. subtilis* and *E. coli* verified the hypotheses of flagella flipping [16]. We investigated the effects of flagella truncation on the reversal behaviour, and results imply a reduction in flagella number reduces the swimming velocity and reversal probability; although the results are not fully conclusive. We investigated how reversal probability changes when cells are swimming in groups by examining the velocity profiles of single cells. The experiment showed hydrodynamic interactions between neighbouring cells assisting the reversals and inducing multiple cells to reverse simultaneously, providing strong evidence of quorum polarity [14, 16]. Finally, collective behaviour in a semi-dilute regime was investigated. A drop of a suspension of cells containing a small tracer amount of fluorescently labelled *B. subtilis* was confined between two coverslips, providing our system which we could examine how stained and non-stained cells interact in the setting of collective behaviour. This enables for the first time direct visualization of flagella filaments and bundle arrangements in the setting of collective behaviour. Using a 2D particle tracking technique the mean squared displacement was extracted for active swimmers and for 4 μm passive tracers at various cell concentrations $\varphi_e = 0.03 - 0.09$. The results typically showed a super diffusive regime at short time scales and a diffusive regime and at longer time scales. The crossover time for passive tracer particles increased proportionally with increasing concentration consistent with previous finding [11], however for active swimmers the opposite trend is observed consistent with recent simulation work [17].

We presented fluorescent labelling of *B. Subtilis* cells revealing that cells swim with multiple flagella bundles, similar to filamentous *E. coli* cells discussed in *Chapter 5*. Due to camera limitations it was not possible to examine the polymorphic transitions with sufficient resolution during tumble events. Thus more sensitive camera would also enable one to examine the polymorphic transitions with greater detail, and a comparative study to *E. coli* can be conducted. Improved flagella imaging may offer a better understating in thrust generation in *B. subtilis* cells, providing a more complete insight into to collective behaviour. Increased resolution of flagella imaging may shed light onto the polymorphic transitions required to actively recruit adjacent cells into a cohesive swimming direction and leading to collective behaviour. Moreover, one can also study collective behaviour with fluorescently labelled *E. coli* cells in our geometry (between oxygen plasma coverslips) and compare the recruiting mechanism between species, which may provide further insight into how the number of flagella filaments effects the recruitment of cells. Additionally one can also investigate the effects of cell length in regards to collective swimming, and determine if vortex size is dependant on cell length and how cellular reversal behaviour changes as a function of body length.

In this thesis we obtained a data set for the run tumble statistics for *B. subtilis* cells near an interface. It would be complementary to this work if a tracking microscope is used to extract run and tumble in bulk fluid; which can be used for comparative purposes in future studies with *B. subtilis* cells. Developing a method which can systematically remove entire flagella filaments without truncating the remaining flagella filaments would be most beneficial in terms of the presented shearing experiment. Since this would enable one to conclusively examine whether flagella number reduces the probability of reversal events as our results suggests. Finally, now that we have developed a method to sustain collective behaviour in robust samples (samples which not prone to evaporation, drift and rupture like soap films), it now enables one to perform optical trapping of single cells in the setting of collective behaviour. One can perform force measurements to probe the force fluctuations a cell experience during collective behaviour, extending the work of

Soni *et al* [19]. With the force measurement optical tweezers and the novel method of sustaining collective behaviour in 2D with fluorescently labelled cells, it opens up the possibilities to probe long-ranged pattern formation and the onset of collective swimming with more details furthering our understanding of collective swimming behaviour. Moreover, with fluorescently stained cells permits one to investigate flagella the role of flagella interactions in the setting of collective for the first time which can provide fruitful insights into collective behaviour.

Bibliography and References

[1] T. Baba *et al, Construction of the Escherichia coli K-12 in-frame, single-gene knockout mutants: The Keio collection,* Molecular systems biology, **2**:E1–E11, (2006).

[2] T. Ishikawa, G. Sekiya, Y. Imai, and T. Yamaguchi, *Hydrodynamic interactions between two swimming bacteria*. Biophysical Journal, **93**:2217-2225, (2007).

[3] L. H. Cisneros, R. Cortez, C. Dombrowski, R. E. Goldstein and J. O. Kessler, *Fluid dynamics of self-propelled micro organisms form individuals to concentrated population.* Exp. Fluids **43**:737-754, (2007).

[4] M. T. Madigan and J. M. Martinko, *Brock Biology of microorganisms.* Prentice Hall, Eleventh Edition, (2006).

[5] H. C. Berg, *E. coli in Motion,* Biological and Medical Physical Series, Spring Verlag, (2003).

[6] R. D'Ari and O. Huisman, *Novel mechanism of cell division inhibition associated with the SOS response in Escherichia coli*. J. Bacteriol, **15**:243-250, (1983).

[7] G. N. Rolinson, *Effect of β-Lactam Antibiotics on Bacterial Cell Growth Rate.* Journal of General Microbiology, **120**: 317-323, (1980).

[8] A. Nishimura, Y. Hirota , *Coordination of flagellar formation and cell division in Escherichia coli.* Annu. Rep. Natl. Inst. Genet. Mishima **32**:31-33, (1981).

[9] S. Chattopadhyay, R. Moldovan, C. Yeung, and X. L. Wu, *Swimming efficiency of bacterium Escherichia coli*. Proc. Natl. Acad. Sci, USA, **103**:13712–13717, (2006).

[10] N. C. Darnton, L. Turner, S. Rojevsky, and H. C. Berg, *On Torque and Tumbling in Swimming Escherichia coli,* Journal of bacteriology, **189**:1756–1764, (2007).

[11] X. L. Wu and A. Libchaber, *Particle Diffusion in a Quasi-Two-Dimensional Bacterial Bath.* Phys. Rev. Lett, **84**: 3017-3020, (2000).

[12] N. H. Mendelson *et al, Organized cell swimming motion in Bacillus subtilis colonies: Patterns of short-lived whirls and jets.* J. Bact, **181**:600-609, (1999).

[13] C. A Solari, J. O. Kessler, and R. E. Goldstein, *Motility, mixing and multicellularity*. Genet programme evolvable mach, **8**:11-129, (2007).
[14] L. H. Cisneros, R. Cortez, C. Dombrowski, R. E. Goldstein and J. O. Kessler, *Fluid dynamics of self-propelled microorganisms from individuals to concentrated population.* Exp. Fluids **43**:737-754, (2007).
[15] C. Dombrowski, L. Cisneros, S. Chatkaew, R. E. Goldstein, and J. O.Kessler, *Self-concentration and large-scale coherence in bacterial dynamics*. Phys. Rev. Lett. **93**:098103, (2004).
[16] L. Cisneros, C. Dombrowski, R. E. Goldstein and J. O. Kessler, *Reversal of Bacterial Locomotion at an Obstacle.* Phys. Rev. E, **73**: 030901, (2006).
[17] J. P. Hernandez-Ortiz, P. T. UnderHill, and M. D. Graham, *Dynamics of confined suspensions of swimming particles*. J. Phys. Condens. Matter, **21:** 204107, (2009).
[18] P. Freire, R. N. Moreira and C. M.Arraiano, *BolA Inhibits Cell Elongation and Regulates MreB Expression Levels.* J. Mol. Biol, **385**:1345-51, (2009).
[19] G. V. Soni, B. M. Jaffar Ali, Y. Hatwalne, and G. V. Shivashankar, *Single Particle Tracking of Correlated Bacterial Dynamics.* Biophysical. Journal, **84**:2634-2637, (2003).

Appendix A

The following describe the experimental methods to image bacterial near an oxygen plasma treated coverslip which renders the surface hydrophilic.

Cell preparation. A typical single colony of *B. subtilis* YB886 was harvested via a loop form the working plate was used to inoculate a 5 ml of fresh of Luria-Bertani broth in a test tube. Samples were permitted to incubate overnight for 16 hours at 30° C shaking at 200 rpm. Subsequently 50 µl of the stationary phase culture was utilized to inoculate a further 50 ml of LB which was incubate for a further 5-6 hours to mid-exponential phase, $(OD)_{600nm}$ = 1.2. Bright-field observations depict cells swimming at velocities between 20-35 μms^{-1} where ~ 90 % of visualised cells were motile demonstrating classic run and tumble behaviour. 1ml of cell culture was harvested in exponential phase and washed in a motility buffer (**MB**). Washed cells were re-suspended back into 1ml micro test tube at a higher than normal concentrations of approximately 1×10^{9} per ml.

Slide preparation. Coverslips (Menzel-Gläser, 22 × 50mm thickness 0.13-0.17mm, MNJ-350-070 P) where are cleaned with absolute methanol with an ultra fine microfibre cloth. Cleaned coverslips were placed in Plasma Etch system (Model: BT1, Plasma Etch, Carson City) where it was exposed to oxygen plasma for 60 seconds with 75 W plasma power and an oxygen flow rate of 150 sccm (see reference [2]). . Coverslips where subsequently stored in distilled water until they where read for use. Coverslips were dried with compressed air prior to being mounted on the microscope stage; where the surface of the coverslips is rendered hydrophilic; further details see reference [58] in *Chapter 6*.

Imaging. Imaging is performed from below using an inverted microscope, Nikon Eclipse TE2000-U with a 60 × water immersion objective (Plan Apo, N.A 1.2 working distance 0.22mm with collar correction) at room temperature. The microscope was configured with standard *Köhler illumination* where movies and images where acquired from a Marline F-14582 CCD camera at 17fps. For time-lapse recording images were acquired at 1 fps.

Appendix B

Below describes the experimental procedures used to fluorescently label flagella filaments in *B. subtilis* DS1919.

Fluorescent Labelling. *B. subtilis* strain DS1919 was streaked out onto nutrient 1.5 % nutrient agar containing LB-broth and 100 µg/ml of spectinomycin (sigma, S4014). Cell colonies where grown overnight at 37° C until isolated colonies formed. A typical isolated colony was used to inoculate 5

ml of LB-broth in a test-tube with the addition of 100 µg/ml of spectinomycin. The inoculated culture was incubated in an orbital shaker 200 rpm at 30° C. After 16 hours of incubation, a 50µl sample was utilized to inoculate a secondary test tube containing 5 ml of f LB, for approximately 4-5 hours until mid-exponential phase. A 10 µl sample was used to verify bacterial motility prior to staining. 1 ml of the exponential phase sample was harvested at $(OD)_{600nm}$ ~ 1.0 – 1.5, samples where washed centrifuging in eppendorf at 2000 rpm for 5 minutes. Samples were gentle re-suspended and washed once in T–Base buffer (15 mM (NH4)2SO4, 80 mM K2HPO4, 44 mM KH2PO4, 3.4 mM sodium tri-citrate, and 3.0 mM MgSO4·6H20). The supernatant was poured off and re-suspended in 50 µl of T-Base buffer containing mixture of 10 µg/ml of Alexa Fluor 488 C5 maleimide (Molecular Probes). This was incubated for 20 minutes at room temperature 23° C, after staining cells were washed twice with 2 ml T-Base-buffer prior to the cell being re-suspended in 50 µl of motility buffer (0.01 M $KP0_4$, 0.067 M NaCl, 10^{-4} M EDTA [pH 7.0]).

Preparing slides. Fluorescently labelled cells were imaged on spin coated coverslip or on oxygen plasma treated coverslips.

Acquiring images. Fluorescently stained *B. subtilis* cells where imaged at room temperature using Nikon Ti-U Research Inverted epi-fluorescence microscope, in conjunction with either a 60 × water immersion objective (Plan Apo, N.A 1.2 and a working distance of 0.22mm) or a 40 × oil immersion objective (plan Fluor, N.A 1.3 and a working distance of 0.20mm). The microscope was configured with standard *Köhler illumination* and a standard epifluorescence mode for fluorescent imaging. Bright-field and fluorescent images where acquired with a monochrome CoolSnapHQ^2 CCD camera supplied by photometric. The camera is cooled to -30ºC and is capable of acquiring frames up to 100 fps second which was used in conjunction with a commercialized software (Metamoroph Version: 7.5.5.0). Fluorescently labelled cells were imaged with the same camera at 10 fps in synchronization with a mechanical shutter (*Smart*Shutter, Lambda SC control unit) which strobe the illumination source. In florescent mode samples were strobed to prevent unnecessary illumination, which may cause cell damage due to prolonged exposure to excitation intensity. Fluorescent imaging utilized a filter cube 49002 ET-GFP (FITC/Cy2, Chroma Technology Corp), excitation 470 nm and emission 525 nm.

Images analysis. The videos clips where recorded as TIF stacks using the live cell imaging tools in the commercialised Metamorphic software, converting into an .avi format. These videos where later converted into 8-bit grey scale image using National Instrument Vision (Version 7.0, Austin TX). Individual frames where then converted into a virtual TIF stack using ImageJ (http://rsb.info.nih.gov/ij). Sequences of interesting events were manual selected and digitally enhanced (where stated). Track of individual cells was performed manually using the Manual tracking plugin, to determine the average swimming velocity of cells. Calibration of the camera/images was performed using a Richardson slide test slide (Generation 3, model 80302, Electron Microscopy Science).

Appendix C

Below describes the experimental procedures used to create a passive obstacle highlight the cellular reversals without body reorientation. This experiment set-up is analogous to Cisneros *et al* reference [32] *Chapter 6,* where we analyzed both *E. coli* and *B. subtilis* during this experiment.

Cell preparation. Both *E. coil* (HCB1) and *B. subtilis* (YB886 and DS1919) where incubated with motility procedure. The samples were then diluted by a factor of 1:1000 sufficient for isolated bacteria reversal events without interlopers interfering. Fluorescently labelled cell were also used in this experimental configuration.

Preparing slides. Coverslips (Menzel-Gläser, 22 × 50mm thickness 0.13-0.17mm, MNJ-350-070 P) where cleaned with ethanol and ultra fine microfibre cloth before they where spin coated with 1 % agarose (*Sigma*-Aldrich). The advantage of this method renders the surface hydrophilic promoting motility and avoiding tethering of cells. A ~ 700 µm diameter glass sphere is position gently in the centre of the spin coated coverslip with forceps. Subsequently 20 µl of the diluted samples (above) were gently pipetted on top of position bead where the sessile drop coved the base of the glass sphere. To prevent evaporation a humidity chamber was used.

Imaging. Cell imaging was performed from below using an inverted microscope, Nikon Eclipse TE2000-U with a 60 × water immersion objective (Plan Apo, N.A 1.2 working distance 0.22mm with collar correction) which was performed at room temperature. The microscope was configured with standard *Köhler illumination* in bright-field, movies/images where acquired form Marline F-14582 at 17 fps.

Appendix D

Below describes the experimental protocol to suspend *B. subtilis* cells in a monolayer in between two coverslips at a semi-dilute regime. Permitting one to observed reversal behaviour in groups and the near an oxygen contact line.

Cell preparation. *B. subtilis* YB886 where incubated with motility procedure. The samples were then diluted by a factor of 1:600 to a semi-dilute regime ~ 2×10^{8} per ml suspended in motility buffer.

Preparing slides. Coverslips (Menzel-Gläser, 22 × 50mm thickness 0.13-0.17mm, MNJ-350-070 P) where cleaned with ethanol and ultra fine microfibre cloth before they where spin coated with 1 %

agarose (*Sigma*-Aldrich) on a single coverslip. A 5 µl drop of the semi-dilute cells suspension was placed in the centre of the treated coverslip. A secondary cleaned slide coverslip was placed gently on top starting from one edge first. This created a very thin bacteria monolayer where cells are restricted in 2D.

Imaging. Same as previous experiment described above in Appendix D.

Appendix E

The following discuses the protocols for imaging flagella filaments in between two oxygen plasma treated coverslips, enabling flagella filaments to observe in the setting of collective swimming.

Cell preparation. *B. subtilis* strain DS1919 cells were incubated with the motility procedure as previously conducted. Half of the exponential phase sample was fluorescently labelled using the protocol described in Appendix D. Cells which have been fluorescently stained where suspended into motility buffer. 1 ml of the non-stained cells (~ 8×10^{8} cells per ml) were washed in motility buffer, where the two samples were mixed in the ratio of 2:5 of the fluorescently labelled cells. This creates a sample where ~ 20 % of cells are fluorescently labelled acting as tracers.

Slide preparation. Coverslips 22 × 50mm and 22 × 22 mm where initially cleaned with absolute ethanol with an ultra fine microfibre cloth. The cleaned coverslips are placed in (Plasma Etch system: Model: BT1, Plasma Etch, Carson City) where it was exposed to oxygen plasma for 60 seconds with 75 W plasma power and an oxygen flow rate of 150 sccm (see reference [2]). Coverslips where subsequently stored in sterilized distilled water until they where ready for use. Coverslips were dried with compressed air, the 22 × 50 mm coverslip is the base of the sample, where a 2 µl drop of the prepared sample was gently place in the centre of the slide. The secondary smaller coverslip was gently lower onto the drop from creating a thin monolayer of bacterial suspension, where collective behaviour was observed. Typical separation distance was measured as 5 – 6 µm.

Imaging. Cellular imaging was the same as Appendix D where the videos here were recorded at 10 fps.

Appendix F

This section outlines briefly the molecular chemistry involved in *E. coli* flagella staining. Details of fluorescent labelling of cells can be found in reference [3 - 5].

Flagella filaments are comprised of thousands (~ 20,000) subunits of the protein flagellin [6, 7]. Flagellin proteins are made up of peptide chains that form short polymer links of amino acids in a defined sequence. In the case of flagella staining of *E. coli,* the amino acids of most interest are the lysines, *Figure.A.1.* In outer sub-domain structure of flagellin FliC there are three exposed lysine residues [3, 4]. The side-chain of the lysine exposes a NH_2 which is not involved in filament assembly (peptide chain), where both the N-terminus and C-terminus are *Figure.A.3.* The exposed NH_2 molecule can be used as a non-specific binding site for fluorescent dyes, where Turner *et al* experimented with several different Alexa Fluor succinimidyl esters dyes [3]. Since there are several thousand exposed lysine's along flagella filament, labelling the side-chain permits visualization of the entire flagella filaments.

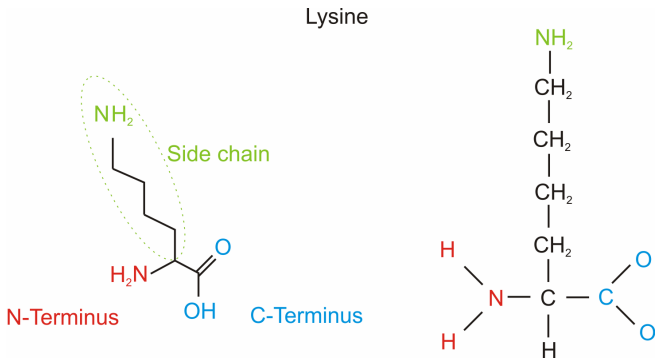

Figure.A.1: Depicts the molecular structure of the α-amino acid lysine resesidue, where NH_2 is the exposed side-chain and N-Terminus and C-Terminus are highighted in red and blue respectively. The side-chain enables non-specific binding of lysine with succinimidyl esters dyes molecules.

Linking of amino acids is formed by a condensation reaction where a peptide bond is formed between the N-Terminus and the C-Terminus to form the structure of the peptide [5]. In a peptide chain there can be several hundred peptide bonds linking various amino acids in a specific sequence known as a peptide sequences. *Figure.A.2* illustrates the formation of the peptide bond between three amino acids found in the peptide sequence of flagellin in K-12 *E. coli* [4][1]. The amino acid

[1] For the DNA codon and nucleotide sequence see reference [33]

sequences of interest are those where a lysine is present (i.e. a stainable lysine amino acids with a free NH_2 binding site), for example, Alanine, Lysine, Aspartic acid (AlaLysAsp). When the peptide bond is formed in a reaction, addition water molecules are released this known as a dehydration synthesis reaction [8]. This reaction can link numerous amino acids inside a peptide chain sequence.

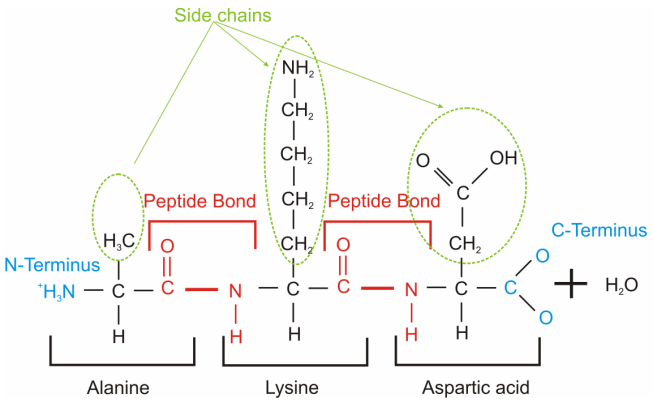

Figure.A.2: Depicts peptide bonds of three amino acids Alanine, Lysine, and Aspartic present in the flagellin peptide chain. At both ends of the peptide chain are the N-Terminus and C-Terminus respectively; the side-chain of each amino acid is not involved in the reaction to from the peptide bonds. Additionally during this reaction, it releases two additional water molecules.

The amino acid lysine presents a side-chain with a free NH_2 molecule, which is used to bind a fluorescent molecule to fluorescently label the entire flagella filament. The fluorescent dye molecule used is Cy3 (PA23001, Amersham Pharmacia Biotech, Newark, NJ) which is extremely reactive, where the molecular structure is illustrated in *Figure.A.3*.

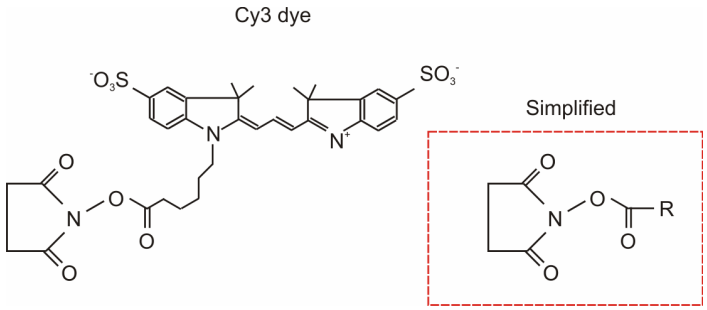

Figure.A.3: Illustrates the molecular structure of Cy3 used in the staining protocol to fluorescently stain flagella filaments in E. coli cells. The inset is the simplified molecule structure; however it only represents the active group involved in the reaction. Where, R is the fluorescent component of the dye molecule that permits fluorescent visualization of flagella filaments (the Ester group type is a very reactive to NH_2).

The labelling reaction is showing in *Figure.A.4* combines the active dye molecules with NH_2 (green reaction). Once the reaction is completed there is strong covalent bond between target lysine and the dye molecule. For convenience the side-chain of the amino acid is often labelled R', where R' is not involved with the construction of the peptide bonds.

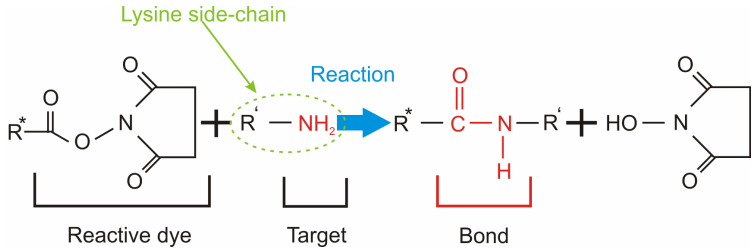

Figure.A.4: Schematic diagram molecular reaction of the dye molecules and the side-chain of the target lysine. The resultant reaction leads to a strong covalent bond between the dye molecules and the expose NH_2 molecule. Where R^* is the fluorescence component of the dye molecule, and R' is the former part of the lysine side-chain apart from the NH_2 molecule.

This method of fluorescently labelling cells was extremely effective where real-time visualisation of flagella filaments were recorded with sufficient detail; with comparable image quality to those presented by Turner *et al* [3, 5].

Supplementary videos

HCB1-Run&Tumble.avi: Fluorescently labelled *E. coli* cells swimming near a surface demonstrating the classic run and tumble behaviour. During tumbles flagella filaments undergo polymorphic transitions which chaotically re-orientates the cell. The tumble is indicted by the red circle.

HCB1-Filament-rotating.avi: A 10 µm filamentous *E. coli* cells swimming freely, with the appearances of body deflections.

HCB1-Filament-rotating-5fps.avi: A swimming filamentous *E. coli* cells recorded with a high speed camera played back at 5 frames per second. Shows periodic body rotation indicated by the kink as it goes in and out of focus.

HCB1-Stained-swimming: Digitally enhanced filamentous *E. coli* cell swimming freely ~ 5 µm above a glass surface. Shows cell with multiple bundles protruding out lateral side walls generating thrust at a tangent. Also shows evidence that the cell body rotates by the location of the flagella filaments.

YB886-Collective-swimming.avi: Closed-packed motile *B. subtilis* cells in a drop exhibiting collective swimming and vortex formation after several minutes.

YB886-Edge-Tracers.avi: Collective swimming behaviour of *B. subtilis* at an edge of a drop seeded with 4 µm tracer particles. These tracer particles exhibit significant enhanced diffusion and mixing due to the collective swimming of cells.

YB886-Time-Lapse-onset.avi: A time-lapse recording of the onset of collective behaviour in *B. subtilis* cells on an oxygen plasma treated surface. Illustrates the progressive formation of vortices and enhanced diffusion of tracer particles.

DS1919-Labelled-run/tumble-5fps.avi: Fluorescently labelled *B. subtilis* performing a run and tumble played back at 5fps. Initially the cell performs a run event where two propulsive bundles are observed, lasting for ~ 1.2 s. The run is terminated by a tumble event where polymorphic transitions occur lasting for fractions of a second, where the cell re-orientates and swims deeper into the sample.

YB886-Reversing-Bright-field.avi: *B. subtilis* cell performing a reversal manoeuvre with out body reorientation when confronted with the contact line of the bead indicated in by the red line.

DS1919-Labelled-Reversing-10fps.avi: Fluorescently labelled *B. subtilis* cell performing a reversal manoeuvre, showing the flagella filaments flipping to the opposing end very rapidly. Video played back at 10 fps to highlight the flagella flipping.

HCB1-Labelled-Reversing-10fps.avi: Fluorescently labelled *E. coli* cell performing a reversal manoeuvre, where flagella filaments flip to the opposing end

forming a new bundle. The video is played back at 10fps where polymorphic transition can be made out.

YB886-Group-Reversal.avi: *B. subtilis* cells suspended between coverslips in a monolayer at the edge of the sample. It shows cell individual cells reversing and occasionally cell reversing simulations in clusters, supportive evidence of quorum polarity.

DS1919-Lablled-Collecitve-swimming.avi: A tracer amount of fluorescently stained *B. subtilis* suspended between two oxygen plasma coverslips exhibiting correlated behaviour in a monolayer. Flagella bundle arrangements are observed in the setting of collective behaviour.

Bibliography and References

[1] K. Barker, *At the bench: a laboratory navigator.* Cold Spring Harbor, N.Y. Cold Spring Harbor Laboratory Press, (2005).

[2] S. M. Hong, S. H. Kim and J. H. Kim, H. I. Hwang, *Hydrophilic Surface Modification of PDMS Using Atmospheric RF Plasma.* Institute of Physics Publishing Journal of Physics: Conference Series **34**:656–661, (2006).

[3] L. Turner, W. S. Ryu and H. C. Berg, *Real-time imaging of fluorescent flagellar filaments.* J. Bacteriol, **182**:2793-2801, (2000).

[4] G. Kuwajima, J. Asaka, T. Fujiwara, K. Node, and E. Kondo, *Nucleotide sequence of the hag gene encoding flagellin of Escherichia coli.* J. Bacteriol, **168**: 1479–1483, (1986).

[5] N. C. Darnton, L. Turner, S. Rojevsky, and H. C. Berg, *On Torque and Tumbling in Swimming Escherichia coli,* Journal of bacteriology, **189**:1756–1764, (2007).

[6] H. C. Berg, *E. coli in Motion,* Biological and Medical Physical Series, Spring Verlag, (2003).

[7] H. C. Berg, *The rotary motor of bacterial flagella,* Annu.Rev.Biochem, **72:**19-54, (2003).

[8] David Hames and Nigel Hooper, *Biochemistry* Third Edition, Taylor and Francis Group published, 0-4153-6778-6, (2005).

Publications

M. Li, and J. Arlt, *Trapping multiple particles in single optical tweezers*. Optics Communications, **281**:135-140, (2008).

L. Wilson, **M. Li**, J. Schwarz-Linek, V. A. Martinez, J. Arlt and W. Poon, '*Darkfield Flicker Microscopy: Measuring Bacterial Swimming at High Speed. In preparation.*